STRESS FIELD CONTROL OF ERUPTION DYNAMICS

EDITED BY: Roberto Sulpizio, Antonio Costa and Geoffrey Wadge
PUBLISHED IN: Frontiers in Earth Science

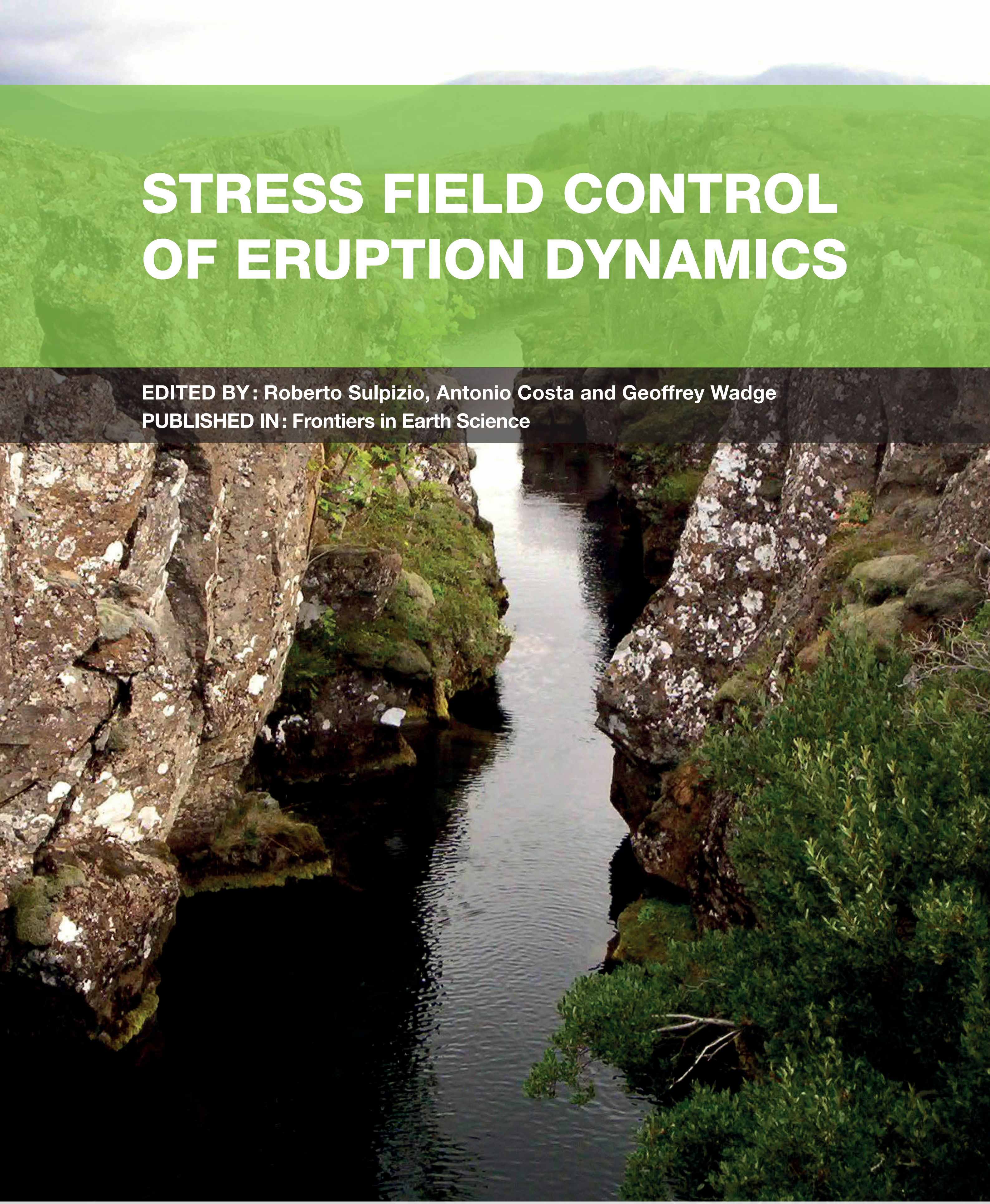

frontiers Research Topics

ISSN 1664-8714
ISBN 978-2-88945-277-4
DOI 10.3389/978-2-88945-277-4

About Frontiers

Frontiers is more than just an open-access publisher of scholarly articles: it is a pioneering approach to the world of academia, radically improving the way scholarly research is managed. The grand vision of Frontiers is a world where all people have an equal opportunity to seek, share and generate knowledge. Frontiers provides immediate and permanent online open access to all its publications, but this alone is not enough to realize our grand goals.

Frontiers Journal Series

The Frontiers Journal Series is a multi-tier and interdisciplinary set of open-access, online journals, promising a paradigm shift from the current review, selection and dissemination processes in academic publishing. All Frontiers journals are driven by researchers for researchers; therefore, they constitute a service to the scholarly community. At the same time, the Frontiers Journal Series operates on a revolutionary invention, the tiered publishing system, initially addressing specific communities of scholars, and gradually climbing up to broader public understanding, thus serving the interests of the lay society, too.

Dedication to Quality

Each Frontiers article is a landmark of the highest quality, thanks to genuinely collaborative interactions between authors and review editors, who include some of the world's best academicians. Research must be certified by peers before entering a stream of knowledge that may eventually reach the public - and shape society; therefore, Frontiers only applies the most rigorous and unbiased reviews.
Frontiers revolutionizes research publishing by freely delivering the most outstanding research, evaluated with no bias from both the academic and social point of view.
By applying the most advanced information technologies, Frontiers is catapulting scholarly publishing into a new generation.

What are Frontiers Research Topics?

Frontiers Research Topics are very popular trademarks of the Frontiers Journals Series: they are collections of at least ten articles, all centered on a particular subject. With their unique mix of varied contributions from Original Research to Review Articles, Frontiers Research Topics unify the most influential researchers, the latest key findings and historical advances in a hot research area! Find out more on how to host your own Frontiers Research Topic or contribute to one as an author by contacting the Frontiers Editorial Office: **researchtopics@frontiersin.org**

STRESS FIELD CONTROL OF ERUPTION DYNAMICS

Topic Editors:
Roberto Sulpizio, Università di Bari, Italy
Antonio Costa, Istituto Nazionale di Geofisica e Vulcanologia, Italy
Geoffrey Wadge, Centre for Observation and Modelling of Earthquakes, Volcanoes and Tectonics (COMET), University of Reading, United Kingdom

The mid-Atlantic ridge emerging to the surface in Pingvellir (Iceland). American plate to the left, European Plate to the right. All deposits are lava flows.

Photo by R. Sulpizio, 2008

Increasing evidence supports the claim that stress changes play a fundamental role in triggering volcanic eruptions. Stress changes may vary in origin to include earthquakes, erosion and landslide processes, deglaciation, or tidal effects. The local stress can also change as response of magma influx from deeper reservoirs and an increase of the magma/gas pressure. The stress transfer may be of great importance in reawakening a dormant system. As an example, significant statistical correlation of large earthquakes and eruptions in time and space was suggested in many works. The interaction may be two-fold; where magma intrusions may change the stress at active faults and trigger earthquakes, while tectonic earthquakes may affect the magmatic system and change the eruption activity.

The change in local tectonic stress has been claimed as trigger of large ignimbrite eruptions or for controlling the eruptive style of explosive eruptions. Sometimes volcano systems that are nested or closely located may become active in chorus; neighbouring volcanoes may interact in the sense that one volcano triggers its neighbouring volcano. However, although there is ample evidence of concurrence, the processes of interacting volcanoes and near- to far-field tectonic stress are not well understood. Some studies suggest that volcanic eruptions are triggered if compressive stress acts at the magma system and “squeezes” out magma. Other studies suggest that extensional stress fields facilitate magma rise and thus encourage eruptions, or that fluctuating compression and extension during the passing of seismic waves trigger eruptions.

This research topic tries to address some of the important open questions in interaction between stress field and volcanic eruption, though bith review papers and new contributions.

Citation: Sulpizio, R., Costa, A., Wadge, G., eds. (2017). Stress Field Control of Eruption Dynamics. Lausanne: Frontiers Media. doi: 10.3389/978-2-88945-277-4

Table of Contents

frontiers in Earth Science

EDITORIAL
published: 11 July 2017
doi: 10.3389/feart.2017.00057

Editorial: Stress Field Control of Eruption Dynamics

Roberto Sulpizio[1], Antonio Costa[2] and Geoffrey Wadge[3]*

[1] *Dipartimento di Scienze della Terra e Geoambientali, Università degli Studi di Bari Aldo Moro, Bari, Italy,* [2] *Istituto Nazionale di Geofisica e Vulcanologia, Bologna, Italy,* [3] *Centre for Observation and Modelling of Earthquakes, Volcanoes and Tectonics (COMET), Department of Meteorology, University of Reading, Reading, United Kingdom*

Keywords: volcanology, stress-field, eruption trigger, eruption dynamics, tectonic stress

Editorial on the Research Topic

Stress Field Control of Eruption Dynamics

The state of stress in the Earth's crust is a fundamental geophysical variable. That stress is transmitted across the boundaries between magma bodies and their host rocks, forming an undoubted potential causal link. But for almost all volcanoes we have no direct observational knowledge of the state of stress within and below them.

We know, in general, that the 3D field of stress acting on a volcanic system can dramatically affect eruption dynamics controlling processes of magma storage and magma ascent to the surface. Stresses act at different scales, and both local to regional stress can significantly affect rock-magma mechanics in a very complex way because of nonlinear interactions between the different parts of the volcanic system and heterogeneity of the Earth's crust. A change in stress within the magmatic system can play a fundamental role in triggering or modifying the style of volcanic eruptions, and even reawakening a dormant system. There are many forcing agents of changes in stress, including earthquakes, erosion and landslides, deglaciation, and tidal effects. The local stress can change also as response of magma influx from deeper reservoirs and an increase of the magma/gas pressure. Such changes can occur on different time scales dictating variations in the behavior of a volcanic system. Change in local tectonic stress has been invoked as a trigger of large ignimbrite eruptions or for controlling the eruptive style of explosive eruptions. Sometimes volcano systems that are closely located may become active in chorus after strong earthquakes. Some studies suggest that volcanic eruptions are triggered if compressive stress acts at the magma system and "squeezes" out magma (Rikitake and Sato, 1989). Other studies suggest that horizontally extensional stress fields facilitate magma rise and thus encourage eruptions (e.g., Gudmundsson, 1990, 2006), or that fluctuating compression and extension during the passing of seismic waves trigger eruptions (Walter and Amelung, 2007; Watt et al., 2009). Stress-sensitive volcanic processes are generally not well understood and we urgently need new observational techniques and improved analytical tools to improve that understanding. All these considerations inspired the Research Topic on "Stress field control of eruption dynamics," which aimed for a thorough discussion about the state of the art, new ideas, perspectives, and challenges of the interplay between stress fields and volcanic activity.

The papers comprising the Research Topic cover a broad range of stress mechanisms affecting volcanic activity. Two reviews introduce the influence of stress change on eruption initiation and dynamics (Sulpizio and Massaro) and stress control on monogenetic volcanism (Martì et al.). The large-scale influence of tectonic stress on volcanism is discussed in two other papers (Wadge et al. Paguican and Bursik), which focus on the East African Rift and the Hat Creek Graben region, USA, respectively. The role of local stress in distinct volcanic scenarios is presented in three papers: syn-eruptive dynamics during caldera forming events (Costa and Martì), the opening of new vents at a mature stratovolcano like Etna (Acocella et al.), and the distribution of eruptive fissures due to

OPEN ACCESS

Edited and reviewed by:
Valerio Acocella,
Roma Tre University, Italy

****Correspondence:***
Roberto Sulpizio
roberto.sulpizio@uniba.it

Specialty section:
This article was submitted to
Volcanology,
a section of the journal
Frontiers in Earth Science

Received: *30 May 2017*
Accepted: *26 June 2017*
Published: *11 July 2017*

Citation:
Sulpizio R, Costa A and Wadge G
(2017) Editorial: Stress Field Control of
Eruption Dynamics.
Front. Earth Sci. 5:57.
doi: 10.3389/feart.2017.00057

magma chamber pressure variations (Geshi and Oikawa). The final article presents a methodology, with a few examples of application, for determining stress field in active volcanoes using focal mechanisms of earthquakes (Massa et al.).

The papers supply an up-to-date view of some important factors controlling the interplay between stress field and volcanic activity, although they represent only a sampling of the possible interactions. It emerges that the stress field can influence the eruption initiation and its dynamics, provided that the volcanic system is sufficiently close to an eruptive threshold. This is because the energy needed to trigger an eruption is usually too large for most induced stress changes to achieve (Sulpizio and Massaro). In the vicinity of large magma chambers the local stress field deviates substantially from the tectonic stress field, and controls the orientation of eruptive fissures (Geshi and Oikawa) and in the opening of new vents (Acocella et al.) even at mature central volcanoes. In the absence of large magma chambers the control of tectonic stress and its local variations play a major role in the location and frequency of volcanic activity, as in the case of monogenetic volcanism (Martì et al.) or in rift systems (Wadge et al.). The interplay between tectonic stress and volcanic activity is also a geomorphologic agent able to shape the landscape, with cascade effects on basin evolution (Paguican and Bursik). For large-scale eruptions, the control of stress field on magma pathways can control the eruptive behavior of caldera forming events, and their intensities (Costa and Martì). Beyond these inferred lines of evidence, the quantification of stress field at volcanic systems remains elusive and difficult to assess. The method based on focal mechanisms of earthquakes (Massa et al.) is valuable in this regard, together with local studies of seismic anisotropy.

Beyond the results described in this Research Topic, a more quantitative understanding of stress field control on the different interacting parts of a volcanic system, acting on different time scales, is crucial for volcanic risk mitigation and represents one of the biggest challenges of the volcanological community. Among many, we believe that the main research lines to be pursued and developed in the near future are those dealing with (i) timing of response of magma reservoirs to external perturbations, (ii) definition of a critical state of a magma batch in relation to an external perturbation, (iii) feedback effects of stress induced by emplacement of magma at shallow crustal levels and growth of magma chambers, (iv) responses of deep magma reservoirs to strong earthquakes and their effects on shallow magma chambers.

AUTHOR CONTRIBUTIONS

All authors listed have made a substantial, direct and intellectual contribution to the work, and approved it for publication.

REFERENCES

Gudmundsson, A. (1990). Emplacement of dikes, sills and crustal magma chambers at divergent plate boundaries. *Tectonophysics* 176, 257–275. doi: 10.1016/0040-1951(90)90073-H

Gudmundsson, A. (2006). How local stresses control magma-chamber ruptures, dyke injections, and eruptions in composite volcanoes. *Earth Sci. Rev.* 79, 1–31. doi: 10.1016/j.earscirev.2006.06.006

Rikitake, T., and Sato, R. (1989). Up-squeezing of magma under tectonic stress. *J. Phys. Earth* 37, 303–311.

Walter, T. R., and Amelung, F. (2007). Volcanic eruptions following M_9 megathrust earthquakes: implications for the Sumatra-Andaman volcanoes. *Geology* 35, 539–542. doi: 10.1130/G234 29A.1

Watt, S. F. L., Pyle, D. M., and Mather, T. A. (2009). The influence of great earthquakes on volcanic eruption rate along the Chilean subduction zone. *Earth Planet. Sci. Lett.* 277, 399–407. doi: 10.1016/j.epsl.2008.11.005

Conflict of Interest Statement: The authors declare that the research was conducted in the absence of any commercial or financial relationships that could be construed as a potential conflict of interest.

frontiers in Earth Science

REVIEW
published: 03 March 2017
doi: 10.3389/feart.2017.00018

Influence of Stress Field Changes on Eruption Initiation and Dynamics: A Review

*Roberto Sulpizio * and Silvia Massaro*

Dipartimento di Scienze della Terra e Geoambientali, Università degli Studi di Bari, Bari, Italy

We review here three main (first-order) mechanisms of stress variation able to influence the triggering of volcanic eruptions and the possible impact on eruption dynamics. They are short- and long-term unloading, seismic energy effects, and changes in far field stress due to geodynamic processes. We present an equilibrium equation for rupture of magma chamber and opening of a dyke up to the surface, taking into account the contribution of each mechanism within the equation. The equation considers the effect of possible superimposition of the three mechanisms with internal processes to the magmatic system, and it is also used for discussing the possible influence on eruption dynamics. The different possible contribution to the eruption triggering are discussed for each mechanism, highlighting how, in many cases, a single mechanism alone is not sufficient for driving eruptive activity if the magmatic system is not close to eruptive conditions.

Keywords: stress change, volcanic eruptions, eruptive dynamics, unloading, seismic energy, far field stress

Edited by:
Thorvaldur Thordarson,
University of Iceland, Iceland

Reviewed by:
Agust Gudmundsson,
University of London, UK
Sonia Calvari,
Istituto Nazionale di Geofisica e Vulcanologia, Italy

***Correspondence:**
Roberto Sulpizio
roberto.sulpizio@uniba.it

Specialty section:
This article was submitted to Volcanology, a section of the journal Frontiers in Earth Science

Received: *27 August 2016*
Accepted: *10 February 2017*
Published: *03 March 2017*

Citation:
Sulpizio R and Massaro S (2017) Influence of Stress Field Changes on Eruption Initiation and Dynamics: A Review. Front. Earth Sci. 5:18. doi: 10.3389/feart.2017.00018

INTRODUCTION

Increasing evidence supports the idea that stress changes play a fundamental role in triggering volcanic eruptions and in controlling their dynamics (Hill et al., 2002; Manga and Brodsky, 2006).

Stress changes in volcanic areas may vary in origin due to short- or long-term processes (Gudmundsson and Philipp, 2006; Andrew and Gudmundsson, 2007; Watt et al., 2008; Plateaux et al., 2014). The first includes earthquakes and landslides (Stein, 1999; Hill et al., 2002; Harris and Ripepe, 2007; Walter, 2007; Walter et al., 2007; Watt et al., 2008; De la Cruz-Reyna et al., 2010), while the second comprises unloading due to erosion and deglaciation (Davydov et al., 2005; Sigmundsson et al., 2010), tidal effects (Sohn, 2004; Cazaneve and Chen, 2010), or changes in the tectonic regime (Ventura and Vilardo, 1999; Waite and Smith, 2004; Diez et al., 2005; Miura and Wada, 2007; Lehto et al., 2010; Carbone et al., 2014). These processes superimpose to the possible local stress variations related to internal dynamics of a volcano, such as pressure increase in the magma chamber due to magma influx from depth or buoyancy induced by magma differentiation processes (Massol and Jaupart, 1999; Gudmundsson, 2006, 2016; Cañon-Tapia, 2014). Although usually claimed for explaining eruptive style transitions (i.e., from effusive to explosive, or from no-activity to eruption, Hasabe et al., 2001; Adams et al., 2006; Ida, 2007; Di Traglia et al., 2009; Schneider et al., 2012; Ripepe et al., 2013; Kereszturi et al., 2014), the magmatic processes internal to a volcano alone are sometimes not sufficient for equalling the elastic energy due to lithostatic loading (e.g., Gudmundsson, 2016; Sulpizio et al., 2016). In other cases the physical and chemical characteristics of the deposits do not support triggering mechanisms like magma mixing or bubble nucleation. For example, arrival of gas rich magma in a magmatic system or magma evolution within the chamber itself are usually claimed for explaining transitions from effusive to explosive eruptions, even in cases in which the geological evidences are lacking (i.e., the erupted material is poorly vesicular, as in the case of many basaltic eruptions; Fink et al., 1992; Wylie et al., 1999). In other cases, the arrival of fresh magma into a magma chamber is postulated as trigger magma chamber rupture and eventually fed an eruption, even in the absence of petrological evidences (i.e., mingling and mixing; e.g., Davì et al., 2011). All these considerations claim for discussion about the state of the art and perspectives about the interplay between volcanic activity and changes in the stress field. This review has not the presumption of being exhaustive of all the knowledge on stress changes and volcanic eruptions, but we will critically review the main mechanisms inducing short- and long-term stress changes at volcanoes, and their possible influence on eruption initiation and its dynamics. The review is intended to focus on the first order effects of stress change. In particular, the changing strength and strain energy due to not homogeneous lithosphere or different volcano edifice (e.g., Gudmundsson, 2012a, 2016) is not explicitly discussed, although they are implicitly contained in the equations describing the driving/resisting pressures. The review is organized in four main chapters: stress changes due to unloading, effects of seismic energy, changes in regional stress field (far field), and influence of stress change on eruption dynamics.

STRESS CHANGES DUE TO UNLOADING

The unloading processes are the most common way to change the lithostatic load. This may induce fracture initiation/propagation, which changes the lithostatic component of the stress at any point in the lithosphere and, ultimately, may result in eruption initiation. The importance of unloading processes on volcanic activity is testified by the long-term eruptive histories of many volcanoes, which reveal that changes in eruption rate and/or magma composition follows partial destruction of the edifice (Presley et al., 1997; Hildenbrand et al., 2004; Hora et al., 2007; Longprè et al., 2009; Boulesteix et al., 2012).

The unloading can be a short- or long-term process, and the different mechanisms will be reviewed following the temporal scale of action.

Long-Term Processes

Many surface load variations occurring over a long time scale (such as deglaciation at mid high latitudes) have been suggested to have a significant impact on eruptive behavior (Jellinek et al., 2004; Sinton et al., 2005; Sigmundsson et al., 2010; Geyer and Bindeman, 2011; Hooper et al., 2011). A retreating ice cap of limited dimensions and thickness (e.g., radius of only a few kilometers) will affect only the shallowest parts of a magmatic system. Conversely, a retreating ice cap with a radius of tens of kilometers or more may influence the generation of melt down to the mantle (Gudmundsson, 1986; Andrew and Gudmundsson, 2007; Sigmundsson et al., 2010).

This can be expressed in a simple way considering the expression of pressure in the elastic Earth:

$$P = p_0(\sigma_{xx} + \sigma_{yy} + \sigma_{zz}) \tag{1}$$

or, in cylindrical coordinates:

$$P = \frac{1}{3}p_0(\sigma_{xx} + \sigma_{yy} + \sigma_{zz}) \tag{2}$$

where $p_0 = rgh$, σ_{rr}, $\sigma_{\theta\theta}$, and σ_{zz} the radial, tangential and vertical stress, respectively (**Table 1**).

Considering a disc load, the vertical stress at a depth z in the Earth crust and distance R from the load center can be expressed as Davis and Selvadurai (2001) and Pinel and Jupart (2004):

$$\sigma_{zz} = p_0\left[1 - \frac{z^3}{\left(R^2 + z^2\right)^{3/2}}\right] \tag{3}$$

The other two horizontal stress components are equal to:

$$\sigma_{rr} = \sigma_{\theta\theta} = \frac{p_0}{2}\left[(1 + 2\nu) - \frac{2(1 + \nu)z}{\sqrt{(R^2 + z^2)}} + \frac{z^3}{(R^2 + z^2)^{3/2}}\right] \tag{4}$$

where ν the Poisson ratio here equal to 0.5. Taking into account equations (2) to (4) the pressure under a disc load overlying an elastic space is:

$$P = \frac{2}{3}p_0(1 + \nu)\left[1 - \frac{z}{\sqrt{(R^2 + z^2)}}\right] \tag{5}$$

It is evident that for $R \rightarrow \infty$ both stress and pressure simplify to lithostatic. The influence of disc load is greater in the upper crust, while it decreases with depth (increasing z).

Using these equations Sigmundsson et al. (2010) calculated the influence of unloading due to melting of an ice cap (**Figure 1**). The calculations were performed for two different ice models, both with radius 50 km and constant thinning rate during 110 years. The first model has a uniform thinning rate of 50 cm year^{-1} (corresponding to surface pressure change of 4.5 kPa year^{-1}). The second model thins by 25 cm year^{-1} between 0 and 30 km, and by 62 cm year^{-1} between 30 and 50 km (**Figure 1**). It can be seen that the pressure decrease is, in average, around 4–5 kPa year^{-1} in the first 10 years, increasing up to 6–7 kPa year^{-1} after 110 years. It means an average reduction of pressure of 0.5–0.6 MPa in about one century. It is worth nothing that the main part of pressure decrease is located in the upper 10–15 km (**Figure 2**), which is also the location of shallow magma chambers and magmatic feeding/conduit systems.

The effects on a shallow magma chamber can be numerically simulated considering it as a cavity of an idealized shape (sphere or ellipsoid) within an elastic homogeneous crust and filled

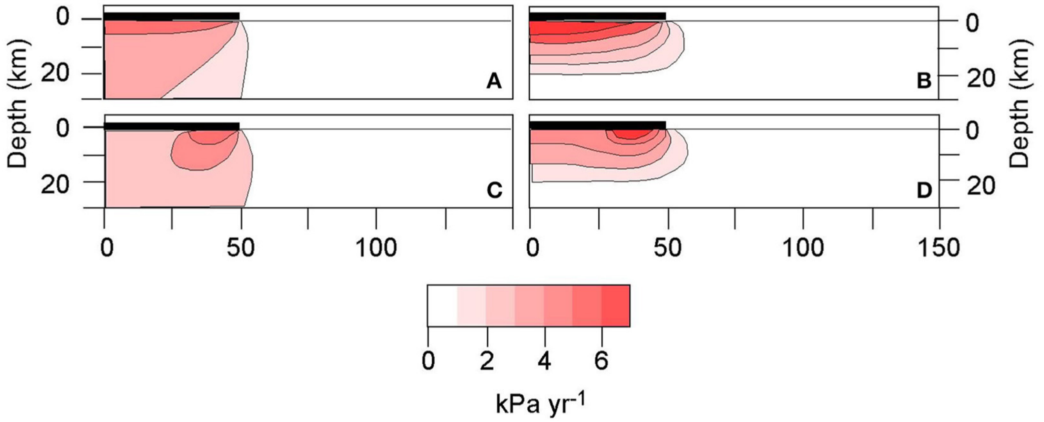

FIGURE 1 | Pressure decrease below a melting ice cap (modified after Sigmundsson et al., 2010). Results shows two different ice caps, both with radius 50 km and constant thinning rate during 110 years. **(A,B)** Uniform thinning rate of 50 cm year^{-1} (corresponding to surface pressure change of 4.5 kPa year^{-1}). **(C,D)** Thinning rate of 25 cm year^{-1} between 0 and 30 km, and of 62 cm year^{-1} between 30 and 50 km. The final volume reduction is the same in both models. **(A,C)** Average yearly stress change in the initial 10 years after thinning begins. **(B,D)** Average yearly stress changes 100–110 years after the beginning of thinning.

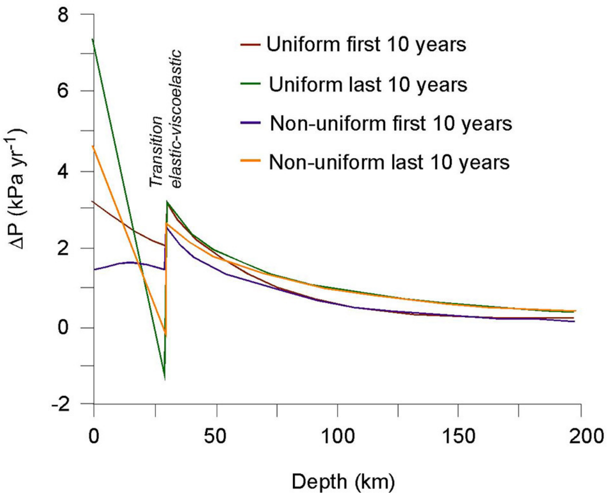

FIGURE 2 | Pressure release under an axisymmetric ice cap vs. depth, calculated for uniform and non-uniform retreating in initial 10 years and last 10 years (modified after Sigmundsson et al., 2010).

with an inviscid fluid. The magma has the same density of the surrounding crust and the reference state is lithostatic. Although strong, these assumptions can provide a first order picture of the unloading effects on a shallow reservoir (Gudmundsson, 2006).

Surface load variation induces a magma pressure change (ΔP_m) and a modification of the excess magma pressure required for dyke initiation P_e (Gudmundsson, 2012b). The failure of the chamber wall that marks the dyke initiation occurs when the minimum compressive deviatoric stress reaches the tensile strength (T_0) of the host rocks (Pinel and Jaupart, 2005; Gudmundsson, 2012b). Applying this rupture criterion in three dimensions, the ΔP required for dyke initiation can be defined (Albino et al., 2010). However, to allow dyke propagation we need a sufficient magma overpressure (P_o, also named driving pressure and net pressure, values up to several tens of MPa), which is the driving mechanism of a hydrofracture (a fluid-driven extension fracture; Gudmundsson, 2012b). Overpressure is the result of the combined effects of the initial excess pressure in the magma chamber, the (eventual) magma buoyancy, and the lithostatic load (Gudmundsson, 2006). It also acts against the normal stress applied on the potential dyke fracture before magma emplacement, and it coincides with the minimum principal compressive stress σ_3. A general form to express overpressure is (Gudmundsson, 1990, 2012b):

$$P_0 = P_e + (\rho_r - \rho_m)\, g h_1 + \sigma_d + R_f \tag{6}$$

where deviatoric stress $\sigma_d = \sigma_1 - \sigma_3$, and ρ_r is the rock density and ρ_m the magma density (**Table 1**). To allow a dyke to reach the surface and feed an eruption a minimum overpressure (ΔP_{0m}) is required, in order to maintain the dyke open (Anderson, 1936; Costa et al., 2007). Taking also into account the viscous and frictional resisting forces per unit area (R_f) the Equation (6) changes into:

$$P_0 - \Delta P_{0m} = P_e + (\rho_r - \rho_m)\, g h_1 + \sigma_d + R_f \tag{7}$$

where h_1 indicates the different height of magma column during dike propagation to the surface.

Equation (6) considers the condition for dyke initiation, while the Equation (7) highlights constrains for dyke to reach the surface and feed an eruption. Because lithospheric inhomogeneity is not here considered, Equation (7) does not contain some important constraints for dyke propagation like stress barriers, elastic mismatch, and Cook-Gordon delamination (Gudmundsson, 2011). Defining ΔF_g as the difference in gravitational force at chamber rupture and at an arbitrary time during dyke propagation [$\Delta F_g = (\rho_r$

TABLE 1 | List of symbols used in the text and equations.

Notation	Description	Unit
σxx, σyy, σzz	Stress component in the Cartesian coordinates	Pa
σrr, $\sigma\theta\theta$, σzz	Stress component in the Cylindrical coordinates	Pa
σ_1	Maximum stress component	Pa
σ_3	Minimum stress component	Pa
σ_d	Deviatoric stress	Pa
σ_l	Lithostatic stress	Pa
σ_e	Seismic stress	Pa
σ_{ff}	Far field stress	Pa
σ_{tec}	Homogeneous horizontal tensile stress	Pa
σ_t	Total stress field	Pa
ν	Poisson's ratio	
g	Gravitational acceleration	m/s^2
h	Height	m
h_1	Height of magma column during dike propagation	m
h_i	Height of the ice cup	m
h_r	Rock thickness	m
R	Distance from the disc load center	m
R_f	Resisting force per unit area	Pa
ρ	Crustal density	kg/m^3
ρ_m	Magma density	kg/m^3
ρ_r	Rock density	kg/m^3
ρ_i	Ice density	kg/m^3
P	Pressure	Pa
P_l	Lithostatic pressure	Pa
P_0	Driving pressure	Pa
P_e	Excess magma pressure required for dyke initiation	Pa
P_u	Unloading pressure	Pa
ΔP	Pressure variation	Pa
ΔP_m	Magma pressure change	Pa
ΔP_{om}	Minimum magma pressure change	Pa
$\Delta_P(K)$	Pressure reduction within the magma chamber induced by the removal of a surface conical load	Pa
ΔF_g	Difference in gravitational force between chamber rupture and an arbitrary time during dyke propagation	N
E	Young Modulus	Pa
K	Bulk Modulus	Pa
T_o	Tensile strength of the host rocks	Pa
V	Initial volume of the reservoir	m^3
ΔV	Volume variation of the reservoir	m^3
V_e	Erupted volume in presence of edifice collapse	m^3
V_n	Erupted volume in absence of edifice collapse	m^3
D	Effective depth accounting for the total deficit of mass with respect to before rifting	m
W	Graben width	m
z	Depth	m
z_c	Depth below the rift	m
z_{in}	Depth of the crustal reservoir	m
z_1, z_2	Depth of the dyke trajectories	m

$- \rho_m)g(h_1 - h)]$, it is possible to descend that for $\Delta P_{0m} < \Delta F_g + R_f$ only dyke injection is possible but not eruption.

An unloading event always reduces lithostatic load, and therefore it induces changes in σ_d because:

$$\begin{aligned}\sigma_d = \sigma_1 - \sigma_3 &= \left(\rho_r h_r - \rho_i h_i\right) g - \frac{\left(\rho_r h_r - \rho_i h_i\right) g}{\nu - 1} \\ &= \left(\rho_r h_r - \rho_i h_i\right) g \left[1 - \frac{1}{\nu - 1}\right]\end{aligned} \tag{8}$$

where ν is the Poisson's ratio, and ρ_i and h_i the density and thickness of ice cap, respectively (**Table 1**). Equation (7) can therefore be written as:

$$\begin{aligned}P_0 - \Delta P_{0m} = {} & P_e + (\rho_r - \rho_m) gh \\ & + \left(\rho_r h_r - \rho_i h_i\right) g \left[1 - \frac{1}{\nu - 1}\right] + R_f\end{aligned} \tag{9}$$

Magma pressure changes strongly depend on the chamber shape as well as on its depth. As a general rule, dyke propagation is favored for spherical and oblate shapes of magma chambers, whereas it is inhibited for prolated ones (Gudmundsson, 2012b).

In any case, models and simple calculations show that the reduction of stress and pressure may range between a few kPa (10 years' time span) up to less than 1 MPa, about three and one orders of magnitude less than the tensile strength of rocks. This means that, in general, the ice thinning effect on the failure of shallow magma chambers is minimal (Andrew and Gudmundsson, 2007; Sigmundsson et al., 2010), and can be decisive only if the magma batch is close to the rupture conditions.

Short-Term Processes

Numerical modeling have linked short time scale redistribution of surface loads, such as partial destruction of edifices or flank collapse events, to eruption triggering and changes in eruption style (e.g., Pinel and Jaupart, 2005; Manconi et al., 2009). Large flank collapses are common phenomena in the evolution of volcanic edifices, and sometimes these events trigger explosive eruptions (Le Friant et al., 2003; Roverato et al., 2011).

The pressure decrease induced within a magma chamber by the partial destruction of a sub-aerial volcanic edifice can be quantified using an elastic model for the two-dimensional plane strain approximation (Pinel and Jaupart, 2005). Using the same approach, Pinel and Albino (2013) calculated the effect of unloading of a conical edifice over an elastic lithosphere, obtaining similar results than the removal of the ice cap. In particular, they considered a very shallow, elliptical magma batch (top 1 km of depth) filled with fluid of the same density of the surrounding rocks and bulk modulus K. Removing a conical load of 2 km radius, 1 km height, and density 2,800 kg/m^3, induces a change in the magma chamber related to:

$$\Delta P = -K \frac{\Delta V}{V} \tag{10}$$

with V being the initial volume of the reservoir (Pinel and Albino, 2013).

In the vicinity of the reservoir the pressure variation within the crust differs from the homogeneous case (**Figure 3**), being

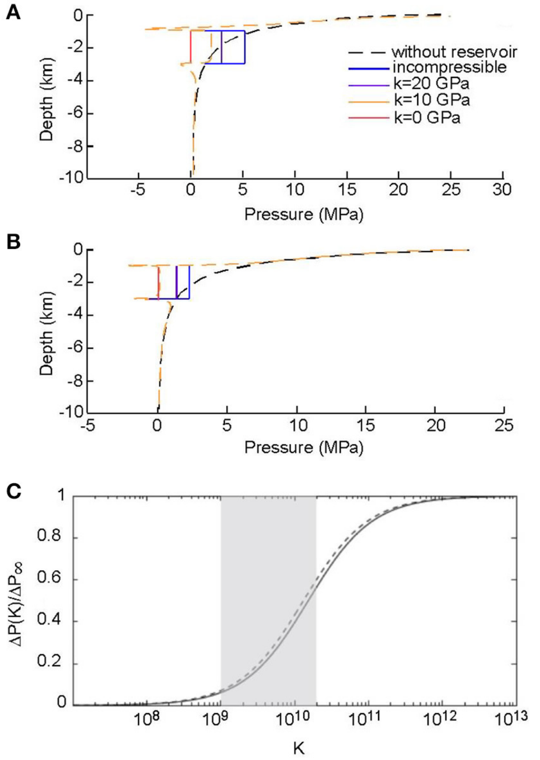

FIGURE 3 | Pressure decrease induced by unloading of a conical edifice (2 km radius, 1 km height, density of 2,800 kg/m^3) within and around a magma chamber. The reservoir is set in an elastic homogeneous space with Young modulus E = 30 GPa and Poisson ratio $\nu = 0.25$. The different lines illustrate the pressure profiles at different values of the magma bulk modulus (from incompressible to compressible magma). **(A)** Spherical chamber (radius 1 km, depth of the chamber top 1 km). **(B)** Prolate chamber (ellipsoid, half-height 1 km, half-width 0.25 km, depth of the chamber top 1 km). **(C)** Pressure reduction within the magma chamber ($\Delta P(K)$) following the removal of a surface conical load ($r = 2$ km, $h = 1$ km, density 2,800 kg/m^3) expressed as a function of the bulk modulus (K) of the magma. Crustal Young modulus and Poisson ratio are equal to 30 GPa and 0.25, respectively. The pressure change is normalized by the pressure change in a incompressible magma (ΔP_∞). The shaded area illustrates the characteristic values for dry magmas. The solid curve is for the spherical chamber and the dashed curve for the prolate one (modified after Pinel and Albino, 2013).

higher for spherical shape than for the prolate one. Pressure also increases at the chamber margins, and is most extreme at the chamber top. This is because the deformation of the magma chamber walls due to unloading is partially counterbalanced by pressure partition within the magma chamber.

The amount of the magma pressure reduction increases with the value of the bulk modulus. This is because for incompressible magmas (larger value of k) no reservoir volume change occurs, and only pressure lowering within the chamber compensates the reduction induced by the unloading event. The effect of compressibility is shown in **Figure 3C**.

Figure 4 shows the pressure reduction within a spherical reservoir with a top at 1 km depth, induced by the removal of the upper 20% volume of the volcano edifice (mean value based on field observations; Voight and Elsworth, 1997). The erupted volume is larger than that in the absence of edifice collapse ($V_e > V_n$; **Table 1**; **Figure 4**) when the small edifices are considered. As the edifice size increases the V_e/V_n ratio decreases. When large strato-volcanoes are partially destroyed by flank collapse this volume reduces to zero, possibly resulting in the abortion of any incipient eruption. Shallow magma batches require smaller edifice size to reach the point of aborted eruption, (**Figure 4A**), whereas deep chambers reduce any effect of edifice collapse on erupted magma volume. This is because any edifice collapse reduces the lithostatic load on the magma batch, and the magma volume required for reaching the eruptive conditions is smaller than in the case of larger edifices or deeper magma chambers (Manconi et al., 2009).

The magma reservoir shape also influences the possibility of eruption following an edifice collapse. **Figure 5** shows that the influence of the collapse is smaller for a prolate reservoir, and a larger edifice size is required than for a spherical reservoir at the same depth. Having a prolate chamber with top at depth of 1 km, eruption is only aborted when the edifice radius is greater than 6 km.

EFFECT OF SEISMIC ENERGY

Earthquakes can stress magmatic systems either through static stresses (the offset of the fault which generates a permanent deformation in the crust) or through dynamic stresses from the seismic waves (Manga and Brodsky, 2006). Both stresses increase with the seismic moment of the earthquake, but they decay in different way with distance r from the generation area. In particular, static stresses decreases as $1/r^3$, whereas dynamic stresses fall off more gradually (as $1/r^{1.66}$) and are proportional to the seismic wave amplitude (e.g., Lay and Wallace, 1995).

The stress transfer due to regional earthquakes may be of great importance in reawakening a dormant system. Previous works suggested a statistical correlation among large earthquakes and eruptions in time and space (Linde and Sacks, 1998; Hill et al., 2002; Marzocchi, 2002; Walter and Amelung, 2007; Walter et al., 2007). However, not all the large earthquakes trigger eruptions, and this is compelling evidence that the magmatic system needs to be ready to erupt under a new energetic equilibrium. This implies that the eruption triggering depends on the initial state of the magmatic system prior to the earthquake (magma composition, volatiles, chamber overpressure, strength of the host rocks, and type, size, and distance of the foci; Hill et al., 2002). In this framework, an important event is the unclamping of previous faults, which is the reduction in normal stress due to earthquake energy.

Dynamic and static deformation due to an earthquake may increase volcanic activity (Hill et al., 2002; Walter and Amelung, 2007). Seismic body and surface waves induce dynamic deformation, whereas displacement across a fault and subsequent viscoelastic relaxation of the crust account for permanent static deformation. A statistically significant response immediately after the earthquake (Linde and Sacks, 1998) has been observed for volcanoes at 750 km or more from the epicenters, suggesting they are triggered by dynamic deformation (Brodsky et al., 1998; Manga and Brodsky, 2006). The effect of static deformation

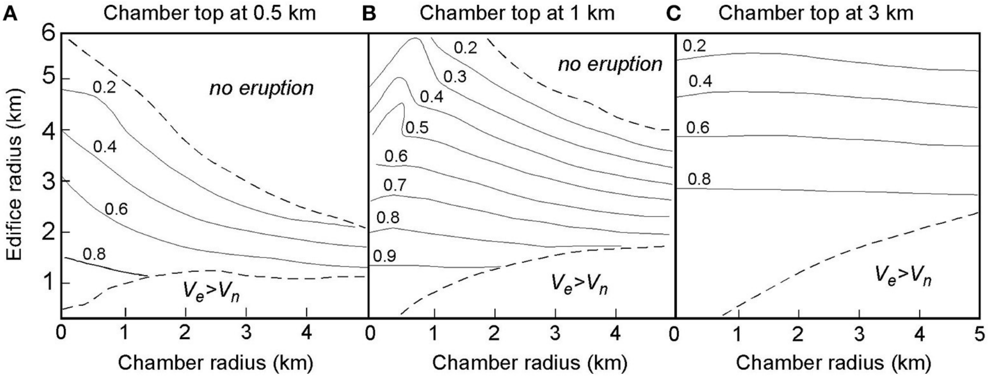

FIGURE 4 | Erupted volume of magma following the removal of the upper 20% of a conical edifice with a slope of 30°. Data presentation is function of the reservoir and edifice radius. Calculations are for a spherical magma chamber filled with incompressible magma. Crustal Poisson ratio is 0.25. Three different values for the magma chamber top depth are considered: **(A)** 0.5 km depth, **(B)** 1 km depth, **(C)** 3 km (modified after Pinel and Albino, 2013).

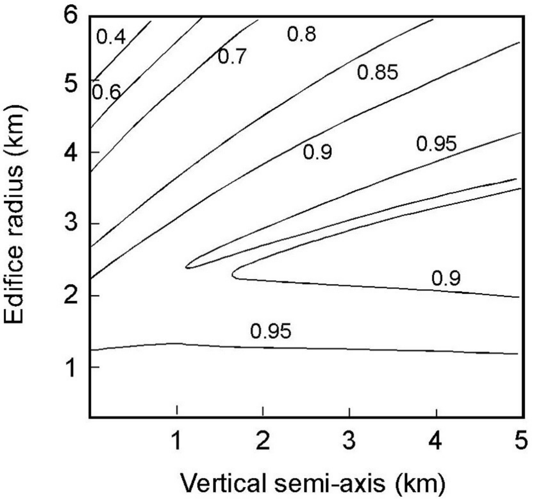

FIGURE 5 | Effects of the removal of the upper 20% volume of a conical edifice (slope of 30°) on the evolution of the erupted volume of magma. Results are presented as a contours of the reservoir vertical semi-axis and edifice radius. Calculations are for a prolate reservoir (top at 1 km depth) filled with incompressible magma. Crustal Poisson ratio = 0.25 (modified after Pinel and Albino, 2013).

in triggering eruptions remains poorly understood and it is unclear whether it is the most effective type of deformation in promoting eruptions (Marzocchi et al., 2002; Selva et al., 2004). The amplitude of static deformation decays more rapidly with distance than the seismic waves (Hill et al., 2002). Follows that to have eruption triggering from static deformation is most likely at volcanoes located in proximity to an earthquake rupture plane.

Classical examples of interaction between earthquakes and volcanic eruptions are the Kamchatka 1952 (M 9.0, followed by renewal of activity at Karpinsky and Maly Semiachik volcanoes, and at the Tao-Rusyr Caldera), Chile 1960 (M 9.5, followed by renewal of activity at Cordón-Caulle Planchón-Peteroa, Tupungatito and Calbuco volcanoes), Alaska 1964 (M 9.2, followed by renewal of activity at Trident and Redoubt volcanoes), Sumatra-Andaman 2004–2005 (M 9.3 and M 8.7, followed by renewal of activity at Talang and Barren Island volcanoes; Sepulveda et al., 2005; Walter and Amelung, 2007). All these examples are from subduction zones, which most of the time are partially locked and accumulate stress that is released during earthquakes (**Figure 6A**). Walter and Amelung (2007) related the triggering of the eruption listed above to the change in volumetric strain, which is the sum of the normal components of the strain tensor. Negative volumetric strain corresponds to volumetric contraction (compressing the rock), and positive volumetric strain corresponds to volumetric expansion (decompressing the rock). Earthquakes in subduction areas are associated with volumetric contraction in the near-trench portion of the forearc and volumetric expansion in the far-trench portion, which is where the volcanic arc is usually located (**Figure 6B**). The main observation is that all the erupted volcanoes underwent volumetric expansion induced by the earthquake. A direct mechanical effect of stress change due to volumetric expansion may be the unclamping of the fissure system. A pre-existing network of cracks may be connected, nucleate and thereby facilitate preferred paths for magma ascent. Unclamping of fracture system was claimed for the earthquake occurred on Kamchatka peninsula on January 1st, 1996 along a SW–NE trending fracture system, which triggered the twin-eruption at the volcanoes Karymsky and Akademia Nauk (Walter, 2007). The earthquake is hypothesized to have prompted dilatation of the magmatic system together with extensional normal stress at intruding N–S trending dykes, allowing magma to propagate to the surface.

Taking into account Equation (10) and adding the contribution of seismic stress, it can be written:

$$
\begin{aligned}
P_0 - \Delta P_{0m} = {} & P_e + (\rho_r - \rho_m)\, gh \\
& + \left(\rho_r h_r - \rho_i h_i\right) g \left[1 - \frac{1}{\nu - 1}\right] + \sigma_e + R_f
\end{aligned}
\tag{11}
$$

NON-SEISMIC CHANGES IN REGIONAL STRESS FIELD

The change in tectonic stress has been claimed as trigger of large ignimbrite eruptions or for controlling the eruptive style of explosive eruptions (Korringa, 1973; Aguirre-Díaz and Labarthe-Hernandez, 2003; Miller and Wark, 2008; Costa et al., 2011).

The first order influence of far-field stress (σ_{ff}) on eruption triggering was investigated using numerical simulations, which demonstrated how the combined effect of crustal extension and magma chamber overpressure can sustain linear dyke-fed explosive eruptions with mass fluxes in excess of 10^{10} kg/s from shallow-seated (4–6 km depth) chambers affected by extensional stress regime (Costa et al., 2011). The model shows that for a far-field stress above the value able to counterbalance the lithostatic pressure at the fragmentation depth (**Figure 7**), a dyke of any length remains opened, and the Mass Eruption Rate (MER) is strongly controlled by the 3D geometry and

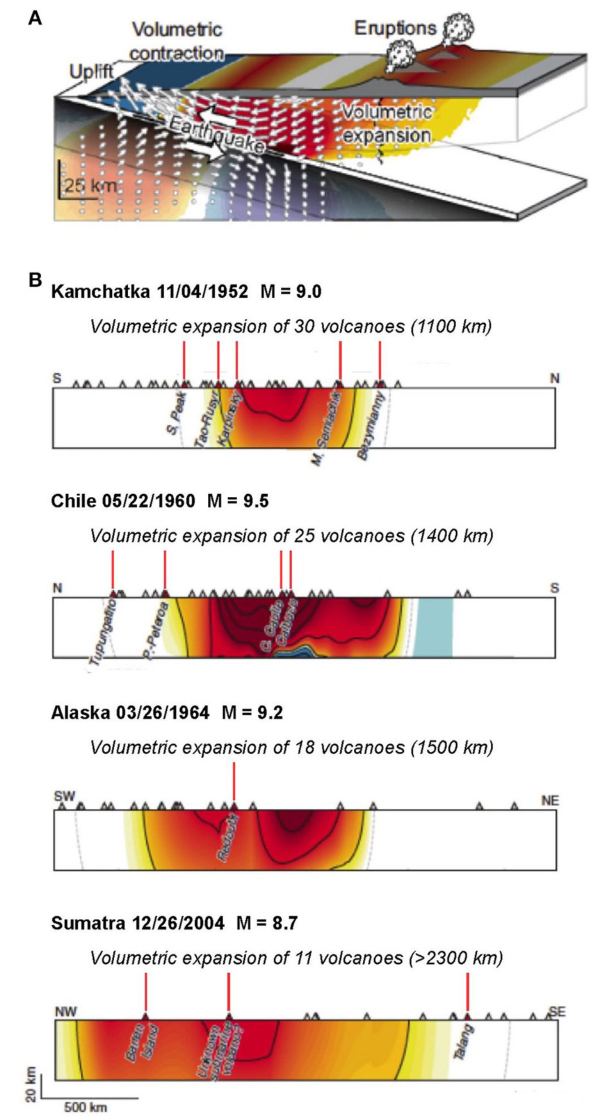

FIGURE 6 | (A) Schematic cross sections of subduction zone. Arrows indicate the displacement field, while colors rank the volumetric deformation (red colors for volumetric expansion, blue colors for volumetric contraction) associated with a megathrust earthquake. **(B)** Volumetric deformation associated with megathrust earthquakes. Triangles indicate the historically active volcanoes. Red lines highlight the volcanoes that erupted within 3 years from earthquakes. Red colors indicate positive strain (volumetric expansion), blue colors indicate negative strain (volumetric contraction). Contours represent 0 μ strain (dashed line) and 5 μ strain increments (solid black lines) (modified after Walter and Amelung, 2007).

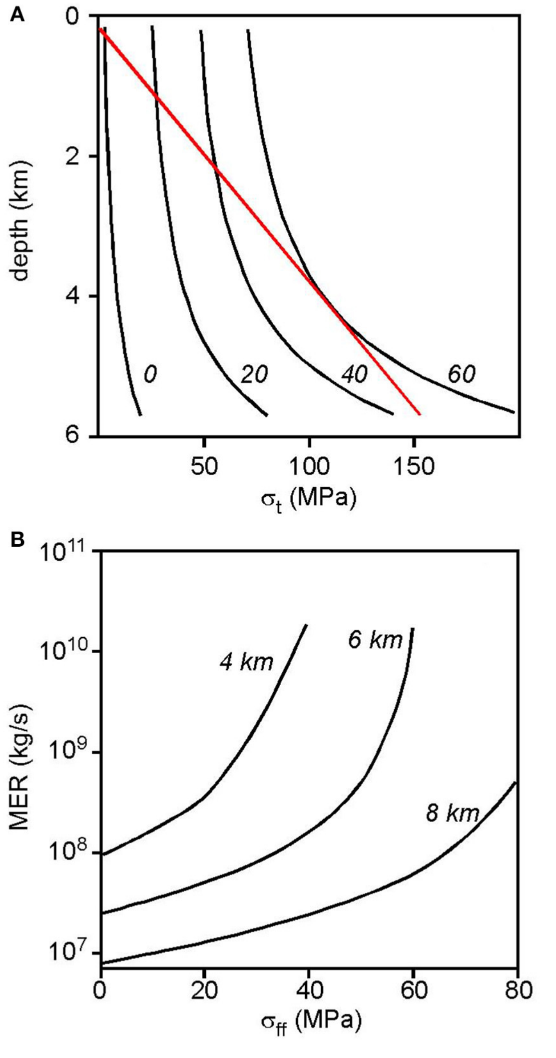

FIGURE 7 | (A) Profile of dyke tensile stress σ_t along the vertical axis obtained using the analytical solution for a pressurized magma chamber under the effect of different far-field extensional stresses. Values between 0 and 60 MPa of the far-field stresses σ_{ff} were considered for a magma chamber with circular cross-section. Red line represents the lithostatic pressure. For σ_{ff} of 40 MPa or larger the dyke remains open throughout its length and magma flow dynamics is mainly controlled by the 3D geometry and extension of the system. **(B)** Maximum Eruption Rate (MER) as a function of extensional stress σ_{ff} for a dyke thickness of 5 m for magma chambers at 4, 6, and 8 km depths and overpressures above lithostatic of 20 MPa, respectively (modified after Costa et al., 2011).

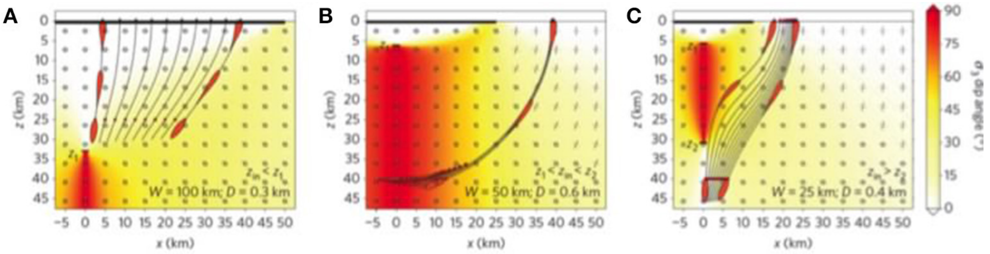

FIGURE 8 | Dyke trajectories for z_{in} above (A), within **(B)**, and below **(C)** the stress barrier zone. Red squares indicate the upper tip of the dyke at injection; red circles indicate that a dyke arrested and formed a sill; red triangles indicate the arrival location at the surface. Black and gray segments show the directions of σ_1 and σ_3, respectively (a circle indicates direction perpendicular to the page), for three nominal sets of graben width (W) and depth (D). The dip angle of σ_3 is color-shaded. Where the dip angle is subvertical (reddish color), a stress barrier to vertical ascent of dykes is acting (modified after Maccaferri et al., 2014).

extension of the system. It is worth noting that the requested value of σ_{ff} is as high as 40–60 MPa, which is not easily matched during normal geodynamic processes. As an example, a homogeneous horizontal tensile stress $\sigma_{tec} = 5$ MPa was used by Maccaferri et al. (2014) for modeling the dyke trajectories in rifting areas. In this model the dyke opens under assigned normal and shear stress given by the internal overpressure and by the shear component of the tectonic plus unloading stresses, respectively. The overpressure within the dyke is set as the difference between the magma pressure and the confining stress, which is the superposition of the lithostatic pressure, the normal component of the topographic unloading and the tectonic stress. When the unloading pressure $P_u = \rho gD$ (ρ is crustal density, g acceleration due to gravity, and D is the effective depth accounting for the total deficit of mass from the topographic depression and low-density sediments with respect to before rifting) dominates over the tectonic tensile stress ($D > \pi\sigma_{tec}/(2\rho g)$, 250 m for $\rho = 3{,}000$ kgm^{-3}), σ_3 becomes vertical beneath the rift in a volume centered at a depth $z_c = \rho gDW/(\pi\sigma_{tec})$, where W is the graben width (**Table 1**; **Figure 8**). The upper limit of the volume is given by $z_1 = (W/2K)(1-(1-K^2)^{1/2})$ and the lower one by $z_2 = (W/2K)(1+(1-K^2)^{1/2})$, where $K = \pi\sigma_{tec}/(2P_0)$ (**Table 1**; Maccaferri et al., 2014).

This volume forms a stress barrier zone, which deflects the ascending dykes to the rift sides.

Sideways from the rift center, σ_3 becomes first inward dipping and then horizontal (**Figure 8**). Three scenarios for dyke propagation and for the final surface distribution of magmatism can occur, depending on where the dykes nucleate relatively to the stress barrier zone. When $z_{in} < z_1$ in-rift volcanism occurs, while off-rift volcanism occurs for $z_1 < z_{in} < z_2$ and $z_{in} > z_2$ (**Table 1**; **Figure 8**).

Incorporating the far-field tectonic stress in Equation (11) we have:

$$P_0 - \Delta P_{0m} = P_e + (\rho_r - \rho_m)\, gh + \left(\rho_r h_r - \rho_i h_i\right) g \left[1 - \frac{1}{\nu - 1}\right] + \sigma_e + \sigma_{tec} + R_f \tag{12}$$

which is the final formulation of driving vs. resisting forces that drives the transition from no eruption to full on eruption.

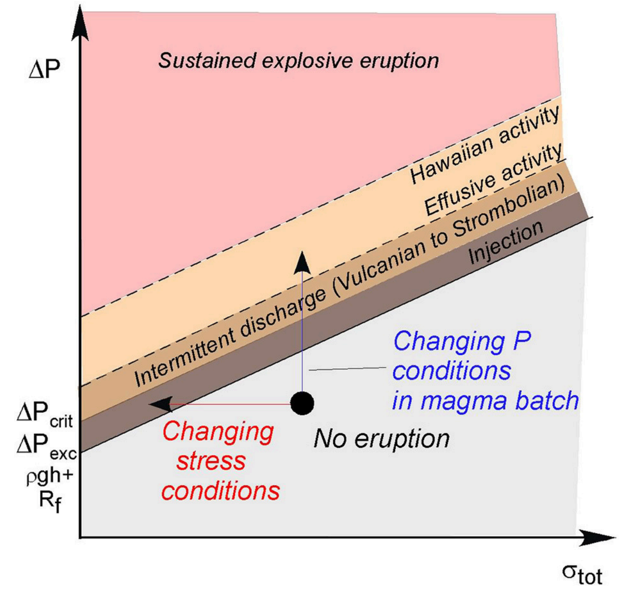

FIGURE 9 | Qualitative representation of the relationships between magmatic overpressure (ΔP) and lithostatic stress (σ_3). Eruption initiation may be triggered by an increase of ΔP at above the critical value ΔP_{crit} (the magma overpressure required to maintain a conduit open from the magma chamber to the surface) or reduction of σ_3 (after Sulpizio et al., 2016).

INFLUENCE ON ERUPTION DYNAMICS

With the only exception of unloading due to ice cap retreat, the above discussed changes in stress field may play a role also in short term variation of eruption style. Complex transitions between effusive and explosive eruptive styles are frequently described in volcanic activity (e.g., Jaupart and Allegre, 1991; Villemant and Boudon, 1998; Adams et al., 2006; Platz et al., 2007) and the alternation of pyroclastic deposits and lavas is common in almost all stratovolcanoes. Shifts in eruptive style have been related to many complex sub-surface processes such as decompression-induced crystallization (Hammer et al., 2000; Blundy and Cashman, 2005), increase in magma viscosity due to groundmass crystallization caused by volatile loss and temperature gradients (Stevenson et al., 1996; Manga, 1998; Melnik and Sparks, 2002; Cashman and Sparks, 2013), and time-dependent release of overpressure due to the contrasting effects of magma viscosity and elastic energy released from country rocks deformation (Wylie et al., 1999).

All these processes can for sure participate to changes in eruptive style, but sharp changes in local or far-field stress may sometimes play a similar role in driving eruptive activity. This is especially true when dealing with changing eruptive style in eruptions or eruptive cycles with similar magmatic composition, which do not account for any petrologic or textural trigger of the changing eruptive behavior. For instance, the interplay between magma overpressure and stress acting on the volcanic system was claimed for explaining the eruptive style transitions of Monte dei Porri (Salina Island, Italy; Sulpizio et al., 2016), and effusive eruptions following local stress decrease due to spreading of the volcanic edifice were repeatedly observed at Mount Etna volcano (Borgia et al., 1992; Froger et al., 2001; Lundgren et al., 2004; Neri et al., 2004).

The contribution of stress lowering to the change of eruptive style can be easily explained using the Equation (12) in the ΔP vs. σ_{tot} space (**Figure 9**; Sulpizio et al., 2016). It shows how a transition from no-eruption to eruption or from a given eruptive style to another is allowed through the superimposition of internal magmatic pressure (increase of ΔP) and changing in the total stress field (σ_t), defined by the sum of all the defined partial stresses defined early.

SUMMARY AND CONCLUSIONS

Understanding the interplay between crustal stress and volcanic activity and its dynamics is essential for comprehension of a number of natural phenomena and for mitigating the related hazards and risk. Significant evidence of coupling between stress change and volcanic events emerges from investigation of tectonic earthquakes, flank collapses, and also long-term processes such as erosion and landslides. The effect of these processes superimposes on changes in magma overpressure, including the growth of gas bubbles and input of new magma in the chamber. This is because, although dyke initiation and propagation to the surface is usually governed by the depth-dependent magma parameters, the source location is also subject to the stress field conditions that vary from one point to another in the crust and that can promote or prevent brittle failures.

During last decades many authors provided precious contributions to this topic, and this review presented the state of the art of the knowledge about some of the main mechanisms inducing stress change and able to influence eruption initiation and dynamics. In particular, we reviewed three main pivotal issues correlated to stress: the unloading and its long- and short-term effects, the seismic energy, and the regional (or far-field) stress changes. Their occurrence alone was used as a preliminary guide in this study.

The contribution of each mechanism has been analyzed, and an equilibrium equation for magma chamber rupture and dyke opening to the surface has been presented. The equation was also used for interpreting the possible changes in eruptive style of single eruptions or eruptive cycles. The three mechanisms can have different impact on magmatic systems, and can influence or not the triggering of volcanic eruptions. However, it emerges clearly from this review how a single mechanism is hardly responsible for eruption initiation, but the concur of internal processes is usually necessary. It emerges how internal (magmatic processes) end external (stress field variations) processes concur in modulating eruptive activity.

AUTHOR CONTRIBUTIONS

All authors listed, have made substantial, direct and intellectual contribution to the work, and approved it for publication.

REFERENCES

Adams, N., Houghton, B. F., Fagents, S. A., and Hildreth, W. (2006). The transition from explosive to effusive eruptive regime: the example of the 1912 Novarupta eruption, Alaska. *Geol. Soc. Am. Bull.* 118, 620–634. doi: 10.1130/B25768.1

Aguirre-Díaz, G., and Labarthe-Hernández, G. (2003). Fissure ignimbrites: fissure-source origin for voluminous ignimbrites of the Sierra Madre Occidental and its relationship with Basin and Range faulting. *Geology* 31, 773–776. doi: 10.1130/G19665.1

Albino, F., Pinel, V., and Sigmundsson, F. (2010). Influence of surface load variations on eruption likelihood: application to two Icelandic subglacial volcanoes, Grimsvötn and Katla. *Geophys. J. Int.* 181, 1510–1524. doi: 10.1111/j.1365-246x.2010.04603.x

Anderson, E. M. (1936). The dynamics of formation of cone sheets, ring dykes and cauldron subsidences. *Proc. R. Soc. Edinb.* 56, 128–163. doi: 10.1017/S0370164600014954

Andrew, R. E. B., and Gudmundsson, A. (2007). Distribution, structure, and formation of Holocene lava shields in Iceland. *J. Volcan. Geotherm. Res.* 168, 137–154. doi: 10.1016/j.jvolgeores.2007.08.011

Blundy, J., and Cashman, K. (2005). Rapid decompression-driven crystallization recorded by melt inclusions from Mount St. Helens volcano. *Geology* 33, 793–796. doi: 10.1130/G21668.1

Borgia, A., Ferrari, L., and Pasquarè, G. (1992). Importance of Gravitational Spreading in the Tectonic and Volcanic Evolution of Mt. Etna. *Nature* 357:231. doi: 10.1038/357231a0

Boulesteix, T., Hildenbrand, A., Gillot, P. Y., and Soler, V. (2012). Eruptive response of oceanic islands to giant landslides: new insigths from the geomorphologic evolution of the Teide-Pico Viejo volcanic complex (Tenerife, Canary). *Geomorphology* 138, 61–73. doi: 10.1016/j.geomorph.2011.08.025

Brodsky, E. E., Sturtevant, B., and Kanamori, H. (1998). Earthquakes, volcanoes, and rectified diffusion. *J. Geophy. Res.* 103, 827–838. doi: 10.1029/98jb02130

Cañon-Tapia, E. (2014). Volcanic eruption triggers: a hierarchical classification. *Earth Sc. Rev.* 129, 100–119. doi: 10.1016/j.earscirev.2013.11.011

Carbone, D., Aloisi, M., Vinciguerra, S., and Puglisi, G. (2014). Stress, strain and mass changes at Mt. Etna during the period between the 1991–93 and 2001 flank eruptions. *Earth Sci. Rev.* 138, 454–468. doi: 10.1016/j.earscirev.2014.07.004

Cashman, K. V., and Sparks, R. S. J. (2013). How volcanoes work: a 25 year perspective. *Geol. Soc. Am. Bull.* 125, 664–690. doi: 10.1130/B30720.1

Cazaneve, A., and Chen, J. (2010). Time-variable gravity from space and present-day mass redistribution in the Earth system. *Earth Planet. Sci. Lett.* 298, 263–274. doi: 10.1016/j.epsl.2010.07.035

Costa, A., Gottsmann, J., Melnik, O., and Sparks, R. S. J. (2011). A stress-controlled mechanism for the intensity of very large magnitude explosive eruptions. *Earth Planet. Sci. Lett.* 310, 161–166. doi: 10.1016/j.epsl.2011.07.024

Costa, A., Melnik, O., and Sparks, R. S. J. (2007). Controls of conduit geometry and wallrock elasticity on lava dome eruptions. *Earth Planet. Sci. Lett.* 260, 137–151. doi: 10.1016/j.epsl.2007.05.024

Davì, M., De Rosa, R., Donato, P., and Sulpizio, R. (2011). The Lami pyroclastic succession (Lipari, Aeolian Islands): a clue for unravelling the eruptive dynamics of the Monte Pilato rhyolitic pumice cone. *J. Volcan. Geotherm. Res.* 201, 285–300. doi: 10.1016/j.jvolgeores.2010.09.010

Davis, R. O., and Selvadurai, A. P. S. (2001). *Elasticity and Geomechanics.* Cambridge, UK: Cambridge University Press 1996.

Davydov, M. N., Kedrinskii, V. K., Chernov, A. A., and Takayama, K. (2005). Generation and evolution of cavitation in magma under dynamic unloading. *J. Appl. Mechan. Technic. Physics* 46, 208–215. doi: 10.1007/s10808-005-0036-2

De la Cruz-Reyna, S., Tárraga, M., Ortiz, R., and Martínez-Bringas, A. (2010). Tectonic earthquakes triggering volcanic seismicity and eruptions. Case studies at Tungurahua and Popocatépetl volcanoes. *J. Volcan. Geotherm. Res.* 193, 37–48. doi: 10.1016/j.jvolgeores.2010.03.005

Diez, M., La Femina, P. C., Connor, C. B., Strauch, W., and Tenorio, T. V. (2005). Evidence for static stress changes triggering the 1999 eruption of Cerro Negro Volcano, Nicaragua and regional aftershock sequences. *Geoph. Res. Lett.* 32, L04309. doi: 10.1029/2004gl021788

Di Traglia, F., Cimarelli, C., de Rita, D., and Gimeno Torrente, D. (2009). Changing eruptive styles in basaltic explosive volcanism: examples from Croscat complet cone, Garrotxa Volcanic Field (NE Iberian Peninsula). *J. Volcan. Geotherm. Res.* 180, 89–109. doi: 10.1016/j.jvolgeores.2008.10.020

Fink, J., Anderson, S. W., and Manley, C. R. (1992). Textural constraints on effusive silicic volcanism: beyond the permeable foam model. *J. Geophys. Res.* 97, 9073–9083. doi: 10.1029/92JB00416

Froger, J. L., Merle, O., and Briole, P. (2001). Active spreading and regional extension at Mount Etna imaged by SAR interferometry. *Earth Planet. Sci. Lett.* 187, 245–258. doi: 10.1016/S0012-821X(01)00290-4

Geyer, A., and Bindeman, I. (2011). Glacial influence on caldera-forming eruptions. *J. Vol. Geotherm. Res.* 202, 127–142. doi: 10.1016/j.jvolgeores.2011.02.001

Gudmundsson, A. (1986). Mechanical aspects of postglacial volcanism and tectonics of the Reykjanes Peninsula, southwest Iceland. *J. Geophys. Res.* 91, 711–721. doi: 10.1029/jb091ib12p12711

Gudmundsson, A. (1990). Emplacement of dikes, sills and crustal magma chambers at divergent plate boundaries. *Tectonophysics* 176, 257–275. doi: 10.1016/0040-1951(90)90073-H

Gudmundsson, A. (2006). How local stresses control magma-chamber ruptures, dyke injections, and eruptions in composite volcanoes. *Earth Sci. Rev.* 79, 1–31. doi: 10.1016/j.earscirev.2006.06.006

Gudmundsson, A. (2011). Deflection of dykes into sills at discontinuities and magma chamber formation. *Tectonophysics* 500, 50–64. doi: 10.1016/j.tecto.2009.10.015

Gudmundsson, A. (2012a). Strengths and strain energies of volcanic edifices: implications for eruptions, collapse calderas, and landslides. *Nat. Hazards Earth Syst. Sci.* 12, 2241–2258. doi: 10.5194/nhess-12-2241-2012

Gudmundsson, A. (2012b). Magma chambers: formation, local stresses, excess pressures, and compartments. *J. Volcanol. Geotherm. Res.* 237–238, 19–41. doi: 10.1016/j.jvolgeores.2012.05.015

Gudmundsson, A. (2016). The mechanics of large volcanic eruptions. *Earth Sci. Rev.* 163, 72–93. doi: 10.1016/j.earscirev.2016.10.003

Gudmundsson, A., and Philipp, S. J. (2006). How local stress fields prevent volcanic eruptions. *J. Vol. Geotherm. Res.* 158, 257–268. doi: 10.1016/j.jvolgeores.2006.06.005

Hammer, J. E., Cashman, K. V., and Voight, B. (2000). Magmatic processes revealed by textural and compositional trends in Merapi dome lavas. *J. Volcanol. Geotherm. Res.* 100, 165–192. doi: 10.1016/S0377-0273(00)00136-0

Harris, A. J. L., and Ripepe, M. (2007). Regional earthquakes as a trigger for enhanced volcanic activity: evidence from MODIS thermal data. *Geoph. Res. Lett.* 34, L02304. doi: 10.1029/2006GL028251

Hasabe, N., Fukutani, A., Sudo, M., and Tagami, T. (2001). Transition of eruptive style in an arc-arc collision zone: K-Ar dating of Quaternary monogenetic and polygenetic volcanoes in the Higashi-Izu region, Izu peninsula, Japan. *Bull. Volcanol.* 63, 377–386. doi: 10.1007/s004450100158

Hildenbrand, A., Gillot, P., and Le Roy, I. (2004). Volcano-tectonic and geochemical evolution of an oceanic intra-plate volcano: Tahiti-Nui (french Polynesia). *Earth Planet. Sci. Lett.* 217, 349–365. doi: 10.1016/S0012-821X(03)00599-5

Hill, D. P., Pollitz, F., and Newhall, C. (2002). Earthquake-volcano interactions. *Phys. Today* 55, 41–47. doi: 10.1063/1.1535006

Hooper, A., Ofeigsson, B., Sigmundsson, F., Lund, B., Einarsson, P., Geirsson, H., et al. (2011). Increased crustal capture of magma at volcanoes with retreating ice cap. *Nat. Geosci.* 4, 783–786. doi: 10.1038/ngeo1269

Hora, J. M., Singer, B. S., and Worner, G. (2007). Volcano evolution and eruptive flux on the thick crust of the Andean Central Volcanic Zone: 40Ar/39Ar constraints from Volcan Parinacota, Chile. *GSA Bull.* 119, 343–362. doi: 10.1130/B25954.1

Ida, Y. (2007). Driving force of lateral permeable gas flow in magma and the criterion of explosive and effusive eruptions. *J. Volcanol. Geotherm. Res.* 162, 172–184. doi: 10.1016/j.jvolgeores.2007.03.005

Jaupart, C., and Allegre, C. (1991). Gas content, eruption rate and instabilities of eruption regime in silicic volcanoes. *Earth Planet. Sci. Lett.* 102, 413–429. doi: 10.1016/0012-821X(91)90032-D

Jellinek, A. M., Manga, M., and Saar, M. O. (2004). Did melting glaciers cause volcanic eruptions in eastern California? Probing the mechanics of dike formation. *J. Geophys. Res.* 109:B09206. doi: 10.1029/2004JB002978

Kereszturi, G., Nemeth, K., Cronin, S. J., Procter, J., and Augustìn-Flores, J. (2014). Influences on the variability of eruption sequences and style transitions in the Aukland Volcanic Field, New Zeland. *J. Volcanol. Geotherm. Res.* 286, 101–115. doi: 10.1016/j.jvolgeores.2014.09.002

Korringa, M. K. (1973). Linear vent area of the Soldier Meadow Tuff, an ash-flow sheet in northwestern Nevada. *Geol. Soc. Am. Bull.* 84, 3849–3866. doi: 10.1130/0016-7606(1973)84<3849:LVAOTS>2.0.CO;2

Lay, T., and Wallace, T. (1995). Modern *Global Seismology,* Vol. 58. London: Academic Press.

Le Friant, A., Boudon, G., Deplus, C., and Villemant, B. (2003). Large-scale flank collapse events during the activity of Montagne Pelè, Martinique, Lesser Antilles, *J. Geophys. Res.* 108, 2055. doi: 10.1029/2001JB001624

Lehto, H. L., Roman, D. C., and Moran, S. C. (2010). Temporal changes in stress preceding the 2004–2008 eruption of Mount St. Helens, Washington. *J. Volcanol. Geotherm. Res.* 198, 129–142. doi: 10.1016/j.jvolgeores.2010.08.015

Linde, A. T., and Sacks, I. S. (1998). Triggering of volcanic eruptions. *Nature* 395, 888–890. doi: 10.1038/27650

Longprè, M.-A., Troll, V. R., Walter, T. R., and Hansteen, T. H. (2009). Volcanic and geochemical evolution of the Teno massif, Tenerife, Canary Islands: some repercussions of giant landslides on ocean island magmatism. *Geochem. Geophys. Geosyst.* 10, Q12017. doi: 10.1029/2009GC002892

Lundgren, P., Casu, F., Manzo, M., Pepe, A., Berardino, P., Sansosti, E., et al. (2004). Gravity and magma induced spreading of Mount Etna volcano revealed by satellite radar interferometry. *J. Geophys. Res.* 31, L04602. doi: 10.1029/2003gl018736

Maccaferri, F., Rivalta, E., Keir, D., and Acocella, V. (2014). Off-rift volcanism in rift zones determined by crustal unloading. *Nat. Geosci. Lett.* 7, 297–300. doi: 10.1038/ngeo2110

Manconi, A., Longprè, M. A., Walter, T. R., Troll, V. R., and Hansteen, T. H. (2009). The effects of flank collapses on volcano plumbing systems. *Geology* 460, 1.099–1.102. doi: 10.1130/g30104a.1

Manga, M. (1998). Rheology of bubble-bearing magmas. *J. Volcanol. Geotherm. Res.* 87, 15–28. doi: 10.1016/S0377-0273(98)00091-2

Manga, M., and Brodsky, E. E. (2006). Seismic triggering of eruptions in the far field: volcanoes and geysers. *Annu. Rev. Earth Planet. Sci.* 34, 263–291. doi: 10.1146/annurev.earth.34.031405.125125

Marzocchi, W. (2002). Remote seismic influence on large explosive eruptions. *J. Geophys. Res.* 107, 2018. doi: 10.1029/2001jb000307

Marzocchi, W., Casarotti, E., and Piersanti, A. (2002). Modeling the stress variations induced by great earthquakes on the largest volcanic eruptions of the 20th Century. *J. Geophy. Res.* 107, 2320. doi: 10.1029/2001jb001391

Massol, H., and Jaupart, C. (1999). The generation of gas overpressure in volcanic eruptions. *Earth Planet. Sc. Lett.* 166, 57–70. doi: 10.1016/S0012-821X(98)00277-5

Melnik, O., and Sparks, R. S. J. (2002). "Dynamics of magma ascent and lava extrusion at Soufrière Hills Volcano, Montserrat," in *The Eruption of Soufrière Hills Volcano, Montserrat, From 1995 to 1999,* Vol. 21, eds T. H. Druitt and B. P. Kokelaar (London: Geological Society), 153–171.

Miller, C., and Wark, D. A. (2008). Supervolcanoes and their explosive supereruptions. *Elements* 4, 11–16. doi: 10.2113/GSELEMENTS.4.1.11

Miura, D., and Wada, Y. (2007). Effects of stress in the evolution of large silicic magmatic systems: an example from the Miocene felsic volcanic field at Kii Peninsula, SW Honshu, Japan. *J. Volcanol. Geotherrm Res.* 167, 300–319. doi: 10.1016/j.jvolgeores.2007.05.017

Neri, M., Acocella, V., and Behncke, B. (2004). The role of the Pernicana Fault System in the spreading of Mt. Etna (Italy) during the 2002–2003 eruption. *Bull. Volcanol.* 66, 417–430. doi: 10.1007/s00445-003-0322-x

Pinel, V., and Albino, F. (2013). Consequences of volcano sector collapse on magmatic storage zones: insights from numerical modeling. *J. Volcanol. Geotherm. Res.* 252, 29–37. doi: 10.1016/j.jvolgeores.2012.11.009

Pinel, V., and Jaupart, C. (2005). Some consequences of volcanic edifice destruction for eruption conditions. *J. Volcanol. Geotherm. Res.* 145, 68–80. doi: 10.1016/j.jvolgeores.2005.01.012

Pinel, V., and Jupart, C. (2004). Magma storage and horizontal dyke injection beneath a volcanic edifice. *Earth Planet. Sci. Lett.* 221, 245–262. doi: 10.1016/S0012-821X(04)00076-7

Plateaux, R., Béthoux, N., Bergerat, F., and Lépinay, B. M. (2014). Volcano-tectonic interactions revealed by inversion of focal mechanisms: stress field insight around and beneath the Vatnajokull ice cap in Iceland. *Front. Earth Sci.* 2:9. doi: 10.3389/feart.2014.00009

Platz, T., Cronin, S. J., Cashman, K. V., Stewart, R. B., and Smith, I. E. M. (2007). Transition from effusive to explosive phases in andesite eruptions: a case-study from the AD1655 eruption of Mt.Taranaki, New Zealand. *J. Volcanol. Geotherm. Res.* 161, 1534. doi: 10.1016/j.jvolgeores.2006.11.005

Presley, T. K., Sinton, J. M., and Pringle, M. (1997). Postshield volcanism and catastrophic mass wasting of the Waianae Volcano, Oahu, Hawaii. *Bull. Volcanol.* 58, 597–616. doi: 10.1007/s004450050165

Ripepe, M., Marchetti, E., Ulivieri, G., Harris, A., Dehn, J., Burton, M., et al. (2013). Effusive to explosive transition during the 2003 eruption of Stromboli volcano. *Geology* 33, 341–344. doi: 10.1130/G21173.1

Roverato, M., Capra, L., Sulpizio, R., and Norini, G. (2011). Stratigraphic reconstruction of two debris avalanche deposits at Colima Volcano (Mexico): insights into pre-failure conditions and climate influence. *J. Volcanol. Geotherm. Res.* 207, 33–46. doi: 10.1016/j.jvolgeores.2011.07.003

Schneider, A., Rempel, A. W., and Cashman, K. V. (2012). Conduit degassing and thermal controls on eruptive styles at Mt. St. Helens. *Earth Planet. Sci. Lett.* 357, 347–354. doi: 10.1016/j.epsl.2012.09.045

Selva, J., Marzocchi, W., Zencher, F., Casarotti, E., Piersanti, A., and Boschi, E. (2004). A forward test for interaction between remote earthquakes and volcanic eruptions: the case of Sumatra (June 2000) and Denali (November 2002) earthquakes. *Earth Planet. Sci. Lett.* 226, 383–395. doi: 10.1016/j.epsl.2004.08.006

Sepulveda, F., Lahsen, A., Bonvalot, S., Cembrano, J., Alvarado, A., and Letelier, P. (2005). Morpho-structural evolution of the Cordón Caulle geothermal region, Southern Volcanic Zone, Chile: insights from gravity and 40Ar/39Ar dating. *J. Volcanol. Geotherm. Res.* 148, 207–233. doi: 10.1016/j.jvolgeores.2005.03.020

Sigmundsson, F., Pinel, V., Lund, B., Albino, F., Pagli, C., Geirsson, H., et al. (2010). Climate effects on volcanism: Influence on magmatic systems of loading and unloading from ice mass variations with examples from Iceland. *Phil. Trans. R. Soc. Lond.* 368, 2.519–2.534. doi: 10.1098/rsta.2010.0042

Sinton, J., Gronvold, K., and Saemundsson, K. (2005). Postglacial eruptive history of the western volcanic zone, Iceland. *Geochem. Geophys. Geosyst.* 6:Q1200. doi: 10.1029/2005GC001021

Sohn, R. A. (2004). Microearthquake patterns following the 1998 eruption of Axial Volcano, Juan de Fuca Ridge: mechanical relaxation and thermal strain. *J. Geophys. Res.* 109, B01101. doi: 10.1029/2003jb002499

Stein, R. S. (1999). The role of stress transfer in earthquake occurrence. *Nature* 402, 605–609. doi: 10.1038/45144

Stevenson, R. J., Dingwell, D. B.,Webb, S. L., and Sharp, T. G. (1996). Viscosity of microlite-bearing rhyolitic obsidians: an experimental study. *Bull. Volcanol.* 58, 298–309. doi: 10.1007/s004450050141

Sulpizio, R., Lucchi, F., Forni, F., Massaro, S., and Tranne, C. (2016). Unravelling the effusive-explosive transitions and the construction of a volcanic cone from geological data: the example of Monte dei Porri eruptive cycle, Salina, Aeolian Islands (Italy). *J. Volcanol. Geotherm. Res.* 327, 1–22. doi: 10.1016/j.jvolgeores.2016.06.024

Ventura, G., and Vilardo, G. (1999). Slip tendency analysis of the Vesuvius faults: implications for the seismotectonic and volcanic hazard assessment. *Geophy. Res. Lett.* 26, 3229–3232. doi: 10.1029/1999GL005393

Villemant, B., and Boudon, G. (1998). Transition from dome-forming to plinian eruptive styles controlled by H_2O and Cl degassing. *Nature* 392, 65–69. doi: 10.1038/32144

Voight, B., and Elsworth, D. (1997). Failure of volcano slopes. *Geotechnique 47*, 535, 1–31. doi: 10.1680/geot.1997.47.1.1

Waite, G. P., and Smith, R. B. (2004). Seismotectonics and stress field of the Yellowstone volcanic plateau from earthquake first-motions and other indicators. *J. Geophys. Res.* 109, B02301. doi: 10.1029/2003JB002675

Walter, T. R. (2007). How a tectonic earthquake may wake up volcanoes: stress transfer during the 1996 earthquake–eruption sequence at the Karymsky Volcanic Group, Kamchatka. *Earth Planet. Sci. Lett.* 264, 347–359. doi: 10.1016/j.epsl.2007.09.006

Walter, T. R., and Amelung, F. (2007). Volcanic eruptions following $M\geq9$ megathrust earthquakes: implications for the Sumatra-Andaman volcanoes. *Geology* 35, 539–542. doi: 10.1130/G23429A.1

Walter, T. R., Wang, R., Zimmer, M., Grosser, H., Luhr, B., and Ratdomopurbo, A. (2007). Volcanic activity influenced by tectonic earthquakes: static and dynamic stress triggering at Mt. Merapi. *Geophys. Res. Lett.* 34, L05304. doi: 10.1029/2006gl028710

Watt, S. F. L., Pyle, D. M., and Mather, T. A. (2008). The influence of great earthquakes on volcanic eruption rate along the Chilean subduction zone. *Earth Planet. Sci. Lett.* 277, 399–407. doi: 10.1016/j.epsl.2008.11.005

Wylie, J. J., Voight, B., and Whiteheed, J. A. (1999). Instability of magma flow from volatile dependent viscosity. *Science* 285, 1883–1885. doi: 10.1126/science.285.5435.1883

Conflict of Interest Statement: The authors declare that the research was conducted in the absence of any commercial or financial relationships that could be construed as a potential conflict of interest.

frontiers in Earth Science

REVIEW
published: 23 December 2016
doi: 10.3389/feart.2016.00106

Stress Controls of Monogenetic Volcanism: A Review

Joan Martí[1]*, Carmen López[2], Stefania Bartolini[1], Laura Becerril[1] and Adelina Geyer[1]

[1] Group of Volcanology, Institute of Earth Sciences Jaume Almera, Agencia Estatal Consejo Superior de Investigaciones Científicasn CSIC, Barcelona, Spain, [2] Instituto Geográfico Nacional, Madrid, Spain

The factors controlling the preparation of volcanic eruptions in monogenetic fields are still poorly understood. The fact that in monogenetic volcanism each eruption has a different vent suggests that volcanic susceptibility has a high degree of randomness, so that accurate forecasting is subjected to a very high uncertainty. Recent studies on monogenetic volcanism reveal how sensitive magma migration is to the existence of changes in the stress field caused by regional and/or local tectonics or rheological contrasts (stratigraphic discontinuities). These stress variations may induce changes in the pattern of further movements of magma, thus conditioning the location of future eruptions. This implies that a precise knowledge of the stress configuration and distribution of rheological and structural discontinuities at crustal level of such volcanic systems would aid in forecasting monogenetic volcanism. This contribution reviews several basic concepts relative to the stress controls of magma transport into the brittle lithosphere, and uses this information to explain how magma migrates inside monogenetic volcanic systems and how it prepares to trigger a new eruption.

Keywords: monogenetic volcanism, magma ascent dynamics, stress field, hazard assessment, volcanic susceptibility

OPEN ACCESS

Edited by:
Geoffrey Wadge,
University of Reading, UK

Reviewed by:
Alessandro Tibaldi,
University of Milano-Bicocca, Italy
Greg A. Valentine,
University at Buffalo, USA

****Correspondence:***
Joan Martí
joan.marti@ictja.csic.es

Specialty section:
This article was submitted to Volcanology,
a section of the journal
Frontiers in Earth Science

Received: *01 November 2016*
Accepted: *25 November 2016*
Published: *23 December 2016*

Citation:
Martí J, López C, Bartolini S, Becerril L and Geyer A (2016) Stress Controls of Monogenetic Volcanism: A Review.
Front. Earth Sci. 4:106.
doi: 10.3389/feart.2016.00106

INTRODUCTION

Monogenetic volcanism is the most extended type of volcanic activity on Earth (Walker, 2000). It is commonly represented by volcanic fields containing tens to thousands of small volcanoes, each being the product of a single eruptive episode, in which different phases or pulses may occur (Walker, 2000; Valentine and Gregg, 2008; Németh, 2010; Németh and Kereszturi, 2015). Monogenetic fields may be active for several millions of years with eruption recurrences ranging from several tens to tens of thousands of years. They are usually mafic in composition and generate relatively small volume eruptions that produce cinder cones and lava flows, as well as occasional phreatomagmatic deposits when interaction between magma and surface water occurs (Lorenz, 1986; Valentine and Gregg, 2008). The distribution of volcanic cones in basaltic monogenetic fields is clearly controlled by regional and local tectonics (Wood, 1980; Pasquarè et al., 1988; Connor, 1990; Connor et al., 1992; Tibaldi, 1995; Walker, 2000; Valentine and Perry, 2007; Le Corvec et al., 2013b). The great variety of eruptive styles, edifice morphologies and deposits in monogenetic volcanoes is the result of a complex combination of internal (magma composition, gas content, rheology, volume) and external (regional and local stress fields, stratigraphic and rheological contrasts in substrate rock, hydrogeology) parameters that characterize each volcanic system (Tibaldi and Lagmay, 2006; Valentine and Gregg, 2008; Németh, 2010; Martí et al., 2011). Monogenetic volcanoes may also occur as flank eruptions in association with polygenetic volcanoes (e.g., El Teide, Martí et al., 2008; Etna, Cappello et al., 2012).

Central or composite volcanoes are characterized by the presence of a magma chamber located a few kilometers below the surface, which exerts a stress field on its surroundings that is superimposed on the regional stress field, thereby controlling potential pathways for magma to the surface (Pinel and Jaupart, 2004; Gudmundsson and Brenner, 2005; Martí and Geyer, 2009, **Figure 1**). On the contrary, in a monogenetic volcanic systems magma does not accumulate in such shallow reservoirs or chambers and tends to rise to the surface from greater depths, usually from intermediate reservoirs located deep in the crust, or even from the source region or shallower levels in the mantle. Thus, the stress field controlling the magma ascent will depend on the stress distribution inside the lithosphere and in particular, on the regional stress field and local stress barriers corresponding to rheological and/or structural discontinuities (Menand, 2008, 2011; Maccaferri et al., 2010, 2011; Gudmundsson, 2011a,b; Bolós et al., 2015). Knowing how these structural controls work and how they may change from one eruption to the next one is crucial to understand why in monogenetic eruptive vents produced under the same regional stress field (i.e., same age period) will tend to cluster in the same area. These volcanic clusters may have lifetimes of hundreds of thousands of years, so there is always a chance that a new volcano will come up in the same place than an old one, just out of random chance, not necessarily implying the initiation of a polygenetic behavior.

An important consequence of these different stress controls between central and monogenetic volcanoes is the accuracy in forecasting new eruptions. While in central volcanoes it is generally assumed that future eruptions will occur through the same vents that have been active in the past, in monogenetic systems forecasting the position of new vents is much more challenging due to this lack of a permanent shallow stress configuration. Spatial analysis addressed to infer the location of future vents (volcanic susceptibility, see Martí and Felpeto, 2010) in monogenetic volcanism generally assumes that the next eruption will occur close to the location of the previous ones (Connor, 1990; Connor et al., 1992, 2000; Ho, 1992, 1995; Martin et al., 1994; Ho and Smith, 1998; Connor and Conway, 2000; Alberico et al., 2002; Martí and Felpeto, 2010; Bebbington and Cronin, 2011; Cappello et al., 2012; Selva et al., 2012; Bartolini et al., 2013; Becerril et al., 2013a; Le Corvec et al., 2013a; Bevilacqua et al., 2015). The reason to make this assumption is based on the fact that in last eruptive episodes volcanoes had formed near previous ones (forming a cluster), so we assume that this behavior will continue. However, this does not necessarily mean they will not occur outside a cluster, just that the probability is weighted by the existence of the cluster.

The transport of magma occurs mostly through sheet intrusions and the conditions of flow in such magma-filled cracks will be governed by rock and fluid mechanics (Pollard, 1969, 1973; Pollard and Muller, 1976; Delaney and Pollard, 1981, 1982; Delaney et al., 1986; Pollard and Segall, 1987; Rubin, 1993a,b, 1995; Dahm, 2000; Gudmundsson, 2011a). Studies on monogenetic volcanism reveal how sensitive magma migration is to the existence of changes in the stress field produced by regional and/or local tectonics or rheological contrasts (stratigraphic discontinuities, sheet intrusions, tectonic fractures, Delaney et al., 1986; Dahm, 2000; Gudmundsson and Philipp, 2006; Gaffney et al., 2007; Menand, 2008, 2011; Taisne and Jaupart, 2009; Maccaferri et al., 2010, 2011; Taisne et al., 2011; Gudmundsson, 2011b; Le Corvec et al., 2013b,c; Rivalta et al., 2015). The presence of such stress barriers may induce stress rotation

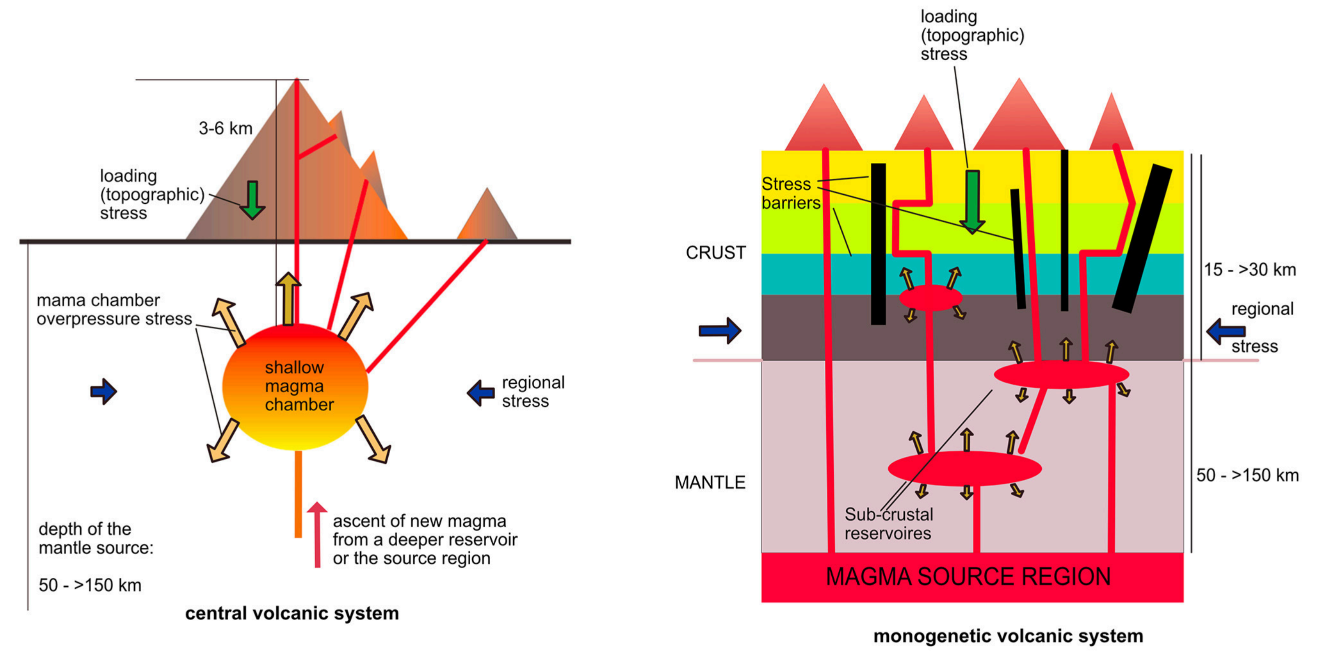

FIGURE 1 | Differences between central and monogenetic volcanic systems (not to scale; see text for more explanation).

and, consequently, changes in the direction of emplacement of magma. Therefore, knowledge of rock stress is crucial to understand how magma will move from its source regions up to the Earth's surface, and to forecast future eruptions.

In this review we will concentrate on the main concepts related to stress controls on magma transport in monogenetic fields, in order to offer a comprehensive picture on the paths that magma may follow inside the volcanic system and on why an eruption will occur from a particular point.

We do not pretend to discuss the different stress constraints that characterize monogenetic versus polygenetic volcanic systems, which would require a different approach. We basically concentrate on some important aspects of magma migration into the brittle lithosphere that certainly apply to monogenetic volcanism, and for which we include simple models specifically designed to understand magma migration in such volcanic systems. However, this does not exclude (for what concern the basic physics) that some of the considerations included here can also be aplicable to central volcanoes. Therefore, we will first review some basic concepts on rock stress, then we will focus our attention on the main physical controls on magma transport in monogenetic fields and, finally, we will discuss on the implications of the stress field on volcanic susceptibility and the forecast of monogenetic eruptions.

STRESS IN THE LITHOSPHERE

In the literature there are excellent experimental and theoretical approaches on magma transport and on the mechanics and fluid-dynamics of magma-filled cracks (e.g., Pollard, 1969, 1973; Pollard and Muller, 1976; Delaney and Pollard, 1981, 1982; Delaney et al., 1986; Pollard and Segall, 1987; Takada, 1989; Gudmundsson, 1990, 2011a,b; Lister and Kerr, 1991; Rubin, 1993a,b; Rubin, 1995; Dahm, 2000; Muller et al., 2001; Roman and Heron, 2007; Menand, 2008, 2011; Taisne and Jaupart, 2009; Maccaferri et al., 2010, 2011; Menand et al., 2010; Taisne et al., 2011; Gudmundsson, 2012; Le Corvec et al., 2013c; Rivalta et al., 2015), as well as on rock stress (e.g., Zang and Stephansson, 2010), and we address the reader to these contributions. In this section we only provide a basic background necessary to follow the rest of this review.

Knowledge of the state of stresses in the Earth's lithosphere is fundamental to understand how magma will migrate and accumulate inside it and, eventually, erupt at the Earth's surface. Stress in the lithosphere may have different origins: tectonic, gravitational, thermal, residual or fluid overpressure (Park, 1988; Zoback, 1992; Zoback and Zoback, 2002; Zang and Stephansson, 2010; Fossen, 2016). Tectonic stresses derive from the relative motion between mantle flow and plate motion, and may be subdivided into first order (plate scale), second order (regional scale), or third order (local scale), depending on the volume in which a stress component is supposed to be uniform in magnitude and orientation (Zoback, 1992; Heidbach et al., 2007; Zang and Stephansson, 2010). Gravitational (loading) stresses correspond to the overlaying rock mass; they increase with depth in the Earth's crust and consider also the stress resulting from Earth's topography near the surface (Zang and Stephansson, 2010). Thermal stresses result from temperature changes in crustal rocks when they are buried, uplifted or exposed to local heat sources (e.g., magma, Turcotte and Schubert, 1982; Fossen, 2016). Residual stresses are those preserved in crustal rocks after the external force or stress field has been changed or removed (e.g., metamorphic transformations, cooling of magmatic intrusions, Fossen, 2016). Finally, we must also consider those stresses that can be imposed on crustal rocks by fluid overpressure, like when fluid is present in porous rocks trapped between non-permeable layers or due to magmatic intrusions (Gudmundsson, 2011a)

All these types of stresses will become components of the stress field that will characterize any point in the Earth's crust, the magnitude and orientation of which will depend on the spatial and temporal scales of observation and the corresponding relative value of each stress component. In a broad sense, it is important to know that first order tectonic stresses (plate scale stresses) are assumed to be constant in the whole thickness of the tectonic plate. Second order tectonic stresses (regional or intraplate scale) may vary over short distances depending on the relative position of the reference point inside a plate and the location of main geological structures, such as regional fault systems, mountain belts, or upwelling mantle plumes, or even the presence of collapse calderas, volcanic edifices or rift systems. Local tectonic stresses are also known as structural stresses (Jaeger and Cook, 1979) and correspond to stress field variations caused by active faults, local inclusions, magmatic intrusions, detachment horizons, and density and rheological contrasts. These forces act as major controls on the stress field orientations when the magnitudes of the horizontal stresses are close to isotropic (Heidbach et al., 2007).

Gravitational or loading stresses may also show significant variations depending on the spatial scale we are considering. At a regional scale it is considered that gravitational stresses increase progressively with depth, and that at a certain depth there are distributed more or less isotropically, thus giving rise to a stress state called lithostatic. However, at more local scales and much shallower depths gravitational stresses may differ significantly from one point to another depending on lateral stratigraphic changes and abrupt variations in topography (Muller et al., 2001; Gudmundsson, 2012). Thermal stresses at regional scales derive from the rheological changes that are produced on crustal rocks due to temperature variations caused by burial or uplift processes in sedimentary basins and orogens, as well as those caused by mantle upwelling in intraplate environments (Turcotte and Schubert, 1982; Schrank et al, 2012). At more local scale, these stresses may be significant around magma intrusions. Residual stresses appear in a rock if elastic strain remains after the external stress field is removed, as it may happen in cementation caused by overburden, metamorphic transformations, or tectonic deformation (Fossen, 2016). Finally, crustal stresses derived from fluid overpressure will appear in relation to fluid filled porous rocks, geothermal fields or magma intrusions (Gudmundsson, 2011a; Shapiro, 2015).

When evaluating the importance of each component on the stress field we should also consider the time scale at which they act or at which they may have a significant role. Stresses and the strain they may produce on the crustal rocks are time dependent, so when estimating the state of stress of a certain point we need to consider also the duration of the stresses acting on that point. For example, while first and second order tectonic stresses and gravitational stresses are more or less constant with regard to time, residual and thermal stresses will only be effective at long-term time scales (thousands to millions of years). In a similar way, fluid overpressure stresses may be effective in very short time scales (e.g., magma intrusions, pore-fluids in surface rock) or at longer time-scales when corresponding to buried fluid-saturated rock (e.g., oil reservoirs). Therefore, to understand how crustal stresses act on a specific point we will need to consider the spatial and temporal scales at which each stress component may operate.

Special attention is required for the local tectonic or structural stresses. These will depend on the mechanical characteristics of the rock mass we are considering. This may be classified as: (1) homogeneous, when the rock mass does not show rheological variations or structural discontinuities; (2) anisotropic, when rock properties vary with direction (i.e., there are rheological variations in the rock mass considered), and (3) heterogeneous, when inclusions of different rocks and/or structural discontinuities are present in the rock mass (Zang and Stephansson, 2010). The consequence of considering different rock mass characteristics is that the configuration of stresses in each of them may differ considerably from one to the other (**Figure 2**). Compared to homogenous rock masses in which the trajectories of the principal stresses will define a regular orthogonal pattern, anisotropic rocks formed by alternating stiff and soft materials will show a pattern oriented toward preferred anisotropy, as soft materials will accumulate higher strain while the stiff ones will attract higher stresses (Zang and Stephansson, 2010). In addition to anisotropies, crustal rock masses may show different scale heterogeneities caused by the presence of structural discontinuities.

MAGMA MOTION

Magma motion in the lithosphere will be basically controlled by the overpressure of magma over that of rock. How this magma overpressure is achieved will be discussed latter. Now it is sufficient to assume that magma is over-pressurized, so it will migrate through the lithosphere controlled by the regional and local stresses that act on it (Takada, 1994; Traversa et al., 2010).

In the source region, magma transport will be dominated by porous flow through a deformable and partially molten matrix, from which it will segregate by compaction of the mantle unmelted residuum (Spera, 1980; McKenzie, 1984, 1985; Rubin, 1993c, 1998). At such depths and when a sufficient volume of magma has been accumulated, thus becoming gravitationally unstable, it will tend to continue ascending in order to equilibrate its excess pressure. It has been assumed that basaltic magma in the mantle may ascent as buoyant diapirs when rocks surrounding magma may deform plastically due to their relative low viscosity (Spera, 1980; Rubin, 1998). This ascending movement of magma will continue until the rocks above behaves as a brittle solid, in moment magma will ascent through fractures in the host rock. The transition from porous flow to flow through magma driven cracks is not only a function of the temperature of the host rock, but also of the rate of strain and the stresses involved (Rubin, 1993c, 1998). The brittle-ductile transition in the crust may be located higher than initiation of dyke propagation, which may occur much deeper, even into the upper mantle. This is not because of the temperature differences in the host rock, but because the timescale of deformation around a dyke is small compared to the viscous relaxation time scale of the medium, so brittle behavior occurs (Rubin, 1993c, 1998). Magma ascent will be halted if the host rock does not fracture in response to the pushing action of magma (Turcotte and Schubert, 1982; Maaloe, 1985; Middleton and Wilcock, 1994). However, if magma overpressure exceeds the cohesive and confining stresses of host rock, this will be broken apart forming a fracture through which magma may intrude and continue its emplacement to shallower levels (Jaeger and Cook, 1979; Spera, 1980; Maaloe, 1985; Rubin, 1993c, 1998; Menand, 2011). This is the most effective mechanism of magma transport in the lithosphere, particularly in the crust, in comparison with the diapiric ascent. In fact, seismic evidence indicates that magma-filled cracks may start to form at depth of 40–50 km or even greater, as it is

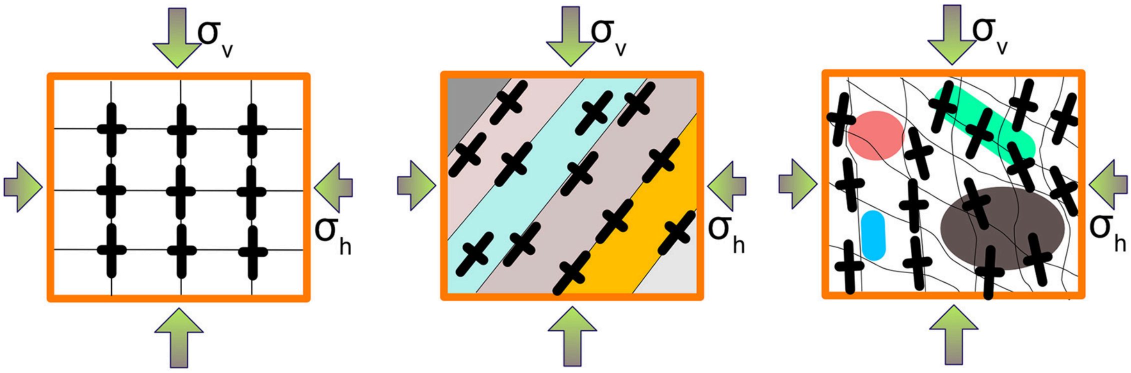

FIGURE 2 | Sketch of the stress field and stress trajectories (solid bars) in homogeneous (left), anisotropic (center), and heterogeneous (right) rocks (adapted from Zang and Stephansson, 2010).

suggested by the existence of earthquakes generated at these depths and by the presence of ophiolite peridotite bodies and other mantle inclusions erupted onto surface (Maaloe, 1985).

Magma-filled fractures or cracks are known as sheets intrusions, being named dykes when they cut across bedding or foliation/fabric in the host material, and sills when they are concordant with that. However, for the purposes of this paper, we will refer vertical or subvertical cases as dykes, and horizontal as sills, with the understanding that in detail it depends on the cross cutting relationships (**Figure 3**). The formation of sheet intrusions is regarded in the framework of hydraulic fracturing. In this context, a hydrofracture is a tension fracture in which the driving tensile stress is the fluid overpressure, so, in our case, the magma overpressure (see Gudmundsson, 2011a). Therefore, to start a sheet intrusion it will require to achieve the conditions for rupture of the rock and hydrofracture initiation (Jaeger and Cook, 1979; Gudmundsson et al., 1999; Gudmundsson, 2011a):

$$p_m \geq \sigma_3 + T \tag{1}$$

where p_m is the total magma pressure, σ_3 is the minor principal compressive stress, and T is the local *in situ* tensile strength of the rock.

Magma migration will be controlled by the regional tectonics and the gravitational stresses but also by local stress barriers defined by crustal heterogeneities such as local tectonic structures and rheological changes in crustal rocks. This means that it will tend to follow a path normal to the minimum compressive stress. If in its ascent to the surface magma finds a rheological or structural contrast between rocks, magma may become arrested or intrude laterally forming a sill (Pasquarè and Tibaldi, 2007; Tibaldi and Pasquarè, 2008; Tibaldi et al., 2008; Maccaferri et al., 2010; Menand, 2011; Gudmundsson, 2011b).

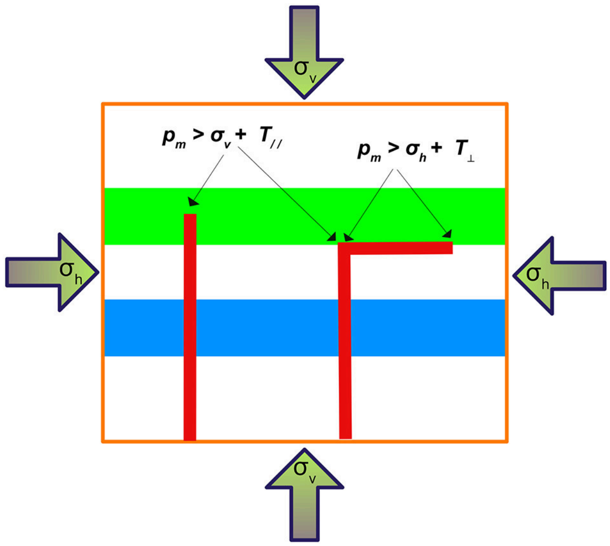

FIGURE 3 | Stress conditions compatible with dyke and sill intrusions. Dykes: Total magma pressure (pm) must be greater than the principal horizontal stress (σ_h) plus the tensile strength of the rock tested in extension parallel to the bedding ($T_{//}$). Sill: pm is greater than the principal vertical stress (σ_v) plus the tensile strength of the rock tested in extension perpendicular to the bedding plane ($T_{\perp}$) (adapted from Price et al., 1990).

As we see in **Figure 3**, the propagation of a sheet intrusion as a dyke or a sill in an anisotropic medium will depend on the stress configuration at the front of the intrusion. If the total magma pressure (p_m) is greater than the principal horizontal stress (σ_h), which may coincide with σ_3, plus the tensile strength of the rock tested in extension parallel to the bedding ($T_{//}$), the intrusion will propagate as a dyke. However, if p_m is greater than the principal vertical stress (σ_v) plus the tensile strength of the rock tested in extension perpendicular to the bedding plane ($T_{\perp}$) the intrusion will propagate as a sill (Price et al., 1990). If the sill is fed by a dyke, as it is illustrated in **Figure 3**, both conditions must be satisfied simultaneously at the junction of the feeder dyke and the sill. Therefore, it follows that (Price et al., 1990):

$$(\sigma_v - \sigma_h) < (T_{//} - T_{\perp}) \tag{2}$$

The tensile strength of a pile of stratified rocks will be determined by the strength of the individual bedding planes, so $T_{\perp}$ will be approximately zero (Price et al., 1990; Gudmundsson, 2011a,b). On the other hand, the tensile strength of most unjoined or unfractured rocks is of the order of 10 MPa or considerably smaller if the rock contains joints or fractures (Touloukian et al., 1989; Price et al., 1990; Gudmundsson, 2011a,b). So, we can deduce that a sill will only occur when the differences in magnitude between the horizontal and vertical stresses are very small (Pollard, 1973; Price et al., 1990). In many situations, if a sill is fed from a perfectly vertical dyke it will favor propagation laterally at both sides of the plane of weakness, while if the feeder dykes is inclined (i.e., oblique to the strata) the sill will tend to propagate only toward the side opposite to the dyke dip (see **Figure 4**). This generalized behavior, however, may change under particular stress configurations and rock rheology contrasts (e.g., Tibaldi and Pasquarè, 2008).

The orientation of the stress field may change (i.e., may rotate with respect to a reference position) depending on the exact contribution of each stress component at each point (Pollard and Muller, 1976; Pollard and Segall, 1987). At the time scale of magma propagation through a fracture (days to months) the near-tip stress field will be essentially controlled by the first and second order stresses, structural and gravitational stresses, the stresses associated with the magma overpressure, which will depend on the fracture geometry and total volume of magma, and occasionally by thermal stresses generated by thermal variations in the magma during emplacement (Turcotte and Schubert, 1982). To predict the direction of propagation of a magma-driven fracture and the possible location of the next monogenetic eruption it is important to understand how these stresses, or the resulting stress field, change with depth.

SHEET INTRUSIONS AND MAGMA OVERPRESSURE

The plumbing system of a monogenetic volcanic field (**Figure 1**) may include a source zone, where magma generates and migrates upwards by gravitationally-induced porous flow, and a series of

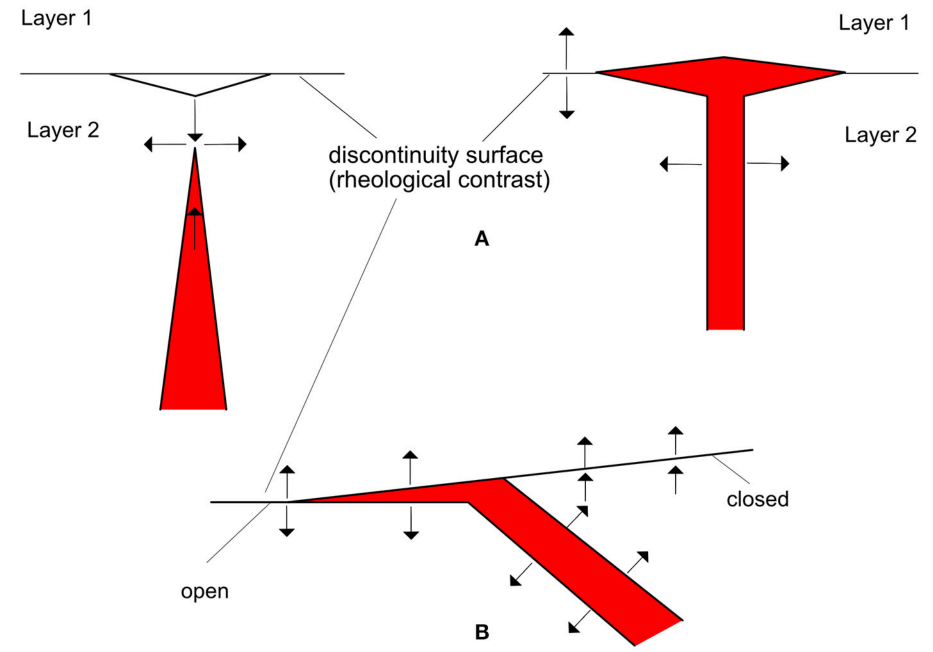

FIGURE 4 | Schematic representation of a discontinuity plane, corresponding to a rheological contrast between two rock beds, in advance of a developing vertical (A) and inclined **(B)** dyke enabling it to form a symmetric **(A)** and an asymmetric **(B)** sill, respectively (adapted from Pollard, 1969, in Price et al., 1990).

intermediate reservoirs where magma may stop and differentiate for a while before continuing its ascent to the surface. This is clearly indicated by the petrology and geochemistry of magmas from monogenetic eruptions, which evidence certain degree of differentiation in most cases and occasional assimilation of crustal rocks that occurred at different depths (Thirlwall et al., 2000; Klügel et al., 2005; Stroncik et al., 2009; Valentine and Hirano, 2010; Brenna et al., 2011; Rowe et al., 2011; Hernando et al., 2014; Albert et al., 2015, 2016; Klugel et al., 2015). These intermediate reservoir zones, which will normally be located at rheological or structural discontinuities inside the lithosphere, do not need to be stable or permanent along the whole history of the volcanic field. Also, there is evidence that in some cases magma erupts directly from the source region, without suffering any differentiation in its journey to the surface (Bacon et al., 1995; Garcia et al., 1995). The reasons magma will either stop at different depths before reaching the surface or will ascend straight from the source region or a deep reservoir, depend on the magma overpressure and the state of stresses inside the lithosphere. This balance between magma pressure and lithospheric stresses will decide whether magma will be able to follow a straight path to the surface or will stop at certain depth, arresting its ascent or continuing it until internal pressure conditions are favorable again. Also, it will control the exact path that magma will follow and, finally, the location of the new vent in case magma has been able to reach the surface. In fact, the proportion of magmatic intrusions that become feeder dykes is minimum compared to the total number of dykes that may be generated during the whole life of a volcanic system (Gudmundsson et al., 1999). So, in order to know if a magma intrusion will reach the surface and cause an eruption we need to ask: (1) will magma have sufficient driving force (magma overpressure) to reach the surface)?, and (2) what is the path it will follow?

To answer the first question we need to understand which is the driving force of magma intrusions. It is obvious that for the same magma driving force, a different stress distribution may either reduce or enhance the possibilities for this magma to reach the surface. **Figure 5** illustrates the concepts of total magma pressure (p_m), magma excess pressure (p_e) and magma overpressure or driving pressure (p_o), which are fundamental to understand magma migration (see Dahm, 2000; Gudmundsson, 2012). We consider a lithostatic reference state, which is the simplest stress model for the interior of the lithosphere, so there is no differential stress at depth ($\sigma_1 = \sigma_3$). In such situation and in equilibrium the total pressure of a deep magma reservoir will be equal to the lithostatic pressure ($\rho_r gh$). If a new injection of magma from the source region (or from a deeper reservoir) enters into the magma reservoir, it will increase the total magma pressure ($p_m = p_l + p_e$) (see Blake, 1981). We assume that the resident and the new magmas are under-saturated in volatiles, so no free gas phase is present, which is a good assumption for basaltic magmas at depths of several tens of kilometers. The increase of magma pressure (excess pressure, p_e) inside the reservoir will force the volume of the reservoir to increase. Depending on the rigidity of the surrounding rocks they will be able to deform elastically to a certain limit, so the reservoir will expand a little bit. If the volume increase permitted by elastic

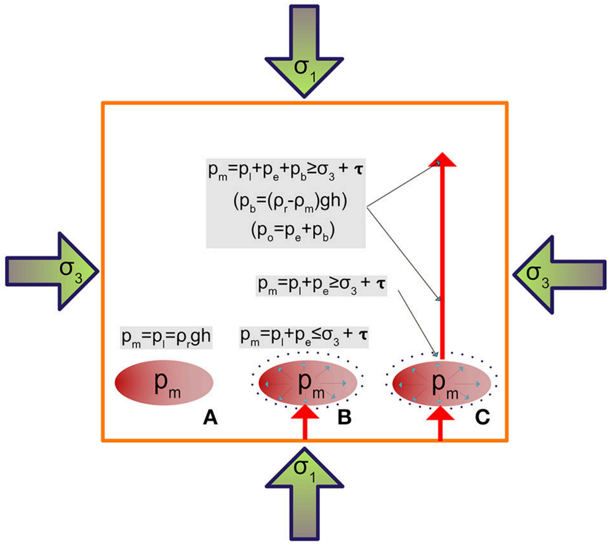

FIGURE 5 | Sketch illustrating the concepts of total magma pressure (p_m), magma excess pressure (p_e) and magma overpressure or driving pressure (p_o), as defined in the text. We consider a lithostatic reference state, which is the simplest stress model for the interior of the lithosphere, so there is no differential stress at depth ($\sigma_1 = \sigma_3$) (see text for more explanation).

expansion of the host rock is sufficient to accommodate the pressure increase, the situation will return to equilibrium until a new intrusion of magma arrives. However, if the elasticity the host rock is exceeded it will fracture due to the tensile stresses, which are generated around the reservoir walls, and magma will be injected into the host rock. Previous calculations have indicated that volume fractions of new injected magma of approximately 0.1% of the volume of the reservoir in the absence of any gas phase are sufficient to produce the excess pressure necessary to trigger a magma injection (Blake, 1981). This volume fraction may increase to approximately 1% of the volume of the reservoir when a gas phase is present in the resident magma (i.e., at much shallower depths) due to the higher compressibility of the resident magma (Bower and Woods, 1997; Folch and Martí, 1998).

The progression of a magma-driven fracture will depend on the total magma pressure, as indicated by Equation (1), which at the moment of the reservoir rupture can be rewritten as (Gudmundsson et al., 1999; Gudmundsson, 2012):

$$p_m = p_l + p_e \geq \sigma_3 + T \tag{3}$$

where p_l is the lithostatic pressure and p_e is the excess pressure above the lithostatic necessary to initiate the rupture of the reservoir walls. At the moment in which magma starts to abandon the reservoir intruding the rock, and because at these depths magma tends to be less dense than the host rock, a buoyancy force (p_b) resulting from the difference between the average densities of the host rock and magma, will be added to the initial magma excess pressure to help driving the sheet intrusion, so the resulting overpressure will be (Gudmundsson et al., 1999; Gudmundsson, 2012):

$$p_o = p_e + p_b = p_e + (\rho_r - \rho_m)gh + \sigma_d \tag{4}$$

where ρ_r is the average host-rock density, ρ_m is the average magma density, g is acceleration due to gravity, h is the depth of the source, and σ_d is the differential stress ($\sigma_d = \sigma_1 - \sigma_3$), which in the case of an isotropic (lithostatic) situation will be 0. To continue the intrusion, magma overpressure must be large enough to fracture the rock and to overcome the viscous forces of resistance opposing to flow (Middleton and Wilcock, 1994). And this will be achieved if a sufficient volume of magma is available at the reservoir from which the intrusion is being pumped up. However, for simplification we have not considered in our calculations the viscous pressure dissipation along the length of the dyke due to magma flow. The exact volume of magma needed to ensure that an intrusion will reach the surface will depend on each case on the physical characteristic of magma and host rock (see Traversa et al., 2010, Equations 15 and 38). Also, magma intrusion must occur at sufficient high rate in order to avoid much cooling of magma that could increase its viscosity in excess, halting motion. If magma intrusion progresses enough to reach shallower levels, it may start degassing due to the decrease of lithostatic pressure. If this gas is retained at the tip of the sheet intrusion it will represent an additional increase of pressure at the interior of the intrusion, but if it escapes through the rock porosity, pressure will decrease as magma density will increase.

As indicated before, to know the exact path a magma intrusion will follow and where it will intersect the surface, we have to consider how the orientation of the stress field may change all along the magma pathway. This requires to know the internal structure of the system, including the location and size of stratigraphic, lithological, rheological and structural discontinuities, lateral and vertical extent of major tectonic features, horizontal distribution of deviatoric stresses, and distribution of loading stresses due to complex topographies. Obviously, this is not an easy task. In fact, in comparison with classical sedimentary basins, the internal geometry of volcanic systems is much more complex due to the irregular stratigraphic relationships shown by volcanic materials, their contrasting lithologies, their affectation by active tectonics, and the numerous magmatic intrusions that may be present. Imaging the interior of volcanic systems at lithospheric or crustal scales with geophysical methods does not provide models sufficiently detailed to detect dykes or sills. In recent years, the application of high resolution shallow geophysical methods has opened a new window to visualize in great detail the internal geology of volcanic systems (e.g., Mrlina et al., 2009; Cassidy and Locke, 2010; Bolós et al., 2012; Barde-Cabusson et al., 2013; Blaikie et al., 2014), but their resolution does not penetrate deeper than a few hundreds of meters. Therefore, obtaining a precise picture of the interior of a volcanic system and how a new injection of magma may cross it to reach the surface is, by now, still difficult. However, having a minimum knowledge at a lithospheric and crustal scale of the main stratigraphic units, the distribution of the main tectonic structures, the orientation of the current regional stress field, and the topography of the area, we can infer the main stress constraints that sheet intrusions may have.

DYNAMICS AND MECHANICS OF SHEETS INTRUSIONS IN THE LITHOSPHERE

We will start examining the conditions to drive a sheet intrusion (dyke) to the surface from four different reservoirs located at different depths, in an isotropic and homogeneous lithosphere. Each reservoir is recharged from below in order to cause the excess pressure necessary to initiate the sheet intrusion (**Figure 6**). The conditions for p_m, p_e, and p_o are as explained above and in **Figure 5**. For each case, we will study the critical influence of the magma reservoir size on eruption likelihood, quantifying the volume required for the creation and growth of a dyke from the reservoir to the Earth's surface, and the magma overpressure achieved in each case inside the dyke. In all cases, we will assume that the geometry of the reservoir allows tensile stresses to concentrate at the center of its upper part, so the sheet intrusion will propagate vertically toward the surface.

To compute the critical volume required for the creation and growth of a dyke we use the mathematical approximation performed by Traversa et al. (2010), which relates the magma reservoir volume, Vr, and the reservoir excess pressure variations due to dyke propagation:

$$V_r = \frac{\Delta V_r}{\exp\left(\Delta P_{rvar}\left(\frac{4G+3K}{4GK}\right)\right) - 1} \tag{5}$$

where ΔVr is the variation (decrease) in reservoir volume produced by the magma injected in the dyke, ΔP_{rvar} is the corresponding decrease of the reservoir excess pressure, and G and K are the shear and bulk moduli of the host rock.

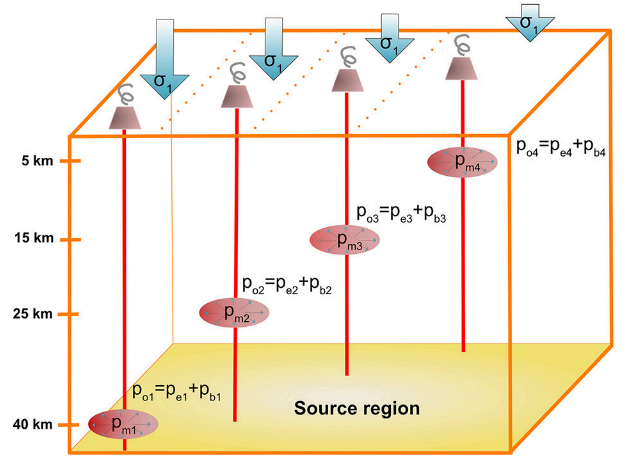

FIGURE 6 | Sketch illustrating a sheet intrusion in a homogeneous and isotropic lithosphere, as described in text.

Combining Equation (5) with Equation (4), which gives us the magma overpressure in the dyke, p_o, and assuming that the decrease of reservoir overpressure is (mainly) caused by the dyke propagation up to the surface, we may establish the approximation:

$$\Delta P_{rvar} \approx p_o \tag{6}$$

With this relation we can calculate the minimum reservoir volume, Vr, required for a dyke injection, ΔVr, for different reservoir depths and density contrast ($\rho_r - \rho_m$) scenarios. **Figure 7** shows the results of model calculations for each scenario. We show different plots with the evolution of the magma overpressure at the dyke tip (in blue) propagating up from the reservoir roof (at 5, 15, 25, and 40 km depth) through the crust. Using Equations (4) and (5) we have calculated the corresponding minimum size of the reservoir at different heights of the dyke (in red) for a common priori magma injection $\Delta Vr = 1.0 \times 10^8$ m^3, which represents the maximum value of intrusions associated with the historical eruptions in the Canary Islands (Becerril et al., 2013b). As excess pressure, p_e, at the time of hydrofracturing formation is normally equal to the tensile strength of the rock (Gudmundsson, 2012), we used a constant = 3 MPa, that represents the most common value of the crustal rocks tensile strength (Gudmundsson, 2012). To estimate the magma overpressure at the dyke tip, p_o, we have also considered the contribution of magma buoyancy, p_b, as indicated in Equation (3). The results obtained applying this simple model (i.e., isotropic and homogeneous lithosphere) show that, depending on where it starts inside the lithosphere, any sheet intrusion will require a specific available volume of magma and a critical overpressure to ensure that it will arrive at the Earth's surface (**Figure 7**). A more realistic approach, even assuming an isotropic and homogeneous lithosphere, would have required considering the exact rheological behavior of the host rock (elastic or rigid) in front of the pressure changes in the reservoir, the rheological changes of magma due to pressure and temperature changes during dyke emplacement, and also the pressure drop due to viscous flow of the magma (see Turcotte and Schubert, 1982; Gudmundsson, 2011a). However, our model offers a first order approach that we consider valid for the purpose of this review. The implications derived from this model will not change in the case of a more realistic heterogeneous and anisotropic lithosphere. However, it will be necessary to know the exact distribution of potential stress barriers inside the lithosphere to be able to predict a magma path. In such cases, any stress barrier caused by a density or rheological contrast, presence of a tectonic structure, or existence of a differential stresses may induce stress rotation and make the sheet intrusion divert from the direction it was propagating, or even to arrest it in case the overpressure required to surpass that obstacle is not achieved. This may explain how dykes may divert into sills forming new magma reservoirs (Menand et al., 2010; Gudmundsson, 2011a), or how dykes or sills may propagate for tens of kilometers inside the crust before becoming vertical again and erupting at surface (e.g., Martí et al., 2013) or stopping before it reaches it (e.g., Wright et al., 2006; Ayele et al, 2007).

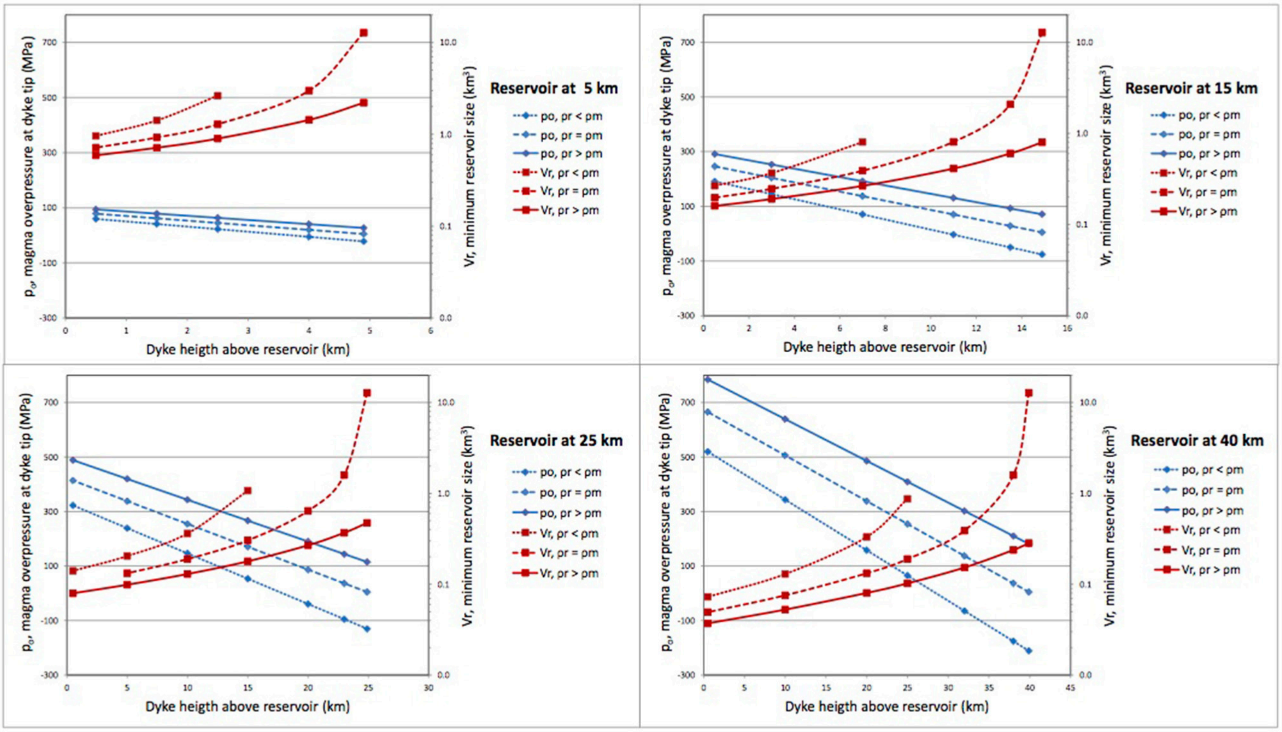

FIGURE 7 | Graph plots showing results concerning magma overpressures and magma volumes required in each scenario of Figure 5. We show different plots with the evolution of the magma overpressure at the dyke tip (in blue) propagating up from the reservoir roof (at 5, 15, 25 and 40 km depth) thought the crust, and the minimum size of the reservoir at different heights of the dyke (in red) for a common priori magma injection $\Delta Vr = 1.0 \times 10^8$ m^3. We have considered three possible cases of positive, null and negative density contrast between the magma and the host rock, with 2.55×10^3 kg/m^3 for a mean value of the magma density range (Murase and Mcbirney, 1973) and 3.0×10^3, 2.55×10^3 and 2.0×10^3 kg/m^3 for host rock, assuming that most crustal rock densities are in that range (Gudmundsson, 2012). We used $K = 1.0 \times 10^9$ Pa for the bulk modulus and $G = 1.13 \times 10^9$ Pa for the shear modulus.

Assuming similar conditions to the previous case for the magma reservoir, we consider now an heterogeneous and anisotropic lithosphere with rheological differences (layers with different color, **Figure 8**) or presence of faults or cracks (black bars, **Figure 8**), each one representing a different stress component in the total stress field. We also include an intermediate stop with the formation of a new intermediate reservoir for calculating what is needed in that case, first to stop magma migration for a while, and second to initiate and sustain a new sheet intrusion from that shallower position, assuming a continuous connection with the deeper reservoir. We assume that rock rheological contrasts hinder magma migration and that the presence of faults and fractures facilitate it (see Delaney et al., 1986; Gaffney et al., 2007; Le Corvec et al., 2013c).

With regard to structural discontinuities we have to differentiate between faults (discontinuity in an homogeneous rock mass that has undergone some relative shear displacement and that is assumed to have material toughness in fracture mode I (extension) equal or close to 0), and fissures, joints or cracks that would represent tensional pre-existing or newly formed rock rupture zones that present a considerable toughness. In other words, it is assumed that faults are already open while joints or cracks will offer a variable resistance to open and propagate under tensile stress depending on the material they form in.

Therefore, for a dyke to open a pre-existing fault magma pressure has to overcome the compressive normal stress on the fault (that keeps the fault closed). Once magma opens the fault, it will starts flowing inside and magma intrusion will continue through the fault plane while the mechanical conditions along it do not change. However, if the fault plane is intersected by other fractures, particularly in the hanging wall, these may capture magma if the pressure required to propagate any of the hanging fractures is less than the pressure required to open and flow along the fault plane (Gaffney et al., 2007). Gaffney et al. (2007), proposed an analytical solution to approximate the conditions under which magma will flow either along the fault or upwards into the hanging wall.

In a heterogeneous rock that contain faults and joints, magma will open a pre-existent fault if magma overpressure is:

$$p_o \geq \sigma_{n,fault} \tag{7}$$

and will open a tensile fracture if magma overpressure is greater than the sum of the normal stress in the fracture, plus the material toughness Γ_I in fracture mode I (an extension fracture). For a fracture length, a, in an infinite or semi-infinite medium with a stress-intensity factor at the fracture tip due to magma pressure

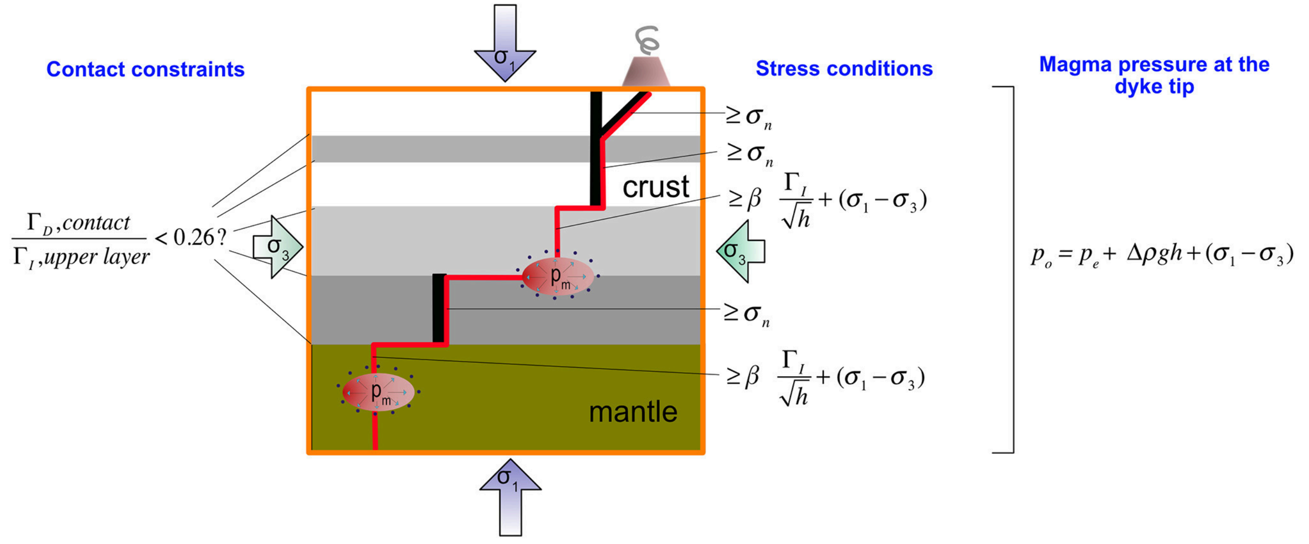

FIGURE 8 | Sketch illustrating the progression of a sheet intrusion in a heterogeneous and anisotropic lithosphere. We include an intermediate stop with the formation of a new intermediate reservoir for calculating what is needed in that case, first to stop magma migration for a while, and second to initiate and sustain a new sheet intrusion from that shallower position, assuming a continuous connection with the deeper reservoir. We assume that rock rheological contrasts hinder magma migration and that the presence of faults and fractures facilitate it. We also indicate the mechanical constraints at each contact between layers of different rheologies, the stress conditions at the tip of the sheet intrusion at different steps of its propagation to the surface, and the magma overpressure in the sheet intrusion at any moment of its emplacement (see text for more explanation).

inside the fracture, K_I, the condition can be written as follows:

$$P_m \geq \frac{K_I}{\beta\sqrt{\pi a}} + \sigma_{n,\,fracture} \tag{8}$$

where the coefficient β accounts for the geometry of the fracture, being in the simplest form (uniform pressurized elliptical flat crack of radius, a, at the edge of a semi-infinite plane), $\beta = 1.12$ (Dundurs, 1969; Rice, 1980; Gaffney et al., 2007) .

If the fault has a dip angle, α, the stress normal to the fault will be:

$$\sigma_n = \sigma_v \cos^2\alpha + \sigma_h \sin^2\alpha \tag{9}$$

Assuming that the vertical stress is gravitational, $\sigma_v = \rho g d$ (ρ the density of the rock, g the gravity acceleration and d the depth) and that the horizontal stress, σ_h, (positive compressive, negative tensile) is proportional to the vertical stress ($\sigma_h = k.\sigma_v$), the minimum fracture length required for a dyke to propagate vertically in a medium where the normal stress on the fracture plane is approximated by the far-field stress, $\sigma = \sigma_h$, is:

$$a_c = \frac{{\Gamma_I}^2}{\pi(\beta\rho g d)^2\left[k\left(\sin^2\alpha - 1\right) + \cos^2\alpha\right]^2} \tag{10}$$

and the critical depth, d_c, for a given fracture length, a, greater the total depth, d, the dyke will propagate vertically:

$$d_c = \frac{\Gamma_I}{\beta\rho g\sqrt{\pi a}\left[k\left(\sin^2\alpha - 1\right) + \cos^2\alpha\right]} \tag{11}$$

Figure 9 shows the results of these second calculations. These results are in good agreement with those obtained by Gaffney et al. (2007). Both show that the minimum length of a vertically-oriented hanging-wall fracture needed to divert magma from a fault plane diminishes considerably with depth. Therefore, for a dyke to be captured by a pre-existing fault that it intersects, the fault will need to be either relatively high-angle, and/or the intersection will be at shallow depths (<3 km). In other words, it is not straightforward for magma to enter a fault in the first place. Once that has happened, then the analysis shown in **Figure 9** applies to the magma subsequently being diverted upward from the fault plane. Therefore, for magma to propagate horizontally at great depth, it will require specific structural and/or mechanical conditions that will force such type of movement instead of migrating vertically toward shallower levels. Another implication of the results shown in **Figure 9** is that, as earthquake magnitude is proportional to the fracture length, the smaller magnitude earthquakes (that would correspond to small fractures opening at the hanging wall) would be observed from very deep to close to the surface, while the greater magnitude earthquakes will only occur closer to the surface (**Figure 9D**).

In the case of a dyke intersecting a stratigraphic discontinuity that represents a rheological contrast between two rock layers, the dyke may become arrested, penetrate the contact, or be deflected along it (He and Hutchison, 1989; He et al., 1994; Gudmundsson, 2011a,b). The general stress conditions for the dyke to continue its propagation or to become a sill have been analyzed before (see **Figures 3**, **4**, and Equation 2). We will examine here the influence of different mechanical properties at both sides of the rheological contact. Following the formulation presented by He and Hutchison (1989) and He et al. (1994) for the case of a dyke crossing a mechanical discontinuity, the condition for

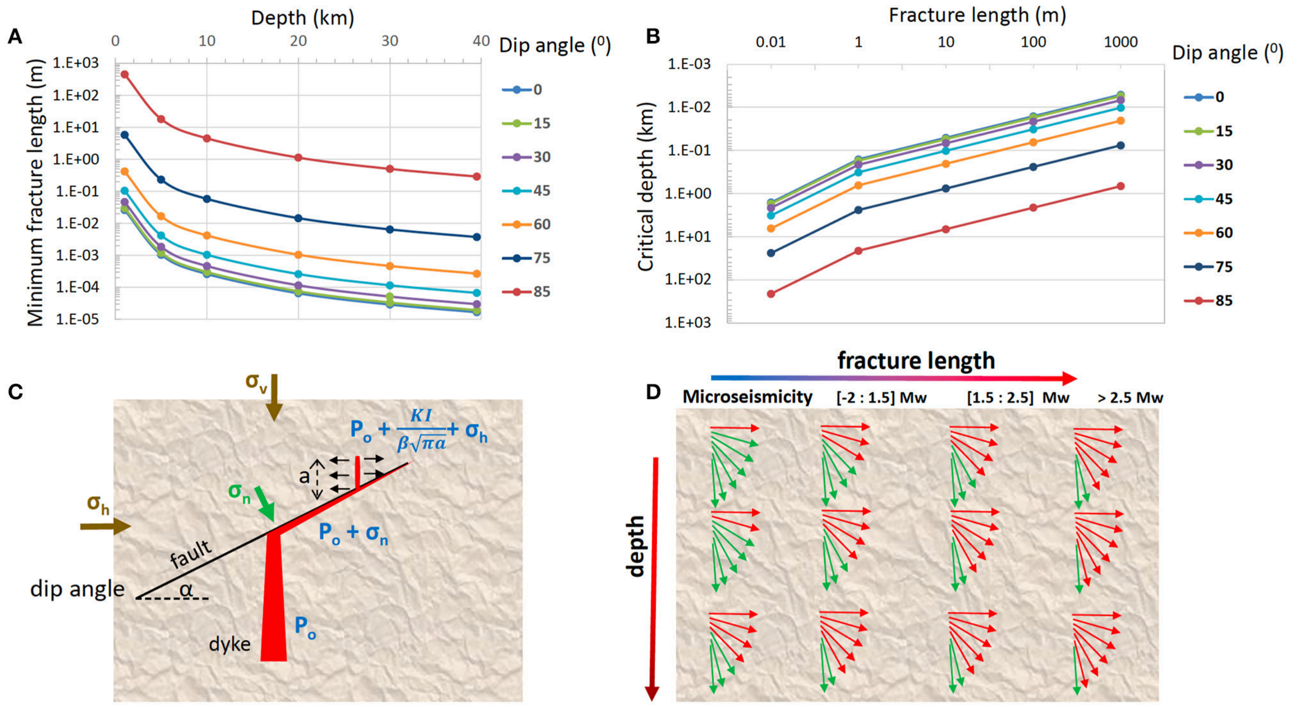

FIGURE 9 | Graph plots showing the results from the scenario illustrated in Figure 8. (A) the minimum length of a vertically-oriented hanging-wall fracture needed to divert magma from a fault plane with normal stress σ_n **(B)** the critical depth for different fault dip angles, α = [0°, 15°, 30°, 45°, 60°, 75°, and 85°], according to the model shown in **(C)**. We have used a fracture toughness typical of basalts, $\Gamma_I = 4$ MPa $m^{1/2}$, β = 1.12 and k = 1/3. In **(D)** we summarize **(A,B)** results: the critical fracture length decreases with depth and for the same depth it is shorter for lower fault dip angles. This means that in the presence of a fractured media, except close to the surface, it will be improbable that a dyke propagates along low angle fault planes (red arrows). However, propagation along long angle fault planes will be facilitated (green arrows) at much lower depths (or much lower σ_V values).

penetrating it depends on the rate of the strain energy release associated with dyke penetration:

$$G_p = \left({}^{(1-\upsilon_1)}\!\big/\!{}_{2\mu_1} \right) . K_I^2 \tag{12}$$

and the strain energy rate associated with deflection (sill formation):

$$G_d = \left(\left({}^{(1-\upsilon_1)}\!\big/\!{}_{\mu_1} \right) + \left({}^{(1-\upsilon_2)}\!\big/\!{}_{\mu_2} \right) \right) . \left(K_I^2 + K_{II}^2 \right) / \left(4.cosh^2\ \pi\varepsilon \right) \tag{13}$$

where, K_I , is the mode I (tensile) stress-intensity factor, K_{II} , the model II (shear) stress-intensity factor, which depends on the magma pressure inside the dyke and on the geometrical properties of the contact, and υ and μ area the Poisson's ratio and shear modulus, respectively, corresponding to layer 1 (upper) and layer 2 (lower), when the dyke in layer 2 tries to penetrate into layer 1.

The dyke is likely to continue its vertical path penetrating into layer 1 if:

$$\frac{G_d}{G_p} < \frac{\Gamma_D}{\Gamma_1} \tag{14}$$

where Γ_1 is the layer 1 mode I toughness and Γ_D is the toughness on layer 2 for the combined models I and II.

For a given dyke-segment length a, reaching the contact, the rate G_d/G_p depends only on the relation of the mechanical properties of both layers and not on the magma pressure, so an increase in magma pressure will imply a longer distance reached by the sheet intrusion but will not influence the direction of emplacement. He and Hutchison (1989) showed that a dyke becomes deflected between two layers of contrasted mechanical properties only if the material toughness of layer 2 is less that 26% of the material toughness of layer 1. So, a dyke will deflect into a sill when $\Gamma_D < 0.26\ \Gamma_1$ and will continue as a dyke crossing the rheological contact when $\Gamma_D > 0.26\ \Gamma_1$. Moreover, when the stiffness (Young modulus, E) of the layer 1 (upper) is less that the stiffness of layer 2, there is generally much less tendency for deflection of a dyke into a sill (Gudmundsson, 2011b), and conversely, being improbable the dyke to penetrate in layer 1 when $E_1 >> E_2$.

Therefore, despite magma overpressure being the driving force for magma to move upwards, it will not control whether a dyke will be deflected into a sill at a rheological contrast or will continue straight. This will be determined by the mechanical contrast between the two rocks. This is an important concept, as higher magma overpressures will only represent longer emplacement distances but not necessarily higher capacities to cross heterogeneous lithologies and to reach the surface. This is particularly applicable to unfractured media. If an ascending dyke intersects a much stronger layer, it is still more likely to continue vertically if there are any vertical/subvertical fractures in that stronger layer, particularly if this occurs at depth as previously indicated by Gaffney et al. (2007), and now in this study (**Figure 9**). Faults and fractures may facilitate paths for magma ascent, as they represent zones of more favorable stress conditions for magma to penetrate into the host rock with lesser energy consumption, as it seems to be confirmed by the structural control in the location of vents observed in most of the monogenetic volcanic fields (e.g., Le Corvec et al., 2013b). However, the effectiveness of structural features to direct magma migration depends on the depth and dip angle of each structure, the pre-existing normal or transtensional faults being very effective in transporting magma at very shallow depths.

DISCUSSION

In this review we have considered the main aspects that govern magma migration in monogenetic volcanic systems. We have tried to offer a comprehensive review of what happens in the plumbing systems of such type of volcanoes and how they prepare for new eruptions. We have not intended to provide a complete review of monogenetic volcanism, for which there are already excellent studies (e.g., Wood, 1980; Tibaldi, 1995; Connor and Conway, 2000; Walker, 2000; Valentine and Gregg, 2008; Németh, 2010; Le Corvec et al., 2013b; Németh and Kereszturi, 2015), but we have tried to clarify the most relevant concepts that need to be understood when conducting hazard assessment in such volcanic fields and, in particular, during the probabilistic analysis of analysis of vent opening (volcanic susceptibility). In this sense, we have concentrated our attention on dyke ascent processes in response to the surrounding environment (stress fields, structures, etc.), but have not considered specifically the potential effect of magma flux and magmatism-induced stresses on the ambient ones. This effect was studied by Valentine and Perry (2007) and Le Corvec et al. (2013c), among others. We have considered it as a long term effect that will determine whether the magmatism responsible for the formation of the volcanic field will respond passively to or will actively overwhelm ambient tectonism, so its potential contribution should be added to the stress field. However, it will not significantly modify the stress configuration that governs sheet intrusion.

The reason why magma will erupt at one specific point and not at any other on the volcanic field depends on how the magma driving force will act against the stresses configuration inside the lithosphere, and not only at surface. This 3D stress configuration results from a combination of regional and local stress components that define for each point a resultant stress field that will determine whether magma will continue or halt its migration, and the path it will follow in the first case. Through the definition of a series of basic concepts and the application of two very simple models, we have tried to explain the first order physical requirements for magma to migrate inside the host rock and why that migration will follow a certain path or direction and not any other.

Monogenetic volcanic fields are well distributed all around the world and in most geodynamic environments. This implies that the geodynamic constraints (i.e., the regional tectonic stresses) do not determine whether or not such type of volcanism will be present in a specific tectonic setting, but contribute to the distribution and extent of monogenetic volcanic fields. A quantitative comparison of a large number of volcanic fields in different settings was provided by Le Corvec et al. (2013b). Monogenetic fields present different characteristics, including eruption frequency, total erupted volumes, or long term magma fluxes, and may correspond to different tectonic settings. However, magma migration processes are basically the same in all cases and differences in location of volcanic vents, extension of the volcanic fields, eruptive recurrence, or temporal and spatial evolution of vent clustering, may be easily interpreted as due to the different regional stresses (tectonics) governing each of them, as a consequence of the different geodynamic settings where they are located.

We have analyzed how magma acquires the necessary overpressure to cause a hydraulic fracture and migrate through it to shallower levels. We have assumed in all cases a scenario defined by the presence of a reservoir over-pressurized by intrusion of new magma from below, and it being this excess pressure that is the driving force to initiate and drive magma intrusion. Fracture propagation is then controlled by the magma overpressure that results from the excess pressure at the source reservoir and the buoyancy component derived from the density differences between magma and host rock. In this scenario there is always a connection between the source reservoir and the propagating sheet intrusion, so the overpressure required to ensure magma propagation is always depending on the source reservoir minimum volume. We have calculated this minimum volume and the resulting magma overpressures for different host rock configurations, and the results obtained show how shallower reservoirs require larger minimum volumes than deeper reservoirs to acquire the necessary magma overpressures to sustain sheet intrusion up to the surface. This is due to the fact that the buoyancy component of the magma overpressure is less effective at shallow depths, so the magma excess pressure (i.e., volume) in the reservoir needs to be higher. From these results it is also important to note the role of the density contrast between magma and host rock, as this also determines the magma excess pressure that will be necessary to ensure effective magma migration and, consequently, will determine the minimum volume the source reservoir will need to have. Magma migration through sheet intrusions in an anisotropic and heterogeneous host rock will be governed by the same principles but requiring higher overpressures to surpass stress barriers that may inhibit magma movement. This will normally imply changes in the direction of the intrusion, so making its paths toward shallower levels unpredictable, except the exact position of such stress barriers at the interior of the volcanic systems is well known. In a similar way, magma migration can change direction when finding structural discontinuities such as normal faults or tensional fractures that may trap magma facilitating its ascent toward shallower levels.

The scenario for magma intrusion that we have considered contrasts with other accepted models of magma propagation through fissures in which the sheet intrusion disconnects from its source as it migrates. In this case (see Rubin, 1995; Valentine and Gregg, 2008) it is assumed that the exsolved gas concentrates at the dyke tip and exerts the maximum overpressure, thus reducing the pressure at the base of the magma column causing the wall rocks to squeeze inward and push the magma upward. However, geophysical monitoring data recorded during recent eruptions (e.g., El Hierro, Martí et al., 2013; Bardarbunga, Gudmundsson et al., 2014; Sigmundsson et al, 2015) confirm that, at least in these cases, there was a continuous connection between the advancing sheet intrusion and an overpressure source during the whole event.

In this conceptualization of how magma migrates inside the host rock, we should not confuse the capacity for magma to create hydraulic fractures (i.e., magma overpressure) with the orientation that these fractures will have (determined by the external stress field components). From the models presented here we can deduce that only at very shallow depth (<3 km) magma overpressure will be the main component of the local stress field. This is an essential concept when dealing with volcano monitoring and eruption forecasting. Most volcanic models or methods that have been developed (Connor, 1990; Connor et al., 1992, 2000; Ho, 1992, 1995; Martin et al., 1994; Ho and Smith, 1998; Connor and Conway, 2000; Alberico et al., 2002; Martí and Felpeto, 2010; Cappello et al., 2012; Selva et al., 2012; Bartolini et al., 2013; Becerril et al., 2013a; Bevilacqua et al., 2015) consider the observable tectonic structures (eruptive fissures, joints, faults, dykes, sills, lineations, vent location) as indicators of paleostresses, so when they are combined with the age at which they formed we can obtain a picture of the stress evolution with time at surface. In this sense, the youngest structures will indicate the most recent stress configuration, and will define the areas with higher probabilities of hosting new vents. According to this assumption and regardless of the interpolation method used to estimate the spatial probabilities, the areas including the most recent structures will receive higher susceptibility values. And this would be a good approach and a reliable result if magma would ascent vertically from the source. However, none of these models consider the regional stress field or the variations of stress with depth. This implies that the result obtained may not be sufficiently precise according to the level of uncertainty that is acceptable in a hazard assessment. In fact, well monitored recent eruptions (e.g., Bardarbunga, El Hierro), even if they do not perfectly represent pure monogenetic eruptions, showed how magma may migrate horizontally for long distances inside the volcanic system, thus making the short term estimate of volcanic susceptibility (i.e., considering monitoring information, see Sobradelo and Martí, 2015) very challenging. Also, previous studies (e.g., Maccaferri et al., 2011; Menand, 2011; Taisne et al., 2011; Gudmundsson, 2011b) and the models presented here indicate how an ascending magma path may be diverted or arrested in a heterogeneous and anisotropic lithosphere, depending on how regional and local stress components will be distributed. Moreover, it is worth mentioning that each new intrusion episode (ending or not with an eruption) may induce changes in the local stress distribution creating new stress barriers that did not exist before and that may affect magma movement in further intrusions.

Therefore, one of the aims of this review has been to add some basic physics to the geological record based hazard models that are being used in monogenetic volcanism, in order to help understanding how they work and the uncertainly that their results may have associated with them. In fact, if volcanoes are clustered or aligned, it is reasonable to use that information to weight spatial probabilities for future events, but it is also important to know that the conditions for such particular distribution of vents depend on how stresses distribute inside the volcanic system and not only at surface. Unfortunately, the uncertainty in the deep subsurface processes and material properties is quite large and largely irreducible. The very basic dyke models we have provided in this review may not help to reduce the uncertainty in forecasting monogenetic eruptions, but we hope they will help to better understand which is the source of that uncertainty.

Of course, if no changes occur in the distribution of regional and gravitation stresses in the area between two successive eruptions, we may consider that magma migration will follow a similar path in both if it starts from a source located in a similar position. So, consequently, the next eruption may occur close to the previous one. The difference in the final position of the new vent may be caused by the influence of very shallow stress barriers created by the intrusion(s) remaining from the last eruptive event. However, the occurrence of clusters of vents of different location and age suggests the existence of significant stress changes at a timescale longer than the eruptive recurrence of the system. Therefore, eruptions occurring under the same regional stress configuration will tend to vent one close to the other, but when tectonic changes have occurred the location of vents will probably change, clustering in another sector of the volcanic field, as it is observed in many monogenetic fields. So, if the time scale for a hazard forecast is short compared to the time scale for changes in the ambient stresses and material properties and magma generation at depth, then a hazard forecast based on a sufficient portion of the history of the volcanic field is reasonable. Anyway, it will be also necessary to assess whether the behavior of the volcanic field has changed over long time scales, and whether there is evidence for sufficient change in a very recent time scale that is not yet reflected in the pattern of volcanism (e.g., Connor et al., 2000, 2009, and references herein).

As we have explained before, when we conduct long term hazard assessment one of the first actions we have to undertake is the evaluation of spatial probability of vent opening. This task will essentially be undertaken based on structural indicators such as position of vents, eruptive fissures, fractures, faults, and dykes, which will be computationally weighted according to their relative age. It will be also important to consider the current configuration of regional horizontal stresses and gravitational stresses in case of abrupt topographies. However, in a volcanic crisis we will need to systematically update this information in real time as soon as monitoring information arrives (see

Sobradelo and Martí, 2015; Bartolini et al., 2016), as the evolution in the position of magma at depth and its potential arrival at surface may change with respect to what was predicted in the long-term susceptibility analysis. Anticipating possible changes of the unrest activity and, consequently, of the potential location of a future vent, will depend on the characteristics of our monitoring network, but also on the knowledge we may have of the internal structure of the volcanic system. The better this is, the more accurate (i.e., less uncertainty) will result our forecasting of the possible eruption.

FINAL REMARKS

Monogenetic volcanic fields are not easy to forecast due to the apparent random character of magma migration inside them. Even during unrest episodes, in which we have real time monitoring data, it is not an easy task to forecast well in advance where the new vent will form, as drastic changes in the direction of magma propagation may occur due the presence of unforeseen stress barriers at the interior of the volcanic system. This review has intended to clarify some basic aspects of magma transport in monogenetic fields, in order to help understanding the sources of uncertainty associated with eruption forecasting in such systems. It is obvious that the more information we will be able to provide on the internal structure of monogenetic fields, the better will be the interpretation of unrest episodes and the anticipation to future eruptions. Unfortunately, it is not easy to know how crustal stresses change with depth and where significant stress barriers may be located in such volcanic systems. Therefore, it is worth insisting on the need to combine geological studies, aimed at characterizing the nature and age of the main structural features observable at surface, together with geophysical studies (e.g., seismic, magnetotelluric, and electric tomographies, high resolution gravimetry, etc) imaging the interior of the volcanic systems, as well as with geodynamic models on regional stresses, to better characterize vents distribution in monogenetic fields. Moreover, the information provided by such multidisciplinary studies should be incorporated and computed into the long and short term susceptibility analysis of such volcanic systems in order to get more precise hazard assessments and, thus, to be able to forecast more accurately what may happen in case of new eruptions.

AUTHOR CONTRIBUTIONS

All authors have participated in the elaboration of this study. JM and CL have written the final version of the manuscript and have participated, together with SB in the elaboration of the models. SB, LB, and AG have elaborated the analysis of different natural examples and have contributed to the preparation of all preliminary drafts.

ACKNOWLEDGMENTS

This research was funded by the European Commission (FP7 Theme: ENV.2011.1.3.3-1; Grant 282759: VUELCO and EC ECHO Grant SI2.695524: VeTOOLS). AG thanks the support provided by the Ramón y Cajal research program (RYC-2012-11024). We thank Gregg Valentine and Alessandro Tibaldi for their useful and constructive reviews.

REFERENCES

Alberico, I., Lirer, L., Petrosino, P., and Scandone, R. (2002). A methodology for the evaluation of long-term volcanic risk from pyroclastic flows in Campi Flegrei (Italy). *J. Volcanol. Geotherm. Res.* 116, 63–78. doi: 10.1016/s0377-0273(02)00211-1

Albert, H., Costa, F., and Martí, J. (2015). Timing of magmatic processes and unrest associated with mafic historical monogenetic eruptions in Tenerife Island. *J. Petrol.* 56, 1945–1966. doi: 10.1093/petrology/egv058

Albert, H., Costa, F., and Martí, J. (2016). Years to weeks of seismic unrest and magmatic intrusions precede monogenetic eruptions. *Geology* 44, 211–214. doi: 10.1130/g37239.1

Ayele, A., Jacques, E., Kassim, M., Kidane, T., Omar, A., Tait, S., et al. (2007), The volcano-seismic crisis in Afar, Ethiopia, starting September 2005. *Earth Planet. Sci. Lett.* 255, 177–187.

Bacon, C. R., Bruggman, P. E., Christiansen, R. L., Clynne, M. A., Donnelly-Nolan, J. M., and Hildreth, W. (1995). Primitive magmas at fives Cascade volcanic fields: melts from hot, heterogeneous sub-arc mantle. *Can. Mineral.* 35, 397–423.

Barde-Cabusson, S., Bolós, X., Pedrazzi, D., Lovera, R., Serra, G., Martí, J., et al. (2013). Electrical resistivity tomography revealing the internal structure of monogenetic volcanoes. *Geophys. Res. Lett.* 40, 2544–2549. doi: 10.1002/grl.50538

Bartolini, S., Cappello, A., Martí, J., and Del Negro, C. (2013). QVAST: a new Quantum GIS plugin for estimating volcanic susceptibility. *Nat. Hazards Earth Syst. Sci.* 13, 3031–3042.

Bartolini, S., Sobradelo, R., and Martí, J. (2016). ST-HASSET for volcanic hazard assessment: a Python tool for evaluating the evolution of unrest indicators. *Comput. Geosci.* 93, 77–87. doi: 10.1016/j.cageo.2016.05.002

Bebbington, M. S., and Cronin, S. (2011). Spatio-temporal hazard estimation in the Auckland Volcanic Field, New Zealand, with a new event-order model. *Bull. Volcanol.* 73, 55–72. doi: 10.1007/s00445-010-0403-6

Becerril, L., Cappello, A., Galindo, I., Neri, M., and Del Negro, C. (2013a). Spatial probability distribution of future volcanic eruptions at El Hierro Island (Canary Islands, Spain). *J. Volcanol. Geotherm. Res.* 257, 21–30.

Becerril, L., Galindo, I., Gudmundsson, A., and Morales, J. M. (2013b). Depth of origin of magma in eruptions. *Sci. Rep.* 3:2762.

Bevilacqua, A., Isaia, R., Neri, A., Vitale, S., Aspinall, W. P., Bisson, M., et al. (2015). Quantifying volcanic hazard at Campi Flegrei caldera (Italy) with uncertainty assessment: 1. Vent opening maps. *J. Geophys. Res. Solid Earth* 120, 2309–2329. doi: 10.1002/2014JB011775

Blaikie, T. N., Ailleres, L., Betts, P. G., and Cas, R. A. F. (2014). A geophysical comparison of the diatremes of simple and complex maar volcanoes, Newer Volcanics Province, south-eastern Australia. *J. Volcanol. Geoth. Res.* 276, 64–81. doi: 10.1016/j.jvolgeores.2014.03.001

Blake, S. (1981). Volcanism and dynamics of open magma chambers. *Nature* 289, 783–785. doi: 10.1038/289783a0

Bolós, X., Martí, J., Becerril, L., Planagomà, L., Grosse, P., and Barde-Cabusson, S. (2015). Volcano-structural analysis of La Garrotxa Volcanic Field (NE Iberia): implications for the plumbing system. *Tectonophysics* 642, 58–70. doi: 10.1016/j.tecto.2014.12.013

Bolós, X., Barde-Cabusson, S., Pedrazzi, D., Martí, J., Casas, A., Himi, M., et al. (2012). Investigation of the inner structure of La Crosa de Sant Dalmai maar (Catalan Volcanic Zone, Spain). *J. Volcanol. Geotherm. Res.* 247–248, 37–48. doi: 10.1016/j.jvolgeores.2012.08.003

Bower, S., and Woods, A. (1997). Control of magma volatile content and chamber depth on the mass erupted during explosive volcanic eruptions. *J. Geophys. Res.* 102, 10273–10290. doi: 10.1029/96jb03176

Brenna, M., Cronin, S. J., Németh, K., Smith, I. E. M., and Sohn, Y. K. (2011). The influence of magma plumbing complexity on monogenetic eruptions, Jeju Island, Korea. *Terra Nova* 23, 70–75. doi: 10.1111/j.1365-3121.2010.00985.x

Cappello, A., Neri, M., Acocella, V., Gallo, G., Vicari, A., and Del Negro, C. (2012). Spatial vent opening probability map of Etna volcano (Sicily, Italy). *Bull. Volcanol.* 74, 2083–2094. doi: 10.1007/s00445-012-0647-4

Cassidy, J., and Locke, C. A. (2010). The Auckland volcanic field, New Zealand: geophysical evidence for structural and spatio-temporal relationships. *J. Volcanol. Geotherm. Res.* 195, 127–137. doi: 10.1016/j.jvolgeores.2010.06.016

Connor, C. B. (1990). Cinder cone clustering in the transMexican Volcanic Belt: implications for structural and petrologic models. *J. Geophys. Res.* 95, 19395–19405. doi: 10.1029/jb095ib12p19395

Connor, C. B., Chapman, N. A., and Connor, L. J. (2009). *Volcanic and Tectonic Hazard Assessment for Nuclear Facilities*. Cambridge, UK: Cambridge University Press. doi: 10.1017/cbo9780511635380

Connor, C. B., Condit, C. D., Crumpler, L. S., and Aubele, J. C. (1992). Evidence of regional structural controls on vent distribution: springerville Volcanic Field, Arizona. *J. Geophys. Res.* 97, 12349–12359. doi: 10.1029/92jb00929

Connor, C. B., and Conway, F. M. (2000). "Basaltic volcanic fields," in *Encyclopedia of Volcanoes,* ed H. Sigurdsson (New York, NY: Academic Press*),* 331–343.

Connor, C., Stamatakos, J. A., Ferrill, D. A., Hill, B. E., Ofoegbu, G. I., Conway, F. M., et al. (2000). Geologic factors controlling patterns of small-volume basaltic volcanism: application to a volcanic hazards assessment at Yucca Mountain, Nevada. *J. Geophys. Res.* 105, 417–432. doi: 10.1029/1999jb900353

Dahm, T. (2000). Numerical simulations of the propagation path and the arrest of fluid-filled fractures in the Earth. *Geophys. J. Int.* 141, 623–638. doi: 10.1046/j.1365-246x.2000.00102.x

Delaney, P. T., and Pollard, D. D. (1981). Deformation of host rocks and flow of magma during growth of minette dykes and breccia-bearing intrusions near Ship Rock, New Mexico, U.S. *Geol. Surv. Prof. Pap*. 1202, 1981.

Delaney, P. T., and Pollard, D. D. (1982). Solidification of basaltic magma during flow in a dyke. *Am. J. Sci.* 282, 856–885.

Delaney, P. T., Pollard, P. P., Ziony, J. I., and McKee, E. H. (1986). Field relations between dykes and joints: emplacement processes and paleostress analysis. *J. Geophys. Res.* 91, 4920–4938.

Dundurs, J. (1969). Edge-bonded dissimilar orthogonal wedges. *J. Appl. Mech.* 36, 650–652.

Folch, A., and Martí, J. (1998). The generation of overpressure in felsic magma chambers by replenishment. *Earth Planet. Sci. Lett.* 163, 301–314. doi: 10.1016/S0012-821X(98)00196-4

Fossen, H. (2016). *Structural Geology*. Cambridge: Cambridge University Press.

Gaffney, E. S., Damjanac, B., and Valantine, G. A. (2007). Localization of volcanic activity: 2. Effects of pre-existing structure. *Earth Planet. Sci. Lett.* 263, 323–338.

Garcia, M. O., Hulsebosch, T. P., and Rhodes, J. M. (1995). Olivine-rich submarine basalts from the southwest rift zone of Mauna Loa volcano: implications for magmatic processes and geo-chemical evolution. *Geophys. Monogr.* 92, 219–239. doi: 10.1029/gm092p0219

Gudmundsson, A. (1990). Emplacement of dykes, sills and crustal magma chambers at divergent plate boundaries. *Tectonophysics* 176, 257–275. doi: 10.1016/0040-1951(90)90073-H

Gudmundsson, A. (2011a). *Rock Fractures in Geological Processes.* Cambridge: Cambridge University Press. doi: 10.1017/CBO9780511975684

Gudmundsson, A. (2011b). Deflection of dykes into sills at discontinuities and magma-chamber formation *Tectonophysics* 500, 50–64.

Gudmundsson, A. (2012). Magma chambers: formation, local stresses, excess pressures, and compartments. *J. Volcanol. Geotherm. Res.* 237–238, 19–41. doi: 10.1016/j.jvolgeores.2012.05.015

Gudmundsson, A., and Brenner, S. L. (2005). On the conditions of sheet injections and eruptions in stratovolcanoes. *Bull. Volcanol.* 67, 768–782. doi: 10.1007/s00445-005-0433-7

Gudmundsson, A., Lecour, N., Mohajeri, N., and Thordarson, T. (2014). Dyke emplacement at Bardarbunga, Iceland, induces unusual stress changes, caldera deformation, and earthquakes. *Bull. Volcanol.* 76:869.

Gudmundsson, A., Marinoni, L. B., and Martí, J. (1999). Injection and arrest of dykes: implications for volcanic hazards. *J. Volcanol. Geotherm. Res*. 88, 1–13. doi: 10.1016/s0377-0273(98)00107-3

Gudmundsson, A., and Philipp, S. L. (2006). How local stress fields prevent volcanic eruptions. *J. Volcanol. Geotherm. Res.* 158, 257–268. doi: 10.1016/j.jvolgeores.2006.06.005

He, M. Y., Evans, A. G., and Hutchinson, J. W. (1994). Crack deflection at an interface between dissimilar elastic materials: role of residual stresses. *Int. J. Solids Struct.* 31, 3443–3455. doi: 10.1016/0020-7683(94)90025-6

He, M. Y., and Hutchison, J. W. (1989). Crack deflection at an interface between dissimilar elastic materials. *Int. J. Solids Struct.* 25, 1053–1067.

Heidbach, O., Reinecker, J., Tingay, M., Müller, B., Sperner, B., Fuchs, K. et al. (2007). Plate boundary forces are not enough: second- and third-order stress patterns highlighted in the World Stress Map database. *Tectonics* 26:TC6014. doi: 10.1029/2007TC002133

Hernando, I. R., Aragon, E., Frei, R., Gonzalez, P. D., and Spakman, W. (2014). Constraints on the origin and evolution of magmas in the Payún Matrú Volcanic Field, Quaternary Andean back-arc of Western Argentina. *J. Petrol.* 55, 209–239. doi: 10.1093/petrology/egt066

Ho, C. H. (1992). Risk assessment for the Yucca Mountain high-level nuclear waste repository site: estimation of volcanic disruption. *Math. Geol.* 24, 347–364. doi: 10.2172/196582

Ho, C. H. (1995). Sensitivity in volcanic hazard assessment for the Yucca Mountain high-level nuclear waste repository site: the model and the data. *Math. Geol.* 27, 239–258. doi: 10.1007/bf02083213

Ho, C. H., and Smith, E. I. (1998). A spatial-temporal/3-D model for volcanic hazard assessment: application to the Yucca Mountain region, Nevada. *Math. Geol.* 30, 497–510.

Jaeger, J. C., and Cook, N. G. W. (1979). *Fundamentals of* Rock Mechanics, *3rd Edn*. London: Chapman ang Hall.

Klügel, A., Hansteen, T. H., and Galipp, K. (2005). Magma storage and underplating beneath Cumbre Vieja Volcano, La Palma (Canary Islands). *Earth Planet. Sci. Lett.* 236, 211–226. doi: 10.1016/j.epsl.2005.04.006

Klugel, A., Longpré, M. A., García-Cañada, L., and Stix, J. (2015). Deep intrusions, lateral magma transport and related uplift at ocean island volcanoes. *Earth Planet. Sci. Lett.* 431, 140–149. doi: 10.1016/j.epsl.2015.09.031

Le Corvec, N., Bebbington, M. S., Linsay, J. M., and McGee, L. E. (2013a). Age, distance, and geochemical evolution within a monogenetic volcanic field: analyzing patterns in the Auckland Volcanic Field eruption sequence. *Geochem. Geophys. Geosyst.* 14, 3648–3665.

Le Corvec, N., Spörli, K. B., Rowland, J., and Lindsay, J. (2013b). Spatial distribution and alignments of volcanic centers: clues to the formation of monogenetic volcanic fields. Earth Sci. *Rev.* 124, 96–114.

Le Corvec, N., Menand, T., and Lindsay, J. (2013c). Interaction of ascending magma with pre-existing crustal fractures in monogenetic basaltic volcanism: an experimental approach. J. *Geophys. Res. Solid Earth* 118, 968–984.

Lister, J., and Kerr, R. (1991). Fluid-mechanical models of crack propagation and their application to magma transport in dykes. *J. Geophys. Res.* 94, 10049–10077. doi: 10.1029/91jb00600

Lorenz, V. (1986). On the growth of maars and diatremes and its relevance to the formation of tuff rings. *Bull. Volcanol.* 48, 265–274. doi: 10.1007/bf01081755

Maaloe, S. (1985). Principles of Igneous Petrology. Berlin: Springer-Verlag. doi: 10.1007/978-3-642-49354-6

Maccaferri, F., Bonafede, M., and Rivalta, E. (2010). A numerical model of dyke propagation in layered elastic media. *Geophys. J. Int.* 180, 1107–1123. doi: 10.1111/j.1365-246X.2009.04495.x

Maccaferri, F., Bonafede, M., and Rivalta, E. (2011). A quantitative study of the mechanisms governing dyke propagation, dyke arrest and sill formation. *J. Volcanol. Geotherm. Res.* 208, 39–50.

Martí, J., and Felpeto, A. (2010). Methodology for the computation of volcanic susceptibility. An example for mafic and felsic eruptions on Tenerife (Canary Islands). *J. Volcanol. Geotherm. Res.* 195, 69–77.

Martí, J., and Geyer, A. (2009). Central vs flank eruptions at Teide–Pico Viejo twin stratovolcanoes (Tenerife, Canary Islands). *J. Volcanol. Geotherm. Res.* 181, 47–60.

Martí, J., Geyer, A., Andujar, J., Teixidó, F., and Costa, F. (2008). Assessing the potential for future explosive activity from Teide–Pico Viejo stratovolcanoes (Tenerife, Canary Islands). *J. Volcanol. Geotherm. Res.* 178, 529–542.

Martí, J., Pinel, V., López, C., Geyer, A., Abella, R., Tárraga, M., et al. (2013). Causes and mechanisms of the 2011–2012 El Hierro (Canary Islands) submarine eruption. *J. Geophys. Res. Solid Earth* 118, 823–839.

Martí, J., Planagumà, L., Geyer, A., Canal, E., and Pedrazzi, D. (2011). Complex interaction between Strombolian and phreatomagmatic eruptions in the Quaternary monogenetic volcanism of the Catalan Volcanic Zone (NE of Spain). *J. Volcanol. Geotherm. Res.* 201, 178–193.

Martin, A. J., Umeda, K., Connor, C. B., Weller, J. N., Zhao, D., and Takahashi, M. (1994). Modeling long-term volcanic hazards through Bayesian inference: an example from the Tohuku volcanic arc Japan. *J. Geophys. Res.* 109, B10208.

McKenzie, D. (1984). The generation and compaction of partially molten rock. *J. Petrol.* 25, 713–765. doi: 10.1093/petrology/25.3.713

McKenzie, D. (1985). The extraction of magma from the crust and mantle. *Earth Planet. Sci. Lett.* 74, 81–91.

Menand, T. (2008). The mechanics and dynamics of sills in layered elastic rocks and their implications for the growth of laccoliths and other igneous complexes. *Earth Planet. Sci. Lett.* 267, 93–99. doi: 10.1016/j.epsl.2007.11.043

Menand, T. (2011). Physical controls and depth of emplacement of igneous bodies: a review. *Tectonophysics* 500, 11–19. doi: 10.1016/j.tecto.2009.10.016

Menand, T., Daniels, K. A., and Benghiat, P. (2010). Dyke propagation and sill formation in a compressive tectonic environment. *J. Geophys. Res.* 115, B08201. doi: 10.1029/2009jb006791

Middleton, G. V., and Wilcock, P. R. (1994). *Mechanics in the Earth and Environmental Sciences*. Cambridge: Cambridge University Press.

Mrlina, J. H., Kämpf, C., Kroner, J., Mingram, M., Stebich, A., Seidl, M. et al. (2009). Discovery of the first Quaternary maar in the Bohemian Massif, Central Europe, based on combined geophysical and geological surveys. *J. Volcanol. Geoth. Res.* 182, 97–112. doi: 10.1016/j.jvolgeores.2009.01.027

Muller, J. R., Ito, G., and Martel, S. J. (2001). Effects of volcano loading on dyke propagation in an elastic half-space. *J. Geophys. Res.* 106, 11101–11113.

Murase, T., and Mcbirney, A. R. (1973). Properties of some common igneous rocks and their melts at high temperatures. *Geol. Soc. Amer. Bull.* 84, 3563–3592. doi: 10.1130/0016-7606(1973)84<3563:poscir>2.0.co;2

Németh, K. (2010). "Monogenetic volcanic fields: Origin, sedimentary record, and relationship with polygenetic volcanism," in *What Is a Volcano?* eds E. Cañón-Tapia and A. Szakács (Boulder, CO: Geological Society of America), 43–66. doi: 10.1130/2010.2470(04)

Németh, K., and Kereszturi, G. (2015). Monogenetic volcanism: personal views and discussion. *Int. J. Earth Sci.* 104, 2131–2146. doi: 10.1007/s00531-015-1243-6

Park, R. G. (1988). *Geological Structures and Moving Plates*. Glasgow: Blackie & Sons Ltd; Bishopbriggs. doi: 10.1007/978-94-017-1685-7

Pasquarè, G., Tibaldi, A., Attolini, C., and Cecconi, G. (1988). Morphometry, spatial distribution and tectonic control of Quaternary volcanoes in norhern Michoacan, Mexico. *Rend. Soc. It. Min. Petr.* 43, 1215–1225.

Pasquarè, F. A., and Tibaldi, A. (2007). Structure of a sheet-laccolith system revealing the interplay between tectonic and magma stresses at Stardalur Volcano, Iceland. *J. Volcanol. Geotherm. Res.* 161, 131–150.

Pinel, V., and Jaupart, C. (2004). Magma storage and horizontal dyke injection beneath a volcanic edifice. *Earth Planet. Sci. Lett.* 221, 245–262. doi: 10.1016/S0012-821X(04)00076-7

Pollard, D. D. (1969). *Aspects of the Mechanics of Sheets Intrusions.* Unpublished M. Sc. dissertation, University of London, UK

Pollard, D. D. (1973). Derivation and evaluation of a mechanical model for sheet intrusions. Tectonophysics 1, 233–269. doi: 10.1016/0040-1951(73)90021-8

Pollard, D. D., and Muller, O. H. (1976). The effects of gradients in regional stress and magma pressure on the form of sheet intrusions in cross section. *J. Geophys. Res.* 81, 975–984. doi: 10.1029/jb081i005p00975

Pollard, D. D., and Segall, P. (1987). "Theoretical displacements and stresses near fractures in rocks: With applications to faults, joints, veins, dykes, and solutions surfaces," in *Fracture Mechanics of Rock*, ed B. B. Atkinson (San Diego, CA; Academic), 277–349. doi: 10.1016/b978-0-12-066266-1.50013-2

Price, N. J., and Cosgrove, J., W (1990). *Analysis of Geological Structures*. Cambridge: Cambridge University Press.

Rice, J. R. (1980). "Mathematical analysis in the mechanics of fracture," in *Fracture, An Advanced Treatise*, Vol II, ed H. Liebowitz (New York, NY: Academic Press), 191–311.

Rivalta, E., Taisne, B., Bunger, A. P., and Katz, R. F. (2015). A review of mechanical models of dyke propagation: schools of thought, results and future directions. *Tectonophysics* 638, 1–42. doi: 10.1016/j.tecto.2014.10.003

Roman, D. C., and Heron, P. (2007). Effect of regional tectonic setting on local fault response to episodes of volcanic activity. *Geophys. Res. Lett.* 34, L13310. doi: 10.1029/2007gl030222

Rowe, M. C., Peate, D. W., and Ukstins-Peate, I. (2011). An investigation into the nature of the magmatic plumbing system at Paricutin volcano, Mexico. *J. Petrol.* 52, 2187–2220. doi: 10.1093/petrology/egr044

Rubin, A. M. (1993a). Tensile fracture of rock at high confining pressure: implications for dyke propagation. *J. Geophys. Res.* 98, 919–935.

Rubin, A. M. (1993b). On the thermal viability of dykes leaving magma chambers. *Geophys. Res. Lett.* 20, 257–260.

Rubin, A. M. (1993c). Dykes vs. diapirs in viscoelastic rock, Earth Planet. *Sci. Lett.* 119, 641–659.

Rubin, A. M. (1995). Propagation of magma-filled cracks. *Annu. Rev. Earth Planet. Sci.* 8, 287–336. doi: 10.1146/annurev.ea.23.050195.001443

Rubin, A. M. (1998). Dyke ascent in partially molten rock. J. Geophys. *Res.* 103, 20, 901–920.

Schrank, C. E., Fusseis, F., Karrech, A., and Regenauer-Lieb, K. (2012), Thermal-elastic stresses and the criticality of the continental crust. *Geochem. Geophys. Geosyst.* 13, Q09005.

Selva, J., Orsi, G., Di Vito, M., Marzocchi,W., and Sandri, L. (2012). Probability hazard map for future vent opening at the Campi Flegrei caldera, Italy. *Bull. Volcanol.* 74, 497–510. doi: 10.1007/s00445-011-0528-2

Shapiro, S. A. (2015). *Fluid Induced Seismicity*. Cambridge: Cambridge University Press. doi: 10.1017/cbo9781139051132

Sigmundsson, F. et al., (2015). Segmented lateral dyke growth in a rifting event at Bardarbunga volcanic system, Iceland. *Nature* 517, 191–195.

Sobradelo, R., and Martí, J. (2015). Short-term volcanic hazard assessment through Bayesian inference: retrospective application to the Pinatubo 1991 volcanic crisis. *J. Volcanol. Geotherm. Res.* 290:111. doi: 10.1016/j.jvolgeores.2014.11.011

Spera, F. J. (1980). "Aspects of magma transport." in *Physics of Magmatic Processes,* ed R. B Hargraves (Princeton, NJ: Princeton University Press), 265–323.

Stroncik, N. A., Klügel, A., and Hansteen, T. H. (2009). The magmatic plumbing system beneath El Hierro (Canary Islands): constraints from phenocrysts and naturally quenched basaltic glasses in submarine rocks. *Contrib. Mineral. Petrol.* 157, 593–607. doi: 10.1007/s00410-008-0354-5

Taisne, B., and Jaupart, C. (2009). Dyke propagation through layered rocks. *J. Geophys. Res.* 114, B09203.

Taisne, B., Tait, S., and Jaupart, C. (2011). Conditions for the arrest of a vertical propagating dyke. *Bull. Volcanol.* 73, 191–204. doi: 10.1007/s00445-010-0440-1

Takada, A. (1989). Magma transport and reservoir formation by a systems of propagating cracks. *Bull. Volcanol.* 52, 118–126. doi: 10.1007/BF00301551

Takada, A. (1994). The influence of regional stress and magmatic input on styles of monogenetic and polygenetic volcanism. *J. Geophys. Res.* 99, 563–513. doi: 10.1029/94jb00494

Thirlwall, M. F., Singer, B. S., and Marriner, G. F. (2000). 39Ar±40Ar ages and geochemistry of the basaltic shield stage of Tenerife, Canary Islands, Spain. *J. Volcanol. Geother. Res.* 103, 247–297.

Tibaldi, A. (1995). Morphology of pyroclastic cones and tectonics. *J. Geophys. Res.* 100, 24521–24535. doi: 10.1029/95jb02250

Tibaldi, A., and Lagmay, A. M. F. (2006). Interaction between volcanoes and their basement. *J. Volcanolo. Geother. Res.* 158, 1–5. doi: 10.1016/j.jvolgeores.2006.04.011

Tibaldi, A., and Pasquarè, F. (2008). A new mode of inner volcano growth: the "flower intrusive structure". *Earth Planet. Sci. Lett.* 271, 202–208. doi: 10.1016/j.epsl.2008.04.009

Tibaldi, A., Vezzoli, L., Pasquarè, F. A., and Rust, D. (2008). Strike-slip fault tectonics and the emplacement of sheet-laccolith systems: the thverfell case study (SW Iceland). *J. Struct. Geol.* 30, 274–290. doi: 10.1016/j.jsg.2007.11.008

Touloukian, Y. S., Judd,W. R., and Roy, R. F. (1989). "Physical properties of rocks and minerals," in *CINDAS Data Series on Material Properties, Group II Properties of special materials, Vol 1–2*. New York, NY: McGraw-Hill.

Traversa, P., Pinel, V., and Grasso, J. (2010). A constant influx model for dyke propagation: implications for magma reservoir dynamics. *J. Geophys. Res.* 115, B01201.

Turcotte, D. L., and Schubert, G. (1982). *Geodynamics: Applications of Continuum Physics to Geological Problems*. New York, NY: John Wiley.

Valentine, G. A., and Gregg, T. K. P. (2008). Continental basaltic volcanoes—Processes and problems. *J. Volcanol. Geother. Res.* 177, 857–873. doi: 10.1016/j.jvolgeores.2008.01.050

Valentine, G. A., and Hirano, N. (2010). Mechanisms of low-flux intraplate volcanic fields – basin and range (North America) and northwest Pacific Ocean. *Geology* 38, 55–58. doi: 10.1130/g30427.1

Valentine, G. A., and Perry, F. V. (2007). Tectonically controlled, time-predictable basaltic volcanism from a lithospheric mantle source (central Basin and Range Province, USA). *Earth Planet. Sci. Lett.* 261, 201–216. doi: 10.1016/j.epsl.2007.06.029

Walker, G. P. L. (2000). "Basaltic volcanoes and volcanic systems," in *Encyclopedia of Volcanoes,* ed H. Sigurdsson (San Francisco, CA: Academic Press), 283–289.

Wood, C. A. (1980). Morphometric evolution of cinder cones. *J. Volcanol. Geother. Res.* 7, 387–413. doi: 10.1016/0377-0273(80)90040-2

Wright, T. J., Ebinger, C., Biggs, J., Ayele, A., Yirgu, G., Keir, D., et al. (2006). Magma-maintained rift segmentation at continental rupture in the 2005 Afar dyking episode. *Nature* 442, 291294. doi: 10.1038/nature04978

Zang, A., and Stephansson, O. (2010). *Stress Field of the Earth's Crust*. Heidelberg: Springer. doi: 10.1007/978-1-4020-8444-7

Zoback, M. D., and Zoback, M. L. (2002). "Stress in the Earth's lithosphere," in *Encyclopedia of Physical Science and Technology, 3rd Edn.*, ed R. A. Meyers (San Diego, CA: Academic Press), 143–154.

Zoback, M. L. (1992). First- and second-order patterns of stress in the lithosphere: the world stress map project. *J. Geophys. Res.* 97, 11703–11728. doi: 10.1029/92jb00132

Conflict of Interest Statement: The authors declare that the research was conducted in the absence of any commercial or financial relationships that could be construed as a potential conflict of interest.

frontiers
in Earth Science

ORIGINAL RESEARCH
published: 30 September 2016
doi: 10.3389/feart.2016.00086

Historical Volcanism and the State of Stress in the East African Rift System

G. Wadge[1]*, **J. Biggs**[2], **R. Lloyd**[2] **and J.-M. Kendall**[2]

[1] Centre for Observation and Modelling of Earthquakes, Volcanoes and Tectonics (COMET), Department of Meteorology, University of Reading, Reading, UK, [2] Centre for Observation and Modelling of Earthquakes, Volcanoes and Tectonics (COMET), School of Earth Sciences, University of Bristol, Bristol, UK

Crustal extension at the East African Rift System (EARS) should, as a tectonic ideal, involve a stress field in which the direction of minimum horizontal stress is perpendicular to the rift. A volcano in such a setting should produce dykes and fissures parallel to the rift. How closely do the volcanoes of the EARS follow this? We answer this question by studying the 21 volcanoes that have erupted historically (since about 1800) and find that 7 match the (approximate) geometrical ideal. At the other 14 volcanoes the orientation of the eruptive fissures/dykes and/or the axes of the host rift segments are oblique to the ideal values. To explain the eruptions at these volcanoes we invoke local (non-plate tectonic) variations of the stress field caused by: crustal heterogeneities and anisotropies (dominated by NW structures in the Protoerozoic basement), transfer zone tectonics at the ends of offset rift segments, gravitational loading by the volcanic edifice (typically those with 1–2 km relief) and magmatic pressure in central reservoirs. We find that the more oblique volcanoes tend to have large edifices, large eruptive volumes, and evolved and mixed magmas capable of explosive behavior. Nine of the volcanoes have calderas of varying ellipticity, 6 of which are large, reservoir-collapse types mainly elongated across rift (e.g., Kone) and 3 are smaller, elongated parallel to the rift and contain active lava lakes (e.g., Erta Ale), suggesting different mechanisms of formation and stress fields. Nyamuragira is the only EARS volcano with enough sufficiently well-documented eruptions to infer its long-term dynamic behavior. Eruptions within 7 km of the volcano are of relatively short duration (<100 days), but eruptions with more distal fissures tend to have lesser obliquity and longer durations, indicating a changing stress field away from the volcano. There were major changes in long-term magma extrusion rates in 1977 (and perhaps in 2002) due to major along-rift dyking events that effectively changed the Nyamuragira stress field and the intrusion/extrusion ratios of eruptions.

Keywords: crustal stress, historical eruptions, East African Rift, oblique motion, eruption dynamics

Edited by:
Agust Gudmundsson,
University of London, UK

Reviewed by:
Roberto Sulpizio,
University of Bari, Italy
Alessandro Tibaldi,
University of Milano-Bicocca, Italy

****Correspondence:***
G. Wadge
g.wadge@reading.ac.uk

Specialty section:
This article was submitted to
Volcanology,
a section of the journal
Frontiers in Earth Science

Received: *25 May 2016*
Accepted: *02 September 2016*
Published: *30 September 2016*

Citation:
Wadge G, Biggs J, Lloyd R and Kendall J-M (2016) Historical Volcanism and the State of Stress in the East African Rift System.
Front. Earth Sci. 4:86.
doi: 10.3389/feart.2016.00086

INTRODUCTION

The East African Rift System (EARS) is a natural laboratory for studies of active continental extension (Ebinger, 2005, 2012). On a continental scale, the stress field of the EARS is governed by mantle buoyancy forces, which drive plate motions and generate dynamic topography; viscous resisting tractions in the plate and mantle; and the gravitational potential energy due to the structure of the crust and lithosphere (e.g., Stamps et al., 2010; Kendall and Lithgow-Bertelloni, 2016). The stresses generated are on the order of 100 MPa, and are not sufficient to break old, cold lithosphere, and continental break-up results from a combination of mechanical stretching, pre-existing weaknesses and thermal weakening by intrusions (Gudmundsson, 2000; Buck, 2004, 2006; Buck et al., 2006; Bialas et al., 2010; Corti, 2012; Kendall and Lithgow-Bertelloni, 2016).

On a local scale, the stress field plays a major role in determining the orientation of magmatic intrusions, particularly dyke formation along extensional fractures and consequently the alignment of fissures and vents at the surface. Work at another divergent plate boundary setting, in Iceland (Gudmundsson, 2000), and elsewhere has produced many insights relevant to our study such as: the different behaviors produced by point and cavity models of magmatic pressure (Gudmundsson, 2006), the mechanical anisotropy of host rocks and the effect this can have on dykes reaching the surface (Gudmundsson, 2003; Gudmundsson and Philipp, 2006), the significance of sill formation on the creation of shallow magma reservoirs beneath central volcanoes (Gudmundsson, 2006) and topography-controlled stress fields guiding the propagation paths of dykes (Acocella and Tibaldi, 2005). Recent examples in the EARS include the 100-km long Dabbahu dyke intrusion in Afar (Wright et al., 2006) and the 2007 Lake Natron dyke intrusion in Tanzania (Calais et al., 2008; Biggs et al., 2009), which were both aligned perpendicular to the plate motion. However, superimposed upon the large-scale stress regime are local stresses related to topography, seismic and magmatic processes (e.g., Biggs et al., 2013b; Maccaferri et al., 2014; Pagli et al., 2014) and which are also seen to control the orientation of magmatic features, such as the Jebel al Tair eruption in the Red Sea (Xu and Jonsson, 2014) and the orientation of fissures around Oldoinyo Lengai in Tanzania (Muirhead et al., 2015).

While GPS measurements can be used to map plate velocities (e.g., Saria et al., 2014), the density of stations is not sufficient to map the short-wavelength spatial and temporal variability of the strain field. Satellite-based InSAR measurements provide high-resolution maps of displacement and have been used to measure regional velocity fields (e.g., Pagli et al., 2014), and once sufficient data is archived Sentinel-1 satellites should routinely provide high resolution and precision measurements on a continental scale.

The purpose of this study is to improve understanding of the roles that crustal stresses have on volcanism in the EARS. In particular, we focus on how the stress field may have played a role in eruptions since 1800, the first such general review. Written records of volcanic eruptions in the EARS extend as far back as the 1840s to 1880s, and oral recollections by inhabitants take the record back to about 1800 in places. In many cases, these records can be used to link lava flows, vents and fissures seen in satellite imagery to specific events, and thus estimate the geometry of the feeding system and volume erupted. More recently (2002–2015), geophysical techniques have been used to observe several rifting episodes in the EARS, including the eruptions from the Western Branch (Nyamuragira, Nyiragongo), Eastern Branch (Oldoinyo Lengai) and Afar (Dabbahu-Manda Harraro, Erte Ale, Alu-Dalafilla, Nabro). In these cases, geodetic and seismic data provide a detailed view of the magmatic plumbing system, which can be combined with studies of erupted products.

In Section Factors that Could Affect Stress and Strain in the EARS, we briefly review the sources and measurements of crustal stress in the EARS and in Section Historical Record summarize the observations of the 21 historical eruptions, and in particular, the orientation of feeding dykes and local structure. In Section Discussion, we synthesize these observations in terms of the magmatic and eruption processes, and the orientation and morphology of crustal and volcanic structures. We conclude that local variations in the stress field, including edifice loading, magma pressure, and transfer zone tectonics as well as crustal heterogeneities and anisotropies play a significant role in the 14 of the 21 historical eruptions, and find evidence that temporal variations in the stress field control eruption dynamics.

FACTORS THAT COULD AFFECT STRESS AND STRAIN IN THE EARS

The first-order plate tectonic model motion for the EARS, supported by GPS measurements (e.g., Saria et al., 2014), shows motion to the ENE in the north, and motion to the ESE in the south of the Arabian and Somalian plates respectively relative to the Nubian plate (**Figure 1**). The boundary forces at the plates' sides and bases and the buoyancy forces from lateral variations in gravitational potential energy are responsible for this motion and the resultant horizontal stress field (Craig et al., 2011; Stamps et al., 2014; **Figure 2A**). A normal faulting regime (vertical stress component (σ_v) greater than the two horizontal stress components: $\sigma_v = \sigma_1 > \sigma_2 > \sigma_3$) dominates in the EARS, with a strike slip regime (vertical stress component is intermediate relative to the horizontal stress components: $\sigma_1 > \sigma_v > \sigma_3$) more evident in some places (e.g., Asal-Ghoubbet Rift, Delvaux and Barth, 2009). For the normal extensional regime, the direction of the maximum horizontal stress $S_{HMAX} = \sigma_2$, should correspond to the direction of dyke propagation, orthogonal to the opening direction or the minimum horizontal stress ($S_{HMIN} = \sigma_3$).

The vertical and horizontal stresses in the Earth's crust generally correspond to the principal stresses (Amadei and Stephansson, 1997). In rift zones the vertical stress is usually the greatest and one of the horizontal stresses the least. The vertical stress in the Earth's crust increases linearly at a rate of about 26 MPa/km (McGarr and Gay, 1978) and is often of near constant orientation, for example throughout the 9 km-deep KTB borehole (Brudy et al., 1997). The horizontal stress is much more variable and the differential value (S_{HMAX}–S_{HMIN}) may be several tens of MPas. This is usually because of abrupt changes in the material properties (e.g., Young's modulus) of different lithologies (Gudmundsson, 2006, 2011a). Also the orientation of the stress field is much more consistent over extended regions than the magnitudes of the stress components.

The principles of the analysis of the stress field in volcanic systems began with Anderson (1936). Nakamura (1977) first showed how volcano stress fields interacted with (plate) tectonic stress fields, such that dyke fissures and surface vents tend to align with the local direction of σ_1. The curvilinear nature of dyke swarms in composite stress fields was demonstrated at the

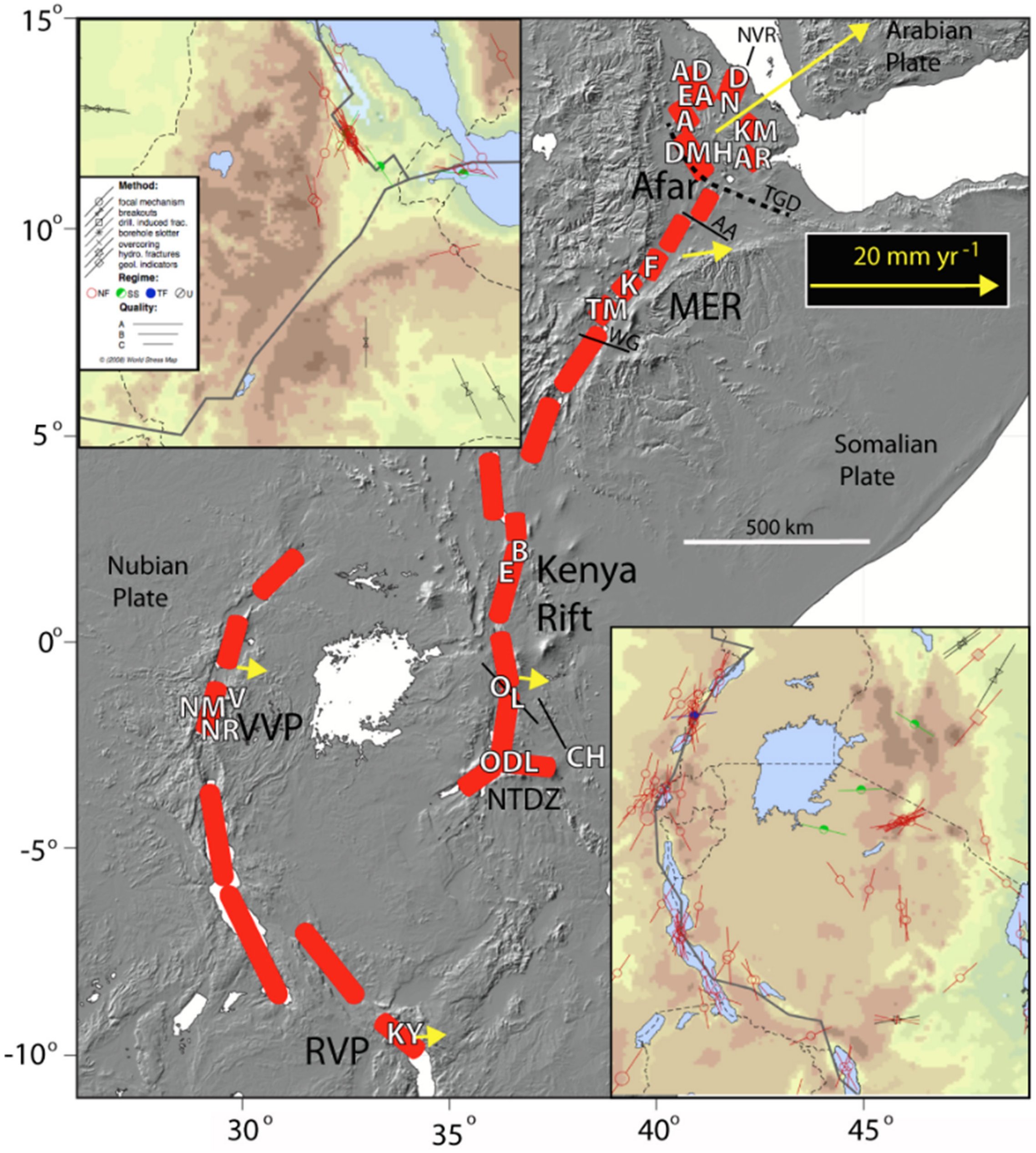

FIGURE 1 | Sketch map of the EARS showing the main rift segments in red. The historically active volcanoes are labeled in white according to their abbreviation in **Table 1**. MER, Main Ethiopian Rift; VVP, Virunga Volcanic Province; NTDZ, North Tanzanian Divergence Zone; and RVP, Rungwe Volcanic Province. The dashed black line in Afar is the Tendahu-Goba'ad Discontinuity. The continuous black lines are inherited discontinuities (AA, Ayelu-Amoissa; WG, Wendo-Genet) discussed in the text. Yellow arrows are vectors of Somalian and Arabian plate motion relative to the Nubian plate. The two colored topographic maps inset in the upper left and lower right corners are from the 2008 version of the World Stress Map (Heidbach et al., 2010) showing locations of the primary crustal stress measurements. Each line symbol is oriented along the maximum horizontal principal stress direction, modulated by method (symbol), inferred tectonic setting (color) and quality (length of line). The thick lines are the plate boundaries, the dashed lines are national boundaries.

Spanish Peaks center (Muller and Pollard, 1977). Multiple factors combining to generate such composite fields have been advocated and analyzed: loading due to the edifice (e.g., Dahm, 2000; Pinel and Jaupart, 2000; Maccaferri et al., 2011) and unloading (e.g., Maccaferri et al., 2014), the effects of volcano morphology (e.g., Tibaldi et al., 2014; Corbi et al., 2015), the generation of magma reservoirs and calderas (e.g., Tibaldi, 2015) and the anisotropy of host rocks (Gudmundsson, 2011a). Many dykes do not propagate all the way to the surface, but may be arrested by layers with variable associated stress (Gudmundsson and Philipp, 2006). Indeed, as we shall see, several EARS volcanoes have demonstrable intrusive to extrusive magma volumetric ratios >1.

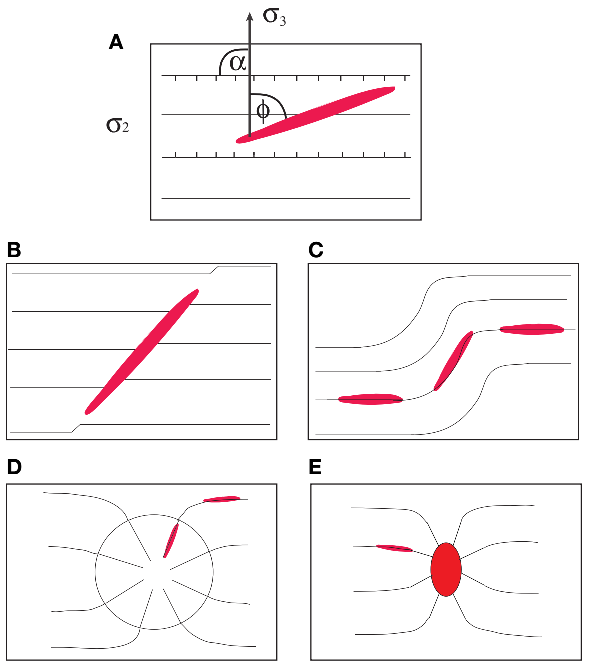

FIGURE 2 | (A) Map view schematic of a dyke (red ellipse) sitting in an extensional stress regime where σ_2 is parallel to the rift boundary faults (ticked). α and ϕ are angles of obliquity (see text for discussion). **(B)** Represents a (red) dyke intruding a pre-existing plane of weakness in basement rocks oblique to σ_2, **(C)** represents the case of dykes following locally variable stress fields in a transfer zone, **(D)** represents the stress field caused by loading of a large volcano superimposed on a regional field. The extent of the edifice is shown by the circle and **(E)** represents a crustal magmatic source (red ellipse) with roughly orthogonal stress contours that rapidly curve to the regional field lines. For other examples of the stress behavior of pressurized cavities in isotropic media see Savin (1961).

Rivalta et al. (2015) provide an overview from the perspective of dyke propagation.

The geometric relationship between plate motion, plate boundary orientation and the resulting structures can be defined according to the model of Tuckwell et al. (1996), who classified geometrical models of mid-ocean ridge spreading, three of which (orthogonal, oblique, transtension) are observed in nature. Robertson et al. (2015) used a similar system to describe the geometry of rift extension, using the Kenyan Rift as an example. The three models can be described using two angles: α is the angle between the rift azimuth and the plate motion direction (S_{HMIN}) and ϕ is the angle between the fault or dyke azimuth and the plate motion direction. **Figure 2A** illustrates the relationship of the two angles. If $\alpha = \phi = 90°$, there is zero obliquity and the rift is considered to be orthogonal, causing normal faulting along the rift margins and rift-parallel dykes to occur in the rift valley. If $\alpha = \phi$ and the dyke is parallel to the rift and both are oblique to the spreading direction then the rift is described as oblique. If $\phi = \alpha/2 + 45°$, the dyke and plate motion are oblique to the rift and the rift is said to be in transtension.

It is commonly observed in the EARS that the direction of dyke propagation is not orthogonal to the first order plate motion, indicating that S_{HMIN} is both regionally and locally variable and that continental rifting is rarely purely orthogonal (**Figure 2A**; e.g., Gudmundsson, 2006).

The stress field can be measured locally, but very sparsely, by several methods operating at different length scales (Amadei and Stephansson, 1997) from earthquake focal mechanisms (Delvaux and Barth, 2009), and seismic anisotropy (Kendall et al., 2005) over tens of kilometers, borehole breakouts at a meter scale and hydro-fracturing over tens to hundreds of meters (Heidbach et al., 2010). In the EARS these local measurements suggest a regional stress field associated with ~100 km-long rift segments. For example focal mechanisms suggest S_{HMIN} = WNW-ESE in the Main Ethiopian Rift (MER) and the Virunga Volcanic Province (VVP); N-S in Natron and ENE-WSW in northern Afar (Delvaux and Barth, 2009; **Figure 1**). On even smaller scales, particularly around large volcanic edifices, the stress field may be even more complex.

We now review the main ways in which the stress and corresponding strain field can be modified locally in the EARS. Regional and local variations in the stress field are associated with (1) regions of complex rift geometry where heterogeneities favor reactivation of non-optimally oriented structures or in transfer zones linked to offsets between rift segments, or (2) magmatic processes including subsurface magma pressure or loading by volcanic edifices (e.g., Keir et al., 2015).

Complexities in Rift Geometry

Variations in density, stiffness (Young's modulus), composition and fracturing of the crust or upper mantle can potentially impact the stress gradients and elastic behavior of the rocks hosting dykes. This applies both to the pre-rifting basement rocks, mainly Proterozoic in age, whose inherited properties, for example crustal fault systems, may have become re-activated during rifting (Coblentz and Sandiford, 1994; Corti, 2009; **Figure 2B**) and to recent structures, including active rift faults and caldera ring faults, which have been shown to act as pathways for both magmatic and hydrothermal fluids (Hutchison et al., 2015). The most obvious heterogeneity is the presence of the Tanzanian Craton (Koptev et al., 2015) which effectively guides the rift as it splits into two arms around a deep keel of Proterozoic rocks.

Pre-existing structures and fabrics that extend to the surface are usually well-mapped using traditional geological techniques or geomagnetic survey, but deeper heterogeneities cannot be observed directly and we rely on the variability of velocity and polarization in seismic records to map anisotropy of the crust and upper mantle. Shear wave splitting techniques using body phases such as SKS are best for exploring mineral (olivine) orientation due to flow in the mantle (Hammond et al., 2014), while teleseismic receiver functions have been used to infer multi-parameter anisotropy of upper mantle and lower crust melt geometry (Hammond, 2014). Shear wave splitting using local earthquakes provides the best resolution in the upper crust and is the most relevant to studies of the stress field beneath local volcanic centers (Keir et al., 2011a).

Offsets in the rift occur because rift segments form in isolation, but eventually grow and interact, causing complexities in the field geometry and local stress field. These include normal fault initiation from tension fractures and en echelon linking of faults

(Gudmundsson et al., 2010; Gudmundsson, 2011b, chapter 14). At mid-ocean ridges, the motion between segments is taken up on transform faults, but during rift development, there may be complex zones of mixed normal, strike-slip (e.g., Spacapan et al., 2016) and even compressional tectonics (e.g., Sachau et al., 2015). These can be several tens of kilometers in extent (Ebinger, 1989; Morley et al., 1990; **Figure 2C**) and are referred to as transfer or accommodation zones.

Magmatic and Volcanic Processes

Volcanic edifices load the crust locally, modifying the stress field. In the vertical plane, differential stress decays in proportion to the edifice radius (Dahm, 2000) and has a negligible effect below the upper crust. The principal stresses also have curving trajectories focused at the point of greatest load beneath the highest part of the edifice (Dahm, 2000). In combination with an extensional tectonic stress field, the effect in the horizontal plane is a radial pattern of maximum compressive stress trajectories within a distance equivalent to the edifice radius, outside of which they bend to become parallel with the tectonic maximum stress trajectory (**Figure 2D**). Volcanoes with a non-circular footprint could produce an asymmetrical stress field (Acocella and Neri, 2009). Roman and Jaupart (2014) argued that this focusing effect tends to lead to the creation of a magma reservoir, which in turn leads to more evolved (buoyant) magmas, effectively preventing the rise of basaltic magma centrally. Gudmundsson (2011a) also showed that horizontal discontinuities can deflect magma from dykes into sills and can enhance the tendency to build a magma reservoir. To reach the surface the stress field along the propagation path of the dyke must be close to homogeneous (Gudmundsson and Philipp, 2006). To achieve this some dykes will tend to follow lateral paths, often breaking the surface at the edges of the edifice (Kervyn et al., 2009).

Ignoring stress concentrations around the reservoir itself, edifice loading may therefore have three first-order effects on volcanic behavior:

- Radial dykes, which beyond the edifice curve into the regional direction of maximum horizontal stress,
- A central, shallow magma reservoir,
- Silicic magmas developing in the reservoir, enabling major explosive eruptions and the mingling of contrasting magmas.

The creation of a rift valley itself produces a linear gravity low that can have the opposite effect to loading, in which magma follows an upward curving stress trajectory and away from a central magma source beneath the valley center (Maccaferri et al., 2014). This may explain the occurrence of some pre-historic volcanic eruptions outside of the rift. Individual fault scarps with relief less than 100 m can influence the trajectory of dyke propagation and focus magmatic pathways into the footwall (Maccaferri et al., 2015).

A large volume of magma may accumulate in the crust because of an inability to rise further. If the magma pressure rises above lithostatic it will exert a positive normal stress on the reservoir walls, eventually leading to one of many fracture initiations and dyke propagations. Gudmundsson (2012) suggests that over the long-term reservoirs with irregular boundaries are thermally and mechanically unstable and will tend to evolve to smoother equilibrium geometries. Most InSAR images of deforming volcanoes, particularly in East Africa show a simple bulls-eye pattern of motion (e.g., Biggs et al., 2009, 2011), equivalent to the deformation produced by a point- or a spherical/ellipsoidal-pressure source, in an isotropic half space, typically attributed to varying pressure within a magma reservoir (**Figure 2E**) and originally analyzed as a either a pressurized point (Anderson, 1936; Mogi, 1958) or pressurized cavity (Savin, 1961). While deformation is an indicator of an active magmatic system and can be shown to have a statistical link to the likelihood of eruption (Biggs et al., 2014), the mechanisms that produce deformation are varied, and implications for the stress field are poorly understood. Caldera systems, in particular, often experience surface deformation without leading to eruption, and this is often linked to changes in the hydrothermal system (e.g., Chiodini et al., 2012; Biggs et al., 2014). If the deformation is linked temporally to an eruption then the stress from a magmatic source can be distinguished from edifice loading (which may have a similar pattern but is static in time), or if the pressure source is wide enough to indicate mid- to deep-crustal levels, and from a geothermal reservoir whose internal pressure is variable. Shallow level dykes and sills with non-recoverable strain are relatively easy to identify from InSAR data (e.g., Bagnardi et al., 2013).

Our understanding of the spatial and temporal variability of stress fields in the EARS is hampered by a lack of measurements of the local stress tensors associated with volcanic events. The new generation of InSAR deformation data may provide improved temporal resolution of source mechanisms. These data need to be better linked to stress field modeling based on solid mechanics and fracture mechanics principles.

HISTORICAL RECORD

The evidence of volcanism associated with rifting in the EARS indicates a long and complex history (Baker et al., 1972). Holocene volcanism is scattered along much of the length of the EARS, but is sparse in places, such as the southwestern part of the Western Rift between the Virunga and Rungwe Volcanic Provinces (VVP, RVP, **Figure 1**). In north Afar, volcanic edifices are elongate shields with axial fissures (e.g., Alu-Dalafilla, Erta Ale, Alayta). Further south, central grabens within a faulted and fissured terrain and a central vent area with a subsided edifice are typical (e.g., Dubbahu-Manda Hararo, Ardoukoba, Kammourta) (Barnie et al., 2015). The Tendao-Goba'ad Discontinuity (TGD) marks the triple junction between the Nubian, Somalian and Arabian plates (Acton et al., 1991). South of this, in the MER, there is an increasingly well-developed rift valley morphology, large normal fault boundaries and central fissure swarms and cones (e.g., Fantale, Kone, Tullu Moje) and large central volcanoes, including calderas (e.g., Corbetti, O'a). Further south, the rift branches around the Tanzanian Craton, with greater seismicity in the western branch than the eastern branch. The southernmost volcanoes of the EARS are located in the Rungwe Province in northern Malawi (Fontijn et al., 2012), south of which, the rifting appears to be amagmatic (e.g., Biggs et al., 2010).

Written records of volcanic eruptions in the EARS extend as far back as the 1840s to 1880s, and oral recollections by inhabitants take the record back to about 1800 in places. This is reflected in the records of the Smithsonian Institution Global Volcanism Program (GVP), which are our starting point. We restrict ourselves to post-1800 data (sensu lato), and the record is almost certainly incomplete. **Figure 3** shows a timeline of the eruptions divided into those in the Afar and those from with the rest of the EARS. Two features are notable, the concentration of eruptions during the 2002–2011 period and the lack of eruptions in Afar for most of the nineteenth century. The latter is likely due to under-reporting small lava flows from axial fissure segments.

We find 21 volcanoes with historically-recorded eruptions (**Figure 1**, **Table 1**), and these are representative of the types of volcanic activity recognized in the EARS over longer periods, with the exception of caldera collapse. The erupted volumes are estimates of widely varying uncertainty and we use them with caution. Most of the lava flows are of distinct outline and we have measured their areas from satellite imagery (GoogleEarth) at uncertainties of a few tens of percent. Mean thicknesses are estimated with uncertainties of 50–100%. Our volume estimates in **Table 1** have an indicative uncertainty of about ±150%. There is a range of four orders of magnitude in these eruption volumes and we think these data generally support the interpretations we later make (**Figures 4**, **7**). The volume uncertainties for Nyamuragira, used in creating **Figures 4**, **5** are, relatively, less than this. Apart from Oldoinyo Lengai and Nyamuragira, no estimates of ash/tephra deposits are represented. Some GVP eruptions are so poorly reported or lacking in useful detail that they have been omitted (Meru, South Island/L. Turkana).

Whilst basalt/basanite/nephelinite lava is the sole product at 14 volcanoes, trachyte and comendite/rhyolite lava flows are well represented at 5 volcanoes and carbonatite lava at Oldoinyo Lengai. Major explosive eruptions occurred at 3 volcanoes: Dubbi, Nabro, and Oldoinyo Lengai, each with two distinctly different magmas involved. Out of an estimated ∼5.2 km^3 of historically erupted lava only 6% is of silicic composition. However, this does not include estimates of the silicic tephra components of the Dubbi and Nabro eruptions, so the actual total and proportion of silicic magma is higher.

Most of the volcanoes have erupted just once in the past 200 years. Erta Ale and Nyiragongo have summit lava lakes, with semi-continuous overturning of magma, but the details of occasional overflows we ignore. Two volcanoes have had multiple significant eruptions: Oldoinyo Lengai and Nyamuragira. The latter has such a rich and complex record that we restrict ourselves to the most recent, 2011–2012 eruption in **Tables 1–3**, but also discuss the earlier record later.

On seven occasions since 2002 detailed geophysical observations from InSAR, GPS and seismicity have been made of eruptions and interpreted in terms of the transport of magma through crustal reservoirs, dykes and onto the surface. We describe these events in Section Geophysically-Observed Eruptions (2002–2015) and in Section Historically-Recorded Eruptions (1800–2002) describe eruptions prior to this time, when observations were mainly based on historical accounts and subsequent mapping.

Geophysically-Observed Eruptions (2002–2015)

Nabro (2011)

This ∼40-day long eruption (Sealing, 2013) had bimodal products with an initial trachyte ash plume that reached the stratosphere and released a huge amount of sulfur dioxide: 1.6 ± 0.3 Tg SO_2 (Carboni et al., 2015), the largest single global emission in the 4 years from 2008 to 2012. The plume was continuous for the first 5 days, after which a trachybasaltic lava flow with a volume of 0.2–0.3 km^3 developed from a 2 km-long NW-trending fissure originating at the pit crater which was then infilled with lava. Goitom et al. (2015) modeled a dyke beneath this fissure. On the basis of post-eruption deformation and seismicity, Hamlyn et al. (2014) argued for a 7 km-deep reservoir with a thrust fault above.

Alu-Dalafilla (2008)

A brief (4 days), high extrusion rate eruption from an en echelon fissure (3.5 km long) on the rift axis between two central volcanoes of the Erta Ale segment, produced a 16 km^2 basalt lava flow field. InSAR modeling required a dyke extending down from the fissure to a ∼1 km deep, 10 km-long, sill and below the center of that, a Mogi (spherical) source at about 4 km depth (Pagli et al., 2012). During the eruption, the dyke inflated by about 5 × 10^6 m^3 whilst the sill and Mogi source contracted by 23 × 10^6 m^3 and

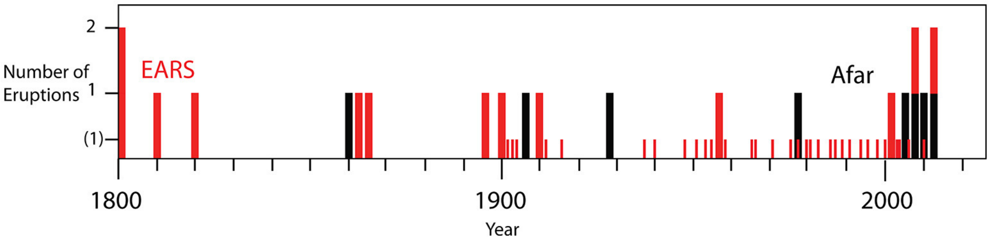

FIGURE 3 | Timeline (1800–2025) of the historical eruptions; one bar of height 1 (y-axis) represents one eruption for that year, 2 represents 2 eruptions. Afar eruptions are shown in black, those in the rest of the EARS in red. The small [height (1)] red bars are the twentieth and twenty first century eruptions of Nyamuragira before 2012 and the eruptions of Oldoinyo Lengai in 1916, 1940, and 1966. Note the preponderance of EARS eruptions between 1800 and 1900.

TABLE 1 | Historical eruptions with dates, durations and product characteristics.

	Volcano	No.[a]	Date[b]	Duration (days)	Eruption products	Deposit Area (km^2)	Thick. (m)[c]	Volume (10^6 m^3)	Extrusion Rate (m^3 s^{-1})	Int/Ext	Reference
D	Dubbi	1	1861	150?	basalt lava (trachyte tephra)	86 + 91	20	3500 lava[d]	270?		Wiart and Oppenheimer, 2000a
								1200–2600	93–186?		Wiart et al., 2000
N	Nabro	1	2011	40	trachybasalt lava (trachyte tephra)	18	20–10	360–180	104–52		Hamlyn et al., 2014 Sealing, 2013 Goitom et al., 2015
AR	Ardoukoba	1	1978	7	basalt lava	1.6	10	16 (170 dyke)	26	11	Allard et al., 1979
KM	Kammourta	1	1928		basalt lava	1.5	(10)	15			Audin et al., 1990
AD	Alu–Dalafilla	1	2008	4	basalt lava	16	(5)	80	231	0.06	Pagli et al., 2012
EA	Erta Ale	>1	2010	11	basalt lava lake overflow			6	6		Field et al., 2012 Acocella, 2006
A	Alayta	1	1906–1907	500?	basalt lava	53	(10)	530?	12?		Gouin, 1979 Barberi et al., 1970
DMH	Dabbahu–Manda Hararo	4	2005, 2007, 2009, 2010	3, 1.75, 2.5, 0.25	rhyolite lava/tephra, 3 basalt lavas	–, 2.2,	–, 3,	0.2, 6.6,	0.8, 55,	–, 10,	Wright et al., 2006
						4.5, 0.2	3, 1.5	15, 0.23	70, 11	4.5, 352	Ayalew et al., 2006 Ferguson et al., 2010 Barnie et al., 2015
F	Fantale	1	1810		basalt lava	5.3	(10)	53			Harris, 1844 Gibson, 1974
K	Kone	1	1820		basalt lava	5.1	(10)	51			Cole, 1969
TM	Tullu Moje	1	∼1900		comendite lava (Giano)	3.3	(30)	100			Bizouard and Di Paula, 1979
B	The Barrier	>1?	1895		mugearite lava	2.8	(5)	14			Dodson, 1963
E	Emuruangogolak	1	1910		comendite lava	3.2	(20)	64			Skinner et al., 1975 Dunkley et al., 1993
L	Longonot	2	1863		2 trachyte lavas	4.5	10	45			Scott, 1980
O	Olkaria	1	∼1800 C[14] 180 ± 50		rhyolite lava (Ololbutnot) pumice flow	4.8	(25)	120			Marshall et al., 2009
CH	Chyulu Hills	2	1865–66		basalt Shaitani lavas Chaimu	7 1.7	(3) (3)	21 5			Scoon, 2015 Spath et al., 2000
ODL	O-D Lengai	many,4 silicate	2007–2008	∼240	carbonatite lava, nephelinite tephra 2 dykes	-		20-10 (90 dyke)	1–0.5	9–4.5	Calais et al., 2008 Kervyn et al., 2010 Biggs et al., 2013a

(Continued)

TABLE 1 | Continued

	Volcano	No.[a]	Date[b]	Duration (days)	Eruption products	Deposit Area (km^2)	Thick. (m)[c]	Volume (10^6 m^3)	Extrusion Rate (m^3 s^{-1})	Int/Ext	Reference
NM	Nyamuragira	many	2011-2012	150	basanite lava	24	13	305 ± 36	25		Albino et al., 2015 Burt et al., 1994
NR	Nyiragongo	2	2002 (1977)	2	nephelinite lava	–		14–34, 210 dyke (22) (212 dyke)		15–6 (10)	Tazieff, 1977 Tedesco et al., 2007 Wauthier et al., 2012 Komorowski et al., 2002
V	Visoke	1	1957	2	olivine-melilitite	0.19	4	0.75	4		Condomines et al., 2015
KY	Kyejo	1	1800	3	tephrite lava	4.3	7	30	116		Fontijn et al., 2012 Harkin, 1960

[a] *Number of eruptions post-1800.*
[b] *Duration of eruption in days.*
[c] *( ) = estimates, this study.*
[d] *Range of lava-only estimates. Tephra volume also considerable.*

7×10^6 m^3, respectively. The volume erupted ($\sim 80 \times 10^6$ m^3) is about three times that indicated by the surface deformation. 0.2 Tg of SO_2 was released in the troposphere (Carboni et al., 2015). Four years before this, in October 2004, an intruding dyke at Dallol on the extreme northern tip of the Erta Ale segment, 50 km NNW of Alu-Dalafilla, was revealed by InSAR (Nobile et al., 2012). This dyke was 9 km long, striking 155° (c.f. 167° Alu-Dalafilla), ~2–6 km-deep, with an intruded volume of about 60×10^6 m^3.

Erta Ale (2010)

A lava lake has been observed over decades at one of two pit craters within the summit caldera of this rift axis shield volcano. The northern pit crater lies at the junction of two rift zones oriented NNW (the rift axis trend) and N (Acocella, 2006). Occasionally, lava levels rise to overflow the pits producing lava flows on the main crater floor. The best-documented example of which occurred in 2010, when about 6×10^6 m^3 of lava was extruded over a few days (Field et al., 2012). We ignore earlier episodes of overflow.

Dabbahu-Manda Hararo (2005–2010)

This was easily the largest known volcano-tectonic event in the EARS. It involved the formation of a near 100 km-long deformation field, with a graben flanked by symmetrical uplifts and evidence of magma transport through two central volcanoes at its northern end (Wright et al., 2006). The 2005 dyke emplaced below the graben had a volume of 1.5–2.0 km^3. A small explosion of rhyolitic tephra and a lava occurred on a 400 m-long fissure at Da'ure' at the northernmost end of the dyke (Ayalew et al., 2006). The small central volcano Gabho, adjacent to this site, had inflated by 12 cm in the year before the eruption from a shallow source. This probably involved the basalt magma that in 2005 intersected a shallow body of rhyolite. Over the next 5 years there were 12 more dykes with an average length of 9.5 km, width of 1.7 m, depth range of 0–10 km and volume of 90×10^6 m^3 (Hamling et al., 2009; Ferguson et al., 2010). These were all fed by a magma source below the middle of the rift segment that deflated as rising magma intruded (Grandin et al., 2009). Of the 12 new pulses of magma, three made it to the surface, in August 2007, June 2009, and May 2010 during brief basaltic fissure eruptions (Ferguson et al., 2010; Barnie et al., 2015). Sulfur dioxide plumes were consistent with volatile loss solely from the extruded volumes of lava.

Oldoinyo Lengai (2007–2008)

A combined dyke and fault motion episode was observed by InSAR at the southern end of the Natron rift segment over several months in 2007–2008 (Baer et al., 2008; Calais et al., 2008). No magma reached the surface above the initial 8 km-long, NE-trending dyke and fault underneath the southern end of the Gelai volcano and the relationship to volcanic activity at Oldoinyo Lengai was inferential. Modeling of later InSAR data by Biggs et al. (2009, 2013a), however, made a convincing deformation link to Oldoinyo Lengai that involved a 4 km-long, E-oriented dyke intrusion and a central point source of deflation. Stress calculations suggest that the initial

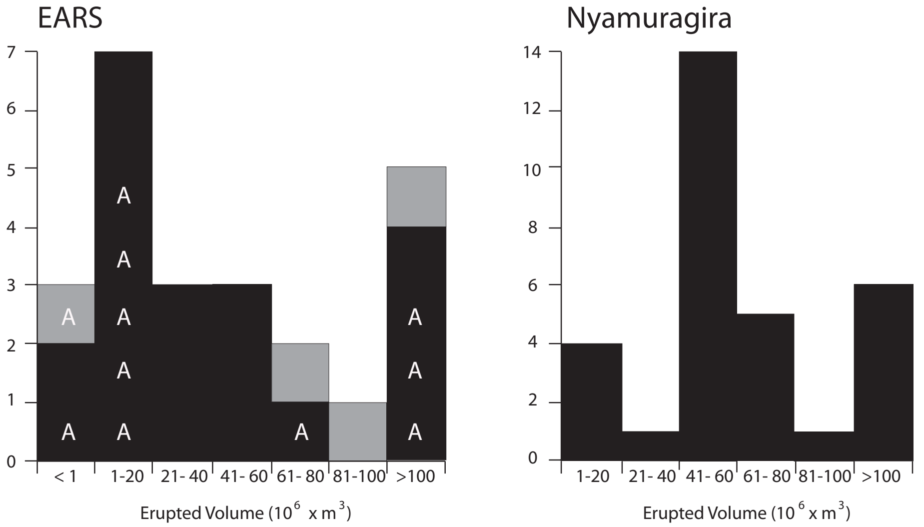

FIGURE 4 | Histograms of the number of eruptions by interval (20 × 10^6 m^3) of volume erupted, for EARS (left) and Nyamuragira (right) between 1902 and 2012. Black represents basalt extrusion and gray represents more silicic lava. All four eruption episodes at DMH are shown in the EARS plot. Eruptions in Afar are denoted by the letter A. Note the factor of 2 difference in the scales depicting the number of eruptions.

rift event could have unclamped the magma chamber beneath Oldoinyo Lengai, leading to bubble exsolution of the nephelinite magma at relatively shallow (∼3 km) depths and a series of explosive eruptions producing at least 10–20 × 10^6 m^3 of tephra. These explosions involved mixtures of nephelinite and natrocarbonatite magmas, probably involving a deep pulse of silicate magma. Major explosive events involving both magma types have occurred in 1916–1917, 1940–1941, 1966–1967, and 2007–2008 (Kervyn et al., 2010).

Nyiragongo (2002)

This eruption involved the formation of a southward propagating fissure, draining the summit lava lake to feed a rapidly advancing lava flow that entered Lake Kivu (Komorowski et al., 2002; Tedesco et al., 2007). In addition, rift-wide extension, detected by InSAR, together with seismicity was interpreted in terms of a southward propagating shallow dyke and a deeper one, 40 km long (Wauthier et al., 2012). Wadge and Burt (2011) argued that a very similar N-S dyke-driven eruption occurred during the only other historical flank eruption in 1977. Like the lava lake at Erta Ale, the Nyiragongo lava lake also lies at the junction of two rift zones diverging by 20°, both active historically: one oriented N (1977 and 2002) and one oriented NNW (1977).

Nyamuragira (2011–2012)

This is Africa's most productive volcano having had over 30 major eruptions in the last 100 years alone (Smets et al., 2010). These eruptions often involved dyke/fissure systems propagating downslope from a caldera above a chamber at ∼3–4 km depth (Toombs and Wadge, 2012; Wauthier et al., 2013) to effusive vents on the flanks. The 2011–2012 eruption was particularly voluminous and long-lived (305 × 10^6 m^3; 143 days) from a NE-oriented fissure12 km from the caldera (Albino et al., 2015). In June 2014, a new lava lake was established in the east pit crater of the caldera (Coppola et al., 2016).

The occurrence of these events within the 2002–2011 interval suggests that either the EARS as a whole experienced an episode of increased extensional susceptibility, or that there have been more of these events in the past that have been missed. Certainly, the Oldoinyo Lengai and Dabbahu Manda-Hararo events left relatively little surface volcanic record given the scale of the events. Biggs et al. (2013b) also showed that recent seismic swarms at Lake Magadi and Lake Manyara had no accompanying deformation associated with a dyke. Dyke events with no magma extrusion almost certainly have been missed over the last 200 years.

Historically-Recorded Eruptions (1800–2002)

Dubbi (1861)

This was a globally significant eruption producing a trachyte ash cloud and perhaps pyroclastic density currents, followed after about 2 days by effusion of basaltic lava flows for perhaps 5 months (Wiart and Oppenheimer, 2000a; Wiart et al., 2000). The total erupted volume was estimated at between 1.2 and 3.6 km^3, depending on interpretation of the age of the lava flows. There was no caldera formation but the initial Plinian column tapped a crustal reservoir of evolved magma. The chain of volcanoes of which Dubbi is the most northerly is the Nabro Volcanic Range (NVR), which is oriented NNE and is distinct from the family of NW-trending rift structures elsewhere in north and central Afar.

Ardoukoba (1978)

This small eruption occurred on the NW-oriented Asal-Ghoubbet Rift, the landward extension of the Gulf of Aden

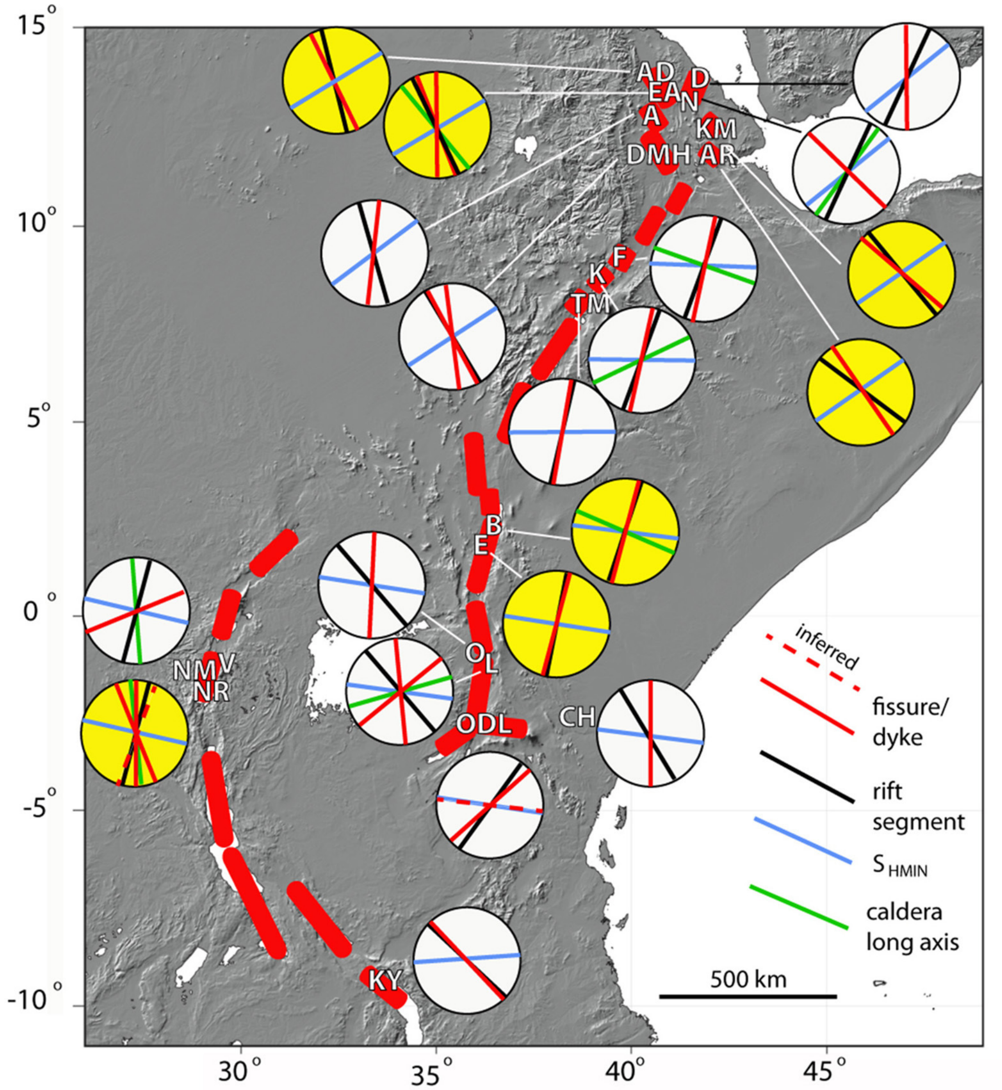

FIGURE 5 | Map of orientation elements in the EARS (Table 2). The red shapes are rift segments with the locations of historical eruptions denoted by their abbreviated names in white (**Table 1**). For each volcano the orientation of the most recent eruptive fissures, rift segment, S_{HMIN} and the long axis of the caldera are shown as diameters of a circle. Red dashed lines indicate inferred dykes. The yellow highlighted volcanoes are those that satisfy the criterion that both α and $\phi > 70°$ and are "orthogonal" (see **Figure 8**).

spreading ridge. Basalt lava was extruded from the northwestern end of the rift axis over 7 days (Allard et al., 1979) and fissuring also extended SE beneath the Gulf of Ghoubbet. The central volcano, Fieale, between Asal and Ghoubbet, marks the main source of mantle magma supply (Doubre et al., 2007). Two dykes were formed: the 4.5 km long, ~2 m opening Asal dyke beneath Ardoukoba and the 8 km long, ~3 m opening Ghoubbet dyke (Tarantola et al., 1979). For 8 years following the eruption, the rift continued to open magmatically with seismicity increasing as opening decreased after 1986 (Doubre et al., 2007). Doubre and Peltzer (2007) considered the Asal-Ghoubbet Rift to be controlled both by the far field plate stress and a locally overpressured magmatic system.

Kammourta (1928)

Like the Ardoukoba eruption this was a small volume basaltic eruption in an axial fissure setting accompanied by strong seismicity, though details are sparse. The main vent was at the southeastern end of a short line of cinder cones. The accompanying seismic crisis lasted about 1 month and produced surface deformation several kilometers to the south (Audin et al., 1990), suggesting a longer dyke fed the eruption, perhaps similar to Ardoukoba. The Kammourta vent occurred near the southeastern end of the Manda-Inakir Rift, which is connected to the equivalent position on the Asal-Ghoubbet Rift about 50 km to the south by a zone of closely spaced left-lateral strike slip faults, the Mak'Arrassou, marking the southwest boundary

TABLE 2 | Orientation information of historical eruptions.

	Volcano	Volcano-Tectonic Segment	Caldera axis azimuth (°)^a	Location of vents	Fissure length (km)	Fissure azimuth (°)	Rift segment azimuth (°)	S_{HMIN} ^{b}(°)	Velocity [mm/yr] ^{c}	Reference
D	Dubbi	NVP	–	Summit fissure	4	000	026	051	21	Wiart and Oppenheimer, 2000a
										McClusky et al., 2010
N	Nabro	NVP	033 ± 1	Pit craters in caldera	2	135	026	051	21	Hamlyn et al., 2014
										Wiart and Oppenheimer, 2000b
										McClusky et al., 2010
AR	Ardoukoba	Asal-Ghoubbet	–	Axial fissure	0.75	143	127	056	19	De Chabalier and Avouac, 1994
								(023)		Tarantola et al., 1979
KM	Kammourta	Manda-Inakir	–	Axial fissure	2.5	130	140	056 (023)	20	Audin et al., 1990
AD	Alu–Dalafilla	Erta Ale	–	En echelon axial fissures	3.5	167	155	060 (080)	14	Pagli et al., 2012
EA	Erta Ale	Erta Ale	142 ± 10	Pit craters in axial caldera	–	160, 180	155	060 (080)	15	Acocella, 2006; Sawyer et al., 2008
A	Alayta	Alayta	–	Fissure, east of shield		008	163	051 (080)	17	Gouin, 1979
DMH	Dabbahu–Manda Hararo	Manda-Hararo	–	Axial fissures in graben	0.4 (2005)	173	150	056	19	Ayalew et al., 2006; Ebinger et al., 2010
					4 (2007)	150		(080)		Ferguson et al., 2010
					5.5 (2009)	150				Barnie et al., 2015
					0.4 (2010)	156				
F	Fantale	Fantale- Dofen	111 ± 2	S. flank outside caldera	2	018	023	093	5	Mazzarini et al., 2013
								(116)		Acocella and Korme, 2002
K	Kone	Bosetti-Kone	066 ± 2	Caldera rim fissure to south		017	023	092	5	Mazzarini et al., 2013
								(116)		Acocella and Korme, 2002
TM	Tullu Moje	Gedemsa-Tullu Moje	–	Monogenetic fissure	–	010	010	091 (116)	4.9	Mazzarini et al., 2013
B	The Barrier	Suguta-Baringo	114 ± 3	Flank cone, fissure to north	1	013	014	096	3.1	Dodson, 1963
										Robertson et al., 2015
E	Emeruan- gogolak	Suguta-Baringo	144 ± 4	Caldera rim to south	0.4	015	012	097	2.9	Bosworth et al., 2003
										Robertson et al., 2015
										Dunkley et al., 1993
L	Longonot	Naivasha	074 ±12	Radial NNW and SW fissure in caldera	1	176, 050	140	097	2.3	Scott, 1980

(Continued)

TABLE 2 | Continued

	Volcano	Volcano-Tectonic Segment	Caldera axis azimuth (°)[a]	Location of vents	Fissure length (km)	Fissure azimuth (°)	Rift segment azimuth (°)	S_{HMIN} [b](°)	Velocity [mm/yr] [c]	Reference
										Robertson et al., 2015
O	Olkaria	Naivasha	–	Monogenetic flows	1.5	002	140	097	2.3	Karingithi et al., 2010
CH	Chyulu Hills	Off-rift	–	Monogenetic cones	–	000	150	099	1.4	Isola et al., 2014
ODL	O-D Lengai	Natron	–	Central cone	(3.8, 8) [d]	100[d]	033	099	1.4	Biggs et al., 2013a
						(048)		(173)		Muirhead et al., 2015
NM	Nyamuragira	VVP	173 ± 7	NE flank fissure/cone, caldera	1.1	070	015	102	2.3	Albino et al., 2015
								(132)		Wadge and Burt, 2011
										Wauthier et al., 2013
										Wood et al., 2015
NR	Nyiragongo	VVP	172 ± 25	S/NW flank fissures drain lava lake	12	000, 160	015	102	2.3	Wauthier et al., 2012
					(40)	(017 dyke)		(132)		Wood et al., 2015
V	Visoke	VVP	–	Monogenetic cone=Mugogo	–	–	015	102	2.3	Condomines et al., 2015
								(132)		Wood et al., 2015
KY	Kyejo	RVP	–	NW fissure cone= Fiteke	0.7	138	135	085	2.2	Fontijn et al., 2010
								(040)		Harkin, 1960

[a] *Using method Szpak et al. (2015) (http://cs.adelaide.edu.au/~wojtek/papers/ellipsefitJournal.pdf).*

[b] *S_{HMIN} = Minimum horizontal stress azimuth assumed to be same as the plate tectonic model directions of motion based on McClusky et al. (2010) for Afar, and Saria et al. (2014) for rest of EARS,. Values in brackets are the equivalent, binned by rift segment, values from the Delvaux and Barth (2009) stress field model.*

[c] *Plate motion velocities from McClusky et al. (2010) for Afar and Saria et al. (2014) for the rest of EARS.*

[d] *Modeled dyke azimuths that did not reach surface (Biggs et al., 2013a).*

TABLE 3 | Factors affecting the regional and local stress fields of the historical eruptions.

	Volcano	Basement Heterogeneities/Anisotropies	Transfer Zones	Edifice Height^a (m)	Magmatic Pressure Sources	α^b (°)	Φ^c (°)	Reference
D	Dubbi	N Proterozoic basement?	Danakil block differential rotation?	1300	probably	−25	+51	Mohr, 1978; Barberi and Varet, 1977
N	Nabro	N Proterozoic basement?	Danakil block differential rotation?	1700	7 km deep reservoir	−25	−84	Hamlyn et al., 2014
AR	Ardoukoba	140° fast wave anisotropy	no	no	7 km reservoir, co-, post-eruption	+71	−87	Cattin et al., 2005
					Extending > plate velocity. Fluid injection from overpressured magma			Doubre and Peltzer, 2007; Keir et al., 2011a
KM	Kammourta	–	no	no	Surface fault deformation up to 10 km from vent–dyke?	+84	−74	Audin et al., 1990
AD	Alu–Dalafilla	–	no	no	Co- and post-. Dyke above 10 km long sill with 2 segments at 1 km depth and reservoir at 4 km	−85	−73	Pagli et al., 2012
EA	Erta Ale	–	no	600	No, relieved by lava lake	−85	−80	Acocella, 2006
							−60	
A	Alayta	166° fast wave anisotropy	no	no	–	−68	+43	Keir et al., 2011a
DMH	Dabbahu–Manda Hararo	145° fast wave anisotropy	no	no	Co- and inter- at north end. Gabho (∼3 km),	−86	−63	Field et al., 2012
					Dabbahu (stacked sills 1–5 km deep).			Barnie et al., 2015
					Segment center focused dyke opening.			Keir et al., 2011a
					Extension stress varies either side of center			
F	Fantale	042° fast wave seismic anisotropy	End of segment?	1000	No InSAR deformation: 1993–2010	−70	+57	Kendall et al., 2005
								Keir et al., 2011a
								Biggs et al., 2011
K	Kone	020° fast wave seismic anisotropy	no	no	No InSAR deformation: 1993–2010	−69	+58	Kendall et al., 2005
								Keir et al., 2011a
								Biggs et al., 2011
TM	Tullu Moje	0175° fast wave seismic anisotropy	no	no	No InSAR deformation: 1993–2010	−81	+67	Kendall et al., 2005
								Keir et al., 2011a
								Biggs et al., 2011
B	The Barrier	–	End of segment?	600	–	−82	+91	
E	Emeruangogolak	–	–	700	No InSAR deformation: 1997–2006	−85	+88	Biggs et al., 2009

(Continued)

TABLE 3 | Continued

	Volcano	Basement Heterogeneities/Anisotropies	Transfer Zones	Edifice Height^a (m)	Magmatic Pressure Sources	α^b (°)	Φ^c (°)	Reference
L	Longonot	NW Proterozoic shear zones	End of segment/bend	1000	~9 cm uplift in 2004–2006, 4 km deep source in caldera magmatic or geothermal?	+37	+53	Biggs et al., 2011
							−79	Robertson et al., 2015
O	Olkaria	NW Proterozoic shear zones	End of segment/bend	no	–	+43	−79	Robertson et al., 2015
CH	Chyulu Hills	NW Proterozoic shear zones	–	no	–	+51	−79	Robertson et al., 2015
ODL	O-D Lengai	–	North Tanzanian	2000	Co- and inter- deformation. 3 km deep reservoir	−68	1	Biggs et al., 2013a
			Divergence				+51	
NM	Nyamuragira	N and NW Proterozoic faults and folds	Virunga or north part of Kivu	1550	Co- and inter- deformation. 3–4 km deep reservoir	−87	+28	
								Fernandez-Alonso and Theunissen, 1998
								Wood et al., 2015
								Wauthier et al., 2013
								Toombs and Wadge, 2012
NR	Nyiragongo	N and NW Proterozoic faults and folds	Virunga or north part of Kivu	2000	No, relieved by lava lake	−87	+78	Fernandez-Alonso and Theunissen, 1998
					Rare co- eruption dyking/faulting			Wood et al., 2015
								Wauthier et al., 2012
V	Visoke	–	Virunga ?	no	No, sourced direct from mantle	−87	–	Condomines et al., 2015
KY	Kyejo	NW (minor WNW) Proterozoic foliation/ faults	Rukwa-Malawi-Usango rifts	700	–	+50	−39	Fontijn et al., 2010, 2012
								Harkin, 1960

[a] *Edifice heights <500 m considered to have negligible effect.*

[b] *α = angle between the normal to the rift plate boundary and the plate motion direction.*

[c] *θ = angle between the eruption fissure/dyke and the plate motion direction.*

of the Danakil Block (Vellutini, 1990), and perhaps caused by counter-clockwise rotation of it.

Alayta (1906–1907)

A significant eruption with considerable felt seismicity was recognized in 1906 and 1907 from observers about 200 km to the east, who mistakenly attributed it to the Afdera volcano (Gouin, 1979). Reports suggest it may have occurred between March 1906 and August 1907 (Gouin, 1979). Its true location among the fissure-fed flow fields east of the Alayta shield was confirmed by Barberi et al. (1970). The lava flow emitted by the eruption has not been identified for certain, but satellite images show a large, bifurcating lava flow field with one arm to the east and the other to the northeast and source vents (at 13° 00′ N 40° 41′ E) and a source fissure apparently oriented N (CNR-CNRS, 1973). We take this to be the product of the 1906–1907 eruption. Another reported eruption in 1915 has no useful information.

Fantale (∼1810)

This silicic, composite volcano mainly comprises rhyolite tuffs and lava domes and has a summit caldera. In about 1810 (Harris, 1844) there was a basaltic eruption, low on the southern flank with a chain of cones oriented NNE, parallel to the Wonji Fault Belt (Acocella et al., 2002). The lava flow extended south to Lake Metahara (Gibson, 1974).

Kone (∼1820)

Kone or Gariboldi is a complex of silicic calderas and basaltic cinder cones, similar to Fantale 30 km to the NE. A fissure about 2 km long trending NNE at the junction of the two most recent calderas was the source of basaltic lava flows in 1820 (Cole, 1969).

Tullu Moje (1900)

Tullu Moje comprises a widely distributed field of vents. Two comendite lava flows, termed Giano (Bizouard and Di Paula, 1979), were erupted from a fissure oriented 010° on the rift floor southeast of Lake Koka. A "pitchstone" ashfall was reported to have destroyed crops in 1900 (Gouin, 1979, p. 105). Another eruption is also reported from 1775 ± 25 years. The Giano flows are assumed to be the product of the 1900 eruption.

The Barrier (1895)

Following its discovery in 1888, this volcano complex which straddles the rift at the southern end of Lake Turkana has been described, rather confusingly, as in eruption several times (1888, 1895, 1897, 1917, 1921; Cavendish, 1897; Champion, 1935), involving two scoria cones (Teleki's cone to the north and Andrew's cone to the south of the main edifice; Dunkley et al., 1993). Dodson (1963) mapped the last, mugearitic, lava flow from Teleki's cone, presumed to have been erupted in 1895 [paleomagnetic dating is consistent with this (Skinner et al., 1975)]. It is possible that basaltic flows from Andrew's cone are also post-1800, but there is no good evidence yet.

Emuruangogolak (1910)

This shield volcano has a summit caldera and flank trachyte and basalt lava flows. The latest lava flow is of comendite, ∼4 km long and dated magnetically as 1910 ± 50 years (Skinner et al., 1975). The vent sits on a NNE-trending fissure at a break in slope on the southern side of the volcano (Dunkley et al., 1993).

Longonot (∼1863)

Two trachyte lava flows were extruded on the southwest and northern flanks of Longonot. Their feeding fissures are radial with respect to the summit pit crater and the flows are in a similar state of preservation (Scott, 1980). Thompson and Dodson (1963) quote L.S.B. Leakey as having spoken to a tribesman who claimed to have witnessed activity at Longonot in the mid-1800s. It is presumed that these two lava flows were both produced then, around 1863.

Olkaria (∼1800)

This is a complex of peralkaline rhyolite lava flows erupted from at least 13 centers over the last 20 kyear (Marshall et al., 2009). The youngest of these is the Ololbutnot flow which has a C^{14} date of 180 ± 50 year BP (1720–1820) derived from carbonized wood associated with a pumice flow.

Chyulu Hills (1865)

This monogenetic field of vents and scoria cones extends for over 100 km following a northwest trend, well to the east of the rift in southern Kenya. The younger vents are in the south and the youngest are the Shaitani and Chaimu cinder cones and basanite lava flows which were emplaced in 1865 (Spath et al., 2000; Scoon, 2015). The fissures feeding the cones of both these have a N trend.

Visoke (1957)

A 2-day eruption 10 km north of Visoke volcano in the VVP produced a 1 km-long lava flow and a 40 m-high scoria cone. There is no discernible eruptive fissure but the 1957 eruption was not located on the prominent NE oriented fissure zone that runs between Visoke and Sabinyo volcanoes. This is the only known historical eruption of an olivine melilitite lava anywhere. Its unusual geochemistry means that it is not related to Visoke volcano, nor to the other Virunga volcanoes, but rather was directly sourced from the mantle as a very early stage foiditic magma, such as fed the early Nyamuragira volcano (Condomines et al., 2015).

Kyejo (1800)

The only historical eruption from the Rungwe Volcanic Province (RVP) comprised a tephrite lava flow from a NW-oriented fissure on the northern slopes of the Kyejo central volcano. The Fiteko cone appears to be the source of the most recent flow. The age of the eruption is based on oral tradition (Harkin, 1960). Whilst there is some uncertainty about the lava flow at source (Fontijn et al., 2012) the area covered by the flow is distinct.

DISCUSSION

Eruption Characteristics

Despite an extensive geological record of explosive volcanism in EARS, in the form of large calderas and widespread tephra layers (e.g., Hutchison et al., 2015), there have only been two historical eruptions with VEI $\geq$ 4: at Dubbi in 1861 and Nabro in 2011. Both were explosive in their initial stages, generating large, but unmeasured silicic tephra deposits, followed by large volume basaltic lava flows, suggesting that prior to eruption, batches of basaltic magma intersected high-level bodies of trachyte magma. Oldoinyo Lengai also displays explosive behavior, and although the 2007–2008 eruption was VEI3, it was more protracted than at Dubbi or Nabro, lasting several months. Like Dubbi and Nabro this involved rising mafic magma from depth intersecting a shallow reservoir with magma of a more evolved composition. Similar explosive eruptions occurred in 1916–1917, 1940–1941, and 1966–1967, but this 20–40-year cyclicity of magma mixing events is not seen elsewhere in the EARS. Low intensity explosivity, involving ash fall and column collapse, is thought to have accompanied at least two of the three main cases of rhyolitic lava flow in the EARS, with reports of "pitchstone" ashfall from the 1900 eruption of Tullu Moje, and the pumice flow associated with the Ololbutnot rhyolite lava flow at Olkaria.

Historically, effusive eruptions have been more common than explosive eruptions in the EARS and the volumes of individual lava flows range over four orders of magnitude, from 10^5 m^3 for the small eruptions associated with the 2005–2010 dyke intrusion at DMH to 10^9 m^3 for the 1861 lava flow at Dubbi. The Dubbi lava flow, although of somewhat uncertain volume, is of comparable magnitude to that of the combined intruded dyke volume of the DMH 2005–2010 event. A low-volume lava flow from the 1957 Visoke eruption, seems to have been a rare, directly mantle-fed, monogenetic event. Between these two extremes, the volume distribution is bimodal as plotted in **Figure 4**. The lower value mode is the $1–20 \times 10^6 m^3$ bin and the upper mode bin is unbounded and thus represents the high-volume tail of the distribution. Eruptions in Afar contribute disproportionately to the lower volume counts, suggesting that the bimodal distribution may be a result of recording bias: historical records only include the largest volume flows, while the more complete geophysical record only extends for a few decades and is dominated by the recent small flows in Afar. The equivalent plot for the volumes of the 31 flank eruptions of Nyamuragira from 1901 to 2012 is also shown in **Figure 4** (note that the 2011–2012 volume has been used in both plots). The mode at Nyamuragira is at the $41–60 \times 10^6$ m^3 bin, five-times the value for the EARS mode, and there are no silicic or very low volume eruptions.

Of the 21 eruptions, we know the durations of 15 (**Table 1**). The distribution of durations is strongly skewed, with 10 of the eruptions lasting less than 20 days (and 8 lasting less than 5 days). Four eruptions lasted 150 or more days. Three of the long-duration eruptions: Dubbi (150 days), Alayta (500 days), Nyamuragira (150 days) also had large extruded volumes ($>300 \times 10^6, m^3$). Eruption-averaged extrusion rates range from about 1 to 270 m^3 s^{-1}, typical of volcanoes elsewhere (Harris et al., 2007). Nyamuragira is the only volcano with enough measured eruptions to estimate time-variable extrusion rates: 0.47 m^3 s^{-1} before 1980 and 1.13 m^3 s^{-1} during 1980–2002. This marked, long-term change in surface supply was probably caused by the 1977 Nyiragongo volcano-tectonic event changing the stress field beneath its neighboring volcano (Wadge and Burt, 2011).

The apparent increase in volcano-tectonic activity in the EARS between 2002 and 2011 may have been due to a plate boundary-wide adjustment of stresses, but could also be the result of reporting bias due to the increased use of InSAR. The lack of equivalent events in the 5 years since 2011 suggests the former. Pagli et al. (2014) demonstrate that the DMH dyke intrusion altered the strain field for at least 5 years after the event, over distances of 200 km, including the area around several other volcanic systems in Afar. There is little evidence for an increase in activity elsewhere in the EARS; Oldoinyo Lengai and Nyamuragira erupt frequently and the 2007–2008 eruption at Oldoinyo Lengai fits the established pattern of 20–40 year periodicity in explosive episodes. Biggs et al. (2016) used observations from the Kenyan Rift to show that even small changes in strain associated with minor unrest can affect multiple reservoirs beneath individual volcanoes, but typically do not extend to neighboring volcanoes at distances >10 km. The hypothesis could be tested by (1) improving the historical record by dating the numerous small-volume lava flows found at volcanoes in the EARS (e.g., Hutchison et al., 2015) and (2) constructing 3-D velocity fields from InSAR and GPS (e.g., Pagli et al., 2014).

Subsurface Magmatic Systems

Many of the volcanoes of the EARS are known to be deforming and/or seismically active (**Table 3**), but the link to eruption is statistically weak (Biggs et al., 2014) and it is unclear whether the source of the unrest is magmatic or hydrothermal. For the deformation events associated with eruptions, shallow (<5 km deep) dykes and sills dominate the co-eruption motion signals: Ardoukoba in 1978, Alu-Dalafilla in 2008, Dabbahu-Manda Hararo in 2005, 2007, 2009, 2010, Oldoinyo Lengai in 2007–2008, Nyamuragira in 2012 and Nyiragongo in 2002. Where model inversion of InSAR data associated with the eruption calls for deeper magmatic sources below the shallow dykes and sills (Segall, 2010), the data have not warranted more complexity than a Mogi point source: Nabro in 2011 (7 km deep), Alu-Dalafilla in 2008 (4 km), Dabbahu-Manda Hararo from 2005 to 2010 (10 km), Nyamuragira from 1996 to 2012 (4 km) (Wauthier et al., 2013). For unrest signals not associated with eruption, the source is one or more shallow reservoirs (<8 km) with lateral interactions limited to distances of <10 km (Biggs et al., 2016). The deformation patterns are typically radially symmetric, so we have no good evidence for magma reservoir shapes (e.g., ellipsoidal) that can be used to infer the relationship to the horizontal differential stress field.

The ratio of intruded to extruded magma can give insight into the subsurface rheology and stress field. However, for many of the older historical eruptions, no geodetic data was available, and only the extrusive component of the total magma budget of the event is known, while for some of the recent dyke emplacement events, 9 of the 13 in the 2005–2010 DMH episode, there was no extrusive component. Where available, intrusion/extrusion ratios are in the range 4–15 (**Table 1**), the exception being the small 2010 extrusive volume at DMH which was dwarfed by a much larger dyke to give an intrusion/extrusion ratio of 352. Any increase in the external stress normal to a magma-filled dyke will tend to close it and force magma to the surface, decreasing the ratio. The largest volume lava flow erupted at or close to the axial rift was at Alayta, where the high obliquity of the dyke ($\phi = 43°$) may have been sufficient to force a greater proportion of magma from a large parental dyke to the surface than elsewhere.

Orientations of Eruptive Fissures and Dykes

The orientations of the historical eruptive fissures or dykes are shown in **Figure 5**, along with the orientation of the rift segment, the current direction of plate motion, S_{HMIN} and the long axis of the caldera. The regional pattern of historical fissuring in Afar is shown in **Figure 6**. The majority of the recent eruptive fissures and dykes in Afar (Alu-Dalafilla, Erta Ale, and DMH, and Ardoukoba and Kammourta, further east) share a narrow range of orientations around NW to NNW as we would expect for purely extensional regimes. The orientation of the Alayta eruptive fissure is N and the crustal fabric near Alayta reported in Section Orientation and Influence of Structural Fabric and Anisotropy suggests that Alayta has some degree of oblique structural control. The NVR crosses the Danakil microplate as a 0.26° trending structure that obliquely links the spreading axes of Afar and the Red Sea (Barberi and Varet, 1977). The NVR may be the locus of local counter-clockwise motion within the Danakil Block (McClusky et al., 2010; **Figure 4**). The eruptive fissure at Nabro trends NW like the majority of Afar volcanoes, but the other active NVR volcano, Dubbi, has a N-trending fissure similar to Alayta.

The five eruption sites in the northern parts of the MER and the Kenya Rift show very close alignment between the border faults and recent eruptive fissures, however, in some cases this is oblique to either the long-axis of the caldera (Kone) or the current plate motion (Fantale). In the southern Kenyan Rift (Longonot, Olkaria and off-rift Chyulu Hills), the recent fissures are aligned with the current plate motion direction, but oblique to the rift border faults.

Oldoinyo Lengai shows structural elements at many orientations suggesting a radial stress field. Oldoinyo Lengai sits within the North Tanzanian Divergent Zone, a region of complex tectonic adjustments (Muirhead et al., 2015) and beneath a large edifice. The detection of two, non-erupting, dyke-forming events at different times during the 2007–2008

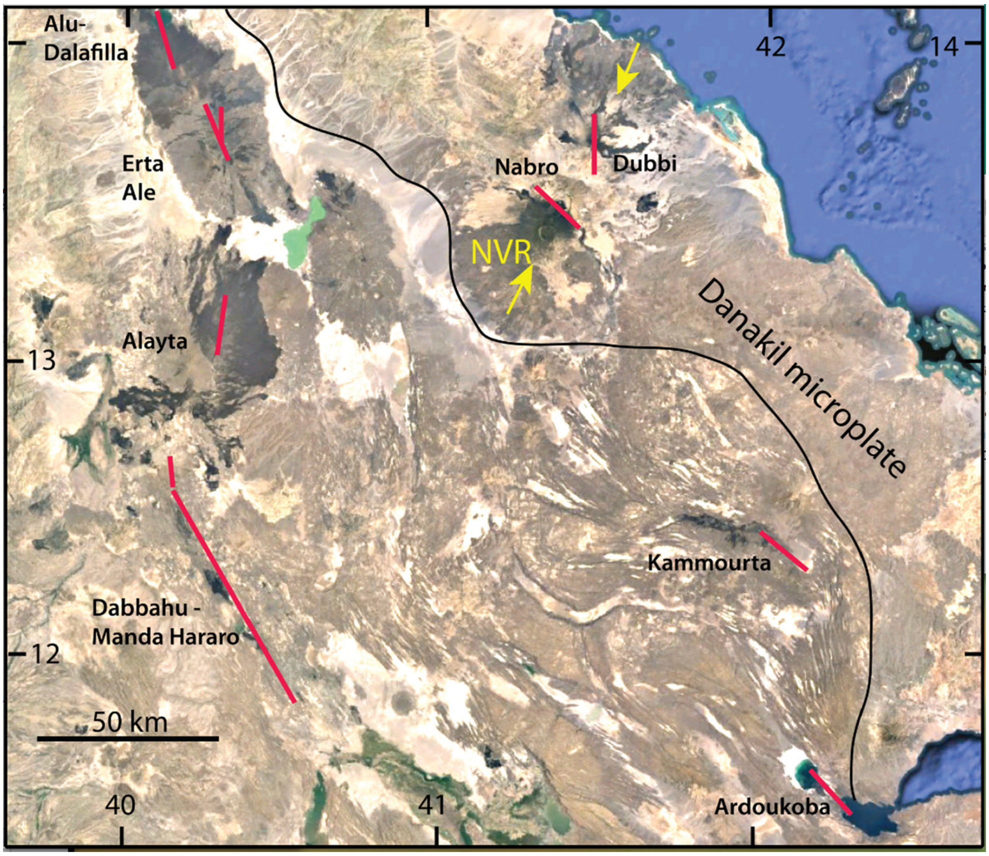

FIGURE 6 | Image map (based on Google Earth) of central Afar showing the locations and orientations of the fissures produced by the historical eruptions (red lines). The lengths of fissures is schematic, particularly for Dabbahu-Manda Hararo which was largely an intrusive event. The yellow arrows indicate the Nabbro Volcanic Range (NVR) which crosses the Danakil microplate whose southwestern margin is shown by the black line. The grid marks are in degrees of latitude and longitude.

eruptions that are strongly oblique to each other (Biggs et al., 2013a) and multiple radial fissures (Muirhead et al., 2015) indicates that stress is locally variable, with edifice loading and magma pressure sufficient to exceed the regional stress field close to the volcano (Biggs et al., 2013b). These observations are similar to the eruption of Jabal al Tair in 2007, just to the north of our area, which displayed an eruptive dyke perpendicular to the rift direction (Xu and Jonsson, 2014).

At Nyiragongo and Nyamuragira, the current plate motion direction is ESE, but the trends of the eruptive fissures are more oblique and variable, from ENE to WNW. Proterozoic N and NW-oriented basement features may be responsible for the N and NNW fissure zones, to the south of Nyiragongo and between the two volcanoes respectively (**Figure 7**). These zones may also be the conduits of stress transfer at the northern end of the Kivu Rift and have played a large role in the historical volcanism. Both volcanoes have large edifices with flank eruptions extending out to over 20 km. Beyond about 7 km on Nyamuragira the orientation of some fissures curve to rift boundary orientation as would be expected for combined edifice-tectonic stress fields (**Figure 2D**). The clear increase in extrusive output of Nyamuragira, following the 1977 volcano-tectonic event at Nyiragongo, was attributed to a change in the local stress field (Wadge and Burt, 2011). After 1977, the NE-trending fissure zone southwest of Nyamuragira became inactive whilst the equivalent ENE-trending zone east of the edifice became active (**Figure 7**). The cumulative volume erupted within 7 km of the caldera increased from 210 to 560 × 10^6 m^3 over periods of 28 (1948–1976) and 25 (1977–2002) years, respectively, whilst the equivalent volume beyond 7 km distance increased from 211 to 407 × 10^6 m^3. We interpret this as an increased tendency for magma to reach the surface, particularly centrally, beneath Nyamuragira following the 1977 event. Although we cannot prove it (e.g., from InSAR measurements), we concur with Wadge and Burt that the intrusive/extrusive ratio was generally higher for eruptions prior to 1977 and a larger proportion of the deep magma supply was diverted to intrusions rather than reaching the surface compared to the behavior in the post-1977 period.

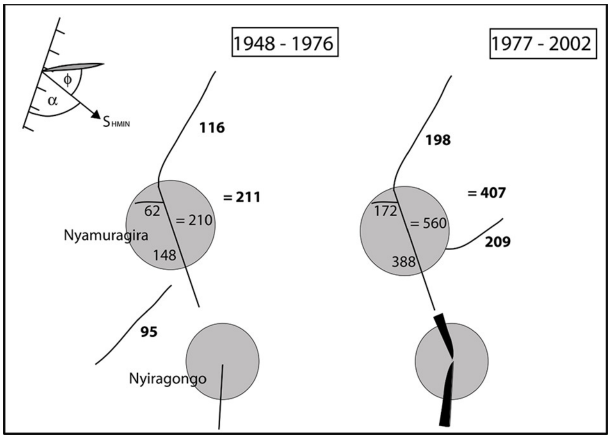

FIGURE 7 | Schematic of the eruptive fissure system of Nyamuragira and output of lava for two periods: 1948–1976 and 1977–2002, separated by the volcano-tectonic event at Nyiragongo volcano in 1977, shown as the black blade symbol representing a major dyke emplacement. The Nyamuragira gray circle represents a 7 km radius of edifice stress influence. The numbers associated with each fissure (line segment) are the cumulative volumes (10^6 × m^3) erupted from that fissure zone over that period. The bold numbers are those from eruptions outside the 7 km radius edifice. In the top left corner is a schematic representation of the geometry of the rift azimuth (ticked line), extension direction σ_3, and the obliquity angles α and ϕ for Nyamuragira.

The obliquities of the eruption sites are summarized in **Figure 8** in terms of the angular measures α and ϕ, together with the eruption volumes and edifice heights. There are 7 eruptions that fit the orthogonal model (allowing for up to 20° error) and sit within the gray quadrant of **Figure 8**. There is no obvious clustering of values round the oblique and transtension model axes, suggesting that processes other than plate tectonic-derived horizontal stress fields are dominant. Large volume eruptions (the five largest being Dubbi, Nabro, Alayta, Olkaria and Nyamuragira) or eruptions that are long-lived (e.g., Oldoinyo Lengai) or with large edifices (Nabro, Nyamuragira, Oldoinyo Lengai) tend to have high obliquity indicating that the tectonic stress field is less dominant in these cases.

In Afar, two NVP volcanoes, Dubbi and Nabro have edifices 1300 and 1700 m high respectively and both have erupted

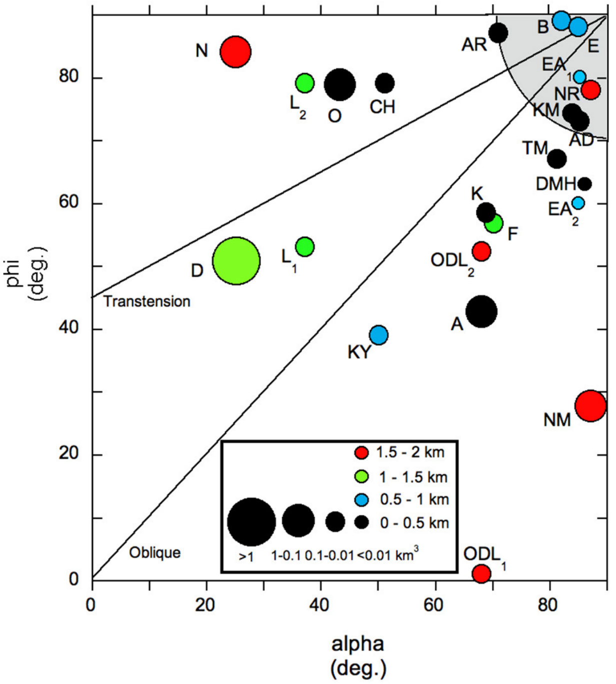

FIGURE 8 | Plot of the α and ϕ obliquity angles (Figure 3) for each historical eruption site (labeled as in the code used in Table 1). The size of the circle denotes one of four ranges of erupted volume and the color denotes one of four ranges of edifice height. The shaded circular quadrant at 90–90° represents the field of orthogonal volcanoes allowing for 20° of error in both alpha and phi. Note that 3 volcanoes have more than one dot, corresponding to multiple-oriented dykes.

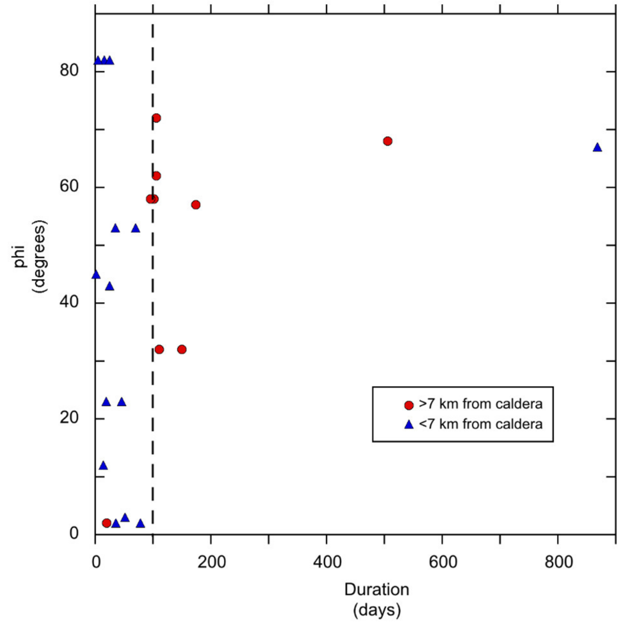

FIGURE 9 | Plot of ϕ against duration of eruptions at Nyamuragira for the period 1938–2012. Eruption sites located <7 km from the caldera are plotted as blue triangles, >7 km as red circles. All but one of the former group have short-lived eruptions (<100 days, dashed black line) and all but one of the latter group have long-lived eruptions.

compositionally zoned magma from central reservoirs, one of the theoretical characteristics of loading-induced development of volcanic systems discussed in Section Magmatic and Volcanic Processes. There is strong loading evidence in the VVP, specifically the observed westward tilting of the Karisimbi edifice that fits a combined asymmetric extension-loading model (Wood et al., 2015).

Figure 9 shows the duration of eruption at Nyamuragira plotted against ϕ for those eruptions with known fissure orientations. With one exception, all the long-duration (>100-days) eruptions are located >7 km from the caldera (red circles in **Figure 9**) and mostly have high values of ϕ (30–80°) supporting the argument of Wadge and Burt (2011) that eruptions fed by dykes parallel/subparallel to the rift axis were longer-lived and generally had more voluminous lava flows than those fed by rift-orthogonal dykes.

Orientation and Influence of Structural Fabric and Anisotropy

Structural trends in the Proterozoic basement have been shown to play a role in several of the recent magmatic episodes in the EARS. The Ayelu–Amoissa dyke in the northernmost MER was inferred by Keir et al. (2011b) to owe its ESE strike (**Figure 1**) to an Oligo-Miocene structure associated with an earlier phase of opening of the Gulf of Aden. The NW-SE oriented field of monogenetic vents at Chyulu Hills, situated about 150 km to the southeast of the Kenya Rift is another likely example of the influence of the local NNW-trending structural fabric (Isola et al., 2014). In the western arm of the EARS at the VVP, the Proterozoic basement trends are N and NW (Fernandez-Alonso and Theunissen, 1998), both of which seem to play a role in guiding volcanic structures. In the RVP, Kyejo is located close to the junction of the Rukwa, Malawi and Usango rift segments and its historical eruptive fissure is oriented parallel to the dominant NW oriented basement structures (Harkin, 1960; Fontijn et al., 2010).

Seismic anisotropy is an indicator of structural fabric and may reflect a range of structural elements including some which relate to the current stress field (e.g., flow in the mantle, alignment of melt pockets), and others that may not (e.g., pre-existing structural fabrics). In the mantle, the patterns of anisotropy show little spatial variability and are thought to represent alignment of olivine crystals associated with asthenospheric flow. For example, the NE-SW anisotropy beneath Ethiopia is believed to represent flow at depths >100 km (Hammond et al., 2014). Shear-wave splitting of teleseismic events show melt-filled cracks at lower crust and upper mantle depths produce anisotropy trending 0.25° (Kendall et al., 2005). Crustal anisotropy is more variable, and reflects major structural features, for example in Afar, north of the Tendaho-Gobad Discontinuity (TGD), there is a high degree of anisotropy and the fast direction is oriented NNW, but to the south, the anisotropy is more moderate and the fast direction is orientated NNE (Keir et al., 2011a). In Kenya and Tanzania there are regional teleseismic event surveys (e.g., Walker et al., 2004), but only a few shallow crustal seismic anisotropy studies south of Ethiopia, and in the Western Rift, for example in the Ruwenzori segment (Batte et al., 2014). Preliminary teleseismic results from the VVP/Kivu, indicate a deep northeasterly oriented fabric (Zal et al., 2014).

For most of the volcanoes in Afar, the NNW orientation of the seismic anisotropy is similar to that of the rift axis (e.g., Ardoukoba and DMH). However, at Alayta, which lies close to the seismic station BOOE (Keir et al., 2011a; **Figure 3A**), the fast anisotropy direction is rotated clockwise relative to the segment axis, with an azimuth of 166°. This is the same sense of rotation as the Alayta 1906–1907 eruption fissure relative to the segment axis and may reflect the obliquity of recent dykes. The closest measurements to recent eruptions in the northern MER (Fantale, Kone, and Tullu Moje) show fast anisotropic directions of NW, NNW, and N, respectively (Keir et al., 2011a). These volcanoes lie on neighboring, en echelon, magmatic segments oriented generally NNW to NW, with superimposed faulting and fissuring oriented NNW, the Wonji Fault Belt. In the southern MER, the geothermally and seismically active, but not eruptive, Aluto and Corbetti volcanoes show strong degrees of anisotropy (Nowacki et al., 2016). Aluto shows a fast shear wave polarization oriented parallel to the WFB, but at Corbetti the splitting trends ESE, parallel to the Wendo-Genet scarp, representing an inherited crustal structure (**Figure 1**). As yet, there has been no evidence of temporal variation of anisotropy episodes of high-level magma pressurization at any of the EARS volcanoes as seen elsewhere (e.g., Savage et al., 2010), but appropriate experiments have yet to be undertaken.

Inherited structures have been proposed to explain the eccentricity of calderas in the MER and Kenya Rifts (Acocella et al., 2002; Robertson et al., 2015). Robertson et al. (2015) argued that NW, trans-rift fault structures in the basement of the Kenya Rift led to elongate reservoirs beneath the southern population of elliptical calderas, including Longonot. Acocella et al. (2002) suggested that E-W inherited structures in the MER controlled the E-W elongated Kone, Fantale, and Gedemsa calderas. In contrast, Bosworth et al. (2003) argued that the caldera eccentricity in the Kenya Rift was due to preferential spalling of wall rocks into magma chambers in the direction of S_{HMIN}. They also made a case for clockwise rotation of the horizontal stress axes of 19° over ~30 ka between the formation of The Barrier and Emuruangogolak calderas.

Nine of our historically active volcanoes have calderas (**Table 2**, **Figure 5**). They fall into two distinct groups: group 1 (Nabro, Fantale, Kone, The Barrier, Emeruangogolak, Longonot) and, group 2 (Erta Ale, Nyamuragira, Nyiragongo). The group 1 calderas are large and ellipsoidal, consistent with magma reservoir collapse origins. Two of them, Fantale, and The Barrier, have roughly orthogonal geometries with caldera axes elongated within ±15° of the spreading direction (**Table 2**). This supports the arguments of Acocella et al. (2002) and Robertson et al. (2015) that although the current stress regime dominates recent eruptive fissures and dykes, it is not the dominant control on caldera orientation or crustal magma storage. The group 2 calderas are smaller and contain persistent or recently active lava lakes in pit craters. The presence of lava lakes at these calderas requires some longevity of magma supply (the lakes are present for tens to hundreds of years), the conditions for maintaining persistent surface storage, a non-dyke (i.e., non-freezing/closing) conduit and a likely simple plumbing system. They also have a low eccentricity, but are elongated approximately parallel to where two fissure zones intersect obliquely [<30°, see e.g., Acocella (2006) for a sketch of Erta Ale]. These observations suggest that crustal stresses have a controlling influence on magmatic processes, independent of buoyancy. Each of the group 2 calderas (in addition to the other long-lived and ephemeral lava lakes such as at Masaya, Kilauea, Ambrym and Erebus) occur at the elbow of a change in the rift orientation (0° to 150° at Erta Ale, 0° to 160° at Nyiragongo and 150° to 170° at Nyamuragira). It is therefore probable that this jag in spreading segments provides the continuous, highly localized low horizontal stresses beneath these calderas, but rapid enough extension rates to maintain magma supply, required to maintain lava lakes. Oppenheimer and Francis (1998) suggested that there is a highly localized (<700 m diameter) magma body at shallow depth (few km), consistent with low horizontal stresses. Coppola et al. (2016) make a strong case that the re-instatement of the Nyamuragira lava lake in 2014 was made possible by a change in the volcano's stress field following the very voluminous flank eruption in 2011–2012.

CONCLUSIONS

We have documented 21 historical eruptions in the EARS over approximately the last 200 years. They have erupted a minimum of about 5 km^3 of magma, mainly varieties of basalt. Surface deformation associated with these eruptions has been recorded by InSAR or ground survey in 7 cases. All have involved dykes (sills) and shallow (<10 km depth) magma reservoirs and high intrusive/extrusive ratios (mainly 4–15). Of these 21 eruptions, only 7 of the associated fissures/dykes lie within 20° of the orthogonal to the plate spreading direction, (ϕ), and parallel to the rift axis, the expected geometry for an extensional plate boundary (**Table 3**, **Figure 8**). The predominance of non-orthogonal geometries demonstrates that other factors are present in the development of volcanism during the early stages of continental rifting.

We find evidence for four ways to modify the regional plate tectonic stress field beneath these volcanoes: the effects of inherited crustal fabric and anisotropy, the existence of oblique structures in transfer zones between rift segments, crustal loading by large volcanic edifices and the pressures exerted by magma stored and transported within the crust.

Shear wave-splitting studies of crustal and mantle anisotropies, in Afar and MER show that sharp discontinuities (at the 10 km + scale) in orientation and magnitude in the stress field must exist, particularly across structural boundaries. Current evidence points to dykes and aligned melt enclaves as being responsible for variable anisotropy (Keir et al., 2015). The evidence for crustal heterogeneities in the form of inherited faults and other old structures is clear throughout the rift; NW structures (with N and WNW variants) that formed in Proterozoic crust dominate in both arms of the EARS. Examples include the Ayelu-Amoissa (2000) dyke event in southern Afar which followed a rift-orthogonal trend (Keir et al., 2011b) and the NW-trending Chyulu Hills monogentic field of volcanoes that runs oblique to the Kenyan Rift. Non-orthogonal crustal extension is accommodated in transfer zones between segments, which may re-activate existing basement faults or generate new ones. The stress field in the transfer zones is complex and not aligned with the current plate motion meaning the resulting volcanism typically has highly oblique elements. Examples include Oldoinyo Lengai in the NTDZ and Nyamuragira at the northern end of the Kivu rift segment.

The stress fields associated with tall edifices play a strong role in the EARS. Based on the following characteristics: radial dykes (curving with distance from the volcano and at shallow depth to meet the regional stress field, **Figure 2D**; c.f. Roman and Jaupart, 2014), a central magma reservoir, and explosive silicic magmas, mingling with mafic magma, we recognize 6 volcanoes that show some of these characteristics, all with edifice heights in the range 1–2 km. Nabro, Dubbi, and Oldoinyo Lengai show explosive eruptions with evolved magmas. Longonot, Oldoinyo Lengai, Nyamuragira, and Nyiragongo show evidence of radial dykes and a shallow central magma reservoir. Tibaldi et al. (2014) consider Nyiragongo to be an example of a volcano with a divergent rift system based on analysis of scoria cone distribution, but we argue that Nyiragongo does not have the highly elliptical footprint typical of such volcanoes and the splay of the rift fissures is better explained by transfer zone tectonics (**Figure 7**).

Overpressured magma reservoirs including major dykes (and sills) have yielded excellent InSAR signals in recent years that have been modeled in terms of the rise and partitioning of intrusive and extrusive volumes of magma. However, models have been unable to identify non-point source volumes for reservoirs and hence infer the 3D stress field. There is some evidence that the proportion of magma reaching the surface via rift-aligned dykes (e.g., DMH) is less than at more oblique dykes (e.g., Alayta).

However, Nyamuragira is the only EARS volcano with enough sufficiently well-documented eruptions to infer its long-term dynamic behavior. Stochastic modeling demonstrated a propensity for its shallow crustal reservoir to behave in a pressure-cooker/volume-limited manner (Burt et al., 1994) and exponential decay of extrusion rate decay during eruptions (Wadge and Burt, 2011). Eruptions within 7 km of the volcano are of relatively short duration (<100 days), but eruptions with more distal fissures tend to have greater values of ϕ and longer durations. There were major changes in long-term magma extrusion rates in 1977 (and perhaps in 2002) due to major along-rift dyking events that effectively changed the Nyamuragira stress field and the intrusion/extrusion ratios of eruptions.

AUTHOR CONTRIBUTIONS

GW: Lead author. Instigator of idea. Chief editor of manuscript. Focus on historical volcanism. JB: Contribution mainly on InSAR and tectonics. RL: Responsible for work on calderas. JK: Responsible for material on seismic anisotropy.

ACKNOWLEDGMENTS

GW and JB are members of the NERC LICS (Looking Inside the Continents from Space) consortium (grant NE/K010956/1) and the Centre for the Observation and Modelling of Earthquakes, Volcanoes and Tectonics (COMET) network, JB and JK are supported by the NERC RiftVolc consortium (grant NE/L013932/1). RL is supported by a NERC studentship tied to LICS. All the research data are within the paper. We thank the editor and two anonymous referees for their reviews and Professor Agust Gudmundsson for his valuable advice on the relevance of the published results of numerical models of extensional stress fields.

REFERENCES

Acocella, V. (2006). Regional and local tectonics at Erta Ale caldera, Afar (Ethiopia). *J. Struct. Geol.* 28, 1808–1820. doi: 10.1016/j.jsg.2006.06.014

Acocella, V., and Korme, T. (2002). Holocene extension direction along the Main Ethiopian Rift, East Africa. *Terra Nova* 14, 191–197. doi: 10.1046/j.1365-3121.2002.00403.x

Acocella, V., and Tibaldi, A. (2005). Dike propagation driven by volcano collapse: a general model tested at Stromboli, Italy. *Geophys. Res. Lett.* 32:L08308. doi: 10.1029/2004GL022248

Acocella, V., Korme, T., Salvini, F., and Funiciello, R. (2002). Elliptical calderas in the Ethiopian Rift: control of pre-existing structures. *J. Volcanol. Geotherm. Res.* 119, 189–203. doi: 10.1016/S0377-0273(02)00342-6

Acocella, V., and Neri, M. (2009). Dike propagation in volcanic edifices: overview and possible developments. *Tectonophysics* 471, 67–77. doi: 10.1016/j.tecto.2008.10.002

Acton, G. D., Stein, S., and Engeln, F. (1991). Block rotation and continental extension in Afar: a comparison to oceanic microplate systems. *Tectonophysics* 10, 501–526. doi: 10.1029/90tc01792

Albino, F., Smets, B., d'Oreye, N., and Kervyn, F. (2015). High resolution TanDEM-X DEM: an accurate method to estimate lava flow volumes at Nyamuragira. *J. Geophys. Res. Solid Earth* 120, 4189–4207. doi: 10.1002/2015JB011988

Allard, P., Tazieff, H., and Dajlevic, D. (1979). Observations of seafloor spreading in Afar during the November 1978 fissure eruption. *Nature* 279, 30–33. doi: 10.1038/279030a0

Amadei, B., and Stephansson, O. (1997). *Rock Stress and its Measurement*. London: Chapman Hall.

Anderson, E. M. (1936). The dynamics of formation of cone sheets, ring dykes and cauldron subsidence. *Proc. R. Soc. Edin.* 56, 128–163. doi: 10.1017/S0370164600014954

Audin, J., Vellutini, P. J., Coulon, C., Piguet, P., and Vincent, J. (1990). The 1928-1929 eruption of Kammourta volcano – evidence of tectono-magmatic activity in the Manda-Inakir Rift and comparison with the Assal Rift, Afar Depression, Republic of Djibouti. *Bull. Volcanol.* 52, 551–561. doi: 10.1007/BF00301536

Ayalew, D., Dell'Erba, F., di Vito, M. A., Orsi, G., Yirgu, G., Dingwell, D., et al. (2006). The Da' Ure' eruption at the Boyna volcanic complex during the September 2005 Afar extension episode. *Am. Geophys. Union, Fall Meeting Abstract* T33E-02A.

Baer, G., Hamiel, Y., Shamir, G., and Nof, R. (2008). Evolution of a magma-driven earthquake swarm and triggering of the nearby Oldoinyo Lengai eruption, as resolved by InSAR, ground observations and elastic modelling, East African Rift, 2007. *Earth Planet. Sci. Lett.* 272, 339–352. doi: 10.1016/j.epsl.2008.04.052

Bagnardi, M., Amelung, F., and Poland, M. P. (2013). A new model for the growth of basaltic shields based on deformation. *Earth Planet. Sci. Lett.* 377, 358–366. doi: 10.1016/j.epsl.2013.07.016

Baker, B. H., Mohr, P. A., and Williams, L. A. J. (1972). Geology of the Eastern Rift System of Africa. *Geol. Soc. Am. Spec. Pap.* 136, 1–67. doi: 10.1130/SPE136-p1

Barberi, F., Borsi, S., Ferrara, G., Marinelli, G., and Varet, J. (1970). Relations between tectonics and magmatology in the northern Danakil Depression (Ethiopia). *Phil. Trans. R. Soc. Lond. A* 267, 293–311. doi: 10.1098/rsta.1970.0037

Barberi, F., and Varet, J. (1977). Volcanism of Afar: small scale plate tectonics implications. *Bull. Geol. Soc. Am.* 88, 1251–1266.

Barnie, T. D., Keir, D., Hamling, I., Hofmann, B., Belachew, M., Carn, S., et al. (2015). "A multidisciplinary study of the final episode of the Manda Hararo dyke sequence, Ethiopia and implications for trends in volcanism during rifting cycle," in *Magmatic Rifting and Active Volcanism*, eds T. J. Wright, A. Ayele, D. J. Ferguson, T. Kidane, and C. Vye-Brown (London: Geological Society), 420.

Batte, A. G., Rumpker, G., Lindenfeld, M., and Schuman, A. (2014). Structurally controlled seismic anisotropy above small earthquakes in crust rocks beneath the Ruwenzori region, Albertine Rift, Ugand. *J. African Earth Sci.* 100, 579–585. doi: 10.1016/j.jafrearsci.2014.08.001

Bialas, R. W., Buck, W. R., and Qin, R. (2010). How much magma is required to rift a continent? *Earth Planet. Sci.* 292, 68–78. doi: 10.1016/j.epsl.2010.01.021

Biggs, J., Anthony, E. Y., and Ebinger, C. J. (2009). Multiple inflation and deflation events at Kenyan volcanoes, East African Rift. *Geology* 37, 979–982. doi: 10.1130/G30133A.1

Biggs, J., Bastow, I. D., Keir, D., and Lewi, E. (2011). Pulses of deformation reveal frequently recurring shallow magmatic activity beneath the Main Ethiopian Rift. *Geochem. Geophys. Geosystems*. 12, Q0AB10. doi: 10.1029/2011gc003662

Biggs, J., Chivers, M., and Hutchinson, M. C. (2013a). Surface deformation and stress interactions during the 2007-2010 sequence of earthquakes, dyke intrusion and eruption in northern Tanzania. *Geophys. J. Int.* 195, 16–26. doi: 10.1093/gji/ggt226

Biggs, J., Ebmeier, S. K., Aspinall, W. P., Lu, Z., Pritchard, M. E., Sparks, R. S. J., et al. (2014). Global link between deformation and volcanic eruption quantified by satellite imagery. *Nat. Commun.* 5:3471. doi: 10.1038/ncomms4471

Biggs, J., Nissen, E., Craig, T., Jackson, J., and Robinson, D. P. (2010). Breaking up the hanging wall of a rift-border fault: the 2009 Karonga earthquakes, Malawi. *Geophys. Res. Lett.* 37:L11305. doi: 10.1029/2010GL043179

Biggs, J., Robertson, E., and Cashman, K. (2016). The lateral extent of volcanic interactions during unrest and eruption. *Nat. Geosci.* 9, 308–311. doi: 10.1038/ngeo2658

Biggs, J., Robertson, E., and Mace, M. (2013b). "ISMER – active magmatic processes in the East African Rift: a satellite radar perspective," in *Remote*

Sensing Advances for Earth System Science, eds D. Fernandez-Prieto and R. Sabia (Berlin; Heidelberg: Springer), 81–91.

Bizouard, H., and Di Paula, G. M. (1979). "Mineralogy of the Tullu Moje active volcanic area (Arussi: Ethiopian Rift valley)," in *Petrology and Geochemistry of Continental Rifts*, eds E.-R. Neumann and I. B. Ramberg (Dordrecht: D. Reidel Co.), 87–100.

Bosworth, W., Burke, K., and Strecker, M. (2003). Effect of stress fields on magma chamber stability and the formation of collapse calderas. *Tectonics* 22, 1042. doi: 10.1029/2002TC001369

Brudy, M., Zoback, M. D., Fuchs, K., Rummel, F., and Baumgartner, J. (1997). Estimation of the complete stress tensor to 8 km depth in the KTB scientific drill holes: implications for crustal strength. *J. Geophys. Res.* 102, 18453–18475. doi: 10.1029/96JB02942

Buck, W. R. (2004). "Consequences of asthenospheric variability on continental rifting," in *Rheology and Deformation of the Lithosphere at Continental Margins,* eds G. D. Karner, B. Taylor, N. W. Driscoll, and D. L. Kohlsted (New York, NY: Columbia University Press), 1–30.

Buck, W. R. (2006). "The role of magma in the development of the Afro-Arabian Rift System," in *The Afar Volcanic Province within the East African Rift System*, eds G. Yirgu, C. J. Ebinger, and P. K. H. Maguire (London: Geological Society), 259, 43–54.

Buck, W. R., Einarsson, P., and Bransdottir, B. (2006). Tectonic stress and magma chamber size as controls on dike propagation: constraints from the 1975-1984 Krafla rifting episode. *J. Geophys. Res.* 111, B12404. doi: 10.1029/2005jb003879

Burt, M. L., Wadge, G., and Scott, W. A. (1994). Simple stochastic modelling of the eruption history of a basaltic volcano: Nyamuragira, Zaire. *Bull. Volcanol.* 56, 87–97. doi: 10.1007/BF00304104

Calais, E., d'Oreye, N., Albaric, J., Deschamps, A., Delvaux, D., Déverchère, J., et al. (2008). Strain accommodation by slow slip and dyking in a youthful continental rift, East Africa. *Nature* 456, 783–787. doi: 10.1038/nature07478

Carboni, E., Grainger, R. G., Mather, T. A., Pyle, D. M., Thomas, G., Siddans, R., et al. (2015). The vertical distribution of volcanic SO_2 plumes measured by IASI. *Atmos. Chem. Phys. Discuss.* 15, 24643–24693. doi: 10.5194/acpd-15-24643-2015

Cattin, R., Doubre, C., de Chabalier, J.-B., King, G., Vigny, C., Avouac, J.-P., et al. (2005). Numerical modelling of Quaternary deformation and post-rifting displacement in the Asal-Ghoubbet rift (Djibouti, Africa). *Earth Planet. Sci. Lett.* 239, 352–367. doi: 10.1016/j.epsl.2005.07.028

Cavendish, H. S. H. (1897). Through Somaliland and around the south of Lake Rudolf. *Geogr. J.* 11, 372–393.

Champion, A. M. (1935). Teleki's Volcano and the lava fields at the southern end of Lake Rudolf. *Geogr. J.* 85, 323–336. doi: 10.2307/1785591

Chiodini, G., Caliro, S., De Martino, P., Avino, R., and Gherardai, F. (2012). Early signals of new volcanic unrest at Campi Flegrei caldera. Insights from geochemical data and physical simulations. *Geology* 40, 943–946. doi: 10.1130/G33251.1

CNR-CNRS Afar Team (1973). Geology of northern Afar (Ethiopia). *Rev. Geog. Phys. Geol. Dynam.* 15, 443–490.

Coblentz, D. D., and Sandiford, M. (1994). Tectonic stresses in the African plate: constraints of the ambient lithospheric stress state. *Geology* 22, 831–834.

Cole, J. W. (1969). The Gariboldi volcanic complex. *Bull. Volcanol.* 33, 566–578. doi: 10.1007/BF02596525

Condomines, M., Carpentier, M., and Ongendangenda, T. (2015). Extreme radium deficit in the 1957 AD Mugogo lava (Virunga volcanic field Africa): its bearing on olivine-melilitite genesis. *Contrib. Mineral. Petrol.* 169:29 doi: 10.1007/s00410-015-1124-9

Coppola, D., Campion, R., Laiolo, M., Cuoco, E., Balgizi, C., Ripepe, M., et al. (2016). Birth of a lava lake: Nyamuragira volcano 2011-2015. *Bull. Volcanol.* 78:20. doi: 10.1007/s00445-016-1014-7

Corbi, F., Rivalta, E., Pinel, V., Maccaferri, F., Bagnardi, M., and Acocella, V. (2015). How caldera collapse shapes the shallow emplacement and transfer of magma in active volcanoes. *Earth Planet. Sci. Lett.* 431, 287–293. doi: 10.1016/j.epsl.2015.09.028

Corti, G. (2009). Continental rift evolution from rift initiation to incipient breakup in the Main Ethiopian Rift, East Africa. *Earth Sci. Rev.* 96, 1–53. doi: 10.1016/j.earscirev.2009.06.005

Corti, G. (2012). Evolution and characteristics of continental rifting: analog modeling-inspired view and comparison with examples from the East African Rift System. *Tectonophysics* 522, 1–33. doi: 10.1016/j.tecto.2011.06.010

Craig, T. J., Jackson, J. A., Priestley, K., and McKenzie, D. (2011). Earthquake distribution patterns in Africa: their relationship to variations in lithospheric and geological structure, and their rheological implications. *Geophys. J. Int.* 185, 403–434. doi: 10.1111/j.1365-246X.2011.04950.x

Dahm, T. (2000). Numerical simulations of the propagation path and the arrest of fluid-filled fractures in the Earth. *Geophys. J. Int.* 141, 623–638. doi: 10.1046/j.1365-246x.2000.00102.x

De Chabalier, J.-B., and Avouac, J.-P. (1994). Kinematics of the Asal rift (Djibouti) determined from the deformation of Feale Volcano. *Science* 265, 1677–1681. doi: 10.1126/science.265.5179.1677

Delvaux, D., and Barth, A. (2009). African stress pattern from formal inversion of focal mechanism data. *Tectonophysics* 482, 105–129. doi: 10.1016/j.tecto.2009.05.009

Dodson, R. G. (1963). The geology of the South Horr area. *Rep. Geol. Surv. Kenya* 60, 1–53.

Doubre, C., Manighetti, I., Dorbath, L., Dorbath, C., Bertil, D., and Delmond, J. C. (2007). Crustal structure and magmato-tectonic processes in an active rift (Asal-Ghoubbet, Afar, East Africa): 2. Insights from the 23-year recording of seismicity since the rifting event. *J. Geophys. Res*. 112:B05406. doi: 10.1029/2006 JB004333

Doubre, C., and Peltzer, G. (2007). Fluid-controlled faulting processes in the Asal-Rift, Djibouti, from 8-yr of radar interferometry observations. *Geology* 35, 69–72. doi: 10.1130/G23022A.1

Dunkley, P. N., Smith, M., Allen, D. J., and Darling, W. G. (1993). The geothermal activity and geology of the northern section of the Kenya Rift Valley. *Br. Geol. Surv. Res. Rep.* SC/93/1, 1–185.

Ebinger, C. J. (1989). Geometric and kinematic development of border faults and accommodation zones, Kivu-Rusizi Rift, Africa. *Tectonics* 8, 117–133. doi: 10.1029/TC008i001p00117

Ebinger, C. J. (2005). Continental break-up: the East African perspective. *Astron. Geophys.* 46, 2–16. doi: 10.1111/j.1468-4004.2005.46216.x

Ebinger, C. J. (2012). "Evolution of the Cenozoic East African Rift System: cratons, plumes and continental breakup," in *Regional Geology and Tectonics. Phanerozoic Rift Systems and Sedimentary Basins*, eds D. G. Robson and A. W. Bally (Amsterdam: Elsevier), 133–156.

Ebinger, C. J., Ayele, A., Keir, D., Rowland, J., Yirgu, G., Wright, T., et al. (2010). Length and timescales of rift faulting and magma intrusion: the Afar rifting cycle from 2005 to present. *Annu. Rev. Earth Planet. Sci.* 38, 439–466. doi: 10.1146/annurev-earth-040809-152333

Ferguson, D. J., Barnie, T. D., Pyle, D. M., Oppenheimer, C., Yirgu, G., Lewi, E., et al. (2010). Recent rift-related volcanism in Afar, Ethiopia. *Earth Planet. Sci. Lett.* 292, 409–418. doi: 10.1016/j.epsl.2010.02.010

Fernandez-Alonso, M., and Theunissen, K. (1998). Airborne geophysics and geochemistry provide new insights in the intracontinental evolution of the Mesoproterozoic Kibaran belt (Central Africa). *Geol. Mag.* 135, 203–216. doi: 10.1017/S0016756898008310

Field, L., Barnie, T., Blundy, J., Brooker, R. A., Keir, D., Lewi, E., et al. (2012). Integrated field satellite and petrological observations of the November 2010 eruption of Erta Ale. *Bull. Volcanol.* 74, 2251–2271. doi: 10.1007/s00445-012-0660-7

Fontijn, K., Delvaux, D., Ernst, G. G. J., Kervyn, M., Mbede, E., and Jacobs, P. (2010). Tectonic control over active volcanism at a range of scales: case of the Rungwe Volcanic Province, SW Tanzania; and hazard implications. *J. Afr. Earth Sci.* 5, 764–777. doi: 10.1016/j.jafrearsci.2009.11.011

Fontijn, K., Williamson, D., Mbede, E., and Ernst, G. G. J. (2012). The Rungwe Volcanic Province, Tanzania – a volcanological review. *J. Afr. Earth Sci.* 63, 12–31. doi: 10.1016/j.jafrearsci.2011.11.005

Gibson, I. L. (1974). A review of the geology, petrology and geochemistry of the Volcano Fantale. *Bull. Volcanol.* 38, 791–802. doi: 10.1007/BF02596908

Goitom, B., Oppenheimer, C., Hammond, J. O., Grandin, R., Barnie, T., Donovan, A., et al. (2015). First recorded eruption of Nabro volcano, Eritrea, 2011. *Bull. Volcanol.* 77:85. doi: 10.1007/s00445-015-0966-3

Gouin, P. (1979). *Earthquake History of Ethiopia and the Horn of Africa*. Ottawa: International Development Research Centre.

Grandin, R., Socquet, A., Binet, R., Klinger, Y., Jacques, E., de Chabalier, J.-B., et al. (2009). September 2005 Manda Hararo-Dabbahu rifting event, Afar (Ethiopia): constraints provided by geodetic data. *J. Geophys. Res.* 114:B08404. doi: 10.1029/2008JB005843

Gudmundsson, A. (2000). Dynamics of volcanic systems in Iceland: example of tectonism and volcanism at juxtaposed hot spot and mid-ocean ridge systems. *Annu. Rev. Earth Planet. Sci.* 28, 107–140. doi: 10.1146/annurev.earth.28.1.107

Gudmundsson, A. (2003). Surface stresses associated with arrested dykes in rift zones. *Bull. Volcanol.* 65, 606–619. doi: 10.1007/s00445-003-0289-7

Gudmundsson, A. (2006). How local stresses control magma chamber ruptures, dyke injections, and eruptions in composite volcanoes. *Earth Sci. Rev.* 79, 1–31. doi: 10.1016/j.earscirev.2006.06.006

Gudmundsson, A. (2011a). Deflection of dykes into sills at discontinuities and magma chamber formation. *Tectonophysics* 500, 50–64. doi: 10.1016/j.tecto.2009.10.015

Gudmundsson, A. (2011b). *Rock Fractures in Geological Processes*. Cambridge: Cambridge University Press.

Gudmundsson, A. (2012). Magma chambers:formation,local stresses, excess pressures, and compartments. *J. Volcanol. Geotherm. Res.* 237–238, 19–41.

Gudmundsson, A., and Philipp, S. J. (2006). How local stress fields prevent volcanic eruptions. *J. Volcanol. Geotherm. Res.* 158, 257–268. doi: 10.1016/j.jvolgeores.2006.06.005

Gudmundsson, A., Simmenes, T. H., Larsen, B., and Philipp, S. L. (2010). Effects of internal structure and local stresses on fracture propagation, deflection and arrest in fault zones. *J. Struct. Geol.* 32, 1643–1655. doi: 10.1016/j.jsg.2009.08.013

Hamling, I. J., Ayele, A., Bennati, L., Calais, E., Ebinger, C. J., Keir, D., et al. (2009). Geodetic observations of the ongoing Dabbahu rifting episode: new dyke intrusions in 2006 and 2007. *Geophys. J. Int.* 178, 989–1003. doi: 10.1111/j.1365-246X.2009.04163.x

Hamlyn, J. E., Keir, D., Wright, T. J., Neuberg, J. W., Goitom, B., Hammond, J. O. S., et al. (2014). Seismicity and subsidence following the 2011 Nabro eruption, Eritrea: insights into the plumbing system of an off-rift volcano. *J. Geophys. Res. Solid Earth* 119, 8267–8282. doi: 10.1002/2014JB011395

Hammond, J. O. S. (2014). Constraining melt geometries beneath the Afar Depression, Ethiopia from teleseismic receiver functions: the anisotropic H-k stacking technique. *Geochem. Geophys. Geosyst.* 15, 1316–1332. doi: 10.1002/2013gc005186

Hammond, J. O. S., Kendall, J.-M., Wookey, J., Sturat, G. W., Keir, D., and Ayele, A. (2014). Differentiating flow, melt or fossil seismic anisotropy beneath Ethiopia. *Geochem. Geophys. Geosyst.* 15, 1878–1894. doi: 10.1002/2013gc005185

Harkin, D. A. (1960). The Rungwe volcanics at the northern end of Lake Nyasa. *Geol. Survey Tanganyika Memoir* II, 172.

Harris, A. J. L., Dehn, J., and Calvari, S. (2007). Lava effusion rate definition and measurement: a review. *Bull. Volcanol.* 70, 1–22. doi: 10.1007/s00445-007-0120-y

Harris, W. C. (1844). *The Highlands of Ethiopia, Vol. III*. London: Longman, Brown, Green, Longmans.

Heidbach, O., Tingay, M., Barth, A., Reinecher, J., Kurfess, J., and Muller, B. (2010). Global crustal stress pattern based on the World Stress Map database release 2008. *Tectonophysics* 482, 3–15. doi: 10.1016/j.tecto.2009.07.023

Hutchison, W., Mather, T. A., Pyle, D. M., Biggs, J., and Yirgu, G. (2015). Structural controls on fluid pathways in an active rift system: a case study of the Aluto volcanic complex. *Geosphere* 11, 542–562. doi: 10.1130/GES01119.1

Isola, I., Mazzarini, F., Bonini, M., and Corti, G. (2014). Spatial variability of volcanic features in early-stage rift settings: the case of the Tanzanian Divergence, East African rift system. *Terra Nova* 26, 461–468. doi: 10.1111/ter.12121

Karingithi, C. W., Arnorsson, S., and Gronvold, K. (2010). Processes controlling aquifer fluid compositions in the Olkaria geothermal system, Kenya. *J. Volcanol. Geotherm. Res.* 196, 57–56. doi: 10.1016/j.jvolgeores.2010.07.008

Keir, D., Bastow, I. D., Corti, G., Mazzarini, F., and Rooney, T. O. (2015). The origin of along-rift variations in faulting and magmatism in the Ethiopian Rift. *Tectonics* 34, 464–477. doi: 10.1002/2014TC003698

Keir, D., Belachew, M., Ebinger, C. J., Kendall, J.-M., Hammond, J. O. S., Stuart, G. W., et al. (2011a). Mapping the evolving strain field during continental breakup from crustal anisotropy in the Afar Depression. *Nat. Commun.* 2:285. doi :10.1038/ncomms1287

Keir, D., Pagli, C., Bastow, I. D., and Ayele, A. (2011b). The magma assisted removal of Arabia in Afar: evidence from dike injection in the Ethiopian rift captured using InSAR and seismicity. *Tectonics* 30:TC2008. doi: 10.1029/2010TC002785

Kendall, J.-M., and Lithgow-Bertelloni, S. (2016). Why is Africa rifting? *Geol. Soc. Lond.* 420, 11–30. doi: 10.1144/SP420.17

Kendall, J.-M., Stuart, G. W., Ebinger, C. J., Bastow, I. D., and Keir, D. (2005). Magma-assisted rifting in Ethiopia. *Nature* 433, 146–148. doi: 10.1038/nature03161

Kervyn, M., Ernst, G. G. J., van Wyk de Vries, B., Mathieu, L., and Jacobs, P. (2009). Volcano load control on dyke propagation and vent distribution: insights from analogue modeling. *J. Geophys. Res.* 114:B03401. doi: 10.1029/2008jb005653

Kervyn, M., Ernst, G. J., Keller, J., Vaughan, R. G., Klaudius, J., Pradal, E., et al. (2010). Fundamental changes in the activity of the natrocarbonatite volcano Oldoinyo Lengai, Tanzania: eruptive behaviour during the 2007-2008 explosive eruptions. *Bull. Volcanol.* 72, 913–931. doi: 10.1007/s00445-010-0360-0

Komorowski, J.-C., Tedesco, D., Kasereka, M., Allard, P., Papale, P., Vaselli, O., et al. (2002). The January 2002 flank eruption of the Nyiragongo Volcano (Democratic Republic of Congo): chronology, evidence for a tectonic rift trigger and impact of lava flows on the city of Goma. *Acta Vulcanol.* 14, 27–62. doi: 10.1400/19077

Koptev, A., Calais, E., Burov, E., Leroy, S., and Gerya, T. (2015). Dual continental rift systems generated by plume-lithosphere interaction. *Nat. Geosci.* 8, 388–392. doi: 10.1038/ngeo2401

Maccaferri, F., Acocella, V., and Rivalta, E. (2015). How the differential load induced by normal fault scarps controls the distribution of monogenetic volcanism. *Geophys. Res. Lett.* 42, 7507–7512. doi: 10.1002/2015GL065638

Maccaferri, F., Bonafede, M., and Rivalta, E. A. (2011). A quantitative study of the mechanisms governing dike propagation, dike arrest and sill formation. *J. Volcanol. Geotherm. Res.* 208, 39–50. doi: 10.1016/j.jvolgeores.2011.09.001

Maccaferri, F., Rivalta, E., Keir, D., and Accocella, V. (2014). Off-rift volcanism in rift zones determined by crustal unloading. *Nat. Geosci.* 7, 297–300. doi: 10.1038/ngeo2110

Marshall, A. S., Macdonald, R., Rogers, N. W., Fitton, J. G., Tindel, A. G., Nejbert, K., et al. (2009). Fractionation of peralkaline silicic magma: the Greater Olkaria Volcanic Complex, Kenya Rift Valley. *J. Petrol.* 50, 323–359. doi: 10.1093/petrology/egp001

Mazzarini, F., Keir, D., and Isola, I. (2013). Spatial relationship between earthquakes and volcanic vents in the central-northern Main Ethiopian Rift. *J. Volcanol. Geotherm. Res.* 262, 123–133. doi: 10.1016/j.jvolgeores.2013.05.007

McClusky, S., Reilinger, R., Ogubazhgi, G., Amelson, A., Healeb, B., Vernant, P., et al. (2010). Kinematics of the southern Red Sea-Afar triple junction and implications for plate dynamics. *Geophys. Res. Lett.* 37:L05301. doi: 10.1029/2009gl041127

McGarr, A., and Gay, N. C. (1978). State of stress in the Earth's crust. *Annu. Rev. Earth Planet. Sci.* 6, 405–436. doi: 10.1146/annurev.ea.06.050178.002201

Mogi, K. (1958). Relations between eruptions of various volcanoes and the deformations of the ground surfaces around them. *Bull. Earthq. Res. Inst.* 36, 99–134.

Mohr, P. (1978). Afar. *Annu. Rev. Earth Planet. Sci.* 6, 145–172. doi: 10.1146/annurev.ea.06.050178.001045

Morley, C. K., Nelson, R. A., Patton, T. L., and Munn, S. G. (1990). Transfer zones in the East African Rift System and their relevance to hydrocarbon exploration in rifts. *Bull. Am. Assoc. Petrol. Geologists* 74, 1234–1253.

Muirhead, J. D., Kattenhorn, S. A., and Le Corvec, N. (2015). Varying styles of magmatic strain accommodation across the East African Rift. *Geochem. Geophys. Geosystems* 16, 2775–2795. doi: 10.1002/2015gc005918

Muller, O. H., and Pollard, D. D. (1977). The stress state near Spanish Peaks, Colorado, determined from a dike pattern. *Pure Appl. Geophys.* 115, 69–86. doi: 10.1007/BF01637098

Nakamura, K. (1977). Volcanoes as possible indicators of tectonic stress orientation – principle and proposal. *J. Volcanol. Geotherm. Res.* 2, 1–16. doi: 10.1016/0377-0273(77)90012-9

Nobile, A., Pagli, C., Keir, D., Wright, T. J., Ayele, A., Ruch, J., et al. (2012). Dike-fault interaction during the 2004 Dallol intrusion at the northern edge of the Erta Ale Ridge (Afar, Ethiopia). *Geophys. Res. Lett.* 39:L19305. doi: 10.1029/2012gl053152

Nowacki, A., Wilks, M., Kendall, J.-M., Biggs, J., Ayele, A., Tulu, B., et al. (2016). *Identifying Deformation Styles and Causes at Two Deforming Volcanoes of the Central Main Ethiopian Rift with Seismic Anisotropy* (Vienna: EGU), EGU2016-11592.

Oppenheimer, C., and Francis, P. (1998). Implications of longeval lava lakes for geomorphological and plutonic processes at Erta 'Ale volcano, Afar. *J. Volcanol. Geotherm. Res.* 80, 101–111. doi: 10.1016/S0377-0273(97)00041-3

Pagli, C., Wang, H., Wright, T. J., Calais, E., and Lewi, E. (2014). Current plate boundary deformation of the Afar rift from a 3-D velocity field inversion of InSAR and GPS. *J. Geophys. Res. Solid Earth* 119, 8562–8575. doi: 10.1002/2014JB011391

Pagli, C., Wright, T. J., Ebinger, C., Yun, S.-H., Cann, J. R., Barnie, T., et al. (2012). Shallow axial magma chamber at the slow spreading Erta Ale Ridge. *Nat. Geosci.* 5, 284–288. doi: 10.1038/ngeo1414

Pinel, V., and Jaupart, C. (2000). The effect of edifice load on magma ascent beneath a volcano. *Phil. Trans. R. Soc. A* 358, 1515–1532. doi: 10.1098/rsta.2000.0601

Rivalta, E., Taisne, B., Bunger, A. P., and Katz, R. F. (2015). A review of mechanical models of dyke propagation: schools of thought, results and future directions. *Tectonophysics* 638, 1–42. doi: 10.1016/j.tecto.2014.10.003

Robertson, E. A. M., Biggs, J., Cashman, K. V., and Floyd, M. A., Vye-Brown, C. (2015). "Influence of regional tectonics and pre-existing structures on the formation of elliptical calderas in the Kenyan Rift," in *Magmatic Rifting and Active Volcanism*, eds T. J. Wright, A. Ayele, D. J. Ferguson, T. Kidane, and C. Vye-Brown (London: Geological Society), 420.

Roman, A., and Jaupart, C. (2014). The impact of a volcanic edifice on intrusive and eruptive activity. *Earth. Planet. Sci. Lett.* 408, 1–8. doi: 10.1016/j.epsl.2014.09.016

Sachau, T., Koehn, D., Stamps, D. S., and Lindenfeld, M. (2015). Fault kinematics and stress fields in the Ruwenzori Mountains, Uganda. *J. Int. Earth Sci*. 105, 1729–1740. doi: 10.1007/s00531-015-1162-6

Saria, E., Calais, E., Stamps,. D. S., Delvaux, D., and Hartnady, C. J. H. (2014). Present-day kinematics of the East African Rift. *J. Geophys. Res.* 119, 3584–3600. doi: 10.1002/2013JB010901

Savage, M. K., Ohminato, T., Aoki, Y., Tsuji, H., and Greve, S. M. (2010). Stress magnitude and its temporal variation at Mt. Asama Volcano, Japan, from seismic anisotropy. *Earth Planet. Sci. Lett.* 290, 403–414. doi: 10.1016/j.epsl.2009.12.037

Savin, G. N. (1961). *Stress Concentration around Holes*. New York, NY: Pergamon.

Sawyer, G. M., Oppenheimer, C., Tsanev, V. I., and Yirgu, G. (2008). Magmatic degassing at Erta 'Ale volcano, Ethiopia. *J. Volcanol. Geotherm. Res.* 178, 837–846. doi: 10.1016/j.jvolgeores.2008.09.017

Scoon, R. (2015). Geotraveller 21: Tsavo, Chyulu Hills and Amboseli, Kenya: ancient landscapes and young volcanism. *Geobulletin Geol. Soc. South Afr.* 58, 45–51. doi: 10.13140/RG.2.1.3634.3206

Scott, S. (1980). The geology of Longonot volcano, central Kenya: a question of volumes. *Phil. Trans. R. Soc. Lond. A* 296, 437–465. doi: 10.1098/rsta.1980.0188

Sealing, C. R. (2013). *Characterizing the First Historic Eruption of Nabro Eritrea: Insights from Thermal and UV Remote Sensing.* Master's thesis, Michigan Technological University. Available online at: digitalcommons.mtu.edu/etds/646

Segall, P. (2010). *Earthquake and Volcano Deformation*. Princeton: Princeton University Press.

Skinner, N. J., Iles, W., and Brock, A. (1975). The secular variation of declination and inclination in Kenya. *Earth Planet. Sci. Lett.* 25, 338–346. doi: 10.1016/0012-821X(75)90251-4

Smets, B., Wauthier, C., and d'Oreye, N. (2010). A new map of the lava flow field of Nyamuragira (D.R.Congo) from satellite imagery. *J. Afr. Earth Sci.* 58, 778–786. doi: 10.1016/jafrearsci.2010.07.005

Spacapan, J. B., Galland, O., Leanza, H. A., and Planke, S. (2016). Control of strike-slip fault on dyke emplacement and morphology. *J. Geol. Soc*. 173, 573–576. doi: 10.1144/jgs2015-166

Spath, A., Le Roex, A. P., and Opiyo-Akech, N. (2000). The petrology of the Chyulu Hills Volcanic Province, southern Kenya. *J. Afr. Earth Sci*. 31, 337–358. doi: 10.1016/S0899-5362(00)00092-0

Stamps, D. S., Flesch, L. M., and Calais, E. (2010). Lithospheric buoyancy forces in Africa from a thin sheet approach. *Int. J. Earth Sci.* 99, 1525–1533. doi: 10.1007/s00531-010-0533-2

Stamps, D. S., Flesch, L. M., Calais, E., and Ghosh, A. (2014). Current kinematics and dynamics of Africa and the East African Rift System. *J. Geophys. Res. Solid Earth* 119, 5161–5186. doi: 10.1002/2013JB010717

Szpak, Z. L., Chojnacki, W., and van den Hengel, A. (2015). Guaranteed ellipse fitting with a confidence region and n uncertainty measure for centre, axes and orientation. *J. Math. Imaging Vis.* 52, 173–199. doi: 10.1007/s10851-014-0536-x

Tarantola, A., Ruegg, J.-C., and Lepine, J. C. (1979). Geodetic evidence for rifting in Afar: a brittle-elastic model of the behaviour of the lithosphere. *Earth Planet. Sci. Lett.* 45, 435–444. doi: 10.1016/0012-821X(79)90142-0

Tazieff, H. (1977). An exceptional eruption: Mt. Nyiragongo, January 10th, 1977. *Bull. Volcanol*. 40, 1–12. doi: 10.1007/BF02596999

Tedesco, D., Vaselli, O., Papale, P., Carn, S. A., Voltaggio, M., Sawyer, G. M., et al. (2007). January 2002 volcano-tectonic eruption of Nyiragongo volcano, Democratic Republic of Congo. *J. Geophys. Res.* 112:B09202. doi: 10.1029/2006JB004762

Thompson, A. O. and Dodson, R. G. (1963). Geology of the Naivasha area. *Rep. Geol. Surv. Kenya* 55, 1–80.

Tibaldi, A. (2015). Structure of volcano plumbing systems: a review of multi-parametric effects. *J. Volcanol. Geotherm. Res.* 298, 85–135. doi: 10.1016/j.jvolgeores.2015.03.023

Tibaldi, A., Bonali, F. L., and Corazzato, C. (2014). The diverging volcanic rift system. *Tectonophysics* 611, 94–113. doi: 10.1016/j.tecto.2013.11.023

Toombs, A., and Wadge, G. (2012). Co-eruptive and inter-eruptive surface deformation measured by satellite radar interferometry at Nyamuragira volcano, D.R.Congo, 1996 to 2010. *J. Volcanol. Geotherm. Res.* 245–246, 98–122. doi: 10.1016/j.jvolgeores.2012.07.005

Tuckwell, G., Bull, J., and Sanderson, D. (1996). Models of fracture orientation at oblique spreading centres. *J. Geol. Soc. Lond.* 153, 185–189. doi: 10.1144/gsjgs.153.2.0185

Vellutini, P. (1990). The Manda-Inakir Rift, Republic of Djibouti: a comparison with the Asal Rift and its geodynamic interpretation. *Tectonophysics* 172, 141–153. doi: 10.1016/0040-1951(90)90065-G

Wadge, G., and Burt, L. (2011). Stress field control of eruption dynamics at a rift volcano: Nyamuragira, D.R.Congo. *J. Volcanol. Geotherm. Res.* 207, 1–15. doi: 10.1016/j.jvolgeores.2011.06.012

Walker, K. T., Nyblade, A. A., Klemperer, S. L., Bokelmann, G. H., and Owens, T. J. (2004). On the relationship between extension and anisotropy: constraints from shear wave splitting across the East African Plateau. *J. Geophys. Res. Solid Earth* 109:B08302. doi: 10.1029/2003jb002866

Wauthier, C., Cayol, V., Kervyn, F., and d'Oreye, N. (2012). Magma sources involved in the 2002 Nyiragongo eruption, as inferred from an InSAR analysis. *J. Geophys. Res.* 117:B05411. doi: 10.1029/2011JB008257

Wauthier, C., Cayol, V., Poland, M., Kervyn, F., d'Oreye, N., Hooper, A., et al. (2013). "Nyamulagira's magma plumbing system inferred from 15 years of InSAR," in *Remote Sensing of Volcanoes and Volcanic Processes: Integrating Observations and Modelling*, eds D. M. Pyle, T. A. Mather, and J. Biggs (London: Geological Society), 380.

Wiart, P. A. M., Oppenheimer, C., and Francis, P. (2000). Eruptive history of Dubbi volcano, northeast Afar (Eritrea), revealed by optical and SAR image interpretation. *Int. J. Remote Sens.* 21, 911–936. doi: 10.1080/014311600210353

Wiart, P., and Oppenheimer, C. (2000a). Largest known historical eruption in Africa: Dubbi volcano, Eritrea, 1861. *Geology* 28, 291–294. doi: 10.1130/0091-7613(2000)28<291:LKHEIA>2.0.CO;2

Wiart, P., and Oppenheimer, C. (2000b). Large magnitude silicic volcanism in north Afar: the Nabbro Volcanic Range and Ma'alatta volcano. *Bull. Volcanol.* 67, 99–115. doi: 10.1007/s00445-004-0362-x

Wood, D. A., Zal, H. J., Scholz, C. A., Ebinger, C. J., and Nizere, I. (2015). Evolution of the Kivu Rift, East Africa: interplay among tectonics, sedimentation and magmatism. *Basin Res*. doi: 10.1111/bre.12143. [Epub ahead of print].

Wright, T. J., Ebinger, C., Biggs, J., Ayele, A., Yirgu, G., Keir, D., et al. (2006). Magma-maintained rift segmentation at continental rupture in the 2005 Afar dyking episode. *Nature* 442, 291–294. doi: 10.1038/nature04978

Xu, W., and Jonsson, S. (2014). The 2007-8 volcanic eruption on Jebel at Tair island (Red Sea) observed by satellite radar and optical images. *Bull. Volcanol.* 76:795. doi: 10.1007/s00445-014-0795-9

Zal, H. J., Wood, D. A., Ebinger, C. J., Scholz, C. A., d'Oreye, N., Carn, S. A., et al. (2014). Kinematics and dynamics of the Kivu Rift System from seismic anisotropy, seismicity and structural analyses [Abstract]. *AGU Fall Meeting 2014 abstract T53B-4676*.

Conflict of Interest Statement: The authors declare that the research was conducted in the absence of any commercial or financial relationships that could be construed as a potential conflict of interest.

frontiers in Earth Science

ORIGINAL RESEARCH
published: 17 November 2016
doi: 10.3389/feart.2016.00099

Orientation of the Eruption Fissures Controlled by a Shallow Magma Chamber in Miyakejima

Nobuo Geshi * *and Teruki Oikawa*

Institute of Earthquake and Volcano Geology, Geological Survey of Japan, National Institute of Advanced Industrial Science and Technology (AIST), Tsukuba, Japan

Orientation of the eruption fissures and composition of the lavas of the Miyakejima volcano is indicative of the competitive processes of the regional tectonic stress and the local stress generated by the activity of a magma plumbing system beneath the volcano. We examined the distributions and magmatic compositions of 23 fissures that formed within the last 2800 years, based on a field survey and a new dataset of ^{14}C ages. The dominant orientation of the eruption fissures in the central portion of the volcano was found to be NE-SW, which is perpendicular to the direction of regional maximum horizontal compressive stress (σ_{Hmax}). Magmas that show evidence of mixing between basaltic and andesitic compositions erupted mainly from the eruption fissures with a higher offset angle from the regional σ_{Hmax} direction. The presence of a dike pattern perpendicular to the direction of maximum compression σ_{Hmax} is an unusual and uncommon feature in volcanoes. Here we investigate the conditions possibly controlling this unexpected dike pattern. The distribution and magmatic compositions of the eruption fissures in Miyakejima volcano highlight the tectonic influence of shallow magma chamber on the development of feeder dikes in a composite volcano. The presence of a shallow dike-shaped magma chamber controls the eccentric distribution of the eruption fissures perpendicular to the present direction of σ_{Hmax}. The injection of basaltic magma into the shallow andesitic magma chamber caused the temporal rise of internal magmatic pressure in the shallow magma chamber which elongates in NE-SW direction. Dikes extending from the andesitic magma chamber intrude along the local stress field which is generated by the internal excess pressure of the andesitic magma chamber. As the result, the eruption fissures trend parallel to the elongation direction of the shallow magma chamber. Some basaltic dikes from the deep-seated magma chamber reach the ground surface without intersection with the andesitic magma chamber. These basaltic dikes develop parallel to the regional compressive stress in NW-SE direction. The patterns of the eruption fissures can be modified in the future as was observed in the case of the destruction of the shallow magma chamber during the 2000 AD eruption.

Keywords: fissure eruption, feeder dike, magma chamber, local stress, Miyakejima

Edited by:
Roberto Sulpizio,
University of Bari, Italy

Reviewed by:
Alessandro Tibaldi,
University of Milano-Bicocca, Italy
Thomas R. Walter,
GFZ Potsdam, Germany

Correspondence:
Nobuo Geshi
geshi-nob@aist.go.jp

Specialty section:
This article was submitted to
Volcanology,
a section of the journal
Frontiers in Earth Science

Received: *28 April 2016*
Accepted: *31 October 2016*
Published: *17 November 2016*

Citation:
Geshi N and Oikawa T (2016)
Orientation of the Eruption Fissures
Controlled by a Shallow Magma
Chamber in Miyakejima.
Front. Earth Sci. 4:99.
doi: 10.3389/feart.2016.00099

INTRODUCTION

Propagation of a dike is controlled by the stress field in its host rock; the orientation of a dike is basically parallel to the maximum compressive axis (σ1) and perpendicular to the minimum compressive axis (σ3). Therefore, the orientation of dikes has been used as an indicator of the stress field in volcanic fields (Nakamura, 1977; Yamaji and Sato, 2011). Dikes will be oriented parallel to the maximum stress axis in a homogeneous stress field. However, the distribution of dikes and eruption fissures in volcanoes display radial, circumferential, and curvature patterns reflecting the local stress in the volcanic edifice (e.g., Chadwick and Howard, 1991). Local disturbances in the stress field of a volcano are caused by the prominent topography of a volcanic edifice (e.g., Tibaldi et al., 2014), flank instability (e.g., Walter et al., 2005), unloading by collapse (Corbi et al., 2015), active faults near the volcanic system (e.g., Seebeck and Nicol, 2009), mechanical heterogeneity in the volcanic edifice and basement (e.g., Letourneur et al., 2008), and the magmatic activity within the volcano (e.g., Chadwick and Dieterich, 1995; Takada, 1997). Recent observations of the dike intrusion events reveal that the stress field in the host rock is affected by the emplacement of intrusions, and consequently feedbacks to the growth of the next dikes (e.g., Bagnardi et al., 2013; Falsaperla and Neri, 2015).

The local pressure source within a volcano is one of the major causes of a local disturbance in the stress field within the volcano (Gudmundsson, 2006). Magma injection into a local magma reservoir results in a rise of magma pressure, and it consequently has a strong influence on the distribution pattern of an eruptive fissure (e.g., Tibaldi, 2015 and the references therein). Therefore, utilizing the knowledge of local disturbances in a stress field within a volcano, we can predict the distribution pattern of fissure eruptions.

Predicting the distribution pattern of flank fissure eruptions is not only pertinent to volcanology but is also of critical importance to hazard management. As the site and orientation of fissure eruptions are controlled by the orientation and propagation direction of the feeder dikes, understanding of the stress field within a volcano and the propagation direction of feeder dikes are crucial to evaluating the risk of flank fissure eruptions (e.g., Gudmundsson, 2006). Flank fissure eruptions are one of the major causes of volcanic disasters (Cappello et al., 2015).

The distribution of the flank fissure eruptions in Miyakejima Island is indicative of the competitive processes of the regional tectonic stress and the local stress generated by the activity of a magma plumbing system beneath the volcano (Nakamura, 1977). The development of a rift zone perpendicular to the regional horizontal compressive axis (σ_{Hmax}) provides a good example of the role of a local stress field within the volcanic edifice on the distribution of the eruption fissures. A combination of the inferences made from geological and petrological investigations and the observations from a recent caldera collapse event reveal the influence of shallow magma chambers on the development of eruption fissures. Here, we examined the distribution patterns of recent eruption fissures, with a new dataset of ^{14}C ages and petrological analysis to reveal the influence of a shallow magma chamber.

BACKGROUND OF MIYAKEJIMA

Tectonic Setting

The northernmost part of the Izu-Bonin volcanic arc, including Miyakejima, is compressed in the NW-SE direction owing to the subduction of the Philippine Sea Plate to the Eurasian Plate (**Figure 1A**). The orientations of several volcanic chains in the northernmost part of the Izu-Bonin volcanic arc are consistent with the NW-SE compression in this area (Nakamura, 1977). Focal mechanisms of the earthquakes in the vicinity of Miyakejima also indicate that the σ_{Hmax} is aligned in the NW-SE direction and σ_{Hmin} in the NE-SW direction (Nishimura, 2011). Orientations of volcanic fissures in the Izu-Tobu monogenic volcanoes, ∼100 km north of Miyakejima, are predominantly NW-SE (Koyama and Umino, 1991). The Izu-Oshima volcano, ∼60 km north of Miyakejima, also has volcanic chains on its flank trending in the WNW-ESE direction in the northwestern flank and in the NW-SE direction in the southeastern flank (Ishizuka et al., 2014). The Hachijojima volcano, ∼100 km south of Miyakejima, has volcanic chains trending in the NW-SE direction (Ishizuka et al., 2008). A regional dike trending in the N45°W direction intruded the submarine area between Miyakejima Island and Kozushima Island during the 2000 AD eruption (**Figure 1A**: Ito and Yoshida, 2002; Yamaoka et al., 2005).

The dominant orientation of the eruption fissures in the Miyakejima volcano is, however, different from its neighboring volcanoes (Nakamura, 1977). The eruption fissures in the Miyakejima volcano are concentrated in the NE-SW direction near the summit, giving rise to a NE-SW rift zone (**Figure 1B**). The eruption fissures tend to curve to trend in the NW-SE direction in the coastal, peripheral part of the island (Nakamura, 1977; Aramaki et al., 1986).

Geology

The Miykejima volcano is a basaltic–andesitic composite volcano sitting on the Izu-Bonin volcanic arc on the Philippine Sea Plate (**Figure 1A**). Miyakejima has a conical volcanic edifice, which extends ∼700 m high above sea level and ∼500 m below sea level (**Figure 1B**). Four eruptions were recorded in the last 100 years, two in the northeastern flank (the 1940 and 1962 eruptions) and two in the southwestern flank (the 1983 eruption and the 2000 submarine eruption).

The development of chains of scoria cones on the flanks of the island indicates the frequent lateral fissure eruptions during the development of the volcano (Tsukui and Suzuki, 1999). Though fissure eruptions occurred throughout the history of the volcano, we focused on the fissure eruptions after the formation of Hachodaira caldera because the formation of the Hachodaira caldera is one of the key events in the development of the volcano. Phreatomagmatic eruptions during the caldera formation produced the Hachodaira ash layer, which provides good key bed in all part of the island. Our new ^{14}C data indicate that the Hachodaira caldera was formed at 2700–2800 years ago.

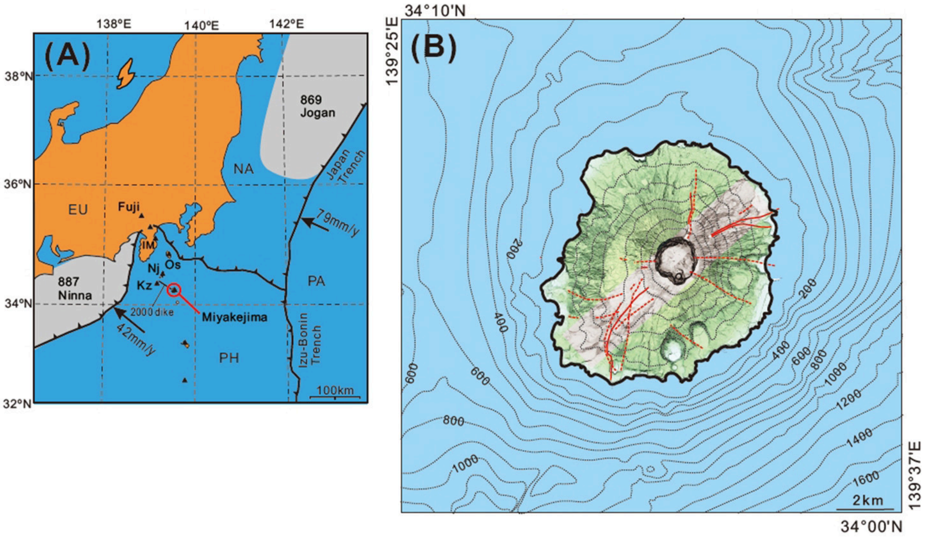

FIGURE 1 | (A) Tectonic setting of the Miyakejima Island. PH, Philippine Sea Plate; PA, Pacific Plate; NA, North America Plate; EU, Eurasia Plate Arrows indicate the direction and speed of the subduction at the trench. Solid triangles show the location of active volcanoes. IM, Izu-Tobu Monogenetic Volcanoes; Os, Izu-Oshima; Nj, Niijima; Kz, Kozushima. Gray areas show the approximate source area of the 869AD Jogan earthquake and the 887AD Ninna-Nankai earthquake. **(B)** Distribution of the eruption fissures. Solid red lines show the eruption fissure in the nineteenth and twentieth centuries. Historical records confirm their ages. Broken red lines show the eruption fissures younger than the seventh century. Their ages are suggested by the ^{14}C age. The shadowed area shows the approximate area of the NE-SW rift zone. Counters are 100 m interval.

A new collapse caldera, which is 1.7 km across, was formed at the summit during the 2000 AD eruption due to the draining of the shallow andesitic magma chamber through a large lateral intrusion (Geshi et al., 2002). Temporal changes of the juvenile material during the eruption show that the dike intrusion to the northwest of the island withdrew andesitic magma from a shallow chamber, which was then replaced by basaltic magma in the later stage of eruption (Geshi et al., 2002).

Magma Plumbing System

The magmas that erupted from Miyakejima volcano within the last 2800 years have been basaltic to andesitic in composition, with whole-rock SiO_2 contents ranging from 50 to 62 wt% (**Figure 2**). The disequilibrium mineral assemblage and the wide and linear variations of the whole-rock composition of the basaltic-andesite of Miyakejima indicate mixing between the basaltic and andesitic end components (Amma-Miyasaka and Nakagawa, 2003; Kuritani et al., 2003). Judging by the narrow diffusion texture at the rim of the olivine phenocrysts, magma mixing occurred just before the eruption (Niihori et al., 2003).

The basaltic magma, which is fed from the deeper chamber, has the whole-rock SiO_2 content of ~50–51 wt%. Equilibrium relationships between minerals and the groundmass suggest that the less-fractionated magmas with basaltic compositions are stored in a magma chamber at around ~200 MPa. Whereas the fractionating magmas with andesitic compositions are stored at a shallower depth at around ~100 MPa (Kuritani et al., 2003; Amma-Miyasaka et al., 2005). These pressures correspond to depth of ~10 km for the basaltic magma and ~5 km for the andesitic magma, respectively.

RECONSTRUCTION OF ERUPTION FISSURES

Distribution and Age of the Eruption Fissures

The distribution and ages of the eruption fissures in Miyakejima were re-examined to reveal the temporal distribution patterns of the flank fissure eruptions in the volcano. The locations and orientations of the eruption fissures were confirmed, based on aerial photographs, a digital elevation model (5 m grid provided by the Geospatial Information Authority of Japan), and our field survey. The ages of each of the eruption fissures were determined by both the stratigraphic relationships of the tephra layers and the ^{14}C dating of the carbonized plant fragments at the base of the tephra layer.

In this study, we focus on the eruption fissures younger than the 2.7–2.8 ka caldera-forming event. We confirmed 23 fissure eruptions in this period (**Table 1**). Among them, sixteen fissure eruptions were identified as being younger than the seventh century Suoana-Kazahaya eruption (**Figure 3** and **Table 1**). The eruption fissures younger than the seventh century are mainly distributed in the NE-SW rift zone. Since the seventh century, four fissure eruptions occurred in the northeastern sector of the volcano, and ten occurred in the southwestern sector of the volcano. Two fissure eruptions (Ninth century and sixteenth century) occurred in the eastern flank. Though the exposure of the eruption fissures before the seventh century is limited owing to the coverage by the younger deposits, we also confirmed the locations and ages of six fissure eruptions between 2.5 ka and the seventh century (**Table 1**). Among the six eruptions,

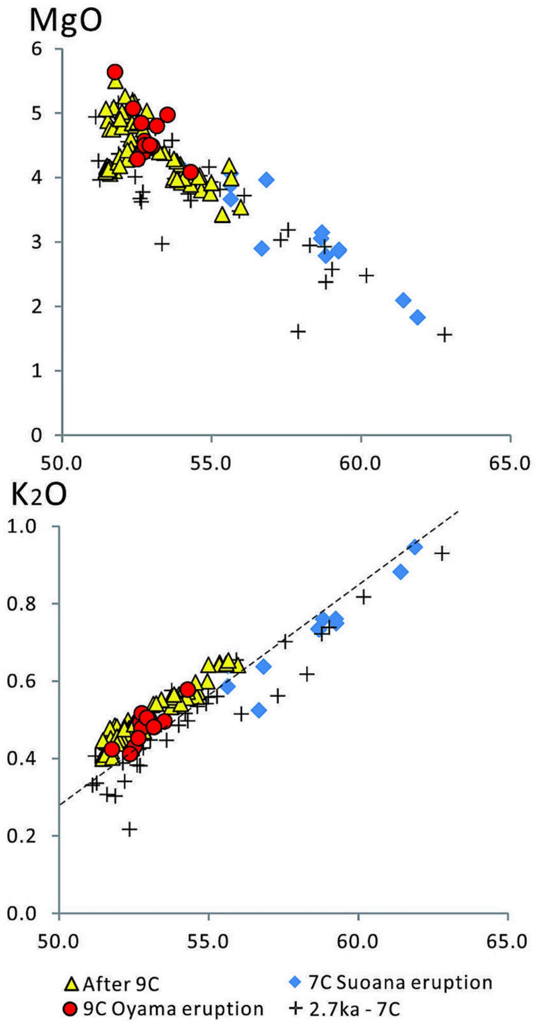

FIGURE 2 | Whole-rock composition of the representative eruptive products of the Miyakejima volcano. Yellow triangles show the composition of the products after the ninth century. Red circles show the products of the ninth-century Oyama-Miikehama eruption. Blue diamonds show the products of the seventh century Suoana-kazahaya eruption. Crosses show the ejecta between 2800 years ago and the seventh century. Broken line shows the approximate boundary between the ejecta before and after the ninth century Oyama-Miikehama eruption.

only two (Hatchodaira and Daihannyayama) occurred in the NE-SW rift.

Here, we introduce the "offset angle" of eruption fissures to evaluate the direction of the eruption fissures (**Figure 4A**). Offset angle is defined as the angle between the strike of the eruption fissure at the near side and the direction of the maximum horizontal compressive stress (σ_{Hmax}). The offset angle varies from 0° (parallel to the σ_{Hmax}) to 90° (perpendicular to the σ_{Hmax}). The direction of σ_{Hmax} is assumed to be N135°E, based on the strike of the regional dike intruded during the 2000 AD eruption (Ito and Yoshida, 2002; Yamaoka et al., 2005). The eruption fissures in the NE-SW rift zone have high offset angles ranging from 40° to 90°.

Magma Composition

The relationship between the orientation of eruption fissures and the composition of magma is investigated. We analyzed the whole-rock compositions of lavas and/or scoria of the fissure eruptions within the last ~2800 years. Whole-rock compositions of the erupted products form a linear compositional trend (**Figure 2**). A detailed examination indicated that the whole-rock K_2O contents of the products after the ninth century are slightly higher than that of the products between 2.8 ka and the seventh century (**Figure 2**).

Whole-rock SiO_2 contents of the lavas from the flank eruptions show wider variations with the increase of the offset angle of the eruption fissure (**Figure 4B**). Basaltic magmas (SiO_2 ~51 wt%) erupted in all directions, whereas the magmas with higher SiO_2 content erupted from the fissures with a higher offset angle (**Figure 4B**). The eruption fissures with offset angles less than 30° erupted basaltic andesite with a <53 wt% of whole-rock SiO_2 content. Andesite with SiO_2 >56 wt% was erupted from two fissures; the seventh century fissure in the northern flank with an offset angle of ~60° and the 2.7–2.8 ka eruption from the southern flank with an offset angle of ~85°.

DISCUSSION

A combined analysis of the location, age, and magmatic composition of the lavas of the eruption fissures in Miyakejima revealed the following facts: (i) The eruption fissures with higher offset angles from the regional compressive direction occurred within the last ~2800 years and formed the NE-SW rift, and (ii) Magmas with significant evidence of magma mixing erupted mainly from the eruption fissures with larger offset angles.

The limited distribution of hybrid magma in the NE-SW rift zone confirms the presence of an andesitic magma chamber beneath the NE-SW rift zone in the summit area. Several previous works on the petrological analysis of Miyakejima (Amma-Miyasaka and Nakagawa, 2003; Kuritani et al., 2003; Niihori et al., 2003; Amma-Miyasaka et al., 2005) show that the magmas that erupted within the last ~2800 years are hybrid with basaltic and andesitic end-components. The mixed end components were stored in a duplicated magma chamber system consisting of a deep-seated basaltic chamber and a shallow andesitic chamber. An analysis of the volatile component concentration of the melt inclusion in the ejecta of the 2000 AD eruption indicates that the equilibrium depth of basaltic magma is ~8 km for basaltic magma and ~3–5 km for andesitic magma (Saito et al., 2005, 2010).

Geophysical and geochemical observations also support the theory of a duplex magma chamber system beneath the Miyakejima before and during the 2000 AD eruption. The existence of a deep-seated basaltic magma chamber is suggested by the presence of the inflation source at around 9.5 km below sea level prior to the eruption (Nishimura et al., 2001). The existence of a shallow magma chamber at ~3–5 km below sea level is suggested by the position of the deflation source during the 2000 eruption (Nishimura et al., 2001), the source depth of the very-long-period seismic signal (Kumagai et al., 2001; Kobayashi et al.,

TABLE 1 | Age, offset angle, and whole-rock composition of fissure eruptions.

Name of eruption	Age	14_C age	Location	Offset angle	Whole-rock SiO$_2$ wt.%
Hatchodaira	2.7–2.8 ka		SW flank	45	56.1–58.8
Kanaso-minami	2.1 ka	2110 ± 30 BP	E flank	50	52.2
Tairayama	2.1 ka		NW flank	19	52.7–53.4
Tairoike	2.0 ka	1950 ± 20 BP	S flank	20	54.0
Daihannyayama	1.8 ka	>1880 ± 30 BP	NE flank	60	54.2
Anegakata	∼2 ka		NW flank	10	50.0
Suoana-Kazahaya	Seventh century	1410 ± 30 yrBP, 1360 ± 20 yrBP	N flank	60	54.0–61.4
Oyama-Miikehama	Ninth century	1240 ± 20 yrBP	E-W summit-flank	50	51.8–54.3
Kamane	0.9 ka	860 ± 20 yrBP	SW flank	80	52.0
Nanto	1085 AD?	750 ± 20 yrBP	SW flank	65	55.0
Hinoyama	1154 AD?	700 ± 20 yrBP, 690 ± 20 yrBP	NE flank	85	53.7
Enokizawa	1469 AD?		W flank	40	52.6–53.2
Sonei-Bokujo			Summit	–	52.2–54.1
Benkene	1535 AD?	340 ± 20 yrBP, 380 ± 20 yrBP, 390 ± 20 yrBP	E flank	15	51.8–52.8
Jinanyama	1595 AD?	315 ± 20 yrBP, 320 ± 20 yrBP	SW flank	85	52.1–52.8
Koshiki-Imasaki	1643 AD	250 ± 20 yrBP	SW flank	70	52.2–52.9
Shinmio	1712 AD?		SW flank	85	55.0
Tatsune	1763 AD?		SW flank	90	52.2
Bunka	1811AD		Summit?	–	
Kasaji-Kannon	1835 AD		W flank	55	56.0
1874 AD (Meiji)	1874 AD		N flank	50	51.9–54.3
1940 AD	1940 AD		NE flank and summit	80	50.8–55.7*
1962 AD	1962 AD		NE flank	80	52.2–54.7*
1983 AD	1983 AD		SW flank	85	52.5–54.7**
2000 AD	2000 AD		SW flank (submarine)	45	51.7–54.0

**Amma-Miyasaka and Nakagawa (2003), **Kuritani et al. (2003).*
Ages with "?" are not supported by the historic records.

2009), and the location of the dike injection at the initial stage of eruption (Ueda et al., 2005; Irwan et al., 2006). Source analysis of the very-long-period seismic signal and tilt change reveals the existence of a vertically aligned and NE-SW elongated ellipsoidal magma chamber at around 2.6 km beneath the south flank of the edifice (Munekane et al., 2016).

These petrological and geophysical observations indicate the existence of a duplicated magma plumbing system with a deep (∼10 km) basaltic chamber and shallow (∼2–5 km) andesitic magma chamber. Intermittent injections of basaltic magma into the shallow andesitic magma chamber formed hybrid magmas with higher SiO$_2$ concentrations. The injection of basaltic magma into a shallow magma chamber also caused rapid rise of internal magmatic pressure in the shallow magma chamber. This rapid increase of internal magmatic pressure may cause the dike propagation from the shallow magma chamber to feed a fissure eruption. Narrow diffusion profile observed in the titanomagnetite crystals of the andesitic ejecta suggests that the rupturing of the magma chamber and fissure eruption occurred within a few hours after the injection of basaltic magma into the andesitic system (Kuritani et al., 2003). A shallow magma chamber with a NE-SW trend and an elongated shape will form a stress field to accommodate the NE-SW trending vertical dikes above the magma chamber (**Figure 5A**). A feeder dike, which propagated from the shallow magma chamber, reached the NE-SW rift zone and erupted magmas with a signature of magma mixing between andesite and basalt.

Development of feeder dike system controlled by a duplex magma chamber proposed for the Miyakejima's system is similar to the feeding system of the 2005 eruption of Fernandina volcano, Galapagos (Chadwick et al., 2011). Petrological evidences of the lavas support the tapping of magma from the shallow magma chamber (Chadwick et al., 2011). The path of the feeder dike followed the maximum compressive stress generated by the overpressurized sill-like chamber (Chadwick and Dieterich, 1995) and also the existence of caldera (Corbi et al., 2015) to form a circumferential fissure. Development of the circumferential inclined sheets in Fernandina is controlled by the shape of the shallow magma chamber (horizontal sill), whereas the vertical dike-like shape of the shallow chamber in Miyakejima forms preferred oriented vertical feeder dikes. Difference of the regional tectonic setting [almost isotropic horizontal stress in Fernandina (Chadwick and Dieterich, 1995) and strong horizontal differential stress in Miyakejima (Nishimura, 2011)] may control the difference of the orientation of the shallow chambers.

Development of the compressive stress field around the shallow andesitic magma chamber is limited at the time of

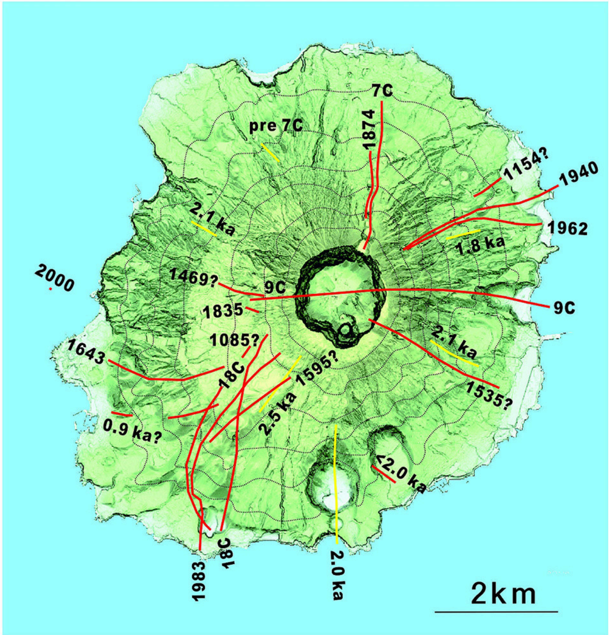

FIGURE 3 | Distribution of the eruption fissures within the last 2500 years. Red lines indicate the eruption fissures that erupted between the seventh century and the present. Yellow lines show the eruption fissures that erupted between 2500 years ago and the seventh century.

basaltic injection because pressure in the shallow andesitic magma chamber drops with the withdrawal of magma to the eruption fissure and/or the relaxation of the host rock surrounding the magma chamber. Some dikes from a deep-seated magma chamber could propagate directly to the ground surface and caused fissure eruptions of basaltic lavas (e.g., the 1535 eruption). In this case, the shallow magma chamber is not affected by the injection and, therefore, the magma chamber did not have any remarkable stress effect on the propagation of the basaltic dike (**Figure 5B**). Propagation of these basaltic dikes is mainly controlled by the regional stress field, and/or local stress field generated by the deep-seated basaltic magma chamber.

Our dataset of the ^{14}C dating shows that the development of the NE-SW rift zone became significant after the ninth century. This suggests that the shallow andesitic magma chamber was formed after the ninth century. The Oyama-Miikehama in the middle of the ninth century eruption erupted a volume of $\sim$0.08 km^3 DRE of basaltic magma (Tsukui and Suzuki, 1999) from the summit crater and an eruption fissure $\sim$5 km in length. The Oyama-Miikehama eruption is the largest eruption within the last $\sim$2800 years after the formation of the Hatchodaira caldera. A part of the basaltic magma, which was intruded during this eruption, formed a secondary magma chamber at a shallow depth and produced andesitic magma with fractional crystallization. A shift from the compositional trend of the eruption products since the ninth century (**Figure 2**) suggests the formation of a new magma system at the Oyama-Miikehama eruption. The existence of a similar secondary magma chamber is also recognized in the neighboring basaltic volcanoes (e.g., source of the 1986 fissure eruption in Izu-Oshima; Nakano and Yamamoto, 1991). NE-SW elongated shape of the shallow magma chamber may control the emplacement direction of the dikes, though the reason why the shallow magma chamber was formed perpendicular to the regional σ_{Hmax} direction is still open to debate. One of the possibilities is the disturbance of stress field by coseismic extensional deformation at the plate boundary earthquake (e.g., The 2011 Tohoku earthquake; Ozawa and Fujita, 2013). Two large trench-type earthquakes occurred in the ninth century (the 869AD Jogan Earthquake M>8.3 at Japan Trench and the 887AD Ninna-Nankai Earthquake Mw>8.6 at Nankai Trough; **Figure 1A**). These earthquakes might change the stress field from the NW-SE compressive state to the NW-SE extensive one in which a NE-SW elongated magma chamber can be formed. Tectonic disturbance is also suggested by frequent and intensive eruptions in the ninth century in the northern part of the Izu area (e.g., eruptions of Kozushima 838AD, Niijima 886AD, Mt. Fuji 864AD; Tsukui et al., 2006).

In the future, distribution pattern of the fissure eruptions in the future can change to a radial or NW-SE trend depending on the properties of the regional tectonic stress. During the caldera formation of the 2000 eruption, the shallow magma chamber of andesitic magma was emptied and collapsed (Geshi et al., 2002). Basaltic ejecta in the later stage of the eruption indicate that the shallow andesitic magma chamber was completely replaced by the basaltic magma. Therefore, the feeder dikes can intrude directly from the deep-seated basaltic magma chamber without any tectonic influence from the shallow magma chamber.

The example of Miyakejima suggests that the location, shape, and orientation of a shallow magma chamber will control the orientation and propagation direction of the feeder dikes. Similar cases where the stress of a magma plumbing system influence dike propagation are recognized in several basaltic volcanoes (e.g., Stromboli: Corazzato et al., 2008). The effect of local stress generated by an additional intrusion can be temporal because the stress relaxation weakens the local stress field in the host rock. The timescale of the stress relaxation is, in general, difficult to evaluate because it depends on the macroscopic viscoelastic behavior of the volcanic edifice which is controlled by the mechanical and thermal structure and the magnitude of the local stress field. Some field observations can suggest the time scale; in the case of Fernandina volcano, the local stress field generated by the emplacement of a sill in 1995 can remain and control the development of the eruption fissure of 2005 (Bagnardi et al., 2013). The local distribution of the eruption fissures may suggest frequent intrusions with a relatively short interval as the case of Miyakejima (2–3 events per 100 years).

The propagation direction of dikes in a volcanic edifice can be also affected by the topographic contrast, especially in an asymmetric edifice (e.g., Tibaldi et al., 2014; Corbi et al., 2015; Rivalta et al., 2015 and references therein).The volcanic edifice of Miyakejima, including its submarine part, has a conical shape without any remarkable bulge along the rift zone (**Figure 1B**). The development of the NE-SW rift zone became significant within the last 2800 years. However, no remarkable change in the shape of the edifice was noted in this period. These facts suggest that the topographic control on the rift development is limited in the case of Miyakejima.

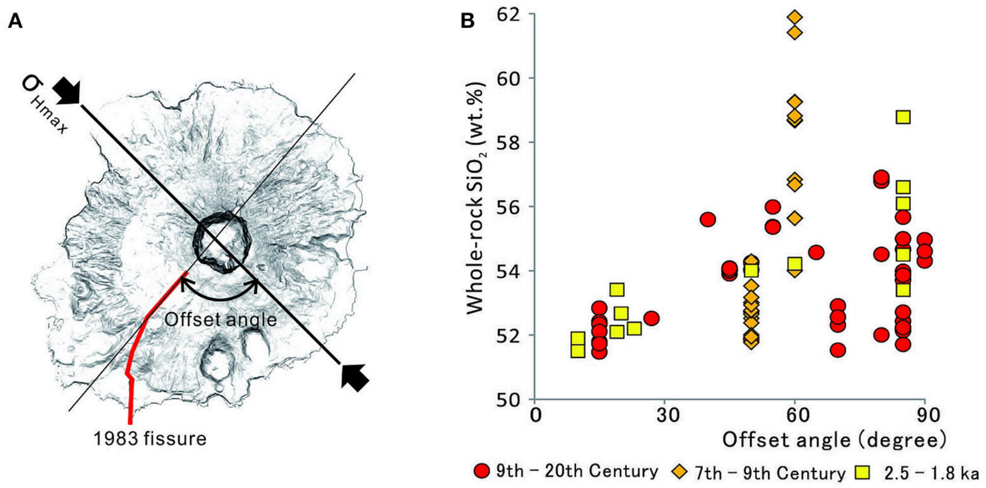

FIGURE 4 | (A) Illustration of the definition of the offset angle of an eruption fissure. **(B)** Whole-rock SiO_2 content of the ejecta from the flank eruption fissures during the last 2800 years plotted against the offset angle of their eruption fissure.

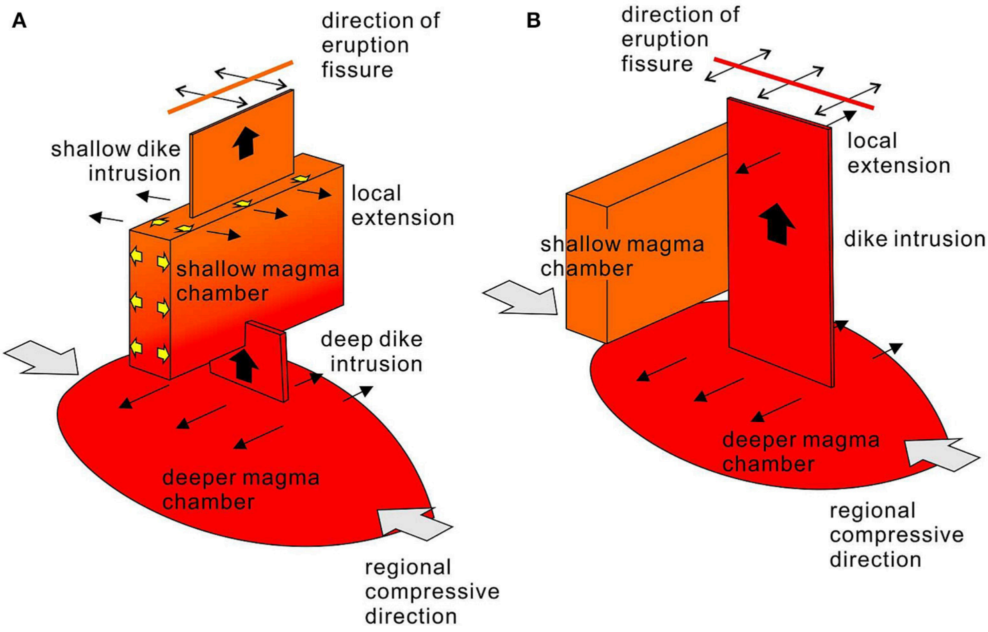

FIGURE 5 | Schematic model of the magma plumbing system of Miyakejima. (A) A basaltic dike extending from the from the deep-seated basaltic magma chamber injected into the shallow magma chamber filled with andesitic magma. Injection causes magma mixing within the shallow chamber and a dike with hybrid magma propagates from the shallow magma chamber. Injection also causes the rapid increase of the internal magma pressure in the shallow magma chamber to a local stress field around the shallow chamber. Orientation of the dike from the shallow magma chamber is mainly controlled by the local stress field generated by the pressurized shallow magma chamber. **(B)** A basaltic dike propagates directly from the deep-seated magma chamber without intersecting the shallow magma chamber. The orientation of the eruption fissure is mainly controlled by the regional stress field.

CONCLUSIONS

Combined analyses of the distribution patterns of the eruption fissures and the magmatic composition of the lavas within the last ∼2800 years reveal that a shallow andesitic magma chamber beneath the summit of Miyakejima volcano controls the orientation of eruption fissures. The injection of basaltic magma into the shallow andesitic magma chamber caused a rapid increase in the internal magmatic pressure in this magma chamber. The local compressive stress field around the andesitic magma chamber controls the orientation of feeder dikes in the NE-SW rift zone. Development of the NE-SW rift zone after a major eruption in the ninth century indicates that the shallow magma chamber is a remnant magma chamber formed during the ninth century eruption.

AUTHOR CONTRIBUTIONS

NG and TO prepares all the field data. NG did the petrological analysis. Reconstruction of the eruption history is mainly by TO. NG and TO build the manuscript.

ACKNOWLEDGMENTS

The field survey in Miyakejima was supported by the village of Miyake and the Japan Metrological Agency. The authors thank Hiroshi Shinohara, Karoly Nemeth, and Rina Noguchi for their assistance during the field survey. The authors also appreciate the reviewers for their critical review comments. The authors also appreciate Roberto Sulpizio and Valerio Acocella for their suggestions.

REFERENCES

Amma-Miyasaka, M., and Nakagawa, M. (2003). Evolution of deeper basaltic and shallower andesitic magmas during the ad 1469–1983 eruptions of Miyake-Jima Volcano, Izu– Mariana Arc: inferences from temporal variations of mineral compositions in crystal-clots. *J. Petrol.* 44, 2113–2138. doi: 10.1093/petrology/egg072

Amma-Miyasaka, M., Nakagawa, M., and Nakada, S. (2005). Magma plumbing system of the 2000 eruption of Miyakejima Volcano, Japan. *Bull. Volcanol.* 67, 254–267. doi: 10.1007/s00445-004-0408-0

Aramaki, S., Hayakawa, Y., Fujii, T., Nakamura, K., and Fukuoka, T. (1986). The October 1983 eruption of Miyakejima volcano. *J. Volcanol. Geotherm. Res.* 29, 203–229. doi: 10.1016/0377-0273(86)90045-4

Bagnardi, M., Amelung, F., and Poland, M. P. (2013). A new model for the growth of basaltic shields based on deformation of Fernandina volcano, Galápagos Islands. *Earth Planet. Sci. Lett.*, 377–378, 358–366. doi: 10.1016/j.epsl.2013.07.016

Cappello, A., Geshi, N., Neri, M., and Del Negro, N. (2015). Lava flow hazards – An impending threat at Miyakejima volcano, Japan. *J. Volcanol. Geotherm. Res.* 308, 1–9. doi: 10.1016/j.jvolgeores.2015.10.005

Chadwick, W. W., and Dieterich, J. H. (1995). Mechanical modeling of circumferential and radial dike intrusion on Galapagos volcanoes. *J. Volcanol. Geotherm. Res.* 66, 37–52. doi: 10.1016/0377-0273(94)00060-T

Chadwick, W. W., and Howard, K. A. (1991). The pattern of pattern of circumferential and radial eruptive fissures on the volcanoes of Fernandina and Isabela islands, Galapagos. *Bull. Volcanol.* 53, 259–275. doi: 10.1007/BF00414523

Chadwick, W. W., Jónsson, S., Geist, D. J., Poland, M., Johnson, D. J., Batt, S., et al. (2011). The May 2005 eruption of Fernandina volcano, Galápagos: The first circumferential dike intrusion observed by GPS and InSAR. *Bull. Volcanol.* 73, 679–697. doi: 10.1007/s00445-010-0433-0

Corazzato, C., Francalanci, L., Menna, M., Petrone, C., Renzulli, A., Tibaldi, A., et al. (2008). What does it guide sheet intrusion in volcanoes? Petrological and structural characters of the Stromboli sheet complex, Italy. *J. Volcanol. Geotherm. Res.* 173, 26–54. doi: 10.1016/j.jvolgeores.2008.01.006

Corbi, F., Rivalta, E., Pinel, V., Maccaferri, F., Bagnardi, M., and Acocella, V. (2015). How caldera collapse shapes the shallow emplacement and transfer of magma in active volcanoes. *Earth Planet Sci. Lett.* 431, 287–293. doi: 10.1016/j.epsl.2015.09.028

Falsaperla, S., and Neri, M. (2015). Seismic footprints of shallow dyke propagation at Etna, Italy. *Sci. Rep.* 5:11908. doi: 10.1038/srep11908

Geshi, N., Shimano, T., Nagai, M., and Nakada, S. (2002). Caldera collapse during the 2000 eruption of Miyakejima volcano, Japan. *Bull. Volcanol.* 64, 55–68. doi: 10.1007/s00445-001-0184-z

Gudmundsson, A. (2006). How local stresses control magma-chamber ruptures, dyke injections, and eruptions in composite volcanoes. *Earth Sci Rev.* 79, 1–31. doi: 10.1016/j.earscirev.2006.06.006

Irwan, M., Kimata, F., and Fujii, N. (2006). Time dependent modeling of magma intrusion during the early stage of the 2000 Miyakejima activity. *J. Volcanol. Geotherm. Res.* 150, 102–112. doi: 10.1016/j.jvolgeores.2005.07.014

Ishizuka, O., Geshi, N., Itoh, J., Kawanabe, Y., and TuZino, T. (2008). The magmatic plumbing of the submarine Hachijo NW volcanic chain, Hachijojima, Japan: long-distance magma transport? *J. Geophys. Res.* 113:B08S08. doi: 10.1029/2007jb005325

Ishizuka, O., Geshi, N., Kawanabe, Y., Ogitsu, I., Taylor, R. N., Tuzino, T., et al. (2014). Long-distance magma transport from arc volcanoes inferred from the submarine eruptive fissures offshore Izu-Oshima volcano, Izu–Bonin arc. *J. Volcanol. Geotherm. Res.* 285, 1–17. doi: 10.1016/j.jvolgeores.2014.08.006

Ito, T., and Yoshida, S. (2002). A dike intrusion model in and around Miyakejima, Niijima and Kozushima in 2000. *Tectonophy* 359, 171–187. doi: 10.1016/S0040-1951(02)00510-3

Kobayashi, T., Ohminato, T., Ida, Y., and Fujita, E. (2009). Very long period seismic signals observed before the caldera formation with the 2000 Miyake-jima volcanic activity, Japan. *J. Geophys. Res.* 114:B02211. doi: 10.1029/2007jb005557

Koyama, M., and Umino, S. (1991). Why does the Higashi-Izu monogenetic volcano group exist in the Izu Peninsula? Relationships between late Quaternary volcanism and tectonics in the northern tip of the Izu-Bonin arc. *J. Phys. Earth.* 39, 391–420. doi: 10.4294/jpe1952.39.391

Kumagai, H., Ohminato, T., Nakano, M., Ooi, M., Kubo, A., Inoue, H., et al. (2001). Very-long-period seismic signals and caldera formation at Miyake Island, Japan, *Science* 293, 687–690. doi: 10.1126/science.1062136

Kuritani, T., Yokoyama, T., Kobayashi, K., and Nakamura, E. (2003). Shift and rotation of composition trends by magma mixing: 1983 Eruption at Miyake-jima Volcano, Japan. *J. Petrol.* 44, 1895–1916. doi: 10.1093/petrology/egg063

Letourneur, L., Peltier, A., Staudacher, T., and Gudmundsson, A. (2008). The effects of rock heterogeneities on dyke paths and asymmetric ground deformation: The example of Piton de la Fournaise (Réunion Island). *J. Volcanol. Geotherm. Res.* 173, 289–302. doi: 10.1016/j.jvolgeores.2008.01.018

Munekane, H., Oikawa, J., and Kobayashi, T. (2016). Mechanisms of step-like tilt changes and very long period seismic signals during the 2000 Miyakejima eruption: insights from kinematic GPS. *J. Geophy. Res. Solid Earth* 121, 2932–2946. doi: 10.1002/2016JB012795

Nakamura, K. (1977). Volcanoes as possible indicators of tectonic stress orientation — principle and proposal. *J. Volcanol. Geotherm. Res.* 2, 1–16. doi: 10.1016/0377-0273(77)90012-9

Nakano, S., and Yamamoto, T. (1991). Chemical variations of magmas at Izu–Oshima volcano, Japan: plagioclase-controlled and differentiated magmas. *Bull. Volcanol.* 53, 112–120. doi: 10.1007/BF00265416

Niihori, K., Tsukui, M., and Kawanabe, Y. (2003). Evolution of magma and magma plumbing system of Miyakejima Volcano in the last 10,000 years. *Bull. Volcanol. Soc. Japan* 48, 387–405.

Nishimura, T. (2011). Back-arc spreading of the northern Izu–Ogasawara (Bonin) Islands arc clarified by GPS data. *Tectonophy* 512, 60–67. doi: 10.1016/j.tecto.2011.09.022

Nishimura, T., Ozawa, S., Murakami, M., Sagiya, T., Tada, T., Kaizu, M., et al. (2001). Crustal deformation caused by magma migration in the northern Izu Islands, Japan. *Geophys. Res. Lett.* 28, 3745–3748. doi: 10.1029/2001GL013051

Ozawa, T., and Fujita, E. (2013). Local deformations around volcanoes associated with the 2011 off the Pacific coast of Tohoku earthquake. *J. Geophy. Res. Solid Earth* 118, 390–405. doi: 10.1029/2011JB009129

Rivalta, E., Taisne, B., Bunger, A., and Katz, R. (2015). A review of mechanical models of dike propagation: schools of thought, results and future directions. *Tectonophysics* 638, 1–42. doi: 10.1016/j.tecto.2014.10.003

Saito, G., Morishita, Y., and Shinohara, H. (2010). Magma plumbing system of the 2000 eruption of Miyakejima volcano, Japan, deduced from volatile and major component contents of olivine-hosted melt inclusions. *J. Geophys. Res.* 115:B11202. doi: 10.1029/2010jb007433

Saito, G., Uto, K., Kazahaya, K., Shinohara, H., Kawanabe, Y., and Satoh, H. (2005). Petrological characteristics and volatile content of magma from the 2000 eruption of Miyakejima Volcano, Japan. *Bull. Volcanol.* 67, 268–280. doi: 10.1007/s00445-004-0409-z

Seebeck, H., and Nicol, H. (2009). Dike intrusion and displacement accumulation at the intersection of the Okataina Volcanic Centre and Paeroa Fault zone, Taupo Rift, New Zealand. *Tectonophy* 475, 575–585. doi: 10.1016/j.tecto.2009.07.009

Takada, A. (1997). Cyclic flank-vent and central-vent eruption patterns. *Bull. Volcanol.* 58, 539–556. doi: 10.1007/s004450050161

Tibaldi, A. (2015). Structure of volcano plumbing systems: a review of multi-parametric effects. *J. Volcanol. Geotherm. Res.* 298, 85–135. doi: 10.1016/j.jvolgeores.2015.03.023

Tibaldi, A., Bonali, F. L., and Corazzato, C. (2014). The diverging volcanic rift system. *Tectonophy* 611, 94–113. doi: 10.1016/j.tecto.2013.11.023

Tsukui, M., Saito, K., and Hayashi, K. (2006). Frequent and intensive eruptions in the 9th century, Izu Islands, Japan: revisions of volcano-stratigraphy based on tephras and historical document. *Bul. Volcanol. Soc. Japan* 51, 327–338.

Tsukui, M., and Suzuki, Y. (1999). Eruptive history of Miyakejima Volcano during the last 7000 years. *Bull. Volcanol. Soc. Japan* 43, 149–166.

Ueda, H., Fujita, E., Ukawa, M., Yamamoto, E., Irwan, M., and Kimata, F. (2005). Magma intrusion and discharge process at the initial stage of the 2000 activity of Miyakejima, central Japan, inferred from tilt and GPS data. *Geophys. J. Int.* 161, 891–906. doi: 10.1111/j.1365-246X.2005.02602.x

Walter, T. R., Troll, V. R., Cailleau, B., Belousov, A., Schmincke, H.-U., Amelung, F., et al. (2005). Rift zone reorganization through flank instability in ocean island volcanoes: an example from Tenerife, Canary Islands. *Bull. Volcanol.* 67, 281–291. doi: 10.1007/s00445-004-0352-z

Yamaji, A., and Sato, K. (2011). Clustering of fracture orientations using a mixed Bingham distribution and its application to paleostress analysis from dike or vein orientations. *J. Struct. Geol.* 33, 1148–1157. doi: 10.1016/j.jsg.2011.05.006

Yamaoka, K., Kawamura, M., Kimata, F., Fujii, N., and Kudo, T. (2005). Dike intrusion associated with the 2000 eruption of Miyakejima Volcano, Japan. *Bull. Volcanol.* 67, 231–242. doi: 10.1007/s00445-004-0406-2

Conflict of Interest Statement: The authors declare that the research was conducted in the absence of any commercial or financial relationships that could be construed as a potential conflict of interest.

frontiers
in Earth Science

ORIGINAL RESEARCH
published: 25 October 2016
doi: 10.3389/feart.2016.00092

Stress Field Control during Large Caldera-Forming Eruptions

Antonio Costa[1] and Joan Martí[2]*

[1] *Istituto Nazionale di Geofisica e Vulcanologia, Bologna, Italy,* [2] *CSIC, Institute of Earth Sciences "Jaume Almera," Barcelona, Spain*

Crustal stress field can have a significant influence on the way magma is channeled through the crust and erupted explosively at the surface. Large Caldera Forming Eruptions (LCFEs) can erupt hundreds to thousands of cubic kilometers of magma in a relatively short time along fissures under the control of a far-field extensional stress. The associated eruption intensities are estimated in the range 10^9–10^{11} kg/s. We analyse syn-eruptive dynamics of LCFEs, by simulating numerically explosive flow of magma through a shallow dyke conduit connected to a shallow magma (3–5 km deep) chamber that in turn is fed by a deeper magma reservoir ($>\sim$10 km deep), both under the action of an extensional far-field stress. Results indicate that huge amounts of high viscosity silicic magma ($>10^7$ Pa s) can be erupted over timescales of a few to several hours. Our study provides answers to outstanding questions relating to the intensity and duration of catastrophic volcanic eruptions in the past. In addition, it presents far-reaching implications for the understanding of dynamics and intensity of large-magnitude volcanic eruptions on Earth and to highlight the necessity of a future research to advance our knowledge of these rare catastrophic events.

Keywords: super-eruptions, magma ascent dynamics, extensional stress, volcanic conduit model, fissure eruptions

Edited by:
Agust Gudmundsson,
Royal Holloway, University of London, UK

Reviewed by:
Hiroaki Komuro,
Shimane University, Japan
Antonio M. Álvarez-Valero,
University of Salamanca, Spain

****Correspondence:***
Antonio Costa
antonio.costa@ingv.it

Specialty section:
This article was submitted to Volcanology,
a section of the journal
Frontiers in Earth Science

Received: *02 August 2016*
Accepted: *07 October 2016*
Published: *25 October 2016*

Citation:
Costa A and Martí J (2016) Stress Field Control during Large Caldera-Forming Eruptions.
Front. Earth Sci. 4:92.
doi: 10.3389/feart.2016.00092

INTRODUCTION

There is compelling evidence that Large Caldera-Forming Eruptions (LCFEs) are characterized by extremely large intensities. Estimations of Mass Eruption Rates (MERs) obtained with different independent methods (Wilson and Walker, 1981; Hildreth and Mahood, 1986; Wilson and Hildreth, 1997; Baines and Sparks, 2005; Costa et al., 2014; Martí et al., 2016; Roche et al., 2016) indicate MERs of the orders 10^9–10^{11} kg/s (e.g., Bishop Tuff, Campanian Ignimbrite, Oruanui eruption, Taupo eruption, Peach Spring Tuff, Young Toba Tuff), implying durations of few to several hours only to evacuate even thousands of km^3 of magma.

Most LCFEs occur in both subduction zone and extensional environments characterized by relatively low rates of magma production (see Jellinek and De Paolo, 2003 and references therein) implying that the thousand km^3 volume magma chambers feeding those events have to accumulate over long periods ($>10^5$ years; Jellinek and De Paolo, 2003).

In order to erupt, magmas stored in relatively shallow chambers (3–8 km; e.g., Smith et al., 2005, 2006; Matthews et al., 2011; Chesner, 2012) normally have to overcome critical overpressures up to $\sim$50 MPa for nucleating new fractures and up to $\sim$10 MPa for propagating magma up to the surface (Rubin, 1995; Jellinek and De Paolo, 2003). Whereas for small magma chambers such overpressures can be easily achieved, for very large chamber volumes it is more problematic to reach such overpressures, and dyke formation and propagation are, as a consequence, inhibited (Jellinek and De Paolo, 2003). In some cases there is clear evidence of new injection of magma (and associated oversaturation of volatiles) as main cause to achieve the required overpressure to open the magma chamber (e.g., Sparks et al., 1977; Pallister et al., 1992; Self, 1992; Folch and Martí, 1998). However, in most large calderas this is not so clear. In contrast, tectonic triggers (i.e., decrease of ambient pressure due to tectonic—earthquake—activity) would be a plausible mechanism (see Aguirre-Díaz and Labarthe-Hernañdez, 2003; Martí et al., 2009), despite they have not been sufficiently explored yet. In the case of tectonic triggers, the magma chamber would evacuate the magma through the pre-existing faults or newly formed fractures without needing any over-pressurization of the magma chamber (Martí et al., 2009).

Irrespectively of the mechanism that leads to the rupture of the magma chamber during caldera eruptions, syn-eruptive dynamics of magma ascent in high intensity eruptions are not clear and there have not been many attempts to quantitatively describe them (Costa et al., 2011). Dykes feeding these eruptions have to be long enough and remain open over much of their length throughout the entire explosive activity. The mechanics of feeding explosive silicic ignimbrite eruptions through a linear fissure (Korringa, 1973; Aguirre-Díaz and Labarthe-Hernañdez, 2003) or from multiple vents along a fissure (Suzuki-Kamata et al., 1993; Wilson, 2001; Smith et al., 2005, 2006; Folch and Martí, 2009) are largely unexplored.

Magma emplacement through dykes and the capability of magma to reach the surface strongly depend on the local stresses across the different layers that constitute the volcano (Gudmundsson, 2006). As explained for instance by Gudmundsson (2006), a dyke propagated upward from a magma chamber can reach the surface only if the stress field along all its path is favorable to magma-fracture propagation. This implies that the stress field has to promote extension-fracture formation as well as keep the stress field homogenized along the entire path of the dyke to the surface.

Moreover, once that a critical magma chamber pressure is reached (e.g., by intrusion of new magma or by evolution of volatiles or both or by external triggering because a fracture can reach the chamber roof) and a dyke can propagate in the surrounding rocks, in order to produce an explosive eruption, magma has to fragment. Because of the typical silicic compositions (e.g., Chesner, 1998, 2012; Matthews et al., 2012) and high crystal contents (e.g., Gottsmann et al., 2009; Costa et al., 2011) effective viscosity of those magmas is very high ($>10^7$ Pa s; e.g., Costa et al., 2011). Since the fragmentation depth is controlled by effective magma viscosity, in order to be able to keep dykes open at deep fragmentation levels it is necessary that local magma overpressure counterbalances the lithostatic load at that depth (Costa et al., 2009, 2011). Hence extremely larger overpressures should be attained.

Concerning this point, Costa et al. (2011) showed that coupling of magma overpressure with the effects of a far-field extensional stress can play a pivotal role. As we mentioned above, most LCFEs have been recorded in extensional environments (e.g., Jellinek and De Paolo, 2003; Sobradelo et al., 2010), but even where LCFEs occur in convergent regions they appear to be associated with local extension (Miller et al., 2008; Acocella and Funiciello, 2010).

Besides tectonic stress, local extension can be produced by the growth of magma chambers and reservoirs exceeding several hundreds of cubic kilometers in volume due to a "magmatic" stress field on local and regional scales. Either counteracts or adds to dominant tectonic stresses depending on the sign and intensity of the far-field stress and on the magma chamber shape and orientation (Gudmundsson, 1988, 1998; Gudmundsson et al., 1997).

In this contribution, we start briefly reviewing the general tectonic settings of LCFEs and other evidence of stress field control during LCFE. Then we summarize the model of Costa et al. (2011) for LCFEs adapted in order to account for the effects of a pressurized magma reservoir (**Figure 1**). Finally, we apply the Costa et al. (2011) model to show how, for magma chamber and reservoir depths and magma properties typical of a LCFE similar to the Young Toba Tuff (YTT), the local stress field, due to the combined effects of relatively low pressurizations of magma chamber and reservoir, and far-field stress, can promote large MERs.

TECTONIC SETTINGS OF LCFEs AND ERUPTION CONDITIONS

Collapse calderas are volcanic subsidence structures that can be recognized in many volcanic systems and may form in any geodynamic environment (Gudmundsson, 1988). However, the largest caldera eruptions, those that erupt hundreds to thousands of cubic kilometers of magma, are invariably associated with silicic magmas and extensional structures occurring mostly in subduction zones, continental rifts or extensional environments of Basin and Range type, always related to a thick continental crust (Geyer and Martí, 2008; Cole et al., 2010; Reyners, 2010; Rowland et al., 2010). This fact suggests that this type of extensional stress is a requisite (or a favorable factor) for the formation of large magma chambers responsible for calderas (see also e.g., Gudmundsson, 1998, 2006; Hughes and Mahood, 2008).

It is generally accepted that there is a positive linear relationship between the area of the caldera and the volume of material extruded during the eruption (Smith, 1979; Spera and Crisp, 1981; Geyer and Martí, 2008). So, large calderas are related to the eruption of large volumes of magma. The tendency of large collapse calderas to form in areas with extensional tectonics and in relatively thick ($\geq$30 km) continental crusts suggests that these conditions are the most favorable to accumulate large volumes of silicic magmas at shallow depths (Sobradelo et al., 2010). Another feature that characterizes large collapse calderas is their association with shallow (3–5 km deep) magma chambers, thus suggesting that mechanical conditions to form such calderas are only achieved under stress configurations related to small aspect ratios, i.e., depth vs. extent of the chamber (Martí et al., 2009; Geyer and Martí, 2014).

The mechanisms by which a magma chamber opens to the surface and then evolves into a caldera-forming event are still

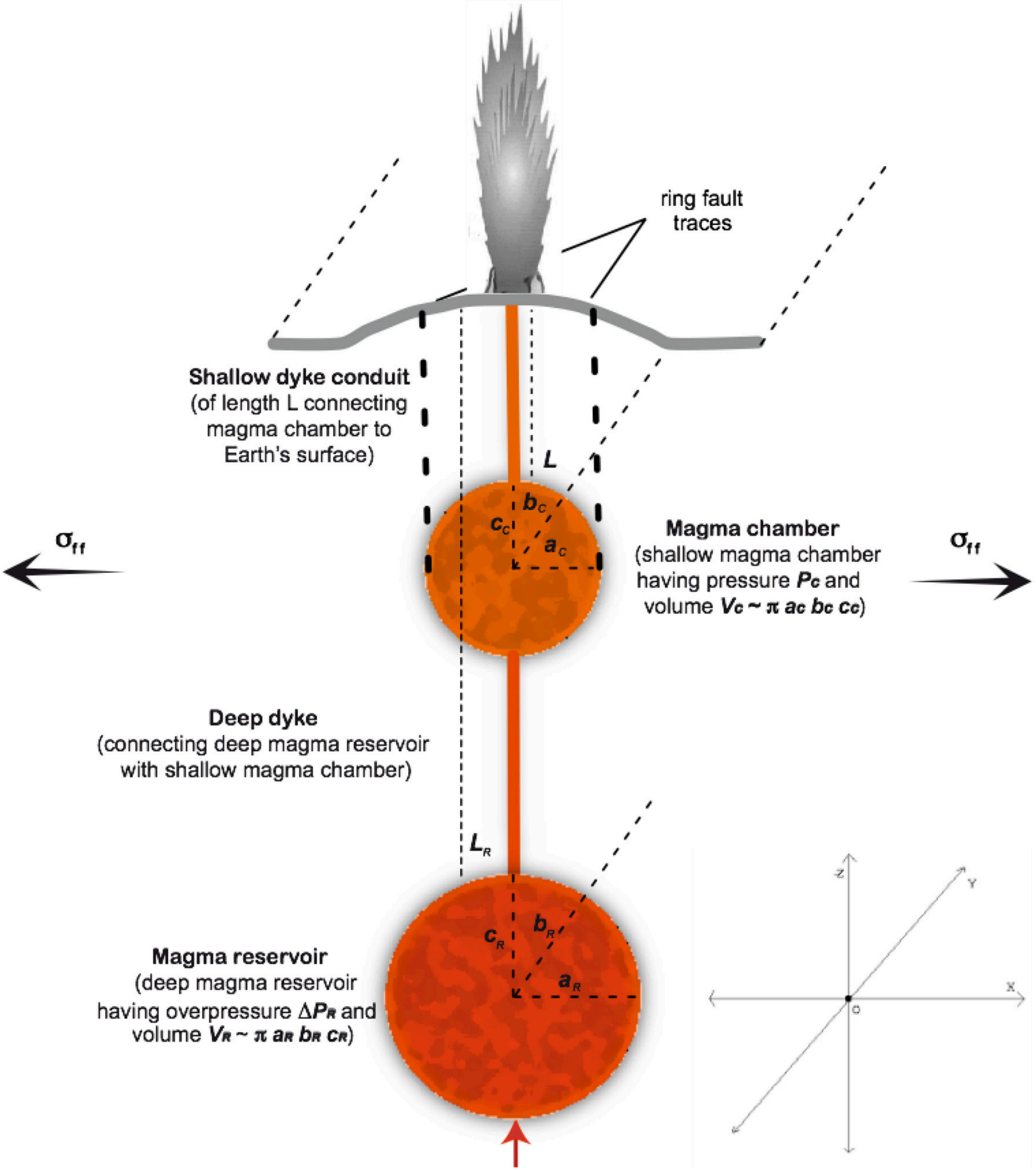

FIGURE 1 | Schematic view of the investigated system. The magma chamber having a roof placed at a depth L, is assumed to be an ellipsoid with semi-axes a_C, b_C, and c_C with $b_C \gg a_C, c_C$ (Costa et al., 2011). The magma reservoir having a roof placed at a depth L_R, is also assumed to be an ellipsoid with semi-axes a_R, b_R, and c_R with $b_R \gg a_R, c_R$. The cross-section of the shallow dyke conduit is assumed to be elliptical with a finite length $2a_d$ (along the y-direction) and width $2b_d$ (along the x-direction).

not fully understood. In any case, there is general consensus that collapse calderas require very specific stress conditions to form, which will be defined by the stress field, size, shape, and depth of the magma chamber, magma rheology and gas content, and state of deformation (e.g., presence of local and regional faults) of the host rock (see Acocella, 2007; Martí et al., 2009; Acocella et al., 2015). Under these circumstances, the rupture of a magma chamber may be an intrinsic cause by an increase of magma pressure due to injection of new magma into the chamber and/or oversaturation of volatiles due to crystallization, or may be favored by outside by reducing stresses through a tectonic event (e.g., earthquake). The mechanisms by which the eruption will progress and caldera will collapse may be different depending on each scenario (see Martí et al., 2009), but it is not the aim of this study to discuss in detail such differences. On the contrary, we will concentrate on common aspects related to magma flow through fractures and on the conditions needed for having large MERs characteristics of LCFEs, regardless on how these fractures have opened.

According to the stratigraphic features shown by caldera forming deposits we can differentiate two main caldera types or end members. One comprises the caldera forming episode preceded by a Plinian eruption that may erupt a considerable volume of magma. This type of calderas, named underpressure calderas by Martí et al. (2009), are characterized in the field by the presence of relatively thick Plinian deposits underlying the caldera-forming ignimbrites, and would correspond to those calderas in which the initiation of caldera collapse requires a substantial decompression of the magma chamber (Druitt and Sparks, 1984). Examples of such calderas are Crater Lake (e.g., Bacon, 1983), Katmai (e.g., Hildreth, 1991), Santorini (e.g., Druitt and Francaviglia, 1992). The other end-member corresponds to those calderas in which caldera collapse starts at the beginning of the eruption, without any Plinian phase preceding it. The succession of deposits that characterize these calderas, called overpressure calderas by Martí et al. (2009), is composed only of the caldera forming ignimbrites, with occasional some minor pyroclastic surge deposits at the base of the caldera-forming succession. In this case, it is interpreted that these calderas start forming since the beginning of the eruption without needing (significant) decompression of the magma chamber (Gudmundsson et al., 1997; Martí et al., 2009). Examples of this type of caldera are La Pacana (e.g., Gardeweg and Ramirez, 1987), Cerro Galán (Folkes et al., 2011), Aguas Calientes (Petrinovic et al., 2010); El Abrigo (Pittari et al., 2008), Bolaños graben caldera (Aguirre-Díaz et al., 2008).

BASIC MODEL OF MAGMA ASCENT DURING LCFEs

Previous numerical models of LCFE were used to study syn-eruptive dynamics of magma ascent of these eruptions. In particular, Folch and Martí (2009) presented simulations of LCFE based on Macedonio et al. (2005) conduit model, considering an initial eruption phase from a central-vent conduit, a transition to peripheral fissure-vent conduits, and a final phase controlled by piston-like subsidence. In line with their results, during the eruption phase from peripheral ring fissures, MERs would increase by almost an order of magnitude. During the piston-like subsidence, pressure increases back to lithostatic and the MER tends to stabilize near these larger values and does not change significantly after the subsidence starts. Because of the limitations of the model and the assumed rigid conduit geometry, the simulations by Folch and Martí (2009) were limited to relatively small MERs, $<10^9$ kg/s. Such low MERs would imply long eruption durations, in the range of few tens to hundreds hours, or longer, even for erupting relatively small volumes of magma.

Contrarily to the simplifying assumptions of most volcanic conduit models, rock mechanics imply the most efficient way of moving magma through cold lithosphere is via dykes (Rubin, 1995), and this is supported from field evidence (e.g., Gudmundsson, 2002) and geophysical analysis (e.g., Hautmann et al., 2009; Sigmundsson et al., 2010). Because the complexity in describing coupled magma-rock dynamics, explosive volcanic eruptions have been commonly modeled in terms of multiphase flows through rigid conduits of a fixed cross-section. Costa et al. (2009) and Costa et al. (2011) generalized Macedonio et al. (2005) model considering magma flow from an elastic dyke with elliptical cross-section emanating from magma chamber reaching the surface as a linear dyke or as dyke evolving to a cylinder at shallower depths. Costa et al. (2011) showed that MERs of the order of 10^9–10^{11} kg/s can be obtained for realistic input parameters if the effect of an extensional stress field on the dynamics of magma ascent is accounted for.

Here we summarize the model proposed by Costa et al. (2011) that is based on the following mass and momentum equations:

$$\frac{\partial}{\partial z}(\rho A U) = 0 \tag{1}$$

and

$$U\frac{\partial U}{\partial z} = -\frac{1}{\rho}\frac{\partial P}{\partial z} - g - f_{ft} \tag{2}$$

where z denotes the vertical coordinate along the dyke axis, $A = \pi a_d b_d$, is the cross-section area of an elliptical dyke having semi-axes a_d and b_d, U is the vertical mixture velocity, g is the gravity acceleration, and f_{ft} is the friction term calculated for an elliptical cross-section (Costa et al., 2009). The model assumes steady-state conditions. This is justified because eruption durations and time-scales of pressure variations at base of the conduit are of the order of hours, much longer than magma travel times in the conduit that are of the order of minutes (e.g., Wilson et al., 1980; Folch et al., 1998).

The model considers that fragmentation occurs when the gas volume fraction, α, reaches a critical value of 0.75 (Sparks, 1978). Despite this simplification, the results are in line with other fragmentation criteria proposed by e.g., Melnik (1999), or Papale (1999).

The dyke semi-axes a_d and b_d depend on the difference between magmatic pressure and normal stress in host rocks ΔP in accord to the following relationships (e.g., Muskhelishvili, 1963; Sneddon and Lowengrub, 1969; Costa et al., 2009):

$$a_d(z) = a_{d0}(z) + \frac{\Delta P}{2G}\left[2(1-\upsilon)\, b_{d0}(z) - (1-2\upsilon) a_{d0}(z)\right] \tag{3a}$$

$$b_d(z) = b_{d0}(z) + \frac{\Delta P}{2G}\left[2(1-\upsilon)\, a_{d0}(z) - (1-2\upsilon) b_{d0}(z)\right] \tag{3b}$$

$$\Delta P = P - (\rho_r g z - \sigma_t) \tag{4}$$

where, G is the rigidity of wallrock, ν is Poisson's ratio, a_{d0} and b_{d0} are the unpressurized values of the semi-axes, σ_t is the tensile stress along the axis of the dyke conduit due to the presence of magma chamber under the effect of an extensional far-field stress σ_{ff} acting on the plane y–z (see **Figure 1**).

As in Costa et al. (2011), as first-order approximation, the tensile stress along the dyke conduit due the effects of magma chamber and reservoir under the effect of an extensional far-field stress is calculated using the general analytical solutions by Gao (1996) obtained in the limit of a plane 2D geometry. Such a first-order approximation can capture general large-scale features (Costa et al., 2011). We would like to remark that, in this way, we account for the effects of magma chamber and reservoir on the tensile stress during magma transport in the shallow dyke conduit but we do not investigate their internal dynamics (out of the scope of this study). Magma chamber pressure is used as boundary condition at the base of the shallow dyke conduit and assumed chamber volumes to estimate durations once we calculated MERs.

The main limitations of the magma transport model presented above and the solving methodology are discussed in Costa et al. (2009) and Costa et al. (2011).

CONTROL OF LOCAL STRESS FIELD ON ERUPTION DYNAMICS AND INTENSITIES

In the framework of the model described in Section Basic Model of Magma Ascent during LCFE, we consider a relatively shallow magma chamber connected to the surface through a shallow dyke conduit. Internal pressures of the shallow chamber range from over- to under-pressure conditions. In terms of stress distribution we also consider the effect of a deeper reservoir that can be in neutral conditions or over-pressurized with respect to the lithostatic loading (**Figure 1**, terminology as in Gudmundsson, 2012). Irrespectively of the process that formed the fracture (magma chamber overpressure or tectonic events), we assume that dyke is already opened and we study syn-eruptive magma transport.

In the approximation of elastic deformation, valid because the short time scales (from few to several hours) characterizing LCFEs, the dyke will tend to open or close as function of the local magmatic pressure with respect the local loading. Besides the lithostatic loading we need to account for the contribution σ_t to the tensile stress along the axis of the shallow dyke conduit, due to the presence of a more or less pressurized magma chamber and reservoir under the effect of an extensional far-field stress. The contribution of an extensional stress on keeping open the base of the dyke was discussed by Costa et al. (2011) who, however, have not considered the effect due to the presence of a deep pressurized reservoir. They described a critical extensional stress that produces a tensile stress at the base of the dyke able to counterbalance the lithostatic loading. Nevertheless, because fragmentation levels during LCFEs are very deep due to the typical large magma viscosities (Costa et al., 2011), the critical extensional stress was very high (σ_{ff} $\approx$50–60 MPa) and close to rifting regime (Turcotte and Schubert, 2002).

Here, our results show that even the contribution of a deep magma reservoir with an over-pressure of about 10 MPa is able to halve critical extensional stresses allowing the dyke to remain open until the magma pressure goes back to sub-neutral conditions. Once formed, a long dyke can remain open even for magma chamber pressures from ∼10 MPa above the lithostatic loading (considered a typical value to propagate a dyke; e.g., Gudmundsson, 2006, 2012) to ∼10 MPa below the lithostatic loading. Once the pressure at the base of the dyke decreases below a critical value, the eruption stops and the system has to recover again large magmatic pressure before it can erupt, i.e. the dyke can act as a valve.

Although, Jellinek and De Paolo (2003) show the difficulty to overpressurize a large magma chamber with typical magma rate production in subduction zone and extensional environments, overpressures of ∼10 MPa could be easily achieved because of magma crystallization (and as we discussed above, magma associated to LCFEs are typically characterized by high crystallinity; Costa et al., 2011). Such overpressures can be sufficient to trigger an eruption, as the roof of the shallow magma chamber can undergo to intensive heating that can significantly weaken the strength of the overlying rocks (Gregg et al., 2012, 2015). Another end-member for triggering the eruption could be when a fracture opens from surface or all through the host rock above the magma chamber if there is a pre-existing fault.

Concerning deep magma reservoirs, overpressures of ∼10 MPa may be generated by the contribution of CO_2 exsolution (e.g., Folch and Martí, 1998; Gudmundsson, 2015).

However, we would like to remark that here we focus on the syn-eruptive dynamics of magma ascent inside the shallow dyke conduit during LCFEs and not on magma chamber dynamics and mechanics able to trigger such eruptions that are likely related to magma chamber roof failure and have been explored by other authors (e.g., Burov and Guillou-Frottier, 1999; Folch and Martí, 2004; Gray and Monaghan, 2004; Gregg et al., 2012, 2015; Geyer and Martí, 2014). For the purposes of this study, aimed at describing the first-order features only, chamber and reservoir shapes are not crucial and for simplicity, as in Costa et al. (2011), we assume them as elongated bodies with circular cross-sections. This choice is consistent with the observation that common geometries are general oblate-ellipsoidal chambers (Gudmundsson, 2012 and references therein). Moreover, as discussed in (Gudmundsson, 2012) long-lived magma chambers cannot have very irregular shapes as their surfaces can be assumed smooth (Jaeger, 1961, 1964; Gudmundsson, 2012). On this basis, under isotropic conditions, on very long time-scales, chamber geometries should tend to become sub-circular.

We also need to consider that the aspect ratio of the caldera produced during those eruptions may not be indicative of the chamber shape because as magma overpressure decreases below a critical value, the shallow dyke cannot anymore be kept opened around the fragmentation depth and tends to collapse forming a local restriction that would stop the eruption (Costa et al., 2009, 2011) even if a large fraction of the stored magma is still in the chamber. Caldera shapes can reflect only chamber cross-sections and the fraction of magma volumes evacuated. However, caldera eruptions tend to erupt all eruptible magma (all magma that may vesiculate and have a density lower than the host rock while the crustal block in collapsing) likely because the control of the piston-like subsidence able to maintain the necessary excess pressure (Martí et al., 2000; Folch and Martí, 2009; Gudmundsson, 2015; Geshi and Miyabuchi, 2016). Also it is common to see in large silicic calderas the emplacement of degassed magma in the form of extrusive dome along the ring faults immediately after caldera formation (e.g., Williams, 1941; Lipman, 1984). This implies that we should not expect a large volume of magma remaining in the chamber. In fact many calderas (see Geyer and Martí, 2008) exhibit post-caldera volcanism of mafic composition, thus indicating that nothing or very little was remaining in the magma chamber after caldera collapse, so deeper mafic magmas can cross it without being trapped (mixed) by the resident magma.

In our model the solution for the stress field is calculated using the general analytical solutions by Gao (1996) valid for a pressurized elliptical hole obtained in the limit of a plane 2D geometry (approximation valid for $c_C \gg a_C, b_C$, and $c_R \gg a_R, b_R$, **Figure 1**). Such solutions also assume that the medium is homogeneous and purely elastic. The elastic rheology is however a reasonable approximation because the time scales of the eruption, that are of the order of few to several hours, are much shorter than the viscous time of the magmatic system, of the order of hundreds of years or longer (Jellinek and De Paolo, 2003). However, concerning assumption of medium homogeneity we need keep in mind that rock stress distribution can be affected by presence of pore fluids, temperature, and alteration of the different layers (Gudmundsson, 2006). Moreover, active faults, block boundaries are neglected. In addition the solution is valid for an unbounded domain, neglects the effect of topography, and the far field stress is assumed to be homogeneous. However, the analytical solution is able to capture first-order, general large- scale features even with all these limitations (Costa et al., 2011).

We applied the model described above to a LCFE similar to YTT for which magma physical parameters, erupted volumes, tectonic settings are known and independent estimations of MERs are available (Costa et al., 2014). In particular, we studied a magma chamber located at 3–5 km depth under extensional far-field stresses, σ_{ff}, ranging from 0 to −50 MPa (**Figure 1**). The upper limit of this spectrum (comparable with stresses needed for nucleating new fractures) can be considered representative of the transition toward an active extensional setting (Turcotte and Schubert, 2002). The stress field perturbation due to a magma reservoir having a top at 10 km depth was also considered.

Concerning magma chamber and reservoir volumes, we assumed a chamber volume, $V_C = \frac{4}{3}\pi a_C b_C c_C$, of ∼5000 km^3 (considering a chamber extension c_C of 100 km, consistent with Toba caldera geometry) and a similar reservoir volume, $V_R = \frac{4}{3}\pi a_R b_R c_R$, of ∼5000 km^3.

Before to proceed, it is useful to summarize some basic effects due to the combination of different magma chamber geometries under the action of a far-field extensional stress. For an elongated magma chamber with a circular cross-section (i.e., with an aspect ratio $a_C/c_C \approx 1$) near neutral pressure conditions, the maximum tensile stress is at the base of the dyke ($x = 0, \quad z = c_C$; **Figure 1**) and in this case is $\sigma_t \approx 3\sigma_{ff}$ (e.g., Gudmundsson, 1988). For a prolate cross-section $\sigma_t \approx (1 + 2a_C/c_C)\sigma_{ff}$ with $a_C \geq c_C$ and $b_C \gg a_C$ (e.g., Gudmundsson, 1988). For an oblate cross-section the maximum stress is at the two lateral tips of the ellipse. The stress along the dyke, connecting the magma chamber to the surface, depends on the intensity of extensional stress, magma chamber pressure, and magma chamber aspect ratio a_C/c_C, magma reservoir depth, magma reservoir aspect ratio a_R/c_R, and magma reservoir overpressure ΔP_R.

Considering the above estimation for the magma chamber volume, and the geometry of the Toba caldera (∼100 × 30 km), the chamber would be roughly approximated by an oblate ellipsoid having an elongation of ∼100 km, a width of ∼30 km, and a height of ∼3 km. However, for the sake of simplicity, consistently with our basic magma conduit flow model and the analytical solution for the stress field, we assumed a chamber (and reservoir) with a circular cross section, $b_C \gg a_C = c_C$ with $2a_C = D_C$ being D_C the equivalent diameter (in our case $D_C \sim 10$ km). In our approximation the maximum effect on the tensile stress is along the dyke conduit at the center of the circular cross section of the chamber, whereas, considering the more realistic case of an oblate ellipsoid, it would be around the lateral tips of the ellipse with an intensity factor an order of magnitude larger due to the different geometry aspect ratio (∼10). We would like to remark that we aim to estimate the order of magnitude control of the stress along the dyke conduit due to magma chamber and reservoir and not investigate their detailed magma-rock mechanics. Our approximation represents a minimum bound for the actual effects on the tensile stress that can be even an order of magnitude larger in case of elongated geometries.

Concerning chemical and physical magma properties of the shallow chamber, we considered a magma composition like that of YTT (e.g., Chesner, 2012; Matthews et al., 2012) characterized by a high SiO_2 content (∼70–75%), a water content of about 5–6%, temperatures of 700–780°C and high crystallinity (up to 40%). These properties are very similar to those characterizing magmas of other LCFEs such as, for example, those associated to the Aira Caldera which erupted more than 300 km^3 of magma (Aramaki, 1984) and to the fissure eruptions of ignimbrite from Southern Sierra Madre Occidental, Mexico (Aguirre-Díaz and Labarthe-Hernañdez, 2003; Gottsmann et al., 2009).

Since our model uses cross-section averaged variables only, magma properties are treated in an approximate way. This includes equilibrium water exsolution, absence of gas overpressure with respect to magma pressure, and constant viscosity assumptions. A more realistic description of the effective viscosity (out of the scope of this paper) should account for the coupling with dissolved water, heat loss, viscous dissipation, crystal resorption, and the associated local effects (Costa and Macedonio, 2005; Costa et al., 2007).

Considering those properties and approximations, using the models of Giordano et al. (2008) for melt viscosity and Costa et al. (2009) and Cimarelli et al. (2011) for accounting for the effects of crystals, we estimated a reference effective magma viscosity of $_{108}$ Pa s. In our simplified model, the main effect of magma viscosity is on magma fragmentation depth as high viscosities tend to move fragmentation level at greater depths, because the critical volume fraction of bubbles is attained earlier upon magma ascent. Initial dyke thickness is assumed to be ∼100 m, consistent with typical values estimated for such magma viscosity (Wada, 1994).

Other simplifications are related to rock properties that, for the sake of simplicity, are assumed constant with depth. Although, the variations with depth of some properties such as the Young modulus are evident (e.g., Paulatto, 2010; Costa et al., 2013), the dependence of others, such as the variation of fracture toughness with confining pressure, is not very clear (Rubin, 1993). For example Abou-Sayed (1977) found a 50% increase for limestone toughness at confining pressure of 7 MPa, whereas Schmidt and Huddle (1977) found almost no increase at a confining pressure of 7 MPa but an increase up to a factor 4 at 60 MPa.

All the model input parameters are reported in **Table 1**.

The effect of the far-field extensional stresses is shown in **Figure 2** where we reported the profiles of the tensile stress, σ_t, along the vertical axis of the shallower dyke conduit for both an unpressurized magma reservoir and for a magma reservoir with 10 MPa overpressure (for each condition three different magma chamber pressures are considered). **Figure 2** shows that, for an unpressurized magma reservoir, σ_t can counterbalance the lithostatic loading at the dyke base only if the far-field stress is about −40 MPa or larger. Whereas when the reservoir has an overpressure of 10 MPa such condition is reached for a far-field stress around −30 MPa or lower.

TABLE 1 | Parameters used in the simulations (estimated from Costa et al., 2011, 2014; Chesner, 2012).

Symbol	Parameter	YTT
x_{tot}	Concentration of dissolved gas	6 wt%
T	Magma temperature	1053 K
x_C	Magma crystal fraction	40 wt%
μ	Magma viscosity	10^8 Pa s
E_D	Dynamic rock Young modulus	40 GPa
G	Static host rock rigidity	6 GPa
υ	Poisson ratio	0.3
β	Bulk modulus of melt/crystal	10 GPa
ρ_{lo}	Density of the melt phase	2300 kg m^{-3}
ρ_{co}	Density of crystals	2800 kg m^{-3}
ρ_r	Host rock density	2600 kg m^{-3}
S	Solubility coefficient	$4.1 \cdot 10^{-6}$ Pa$^{-1/2}$
N	Solubility exponent	0.5
L	Depth of magma chamber roof	5 km
P_C	Magma chamber pressure	115–140 MPa
$2a_C$ (D_C)	Magma chamber width (Equivalent diameter)	30 km (10 km)
$2c_C$ (D_C)	Magma chamber height (Equivalent diameter)	3 km (10 km)
$2b_C$	Magma chamber elongation	100 km
V_C	Magma chamber volume	5000 km^3
L_R	Depth of magma reservoir roof	10 km
$2a_R$	Magma reservoir width	10 km
$2c_R$	Magma reservoir height	10 km
$2b_R$	Magma reservoir elongation	100 km
V_R	Magma reservoir volume	5000 km^3
ΔP_R	Magma reservoir overpressure	0–20 MPa

As shown in **Figure 3**, the increased tensile stress affects the local pressure difference (given as the magma pressure minus the effects of lithostatic loading and tensile stress). In order to get almost neutral conditions at the base of the dyke, in absence of a pressurized reservoir, a far-field stress of about −40 MPa or larger is needed. Whereas, considering a pressurized reservoir a far-field stress of about −30 MPa or lower is enough.

The maximum sustainable length of the shallow dyke conduit (Costa et al., 2009, 2011) and the MER as function of the extensional far-field stress are reported in **Figure 4**. We can see that maximum sustainable lengths of the dyke can range from a few to a few tens kms depending on the extensional far-field stress and magma reservoir overpressure. Similarly the maximum MER can span from 10^9 to about 10^{11} kg/s as function of the extensional stress, magma chamber depth, and magma reservoir overpressure. As it is shown for comparison in **Figure 4** and discussed by Costa et al. (2011), a much shallower magma chamber (e.g., 3 km depth) would be able to erupt higher MER for the same far-field stress.

DISCUSSION AND OPEN PROBLEMS

We have shown that in order to produce extremely large eruption intensities of highly silicic magmas, such as those characterizing LCFEs, it is necessary to consider the effects of the local stress field resulting from the combination of an extensional far-field stress and a pressurized magma reservoir. Our simulations indicate that MERs of $10^{10}-10^{11}$ kg/s are promoted during moderate to high extensional far field stress (20–40 MPa), a pressurized magma reservoir (∼10 MPa), and relatively shallow magma chambers (3–5 km).

We need to remark that these calculations represent a first-order description aimed at capturing some general features and the proper order of magnitude of the estimated quantities. For a more accurate description other factors should be considered besides the approximations described above. A more correct description of a dual magma chamber system (Melnik and Costa, 2014) should consider not only the effect of a pressurized magma reservoir on the tensile stress within the shallow dyke conduit, but even the control of the magma reservoir on the dynamics of the shallow magma chamber. This is important to characterize how the response of the deeper dyke to local pressure variation can alter magma feeding into the chamber on time-scales comparable to the eruption duration. Dealing with such complex dynamics is out the scope of this work and is the subject of ongoing research.

Our study analyses the conditions required to keep magma conduits open during caldera formation and these will be the same irrespectively on how these eruption pathways have been opened. Because the high magma viscosity, fragmentation level is typically very deep (basically at the roof of the chamber). The effect of a far-field extensional stress is needed in order to permit magma pressure can counterbalance lithostatic loading.

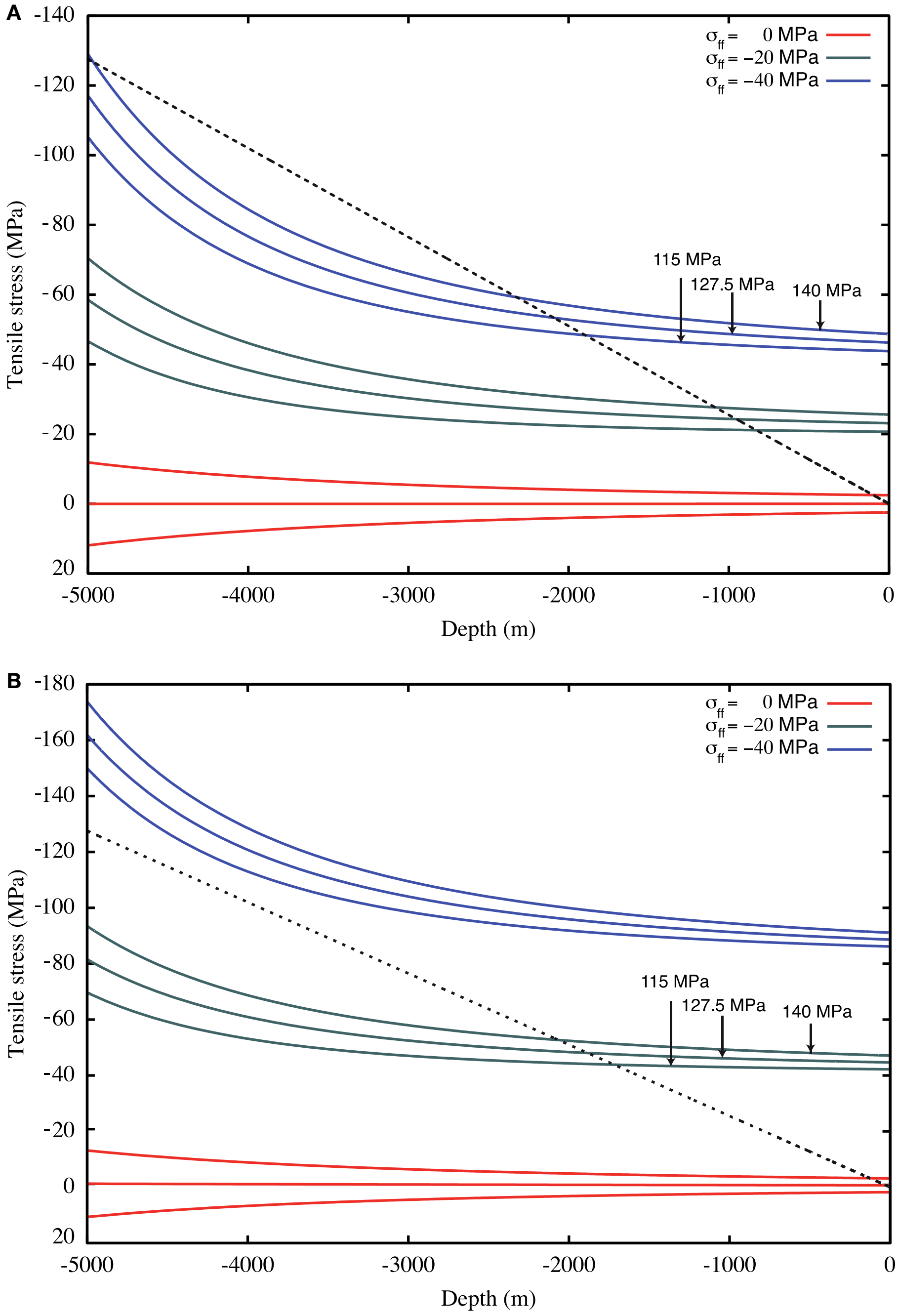

FIGURE 2 | Dyke tensile stress σ_t profile along the vertical axis of the shallower dyke conduit obtained using the analytical solution presented by Gao (1996) for a pressurized magma chamber at 5 km depth (at lithostatic pressure and ±12.5 MPa, as indicated) under the effect of different far-field extensional stresses (from 0 to −40 MPa, as indicated in the figures), for an unpressurized magma reservoir (A) and a pressurized (+10 MPa) reservoir at 10 km depth (B). Dashed line represents the lithostatic pressure. Note that the critical extensional stress that will produce a tensile stress at the dyke base able to counterbalance the lithostatic pressure is different in the two cases: in **(A)** for σ_{ff} of −40 MPa or stronger the dyke remains open, whereas in **(B)**, due to the presence of a pressurized magma reservoir, this critical stress is decreased at 20–30 MPa (for more realistic geometries these effects will be much larger, see Section Discussion and Open Problems).

However, the current model does not consider rock failure occurring in over- and under-pressure conditions (Costa et al., 2009). In our case significant rock failure should occur below and across fragmentation depth (**Figure 3**), implying the partial destruction of the roof of the magma chamber likely moving the fragmentation inside the chamber producing a stable system

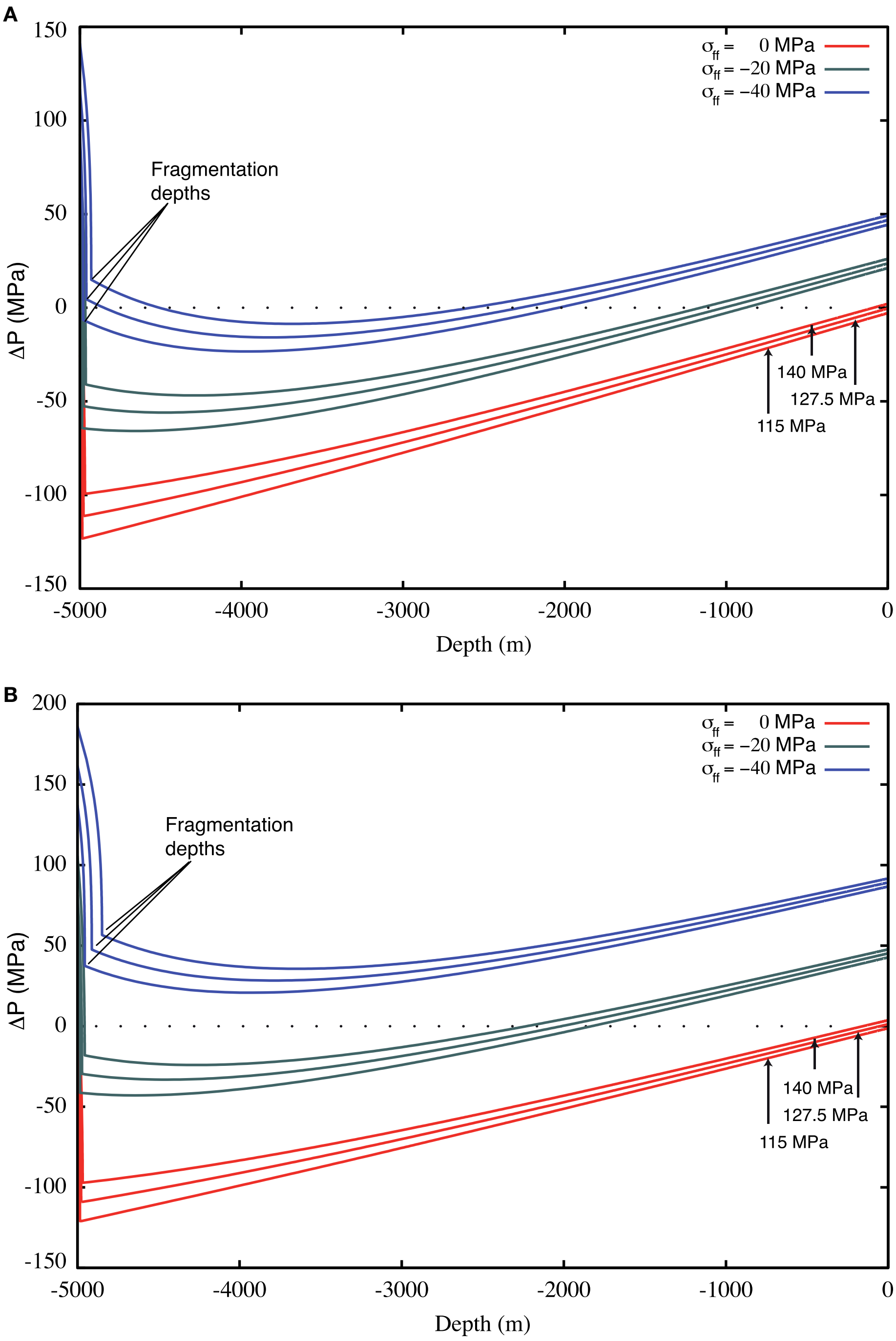

FIGURE 3 | Pressure difference (magma pressure—lithostatic loading—tensile stress) profile along the vertical axis of the shallow dyke conduit obtained using the analytical solution presented by Gao (1996) for a pressurized magma chamber at 5 km depth (at lithostatic pressures and ±12.5 MPa, as indicated) under the effect of different far-field extensional stresses (from 0 to −40 MPa, as indicated in the figures), for a unpressurized magma reservoir (A) and a pressurized (+10 MPa) reservoir at 10 km depth (B). On the top **(A)**, for an unpressurized magma reservoir σ_{ff} moduli larger then 40 MPa are needed to reach neutral conditions along the dyke. On the bottom **(B)**, the presence of a pressurized magma reservoir reduces the critical extensional stress needed to reach neutral conditions at 20–30 MPa.

more suitable to maintain the dyke opened. This implies that, in caldera eruptions that are preceded by a Plinian phase (i.e., MER $\lesssim 10^9$ kg/s; Koyaguchi et al., 2010) for getting a transition to larger MER, the caldera collapse phase must be accompanied by a change in the mechanical conditions of the system that allow magma to fragment much deeper when flowing up through

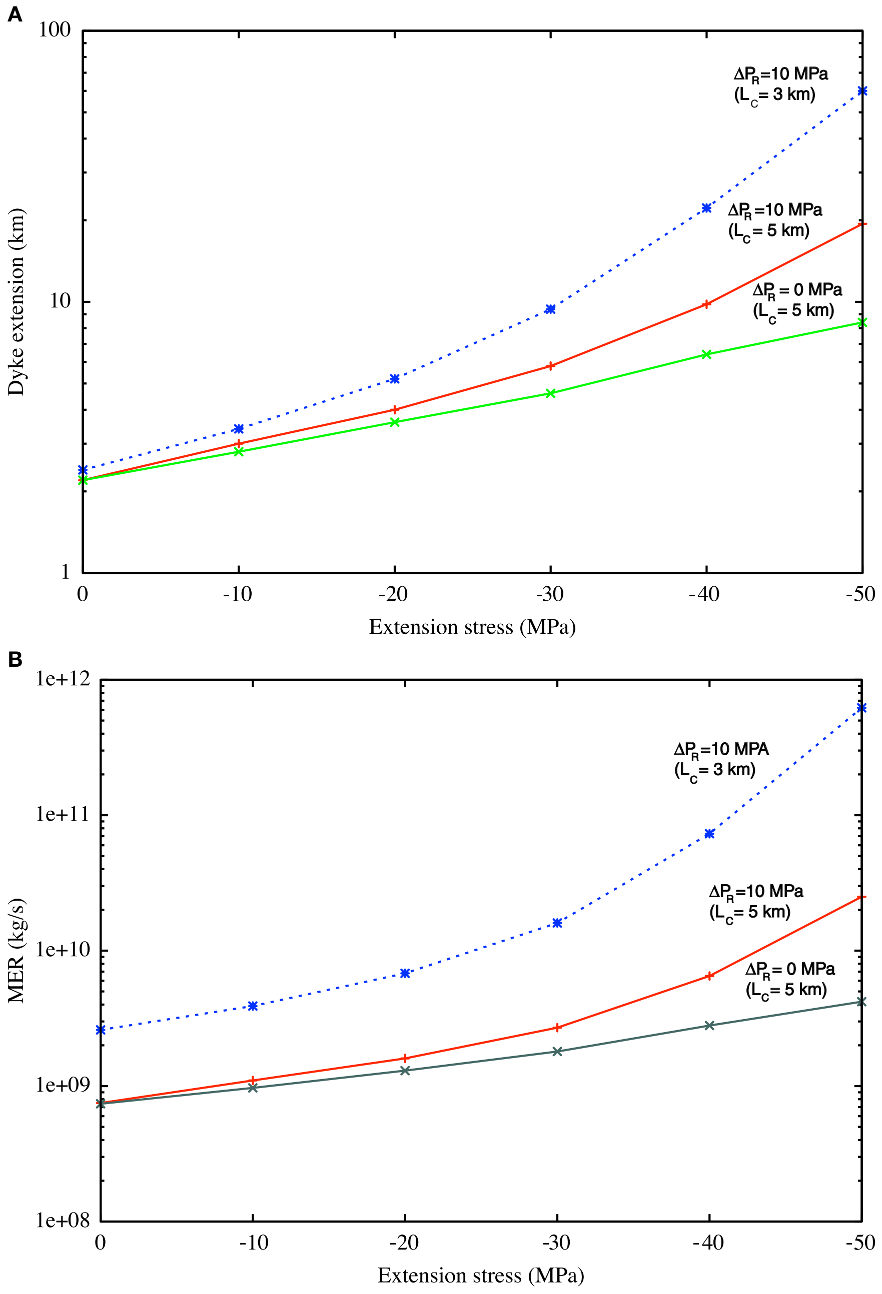

FIGURE 4 | Effects of extensional far-field stress on (A) maximum sustainable length of the shallow dyke conduit and (B) MER. (A) Maximum sustainable lengths of the shallow dyke conduit depend on the extensional far-field stress and magma reservoir overpressure, ranging from a few to a few tens kms. **(B)** Similarly maximum MERs are a function of the extensional stress and magma reservoir overpressure, ranging from 10^9 to 10^{11} kg/s.

the ring fault. This agrees with previous models (e.g., Williams, 1941; Druitt and Sparks, 1984; Martí et al., 2000) that assume a considerable decompression on the magma chamber as a necessary requisite to permit caldera collapse. In the case where a part of the ring fault was open by a tectonic event, the conditions for magma fragmentation to occur very deep in the conduit would be achieved early in the eruption. In such situations it would not be necessary to have a significant decompression of the chamber to allow caldera collapse, as it is suggested by the lack of pre-caldera deposits in many LCFE (Martí et al., 2009).

CONCLUSIONS

Our study indicates that in order to erupt large volumes of silicic magmas during LCFE in relatively short times (e.g., large

MER estimated in the range 10^9-10^{11} kg/s), it is necessary to account for the combined effect of extensional far-field stress and pressurization conditions of magma chambers and reservoirs. In presence of a pressurized deep reservoir even intermediate extensional crustal stresses (20–30 MPa) facilitate an efficient evacuation of large magmatic chambers through a shallow dyke conduit. Largest MERs are promoted in system having a shallow magma chamber (3–5 km). Large MERs are maintained even for under-pressurized magma chamber. Simulation results are consistent with geological observations of LCFE. However, the model assumes that the dyke is already formed and does not account for rock failure that could change drastically the geometry of the system (e.g., chamber roof collapse) as the eruption proceeds. Our results help to address future research aimed to advance our knowledge on the dynamics of these rare catastrophic events.

AUTHOR CONTRIBUTIONS

AC developed the new code version and ran the simulations. AC, JM analyzed the results and wrote the manuscript.

ACKNOWLEDGMENTS

Two reviewers and the editor Agust Gudmundsson are warmly thanked for their constructive feedback. AC is grateful to T. Koyaguchi and P. Gregg for fruitful discussion during his stay at the Earthquake Research Institute, the University of Tokyo.

REFERENCES

Abou-Sayed, A. S. (1977). "Fracture toughness KIC of triaxially loaded Indiana limestone," in *Proc. 17th U.S. Symposium Rock Mechanics* (Keystone).

Acocella, V. (2007). Understanding caldera structure and development: An overview of analogue models compared to natural calderas. *Earth Sci. Rev*. 85, 125–160. doi: 10.1016/j.earscirev. 2007.08.004.

Acocella, V., Di Lorenzo, R., Newhall, C., and Scandone, R. (2015). An overview of recent (1988 to 2014) caldera unrest: knowledge and perspectives. *Rev. Geophys.* 53, 896–955. doi: 10.1002/2015RG000492

Acocella, V., and Funiciello, F. (2010). Kinematic setting and structural control of arc volcanism, Earth Planet. *Sci. Lett*. 289, 43–53. doi: 10.1016/j.epsl.2009.10.027

Aguirre-Díaz, G. J., Labarthe-Hernández, G., Tristán-González, M., Nieto-Obregón, J., and Gutiérrez-Palomares, I. (2008). "Ignimbrite Flare-up and graben-calderas of the Sierra Madre Occidental, Mexico," in *Caldera Volcanism: Analysis, Modelling and Response, Developments in Volcanology,* Vol. 10., eds J. Martí and J. Gottsmann (Amsterdam: Elsevier), 492.

Aguirre-Díaz, G., and Labarthe-Hernañdez, G. (2003). Fissure ignimbrites: fissure-source origin for voluminous ignimbrites of the Sierra Madre Occidental and its relationship with Basin and Range faulting. *Geology* 31, 773–776. doi: 10.1130/G19665.1

Aramaki, S. (1984). Formation of the Aira Caldera, Southern Kyushu, 22,000 Years Ago. *J. Geophys. Res.* 89, 8485–8501.

Bacon, C. R. (1983). Eruptive history of Mount Mazama and Crater Lake Caldera, Cascade Range, U.S.A. *J. Volcanol. Geother. Res.* 18, 57–115.

Baines, P. G., and Sparks, R. S. J. (2005). Dynamics of giant volcanic ash clouds from supervolcanic eruptions. *Geophys. Res. Lett*. 32, L24808. doi: 10.1029/2005GL024597

Burov, E. B., and Guillou-Frottier, L. (1999). Thermomechanical behaviour of large ash flow calderas. *J. Geophys. Res*. 104, 23081–23109. doi: 10.1029/1999JB900227

Chesner, C. A. (1998). Petrogenesis of the Toba Tuffs, Sumatra, Indonesia. *J. Petrol.* 39, 397–438.

Chesner, C. A. (2012). The toba caldera complex. *Quat. Int.* 258, 5–18. doi: 10.1016/j.quaint.2011.09.025

Cimarelli, C., Costa, A., Mueller, S., and Mader, H. (2011). Rheology of magmas with bimodal crystal size and shape distributions: insights from analogue experiments. *Geochem. Geophys. Geosyst*. 12, Q07024. doi: 10.1029/2011GC003606

Cole, J. W., Spinks, K. D., Deering, C. D., Nairn, I. A., and Leonard, G. S. (2010). Volcanic and structural evolution of the Okataina Volcanic Centre; dominantly silicic volcanism associated with the Taupo Rift, New Zealand. *J. Volcanol. Geother. Res.* 190, 123–135. doi: 10.1016/j.jvolgeores.2009. 08.011

Costa, A., Gottsmann, J., Melnik, O., and Sparks, R. S. J. (2011). A stress-controlled mechanism for the intensity of very large magnitude explosive eruptions. *Earth Planet. Sci. Lett.* 310, 161–166. doi: 10.1016/j.epsl.2011.07.024

Costa, A., and Macedonio, G. (2005). Viscous heating effects in fluids with temperature-dependent viscosity: triggering of secondary flows. *J. Fluid Mech.* 540, 21–38. doi: 10.1017/S0022112005006075

Costa, A., Melnik, O., and Vedeneeva, E. (2007). Thermal effects during magma ascent in conduits. *J. Geophys. Res.* 112:B12205. doi: 10.1029/2007JB004985

Costa, A., Smith, V., Macedonio, G., and Matthews, N. (2014). The magnitude and impact of the Youngest Toba Tuff super-eruption. *Front. Earth Sci.* 2:16. doi: 10.3389/feart.2014.00016

Costa, A., Sparks, R. S. J., Macedonio, G., and Melnik, O. (2009). Effects of wall-rock elasticity on magma flow in dykes during explosive eruptions. *Earth Planet. Sci. Lett*. 288, 455–462. doi: 10.1016/j.epsl.2007.05.024

Costa, A., Wadge, G., Stewart, R., and Odbert, H. (2013). Coupled sub-daily and multi-week cycles during the lava dome eruption of Soufriere Hills Volcano, Montserrat. *J. Geophys. Res*. 118, 1895–1903. doi: 10.1002/jgrb. 50095

Druitt, T. H., and Francaviglia, V. (1992). Caldera formation on Santorini and the physiography of the islands in the late Bronze Age. *Bull. Volcanol.* 54, 484–493.

Druitt, T. H., and Sparks, R. S. J. (1984). On the formation of calderas during ignimbrite eruptions. *Nature* 310, 679–681.

Folch, A., and Martí, J. (1998). The generation of overpressure in felsic magma chambers by replenishment. *Earth Planet. Sci. Lett.* 163, 301–314.

Folch, A., and Martí, J. (2004). Geometrical and mechanical constraints on the formation of ring-fault calderas. *Earth Planet. Sci. Lett*. 221, 215–225. doi: 10.1016/S0012-821X(04)00101-3

Folch, A., and Martí, J. (2009). Time-dependent chamber and vent conditions during explosive caldera-forming eruptions. *Earth Planet. Sci. Lett*. 280, 246–253. doi: 10.1016/j.epsl.2009.01.035

Folch, A., Martí, J., Codina, R., and Vazquez, M. (1998). A numerical model for temporal variations durino explosive central vent eruptions. *J. Geophys. Res*. 103, 20883–20899.

Folkes, C. B., Wright, H. M., Cas, R. A. F., de Silva, S. L., Lesti, C., and Viramonte, J. G. (2011). A re-appraisal of the stratigraphy and volcanology of the Cerro Galan volcanic system, NW Argentina. *Bull. Volcanol.* 73:1427–1454. doi: 10.1007/s00445-011-0459-y

Gao, X.-L. (1996). A general solution of an infinite elastic plate with an elliptic hole under biaxial loading. *Int. J. Pres. Ves. Piping* 67, 95–104.

Gardeweg, M., and Ramirez, C. F. (1987). La Pacana caldera and the Atana Ignimbrite - A major ash-flow and resurgent caldera complex in the Andes of northern Chile. *Bull. Volcanol*. 49, 547–566.

Geshi, N., and Miyabuchi, Y. (2016). Conduit enlargement during the precursory Plinian eruption of Aira Caldera, Japan. *Bull. Volcanol.* 78, 63. doi: 10.1007/s00445-016-1057-9

Geyer, A., and Martí, J. (2008). The new worldwide Collapse Caldera Database (CCDB): a tool for studying and understanding caldera processes. *J. Volcanol. Geotherm. Res.* 175, 334–354. doi: 10.1016/j.jvolgeores.2008.03.017

Geyer, A., and Martí, J. (2014). A short review of our current understanding of the development of ring faults during collapse caldera formation. *Front. Earth Sci.* 2:22, doi: 10.3389/feart.2014.00022

Giordano, D., Russel, J. K., and Dingwell, D. B. (2008). Viscosity of magmatic liquids: a model, Earth Planet. *Sci. Lett*. 271, 123–134, doi: 10.1016/j.epsl.2008.03.038

Gottsmann, J., Lavallée, Y., Martí, J., and Aguirre-Díaz, G. (2009). Magma–tectonic interaction and the eruption of silicic batholiths. *Earth Planet. Sci. Lett*. 284, 426–434. doi: 10.1016/j.epsl.2009.05.008

Gray, J. P., and Monaghan, J. J. (2004). Numerical modelling of stress fields and fracture around magma chambers. *J. Volcanol. Geotherm. Res*. 135, 259–283. doi: 10.1016/j.jvolgeores.2004.03.005

Gregg, P. M., de Silva, S. L., Grosfils, E. B., and Parmigiani, J. P. (2012). Catastrophic caldera-forming eruptions: thermomechanics and implications for eruption triggering and maximum caldera dimensions on Earth. *J. Volcanol. Geotherm. Res.* 241–242, 1–12. doi: 10.1016/j.jvolgeores.2012.06.009

Gregg, P. M., Grosfils, E. B., and de Silva, S. L. (2015). Catastrophic caldera-forming eruptions II: the subordinate role of magma buoyancy as an eruption trigger. *J. Volcanol. Geotherm. Res*. 305, 100–113. doi: 10.1016/j.jvolgeores.2015.09.022

Gudmundsson, A. (1988). Effect of tensile stress concentration around magma chambers on intrusion and extrusion frequencies. *J. Volcanol. Geotherm. Res*. 35, 179–194.

Gudmundsson, A. (1998). Formation and development of normal-fault calderas and the initiation of large explosive eruptions. *Bull. Volcanol*. 60, 160–170.

Gudmundsson, A. (2002). Emplacement and arrest of sheets and dykes in central volcanoes. *J. Volcanol. Geotherm. Res*. 116, 279–298. doi: 10.1016/S0377-0273(02)00226-3

Gudmundsson, A. (2006). How local stresses control magma-chamber ruptures, dyke injections, and eruptions in composite volcanoes. *Earth Sci. Rev.* 79, 1–31. doi: 10.1016/j.earscirev.2006.06.006

Gudmundsson, A. (2012). Magma chambers: Formation, local stresses, excess pressures, and compartments. *J. Volcanol. Geotherm. Res*. 237–238, 19–42. doi: 10.1016/j.jvolgeores.2012.05.015

Gudmundsson, A. (2015). Collapse-driven eruptions. *J. Volcanol. Geotherm. Res*. 304, 1–10. doi: 10.1016/j.jvolgeores.2015.07.033

Gudmundsson, A., Martí, J., and Turon, E. (1997). Stress fields generating ring faults in volcanoes. *Geophys. Res. Lett*. 24, 1559–1562. doi: 10.1029/97GL01494

Hautmann, S., Gottsmann, J., Sparks, R. S. J., Costa, A., Melnik, O., and Voight, B. (2009). Modelling ground deformation caused by oscillating overpressure in a dyke conduit at Soufriere Hills Volcano, Montserrat. *Tectonophysics* 471, 87–95. doi: 10.1016/j.tecto.2008.10.021

Hildreth, W. (1991). The timing of caldera collapse at Mount Katmai in response to magma withdrawal toward Novarupta. *Geophys. Res. Lett*. 18, 1541–1544.

Hildreth, W., and Mahood, G. A. (1986). Ring-fracture eruption of the Bishop Tuff. *Geol. Soc. Am. Bull*. 97, 396–403.

Hughes, G. H., and Mahood, G. A. (2008). Tectonic controls on the nature of large silicic calderas in volcanic arcs. *Geology* 36, 627–630. doi: 10.1130/G24796A.1

Jaeger, J. C. (1961). The cooling of irregularly shaped igneous bodies. *Am. J. Sci.* 259, 721–734.

Jaeger, J. C. (1964). Thermal effects of intrusions. *Rev. Geophys.* 2, 443–466.

Jellinek, A. M., and De Paolo, D. J. (2003). A model for the origin of large silicic magma chambers: precursors of caldera-forming eruptions. *Bull. Volcanol*. 65, 363–381. doi: 10.1007/s00445-003-0277-y

Korringa, M. K. (1973). Linear vent area of the Soldier Meadow Tuff, an ash-flow sheet in northwestern Nevada. *Geol. Soc. Am. Bull*. 84, 3849–3866.

Koyaguchi, T., Suzuki, Y. J., and Kozono, T. (2010). Effects of the crater on eruption column dynamics. *J. Geophys. Res*. 115, B07205. doi: 10.1029/2009JB007146

Lipman, P. W. (1984). The roots of ash-flow calderas in North America: windows into the tops of granitic batholiths. *J. Geophys. Res*. 89, 8801–8841.

Macedonio, G., Neri, A., Martí, J., and Folch, A. (2005). Temporal evolution of flow conditions in sustained magmatic explosive eruptions. *J. Volcanol. Geotherm. Res*. 143, 153–172. doi: 10.1016/j.jvolgeores.2004.09.015

Martí, J., Folch, A., Macedonio, G., and Neri, A. (2000). Pressure evolution during caldera forming eruptions. *Earth Planet. Sci. Lett*. 175, 275–287. doi: 10.1016/S0012-821X(99)00296-4

Martí, A., Folch, A., Costa, A., and Engwell, A. (2016). Reconstructing the plinian and co-ignimbrite sources of large volcanic eruptions: a novel approach for the Campanian Ignimbrite. *Nat. Sci. Rep*. 6:21220. doi: 10.1038/srep21220

Martí, J., Geyer, A., and Folch, A. (2009). "A genetic classification of collapse calderas based on field studies, analogue and theoretical modelling," in *Volcanology: the Legacy of GPL Walker,* eds T. Thordarson and S. Self (London: IAVCEI-Geological Socety of London), 249–266.

Matthews, N. E., Pyle, D. M., Smith, V. C., Wilson, C. J. N., Huber, C., and van Hinsberg, V. (2011). Quartz zoning and the pre-eruptive evolution of the ∼340 ka Whakamaru magma systems, New Zealand. *Contr. Mineral. Petrol*. 163, 87–107. doi: 10.1007/s00410-011-0660-1

Matthews, N. E., Smith, V. C., Costa, A., Pyle, D. M., Durant, A. J., and Pearce, N. J. G. (2012). Ultra-distal tephra deposits from super-eruptions: examples from Toba, Indonesia and Taupo Volcanic Zone, New Zealand. *Toba Super Erupt. Impact Ecosys. Hominin* 258, 34–79. doi: 10.1016/j.quaint.2011.07.010

Melnik, O. (1999). Fragmenting magma. *Nature* 397, 394–395.

Melnik, O., and Costa, A. (2014). "Dual chamber-conduit models of non-linear dynamics behaviour at Soufriere Hills volcano," in *The Eruption of Soufriere Hills Volcano, Montserrat from 2000 to 2010*, eds G. Wadge, R. E. A. Robertson and B. Voight (London: Memoir of the Geological Society of London, The Geological Society of London), 501. doi: 10.1144/M39.3

Miller, C., Wark, D., Self, S., Blake, S., and John, D. (2008). (Potentially) Frequently asked questions about supervolcanoes and supereruptions. *Elements* 4, 16.

Muskhelishvili, N. (1963). *Some Basic Problems in the Mathematical Theory of Elasticity*. Leiden: Noordhof.

Pallister, J. S., Hoblitt, R. P., and Reyes, A. G. (1992). A basalt trigger for the 1991 eruptions of Pinatubo volcano. *Nature* 356, 426–428.

Papale, P. (1999). Strain-induced magma fragmentation in explosive eruptions. *Nature* 397, 425–428.

Paulatto, M., Minshull, T. A., Baptie, B., Dean, S., Hammond, J. O. S., Henstock, T., et al. (2010). Upper crustal structure of an active volcano from refraction/reflection tomography, Montserrat, Lesser Antilles. *Geophys. J. Int.* 180, 685–696. doi: 10.1111/j.1365-246X.2009.04445.x

Petrinovic, I., Martí, J., Aguirre-Díaz, G., Guzmán, S., Geyer, A., and Salado Paz, N. (2010). The Cerro Aguas Calientes caldera, NW Argentina: an example of a tectonically controlled, polygenetic collapse caldera, and its regional significance. *J. Volcanol. Geotherm. Res*. 194, 15–26. doi: 10.1016/j.jvolgeores.2010.04.012

Pittari, A., Cas, R. A. F., Wolff, J. A., Nichols, H. J., and Martí, J. (2008). The use of lithic clast distributions in pyroclastic deposits to understand pre- and syn-caldera collapse processes: a case study of the Abrigo Ignimbrite, Tenerife, Canary Islands," in *Caldera Volcanism: Analysis, Modelling and Response: Developments in Volcanology*, eds J. Gottsmann, and J. Martí (Amsterdam: Elsevier), 97–142.

Reyners, M. E. (2010). Stress and strain from earthquakes at the southern termination of the Taupo Volcanic Zone, New Zealand. *J. Volcanol. Geotherm. Res*. 190, 82–88. doi: 10.1016/j.jvolgeores.2009.02.016

Roche, O., Buesch, D. C., and Valentine, G. A. (2016). Slow-moving and far-travelled dense pyroclastic flows during the Peach Spring super-eruption. *Nat. Communic.* 7:10890. doi:10.1038/ncomms10890

Rowland, J. V., Wilson, C. J. N., and Gravley, D. M. (2010). Spatial and temporal variations in magma-assisted rifting, Taupo Volcanic Zone, New Zealand. *J. Volcanol. Geotherm. Res*. 190, 89–108. doi: 10.1016/j.jvolgeores.2009.05.004

Rubin, A. M. (1993). Tensile fracture of rock at high confining pressure: implications for dike propagation. *J. Geophys. Res.* 98, 15919–15935.

Rubin, A. M. (1995). Propagation of magma-filled cracks. *Annu. Rev. Earth Planet. Sci*. 23, 287–336.

Schmidt, R. A., and Huddle, C. W. (1977). Effect of confining pressure on fracture toughness of Indiana limestone. *Int. J. Rock Mech. Min. Sci. Geomech. Abstr*. 14, 289–293.

Self, S. (1992). Krakatau revisited: the course of events and interpretation of the 1883 eruption. *Geol. J.* 28, 109–121.

Sigmundsson, F., Hreinsdóttir, S., Hooper, A., Arnadottir, T., Pedersen, R., Roberts, M. J., et al. (2010). Intrusion triggering of the 2010 Eyjafjallajokull explosive eruption. *Nature* 468, 426–430. doi: 10.1038/nature09558

Smith, R. L. (1979). Ash flow magmatism. *Geol. Soc. Am. Spec. Papers* 180, 5–27.

Smith, V. C., Shane, P. A., Nairn, I. A., and Williams, C. M. (2006). Geochemistry and magmatic properties of eruption episodes from Haroharo Linear Vent Zone, Okataina Volcanic Centre, Taupo Volcanic Zone, New Zealand during the last 10 kyr. *Bull. Volcanol.* 69, 57–88. doi: 10.1007/s00445-006-0056-7

Smith, V. C., Shane, P., and Nairn, I. A. (2005). Trends in rhyolite geochemistry, mineralogy, and magma storage during the last 50 kyr at Okataina and Taupo volcanic centres, Taupo Volcanic Zone, New Zealand. *J. Volcanol. Geotherm. Res.* 148, 372–406. doi: 10.1016/j.jvolgeores.2005.05.005

Sneddon, I. N., and Lowengrub, M. (1969). *Crack Problems in the Classical Theory of Elasticity.* New York, NY: Wiley & Sons.

Sobradelo, R., Geyer, A., and Martí, J. (2010). Statistical data analysis of the CCDB (Collapse Caldera Database): Insights on the formation of caldera systems. *J. Volcanol. Geother. Res.* 198, 241–252. doi: 10.1016/j.jvolgeores.2010.09.003

Sparks, R. S. J. (1978). The dynamics of bubble formation and growth in magmas: a review and analysis. *J. Volcanol. Geotherm. Res.* 3, 1–37.

Sparks, R. S. J., Sigurdsson, H., and Wilson, L. (1977). Magma mixing: a mechanism for triggering acid explosive eruptions. *Nature* 267, 315–318.

Spera, F., and Crisp, J. A. (1981). Eruption volume, periodicity, and caldera area: relationships and inferences on development of compositional zonation in silicic magma chambers. *J. Volcanol. Geother. Res.* 11, 169–187.

Suzuki-Kamata, K., Kamata, H., and Bacon, C. R. (1993). Evolution of the caldera-forming eruption at Crater Lake, Oregon, indicated by component analysis of lithic fragments. *J. Geophys. Res.* 98, 14059–14074.

Turcotte, D. L., and Schubert, G. (2002). *Geodynamics, 2nd Edn.* Cambridge: Cambridge University Press.

Wada, Y. (1994). On the relationship between dike width and magma viscosity. *J. Geophys. Res.* 99, 17743–17755. doi: 10.1029/94JB00929

Williams, H. (1941). "Calderas and their origin," in *Bulletin of the Department of Geological Sciences*, Vol. 25, eds University of California Press (Berkeley, CA: University of California Press), 239–346.

Wilson, C. J. N. (2001). The 26.5 ka Oruanui eruption, New Zealand: an introduction and overview. *J. Volcanol. Geotherm. Res.* 112, 133–174. doi: 10.1016/S0377-0273(01)00239-6

Wilson, C. J. N., and Hildreth, W. (1997). The Bishop Tuff: new insights from eruptive stratigraphy. *J. Geol.* 105, 407–439.

Wilson, C. J. N., and Walker, G. P. L. (1981). "Violence in pyroclastic flow eruptions," in *Tephra Studies,* eds S. Self and R. S. J. Sparks (Dordrecht: D. Reidel), 441–448.

Wilson, L., Sparks, R. S. J., and Walker, G. P. L. (1980). Explosive volcanic eruptions: IV. The control of magma properties and conduit geometry on eruptive column behaviours. *Geophys. J. R. Astron. Soc.* 63, 117–148.

Conflict of Interest Statement: The authors declare that the research was conducted in the absence of any commercial or financial relationships that could be construed as a potential conflict of interest.

frontiers in Earth Science

ORIGINAL RESEARCH
published: 14 June 2016
doi: 10.3389/feart.2016.00067

Why Does a Mature Volcano Need New Vents? The Case of the New Southeast Crater at Etna

Valerio Acocella[1]*, *Marco Neri*[2], *Boris Behncke*[2], *Alessandro Bonforte*[2], *Ciro Del Negro*[2] *and Gaetana Ganci*[2]

[1] *Dipartimento di Scienze, Università degli Studi Roma Tre, Roma, Italy,* [2] *Istituto Nazionale di Geofisica e Vulcanologia, Sezione di Catania, Osservatorio Etneo, Catania, Italy*

Mature volcanoes usually erupt from a persistent summit crater. Permanent shifts in vent location are expected to occur after significant structural variations and are seldom documented. Here, we provide such an example that recently occurred at Etna. Eruptive activity at Mount Etna during 2007 focused at the Southeast Crater (SEC), the youngest (formed in 1971) and most active of the four summit craters, and consisted of six paroxysmal episodes. The related erupted volumes, determined by field-based measurements and radiant heat flux curves measured by satellite, totalled 8.67×10^6 m^3. The first four episodes occurred, between late-March and early-May, from the summit of the SEC and short fissures on its flanks. The last two episodes occurred, in September and November, from a new vent ("pit crater" or "proto-NSEC") at the SE base of the SEC cone; this marked the definitive demise of the old SEC and the shift to the new vent. The latter, fed by NW-SE striking dikes propagating from the SEC conduit, formed since early 2011 an independent cone (the New Southeast Crater, or "NSEC") at the base of the SEC. Detailed geodetic reconstruction and structural field observations allow defining the surface deformation pattern of Mount Etna in the last decade. These suggest that the NSEC developed under the NE–SW trending tensile stresses on the volcano summit promoted by accelerated instability of the NE flank of the volcano during inflation periods. The development of the NSEC is not only important from a structural point of view, as its formation may also lead to an increase in volcanic hazard. The case of the NSEC at Etna here reported shows how flank instability may control the distribution and impact of volcanism, including the prolonged shift of the summit vent activity in a mature volcano.

Keywords: eruptive vents, volcano, stress, flank instability, Etna

OPEN ACCESS

Edited by:
Geoffrey Wadge,
University of Reading, UK

Reviewed by:
Roberto Sulpizio,
Università degli Studi di Bari, Italy
Alessandro Tibaldi,
University of the Studies of Milan Bicocca, Italy

****Correspondence:***
Valerio Acocella
acocella@uniroma3.it

Specialty section:
This article was submitted to Volcanology, a section of the journal Frontiers in Earth Science

Received: *31 March 2016*
Accepted: *23 May 2016*
Published: *14 June 2016*

Citation:
Acocella V, Neri M, Behncke B, Bonforte A, Del Negro C and Ganci G (2016) Why Does a Mature Volcano Need New Vents? The Case of the New Southeast Crater at Etna. Front. Earth Sci. 4:67. doi: 10.3389/feart.2016.00067

INTRODUCTION

Mature stratovolcanoes or composite volcanoes usually erupt from a persistent summit crater. Indeed, most volcanic edifices do not show variations in the location of summit volcanism, constantly erupting from the same vent, and especially on the short-term (100 of years or less). This persistency may be found also after major eruptions, and even when these are associated with important structural variations, as the development of sector collapses, as for example at Bezymianny in 1956 and at Mount St. Helens in 1980 (e.g., Belousov et al., 2007, and references therein). Of course, monogenic dike-fed eruptive fissures on the volcano flanks may develop at any time (Acocella and Neri, 2009, and references therein); however, these eruptions are usually not accompanied by permanent variations in the location of summit activity, so that future eruptions may be expected to occur again from the same summit vent.

Despite this persistency, the geological record of some active volcanoes, not only with calderas, as Sakurajima and Aso (Japan) or Okmok (Aleutians), but also including large edifices, as Etna, show a more complicated eruptive pathway; this displays multiple permanent (associated with stable polygenetic activity) craters or cones, suggesting that the location of volcanism within the edifice may vary. However, on the short term (decades or less) there is poor direct witnessing of any permanent shift (creating a new polygenetic cone or crater) in the location of the eruptive vents within a volcano. The rarity of such occurrence also underlines the difficulty in detecting and understanding the possible processes responsible for the variation in the location of volcanism, which at present remain largely elusive.

Possibly, one of the best-documented shifts in volcanic activity has recently occurred at Etna. Indeed, one of the most intriguing features of Etna is the growing number of its summit craters (**Figure 1**), which has increased from one (the former Central Crater, which had existed for many centuries; Guest, 1973) to four in an interval of just 60 years: the Northeast Crater (1911), the Voragine (1945), the Bocca Nuova (1968), and the Southeast Crater (1971) (Del Negro et al., 2013, and references therein). Since the late-1970s, the Southeast Crater (SEC) has been by far the most active, and evolved from a large collapse pit into a >200 m high cone (Behncke et al., 2006), becoming a distinctive landmark at Etna's summit from the south and the east. After an important episode of flank slip in late 2002, associated with the 2002–2003 eruption (Acocella et al., 2003; Neri et al., 2004), volcanic activity focused on the SEC and, from 2007, at a new vent at its SE base (proto-NSEC). This vent, fed by NW-SE striking dikes propagating from the SEC, formed an independent cone (the New Southeast Crater, or NSEC), starting from January 2011.

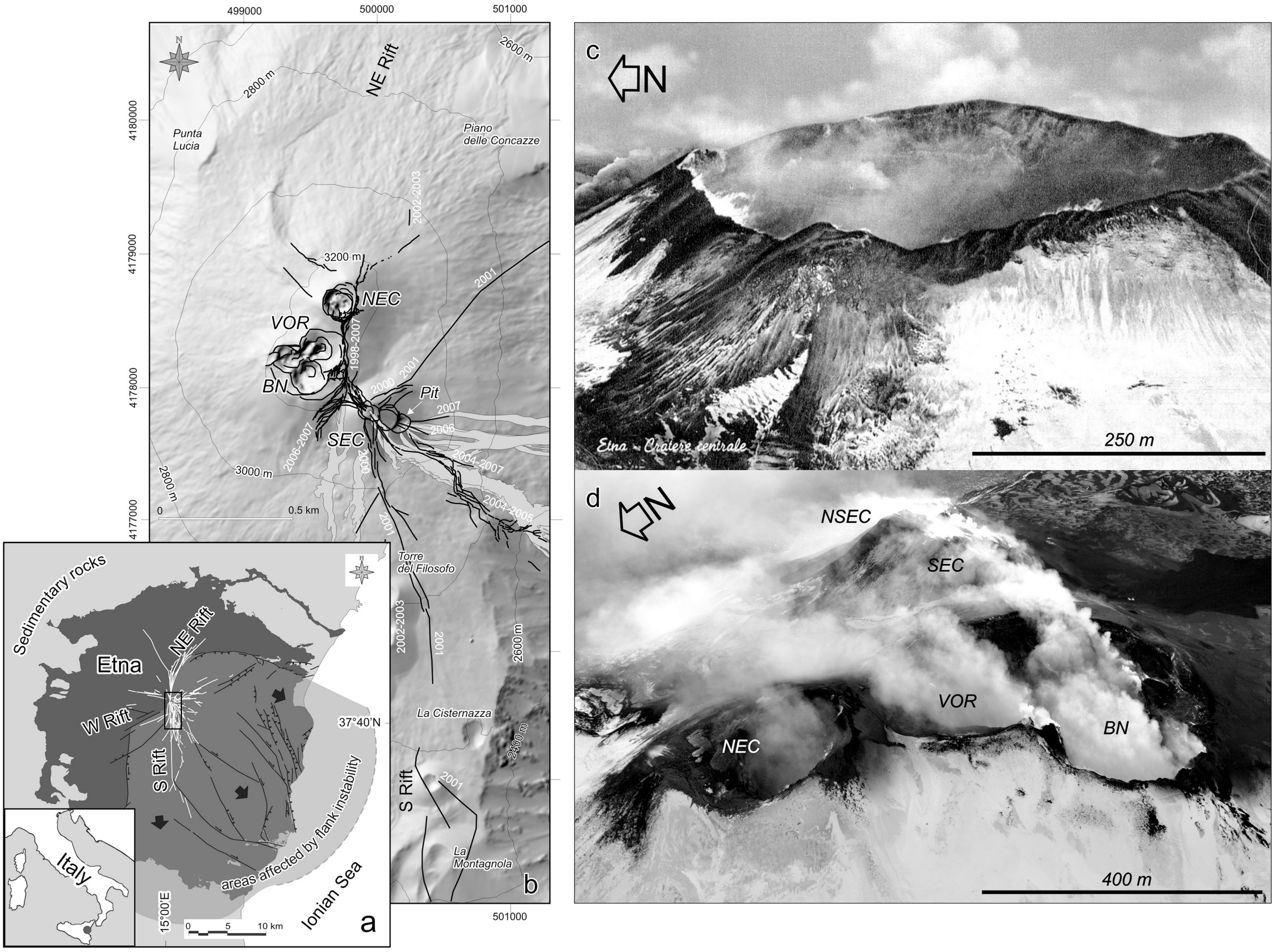

FIGURE 1 | (A) Tectonic framework of Mount Etna, black arrows indicate the unstable eastern and southern flanks of the volcano. **(B)** Eruptive and dry fissures (black lines) opened at the summit of the volcano during 1998–2007, and lava flows erupted in this time interval (light gray). In the last 100 years Etna summit evolved from one Central Crater that existed in the early 20th century **(C)** to 5 summit craters in 2015 **(D)**. VOR, Voragine crater; NEC, Northeast Crater; BN, Bocca Nuova crater; SEC, Southeast Crater; NSEC, New Southeast Crater. Pit, crater discontinuously active in spring 2007. Original photograph in **(C)** was scanned from a postcard that is out of print. The topography in **(B)** is based on a DEM from Bisson et al. (2016).

The shift of the focus of activity from the SEC to the NSEC has been dealt with only marginally in studies dealing with other aspects of the activity in that period (Andronico et al., 2008; Langer et al., 2011; Behncke et al., 2014; Falsaperla et al., 2014; De Beni et al., 2015; Falsaperla and Neri, 2015), and so far remains essentially unexplained.

Here, we describe and quantify the main parameters of the eruptive activity, first at the SEC (spring 2007) and then at the proto-NSEC (summer-fall 2007), using field and satellite data to calculate eruption rates and volumes. Then, using field structural and geodetic (GPS) data, we provide an explanation for the development of the NSEC. In particular, our study at Etna shows how flank instability may control the distribution of volcanism, including the prolonged shift of the summit vent activity at a mature stratovolcano. Overall, this study provides one of the few cases of monitored variation in the location of activity on the summit of a volcanic edifice.

RECENT EVOLUTION AND DYNAMICS OF ETNA

Since the second half of the 20th century, Etna's eruptive activity has undergone several notable changes. Firstly, it has intensified in terms of eruption frequency, long-term average eruption rate, and explosivity, which is most clearly recently expressed in the occurrence of two explosive flank eruptions (2001 and 2002–2003; Acocella and Neri, 2003; Andronico et al., 2005), and an increasing number of strongly explosive eruptions ("paroxysms") at the summit craters (Allard et al., 2006, and references therein). This activity has been accompanied, in 2001–2010, by accelerated flank instability in the eastern to southern sectors of the volcano (Neri et al., 2004; Neri and Acocella, 2006; Bonforte et al., 2007; Falsaperla et al., 2010). This instability may have been caused by the pressurization induced by rapid and voluminous magma accumulation within and below the edifice (Allard et al., 2006), and may have been the most significant event of this type at Etna for many decades or more. During the 2001 and 2002–2003 eruptions and the flank slip episode, the shallow central conduit system—i.e., the magma pathways leading to the summit craters—was disrupted; activity ceased at the SEC for 5 years, whereas the Bocca Nuova remained largely inactive until 2011, and the Voragine reactivated only in 2013, after more than 13 years of quiescence.

In addition, one of the most peculiar characteristics in the recent change of Etna's dynamics is the appearance of numerous, prolonged series of paroxysmal eruptive episodes at the summit craters since the mid-1960s. Such events had previously occurred once or twice per decade (Behncke and Neri, 2003), but at the turn of the millennium they had become the most characteristic eruptive manifestation at Etna. In particular, out of a total of about 150 paroxysmal eruptive episodes at the summit craters between 1995 and 2001, 105 occurred at the SEC (Behncke et al., 2006). Many of the paroxysms at the SEC were characterized by activity from vents not only at its summit, but also from fissures extending down its north-eastern and southern flanks. This trend remained remarkably stable during the exceptional series of paroxysms in 2000 (Alparone et al., 2003; Behncke et al., 2006) and another sequence of paroxysms in 2001 (**Figure 2A**). In contrast, renewed episodic activity at the SEC in 2006 involved the opening of new vents and fissures on its SE, WNW, and W flanks (Neri et al., 2006; Behncke et al., 2008), marking a rotation by about 90° of the main structural trend at the SEC (**Figure 2A**). In late-2004, during a long-lived effusive lateral eruption from vents to the east of the SEC, a collapse pit opened on its eastern slope (Neri and Acocella, 2006). This pit was filled by renewed activity from the SEC in the fall of 2006 (Behncke et al., 2008), but a new collapse pit formed toward the end of this activity, only to be filled again by renewed SEC activity in the spring of 2007 (Behncke et al., 2014).

Finally, another pit crater formed on the lower east flank of the SEC cone in mid-May 2007 (**Figure 2A**), and 3 months

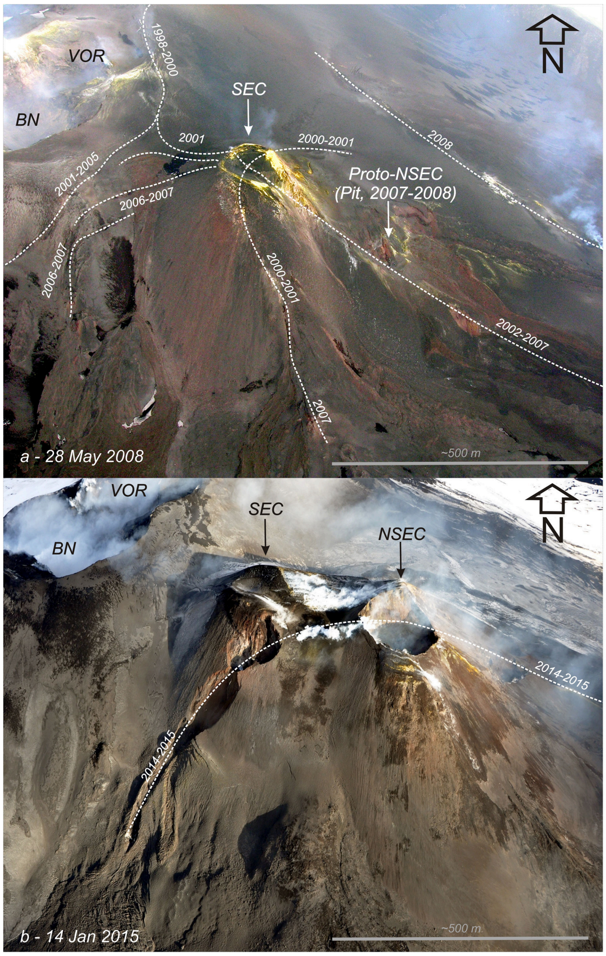

FIGURE 2 | Morpho-structural evolution of the Southeast Crater (SEC) zone in the last decade, interpreting the aerial view from SE taken from a helicopter of the Italian Civil Defense (A) and of the Italian Coast Guard (B). The main eruptive and dry fissures and their age are marked by white dotted lines. **(A)** Location of the "pit crater," formed in the spring of 2007, is the same of the "proto-NSEC" active since autumn 2007. **(B)** The proto-NSEC then evolved into the New Southeast Crater (NSEC), whose cone grew through several tens of paroxysmal eruptions since January 2011.

later this became the focus of renewed eruptive activity, marking a definitive shift from the SEC to the vent which later would became known as the New Southeast Crater (NSEC, **Figure 2B**). Since this pit crater underwent further changes after the 2007 activity, which is described in detail below, we refer to it as "proto-NSEC" to distinguish it from the cone (the NSEC) that started properly growing during the eruptive period initiated in January 2011 (**Figure 2**).

METHODS

Field Observations

Field observations, consisting of volcanological and structural data, were directly acquired in the field since the 1990s and have been integrated by the image analysis of the INGV camera network and by aerial photos taken from helicopters of the Italian Civil Defense and the Italian Coast Guard. Field observations and volcanological and structural mapping consisted of measurements of lava flow fields, eruptive/dry fractures and faults aided by hand-held GPS (lat/lon precision up to 2–4 m). The birth and growth of the NSEC have been documented in detail with the aid of range-finding binoculars connected to GPS (Behncke et al., 2014), as well as LiDAR surveys carried out in 2007 and 2010 (Behncke et al., 2016), and aerophotogrammetry acquired in 2012 and 2014 (De Beni et al., 2015).

Thermal Satellite Data

Satellite data processing techniques have proved well suited to complement field observations for timely detection of eruptive events, as well as extraction of parameters allowing lava flow tracking. Satellite imagery can provide a better understanding of eruptive activity simply by producing more frequent observations at a wide variety of wavelengths. In particular, in the case of short-lived events like lava fountaining episodes, geostationary satellites, with 15 min sample time, provide a unique opportunity to follow the fast evolution of the event from space.

As for the 2007 lava fountains at Mt Etna, data acquired by MODIS (Moderate Resolution Imaging Spectroradiometer) aboard EOS polar-orbiting satellites, and SEVIRI (Spinning Enhanced Visible and InfraRed Imager) aboard the geostationary satellites MSG, were processed via the HOTSAT multiplatform system (Ganci et al., 2011b, 2015). HOTSAT can detect thermal anomalies over volcanic areas and quantify the entity of thermal activity by means of the radiant heat flux computation. Weather conditions play an important role in volcanic activity detection and quantification from satellite, which is the reason why HOTSAT includes a cloud detection algorithm based on textons (Ganci et al., 2011a) and, for each processed images, it provides as output a cloud coverage index. A cloud coverage index equal to 1 means that all the pixels inside the volcanic area are flagged as cloudy; whereas an index of 0 means that no cloudy pixels are detected in the volcanic area. HOTSAT discards those images showing a cloud index >0.5, while a plot of the cloud index is provided with the radiant heat flux to visually check if an attenuated or missing thermal anomaly is due to cloud partial or total obscuration. The system is currently operational on Etna and Stromboli and was tested versus ground-based thermal camera measurements acquired on Etna (Ganci et al., 2013) and on the Nyiragongo lava lake (Spampinato et al., 2013).

Geodetic Data

Ground deformation measurements collected by GPS surveys carried out with the periodic network at Etna from 2005 to 2015 have been exploited to analyse the long-term strain affecting the volcano edifice, with particular focus on its summit. GPS data collected during the surveys, passing through a N-S profile crossing the volcano summit (Puglisi et al., 2004; Puglisi and Bonforte, 2004; Bonforte et al., 2009), allowed strain calculation. Geodetic measurements on the summit part of Etna are possible only in the summer, due to the snow cover during the rest of the year that prevents the access to the highest GPS points. The ground deformation here analyzed has been previously described in terms of displacements of the measurement stations (Bonforte et al., 2008, 2013; Bonaccorso et al., 2011, 2015). Conversely, here we calculate the horizontal strain tensor components by the GridStrain routine developed by Pesci and Teza (2007), already used for investigating the surface deformation of the eastern flank of Etna by Alparone et al. (2011). This algorithm allows us to analyse the strain tensor distribution over an area covered by a geodetic network, starting from station displacements. In our case, a 1500 m spaced grid was set up covering the Etna GPS network and a 2D strain tensor was then calculated at each node of the grid for every subsequent 1-year period from 2005 to 2015.

RESULTS

From SEC to Proto-NSEC: The 2007 Eruptive Activity

The eruptive activity of the SEC in 2007 marks the important shift in the location of volcanism from the SEC to the proto-NSEC and, as such, it is here considered in detail. This activity occurred in two distinct phases. The first lasted from late March until early May and consisted of four paroxysmal episodes (29 March, 11 April, 29 April, and 6–7 May; **Figures 3**, **4A–D**) from the SEC and its flanks, including the proto-NSEC. The first of these was probably the most violent explosive paroxysm at the SEC since 2000, with sustained lava fountaining and a tephra column that produced widespread ash and lapilli falls to the northeast, but its main phase lasted <1 h. The next three eruptive episodes showed a tendency of the activity to become progressively less explosive and more effusive, lasting longer (up to ∼13 h, see **Table 1**). This phase of activity was followed, in mid-May, by the formation of the new collapse pit (proto-NSEC) on the lower ESE flank of the SEC cone. The second phase of activity is characterized only by the activity from the proto-NSEC, without any contribution from the SEC. This second phase started with minor ash emissions from the proto-NSEC in mid-August, and culminated in two episodes of sustained lava fountaining, tephra emission and production of lava flows, on 4–5 September and

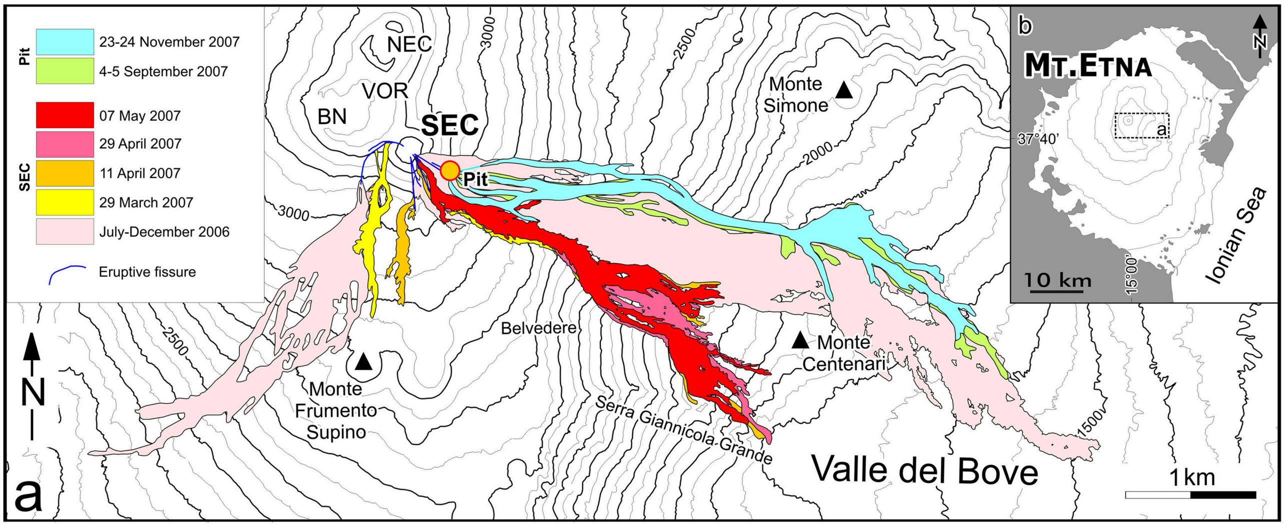

FIGURE 3 | (A) Map of Etna's summit area and upper south and east flanks, showing lava flows emitted during 2007 in different colors and 2006 lavas in Pink. **(B)** Inset shows the location of the area in **(A)**.

23–24 November 2007 (**Figures 3**, **4E,F**). A third paroxysmal eruptive episode, which took place on 10 May 2008, marks the end of the second phase of activity and was followed 3 days later by the onset of Etna's latest flank eruption to date (13 May 2008–6 July 2009). Renewed episodic activity that has been occurring since January 2011 is considered the onset of the phase that has morphologically built the cone, now known as the NSEC, from the proto-NSEC (see Section From Proto-NSEC to NSEC).

Phase 1

29 March Paroxysm

The first of the four eruptive episodes in the spring of 2007 occurred on the morning of 29 March and was probably the most violent paroxysm at the SEC since 2000. The start of the activity at 0524 (GMT = local time-2h) was marked by a sharp increase in the volcanic tremor amplitude. Shortly thereafter, lava fountaining from the summit vent of the SEC reached heights of 600–800 m, and a tephra column rose to several kilometers above the summit, feeding a plume that drifted NE and caused ash and scoria falls at ~6 km from the SEC, and as far as 35 km from Etna's summit (Andronico and Cristaldi, 2007). Fine ash was reported even in southern Calabria, more than 80 km away.

During the climactic activity, lava emission started from two vents located at 3200 and 3190 m above sea level W and SW of the SEC, feeding flows partially overlapped that advanced 1.25 km to the plain between Etna's summit cone complex and the Torre del Filosofo site (**Figures 1**, **4A**). A decrease in the intensity of Strombolian explosions was evident by 0641, marking the imminent cessation of activity. Activity at the SEC summit had diminished to sporadic Strombolian explosions and emission of an ash column, although lava continued to flow through a channel carved into the SE flank of the SEC cone, and then down the steep slope toward the Valle del Bove, that advanced up to 2.35 km from the vent. Here, the lava flow went into contact with snow, producing phreatomagmatic explosions, which in turn produced pyroclastic density currents that sped down the slope. During the following 2 weeks, the volcanic tremor curve showed significant periodic increases similar to the signal accompanying the 29 March paroxysm, but none of these were accompanied by any visible eruptive activity. These events were interpreted as "failed" eruptions by Falsaperla et al. (2014).

11 April Paroxysm

The first signs of the second paroxysm from SEC in 2007 were recorded as a thermal anomaly evident in satellite imagery at 0027 GMT on 11 April. Like its predecessor, this paroxysm was characterized by lava fountaining, lava flow emission, and generation of a tephra column, which this time was driven to the SE, causing tephra falls up to the coastline. Lava was at first emitted from the summit through the channel in the SE flank, and followed a similar path as the 29 March main flow (**Figure 4B**).

Between 0200 and 0300 the activity continued to increase in vigor, and a shift in the wind direction caused ash falls further north. At the peak of the activity, between 0257 and 0412, a short eruptive fissure opened on the lower south flank of the SEC cone, producing fountains from a number of aligned vents and a lava flow, which advanced across the snow-covered plain to the south of the cone (**Figure 4B**). Explosive interaction between lava, snow and meltwater occurred while the flow extended southward, until it stopped at a distance of 0.93 km from its source. The activity at this new fissure lasted only a few hours, and by early morning the paroxysm was over, although both the lava flow to the south and the longer (3.55 km long) flow toward the Valle del Bove continued to advance for several hours during the morning and afternoon of 11 April.

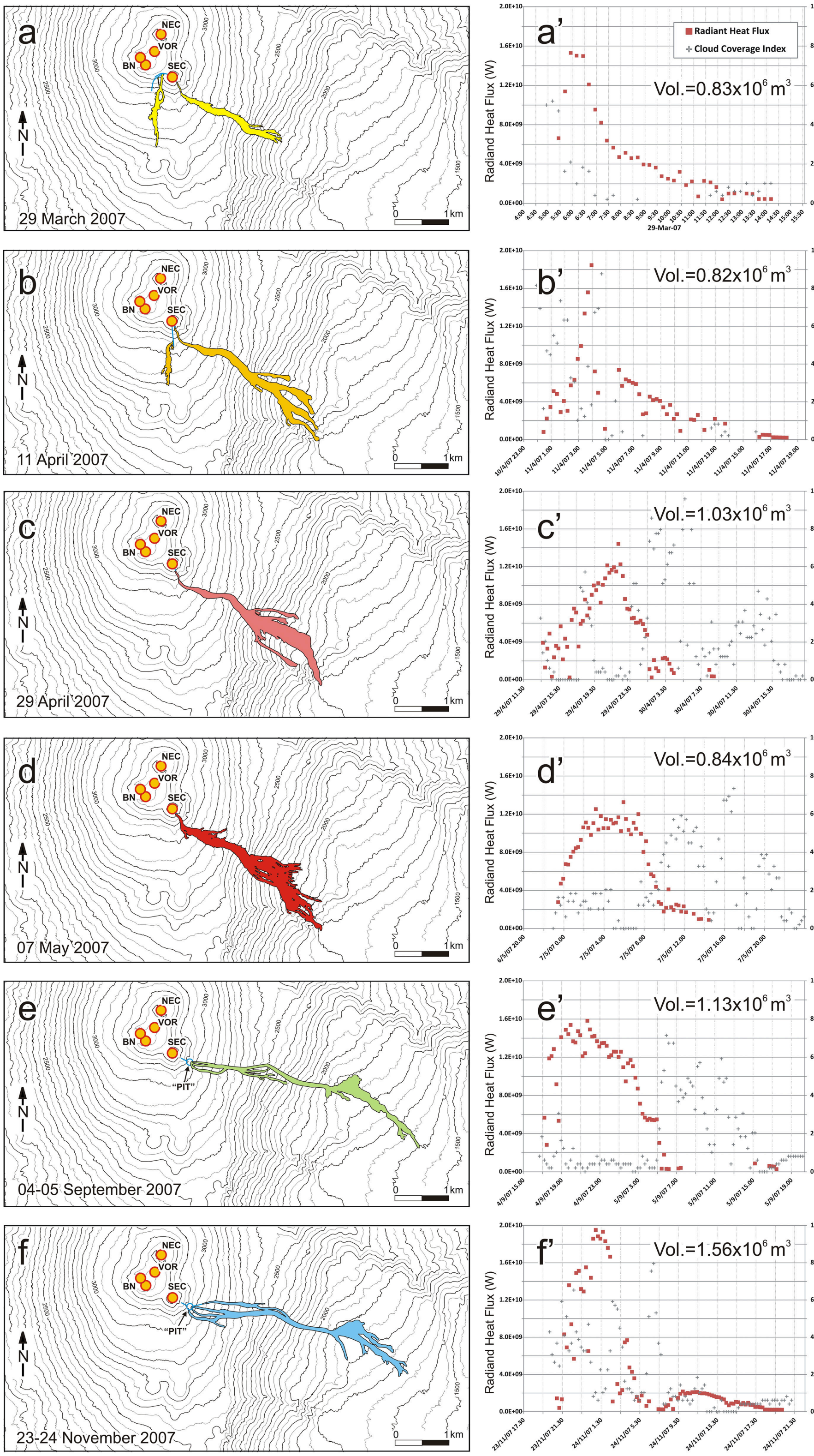

FIGURE 4 | Lava flow maps (A–F) and radiant heat flux curves (A'–F') for the six paroxysmal eruptive episodes at the Southeast Crater and proto-NSEC in 2007.

TABLE 1 | Lava fountain durations and volumes as retrieved from SEVIRI data.

Date	Phase 1 Onset (GMT)	Phase 1 End (GMT)	Duration(hours)	Phase 2 Onset (GMT)	Phase 2 End (GMT)	Duration(hours)	Duration phase 1+2 (hours)	Phase 3 Onset (GMT)	Phase 3 End (GMT)	Duration Phase 3 (hours)	Lava volume (m^3)	Tephra volume (m^3)	Total volume (m^3)	MOR (m^3/s)	Lava area (m^3)	Lava average thickness (m)
29/03	5:24*	5:26	0:02	5:26	6:57	1:33	1:35	6:57	14:12	7:15	8.29E + 05	3.32E + 05	1.16 E + 06	203.694	3.83E + 05	2.2
11/04	0:27	2:57	2:30	2:57	4:12	1:15	3:45	4:12	18:11	13:59	8.21E + 05	3.28E + 05	1.15E + 06	85.091	4.87E + 05	1.7
29/04	9:50*	16:56	7:06	16:56	22:42	5:46	12:52	22:42	8:42	10:00	1.03E + 06	4.10E + 05	1.44 E + 06	30.990	5.00E + 05	2.1
07/05	23:26	0:27	1:01	0:27	7:56	7:29	8:30	7:56	14:42	6:46	8.35E + 05	3.34E + 05	1.17E + 06	38.186	5.83E + 05	1.4
04/09	16:00*	17:42	1:42	17:42	2:42	9:00	10:42	2:42	17:12	14:30	1.13E + 06	4.41E + 05	1.57E + 06	40.883	6.42E + 05	1.8
23/11	16:00*	21:4 2	5:42	21:42	2:26	4:44	10:26	2:26	19:56	17:30	1.56E + 06	6.23E + 05	2.18 E + 06	58.096	7.23E + 05	2.2
							total				6.20E + 06	2.47E + 06	8.67E + 06			

*Times with * are obtained from field observations. Tephra volumes were retrieved from literature (Andronico et al., 2008) or computed as 40% of emitted lava; lava flow areas were measured in the field. MORs were computed as total volumes divided by the eruption durations (Phases 1+2), whereas thickness is obtained from satellite-derived volume (total volumes) divided by lava flow area. MOR, Mean Output Rate.*

29 April Paroxysm

The third paroxysm in the spring of 2007 started from the SEC during the late forenoon of 29 April, from 0950 GMT onward. The eruptive activity increased much more gradually than the early stages of the previous two paroxysms, and it was in full swing by the late afternoon. Explosive activity occurred from several closely spaced vents at the summit of the SEC cone, consisting of nearly continuous strong Strombolian bursts, and a rather dilute tephra column rose a few 100 m above the summit. Lava was delivered from a vent located immediately below the summit of the SEC cone, in a notch that lay at the head of the deep channel carved into the SE flank of the cone during the 2006 activity. The lava flow followed the same path as the main flows of 29 March and 11 April, splitting into numerous branches on the slope before reaching the bottom of the Valle del Bove late that evening, at about 3.6 km from the source (**Figure 4C**). Strombolian activity and lava emission continued until 2242, after which the activity decreased.

7 May Paroxysm

The last of the four paroxysms in the spring of 2007 started shortly before midnight on 6 May, with the onset of Strombolian explosions from a cluster of vents aligned along a short (a few tens of meters long) fissure on the upper SE flank of the SEC cone and at the summit. The climax phase began at 0027 on 7 May, and a lava flow issued from the lower end of the fissure, following the path of the previous lava flows in the direction of the Valle del Bove, reaching a maximum length of 3.38 km (**Figure 4D**). The activity continued at relatively constant levels until 0756, after which the volcanic activity rapidly decreased.

For several weeks, one vent located at the upper end of the 7 May fissure, just below the notch in the SE rim of the crater, was seen to be incandescent at night. In mid-May, a new collapse pit formed on the ESE flank of the SEC cone, in a somewhat lower position than the preceding collapse pits of 2004–2005 and fall 2006. This pit-crater marks the onset of formation of the "proto-NSEC." Ash emissions from this pit occurred on 20 and 24 May, after which there were no eruptive manifestations until mid-August.

Phase 2

On the morning of 15 August, the newly formed proto-NSEC, on the ESE flank of the SEC cone, showed unusual emissions of white vapor, followed in the afternoon by a few bursts of brownish ash. From this moment, the eruptive activity focused at this vent only, without any contribution of the SEC. Similar emissions occurred during the following days, and by 20 August some incandescence could be observed in the emissions at night. From then until the end of August, the explosive activity progressively increased; from the 26th onward the ash content in the emissions decreased and the activity eventually became purely Strombolian. During the first days of September, the explosions produced detonations audible to tens of kilometers away, and sprays of incandescent bombs often fell all over the SEC cone and to distances of several 100 m from its base. Finally, a further increase of the eruptive activity started on the mid-afternoon of 4 September, around 1400 GMT on that day.

4–5 September Paroxysm

The start of sustained lava fountaining from the proto-NSEC ("Pit" in **Figure 4E**) occurred during cloudy weather sometime around 1600 GMT. Soon thereafter, a dark tephra plume rose above the weather clouds and drifted eastward, causing ash falls in areas close to the coastline. When weather clouds finally cleared away at nightfall, a robust jet of incandescent lava was shooting to heights of 400-600 m above the vent, and lava spilled over the rim of the active vent in two places, feeding a flow that advanced toward the Valle del Bove. This activity continued without significant changes for the next ∼9 h, with the lava fountain remaining remarkably stable, and lava advancing 4.6 km across the Valle del Bove, mostly on top of October-December 2006 lavas (**Figure 4E**). At 0242 a decrease in the eruptive intensity was observed; the lava fountain became discontinuous before the end of the paroxysm and was marked by a series of detonations, which launched meter-sized bombs all over the SEC cone.

23–24 November Paroxysm

Following about 2 months of intermittent explosive activity from the proto-NSEC that had been active in August-September, Strombolian explosions began to increase on 22 November. At about 1600 GMT on the following day, a series of explosions from the Bocca Nuova produced dark ash plumes; these were followed by an increase in the intensity of Strombolian activity at the SEC. Between 2030 and 2142, the Strombolian activity passed into sustained fountaining, and lava flowed over the vent's rim in three places, feeding flows toward the ESE and SE (**Figure 4F**). Overall, this paroxysm was similar to that of 4–5 September, except for the following: (a) the fountain was often V-shaped, due to the presence of two closely-spaced vents, (b) the tephra plume was driven NNE, (c) the lava traveled less (∼4 km), largely on top of the 4–5 September flow, and (d) the duration of the paroxysm was 5 h. Like its predecessor, the closing stage of the paroxysm at around 0226 was characterized by bursts of incandescent bombs resembling fireworks and causing detonations.

From Proto-NSEC to NSEC

A third paroxysmal episode from the proto-NSEC occurred on the afternoon of 10 May 2008. This event was less well observed than its two predecessors, because satellite data are sketchy due to dense cloud cover. This paroxysm erupted 5.73×10^6 m^3 of lava (Behncke et al., 2016), and was followed 3 days later by the onset of Etna's latest flank eruption to date (13 May 2008–6 July 2009; Bonaccorso et al., 2009).

Following the long-lived flank eruption of 2008–2009, the proto-NSEC showed occasional signs of reactivation, and its diameter was significantly widened by collapse and by the formation of an additional, but smaller, collapse pit on its eastern rim in November 2009, which soon merged with the proto-NSEC (Behncke et al., 2014, 2016).

Since January 2011, the pit-crater of the proto-NSEC started to build-up a relief (a cone) evolving into the NSEC. The NSEC has been the site of more than 50 eruptive episodes, but since late-2013 there has been a tendency for such episodes to last longer and be less explosive (De Beni et al., 2015). As this new cone began to grow around its eruptive vent, it became evident that the NSEC had permanently taken over the role of Etna's most active summit crater from the SEC.

As of 2016, the NSEC cone, which was built up on sloping terrain, stood at 250–300 m above the former surface, rivaling in height its older "sibling," which it has partly overgrown. Its volume (50×10^6 m^3 as of October 2014; De Beni et al., 2015) is somewhat inferior to that of the old SEC (72×10^6 m^3; Behncke et al., 2006), but nearly all of it was constructed in <3 years. Much of its activity involved the opening of eruptive fissures on the flanks of NSEC growing cone, first seen in August 2011. Between August 2011 and April 2013, much of this activity focused along a NW–SE striking fissure, precisely following the structural axis along which the shift from the SEC to the NSEC had occurred. As the NSEC grew more mature, eruptive vents and fissures opened also into other directions, namely to the SW, SSE, E, and NE of the NSEC.

Erupted Volumes in 2007 from Satellite Data

The six lava fountaining episodes that occurred at Etna during 2007 were detected and monitored by the HOTSAT system. Radiant heat flux curves, as well as cloud coverage index are given for each event in **Figures 4A′–F′**. Radiant heat flux curves generally show peak values around 16 GW during the climax of each event, except for those recorded on 11 April and 23 November, which are close to 20 GW.

These short-lived explosive events show the same features in the thermal signal we recorded during the 13 May 2008 and 2011–2013 lava fountaining episodes at Etna (Bonaccorso et al., 2011; Ganci et al., 2012). Three main phases can be recognized during each episode in the radiant heat flux curve. A first phase that includes the onset of thermal activity and a slow increase of the radiant heat flux; a second phase with scattered high levels of signal, often accompanied by saturated pixels in the MIR (medium infrared) images is linked to the main fountaining phase; and a third phase in which the signal slowly decreases and that is related to the cooling of the lava flow. **Table 1** shows the timing of the different phases for each of the six eruptive episodes in 2007. The duration of the three phases is highly variable, spanning from impulsive events like the one on 29 March, where the first phase is nearly missing and the lava fountaining is brief, to longer events like that on 23 November, in which both the preparatory phase and the fountaining lasted about 5 h, respectively, with a cooling phase of about 17 h.

Since during this type of short-lived events no steady thermal state is reached, the simple conversion between lava flow area and time averaged discharge rate (TADR) cannot be applied (Garel et al., 2015). Therefore, in order to compute the lava volume, we applied the approach of Ganci et al. (2012) by modeling the cooling curve (phase 3) apparent in thermal data acquired by SEVIRI. We take the measured cooling curve and fit this to a theoretical cooling curve. Best fit is achieved by adjusting the area of cooling lava until the measured and theoretical curves match. This technique was tested using ground-based thermal camera images collected during the 12 August 2011 event (Ganci et al., 2013), and the volumes found for all the 2011–2013 events at Etna are in good agreement with field measurements (Behncke et al., 2013; De Beni et al., 2015) and strain meter data processing results (Bonaccorso and Calvari, 2013). Applying the cooling curve modeling we retrieve the lava volume for the six events spanning from 1.15 to 2.18 × 10^6 m^3, as given in **Table 1**.

The Geodetic Frame

The strain tensor evolution around the summit craters and, especially, at the location of SEC and NSEC, shows that, after the deflation accompanying the 2004–2005 eruption (Bonaccorso et al., 2006), an inflation was recorded by the GPS surveys (Bonforte et al., 2008). This inflation produced a dilatation of the summit area and, in particular, in the location of the future NSEC (**Figure 5A**), where an overall NE–SW dilatation of approximately 10 ppm is evident. It is remarkable that the pit crater, which later evolved in the proto-NSEC and finally in the NSEC, opened during this period. The eruptive activity that accompanied and followed the opening of this pit-crater on the eastern flank of SEC in 2007 produced a deflation of the volcano, but the contraction on the summit area was minor (around 2 ppm; **Figure 5B**), especially if compared to the previous dilatation (more than 10 ppm; **Figure 5A**). More significant contraction is visible on the NE flank of the volcano, across the easternmost segment of the Pernicana Fault System (Barreca et al., 2013), but this is a recurrent deformation in this sector of the fault (Bonforte et al., 2007). Later on, from 2007 to 2008, a significant NE–SW stretching of more than 40 ppm of the entire volcano summit has been recorded (**Figure 5C**); this is associated with the intrusion of the NNW-SSE oriented dike on 13 May 2008 that fed the lateral eruption on the upper eastern flank until July 2009 (Bonaccorso et al., 2011; Bonforte et al., 2013). This lateral eruption produced an overall deflation of the edifice but, again, no significant contraction is visible at summit (**Figure 5D**). Once the lateral eruption ended, the volcano inflated again and a homogeneous dilatation is visible on the summit and around the NSEC area after 2009, more intense in 2010 (**Figure 5E**), but continuing until 2011 (**Figure 5F**). From 2011, an overall deflation has been measured, with contraction of the summit area. The contraction of the summit was stronger (∼7 ppm) until 2012, and ENE–WSW-oriented (**Figure 5G**), but it progressively decreased to about 3–4 ppm in the following year (**Figure 5H**) to almost disappear after 2013 (**Figure 5I**). Finally, during 2014–2015, dilatation reappeared, but it affected mostly the southern portion of the summit area, with a NW-SE orientation (**Figure 5J**). This may have prepared the ground for the NE–SW-striking dike intrusion accompanying the paroxysmal episode at the NSEC on 28 December 2014 (Bonforte and Guglielmino, 2015).

DISCUSSION

From SEC to NSEC: Changes in the Eruptive Dynamics

Although it was only with the onset of frequent paroxysmal lava fountaining in early 2011 that the NSEC cone became definitively established as a persistent new summit vent replacing the old SEC, the transition that led to its birth and development had begun as early as 2004, when a pit-crater opened for the first time on the upper east flank of the old SEC cone (Neri and Acocella, 2006). While initially it seemed that this pit resulted from subtraction of magma from below the SEC during the 2004–2005 lateral eruption (Allard et al., 2006), hindsight suggests that it may as well have formed as a result of a more general structural reorganization in the summit area, which eventually led to the birth and establishment of the NSEC.

This process went through several stages, marked by the consecutive formation and filling of a total of four pit-craters lying progressively further southeast (Behncke et al., 2014), as well as various eruptive periods, with activity shifting forth and back between the old SEC and the position of the pit-craters, located along the axis which would be defined by the future NSEC. The first activity at the SEC after 5 years of quiescence, in July 2006, occurred from new vents that lay immediately to the SE and downslope of the first pit crater formed in late-2004, but 1 month later the activity switched back to the summit vent of the SEC. The August-December 2006 eruptive period was concentrated at the summit vent, but activity also occurred from new vents and fissures at the SE base of the SEC cone as well as to the west, in the saddle between the SEC and the Bocca Nuova, and at the southern base of the Bocca Nuova (Behncke et al., 2008; Neri et al., 2008; Favalli et al., 2010). The western vents reactivated during the 29 March 2007 lava fountaining episode, but the later paroxysms in spring 2007, especially those of 29 April and 6-7 May, produced activity exclusively from a fissure that extended for a few tens of meters (<100 m) from the summit down the SE flank of the SEC cone.

Paroxysmal eruptive episodes with lava fountaining, eruption columns and emission of tephra and lava flows have been the hallmark of the SEC since the late-1970s, although the crater also was the site of Strombolian activity accompanied by low-rate (<0.7 m^3/s) lava effusion, as in 1984 and 1996-1998 (Neri et al., 2011). Some of the paroxysms in 1989–1990 were particularly violent and voluminous (rate >120 m^3/s; Bertagnini et al., 1990; Carveni et al., 1994; Neri et al., 2011). However, the paroxysms between 1998 and 2001 were mostly rather short and small-volume events (Behncke et al., 2006), and the eruptive episodes of 2006 and March–May 2007 were similar. During all of this activity, the main vent at the summit of the SEC maintained a diameter of 50–80 m.

In contrast, the paroxysmal episodes at the NSEC have been generally more voluminous since the earliest ones (then at the proto-NSEC) on 4–5 September and 23–24 November 2007 (the 10 May 2008 paroxysm was yet more voluminous). Nearly all of the paroxysms during the long sequence initiated in January 2011 were more voluminous than the largest episodes of 1998-2001. Some of the paroxysms, especially in 2013, feature among the most powerfully explosive events (up to ∼400 m^3/s) at the summit of Etna of the past few centuries (Behncke et al., 2016). Finally, the width of the main vent of the NSEC has been consistently larger (a few tens of meters) than that of the SEC until 2014, when its activity showed a tendency of becoming less violent.

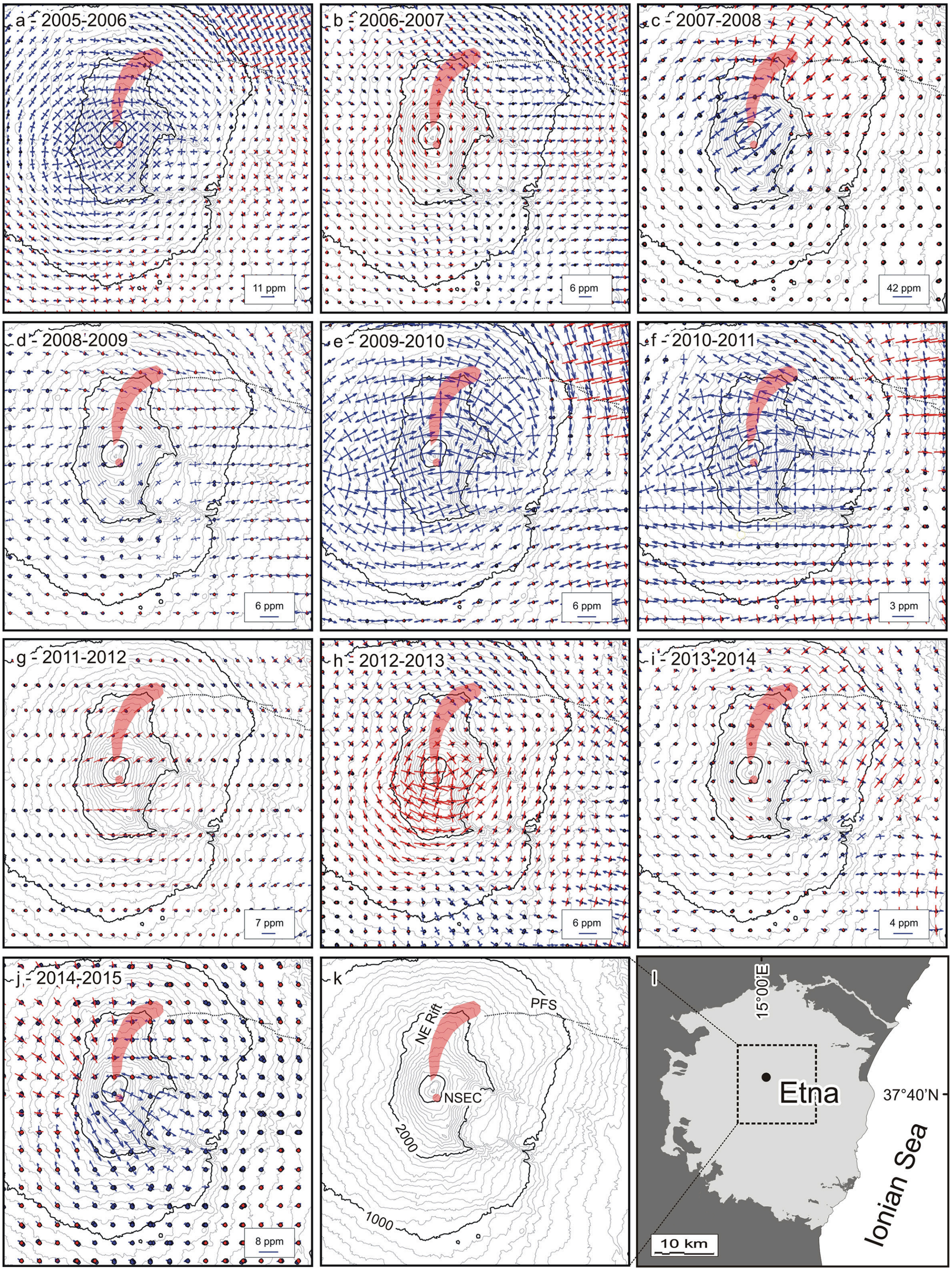

FIGURE 5 | Maps of the horizontal strain tensors distribution above Mt. Etna for subsequent 1-year (from June to the successive June) intervals (A–J). Blue axes are for dilatation, red for contraction. Red shadowed areas indicate the location of NE-Rift and New Southeast Crater NSEC **(K)** in the frame of the volcanic edifice **(L)**. Dashed lines (in **A–K**) mark the Pernicana Fault System (PFS), from Barreca et al. (2013).

All this points to a significant increase in the efficiency of magma transport through the conduit—of the SEC and, moreover, of the NSEC—that may be partly due also to the dilatation in the summit area that facilitated the shift of the axis of the conduit.

Overall, the depicted volcanic activity in the last decade points out to a clear SE shift, of ~0.4 km, in the location of the eruptive vents. This occurred through the development of NW-SE striking eruptive fissures along the SE flank of the SEC, as well as of pit-craters at its base (proto-NSEC), which replaced the activity of the SEC and then evolved in the NSEC. Both the fissures and the pit-craters suggest the lateral propagation of dikes from the SEC.

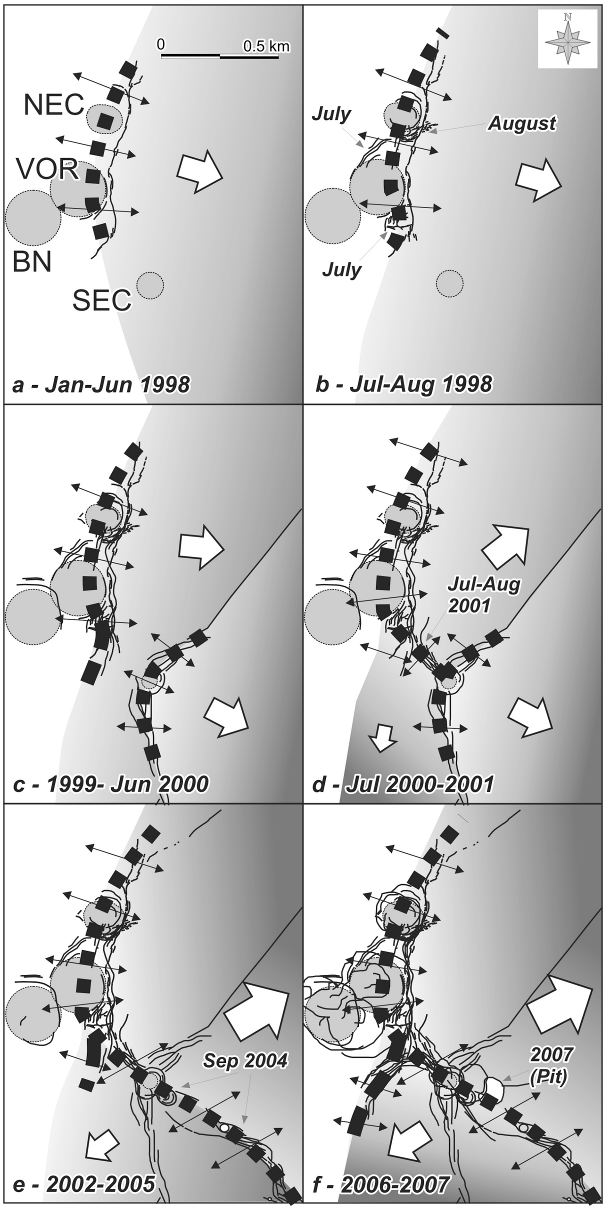

FIGURE 6 | (A–F) Evolution of the summit deformation pattern at Etna from 1998 to 2007, involving the development of extensional fractures and normal faults (modified from Neri and Acocella, 2006).

Evolution of the Fracture Field and Related Stress Conditions

Previous studies (Neri and Acocella, 2006) have shown that N–S oriented fractures formed in the summit crater area since early 1998, from the NE Crater (NEC) to the Voragine Crater (VOR; **Figure 6A**). During July–August 1998, this fracture system enlarged, affecting a larger portion of the summit (**Figure 6B**). During nearly all of its paroxysmal eruptive episodes in 2000, the SEC was affected by N–S eruptive fissures, parallel to the previously formed fracture system (**Figure 6C**). In 2001 the N–S fractures were reactivated and, at the SEC, propagated toward SE (**Figure 6D**). The NW–SE fissures developed in 2004–2005 beyond the SEC, induced by the lateral propagation of NW–SE striking dikes from the SEC, are the easternmost continuation of this newly-oriented fracture field (**Figure 6E**). In 2006–2007 this system was reactivated several times, accompanied by effusive and explosive eruptions (**Figure 6F**). The final shift from the main vent of the SEC cone to the pit crater (proto-NSEC) at its SE base occurred since September 2007.

The overall evolution of the summit fracture field seems to result from two main stress conditions. The first, active until a period between 2001 and 2004, is characterized by an overall E–W extension on the volcano summit. This condition corresponds to the presence of the stationary extensional stress field acting on the longer-term, both at the base and the summit of the volcano (e.g., McGuire and Pullen, 1989; Lanzafame et al., 1997; Solaro et al., 2010). The past decades of activity from the SEC have occurred within such a frame. Although minor shifts in the location of eruptive vents and the formation of fracture systems at the SEC have been common ever since its first eruptions in 1978–1979, the main focus of the activity has remained stable through early May 2007. It was indeed stable enough to build the large SEC cone, which is a true miniature stratovolcano (Behncke et al., 2006), with permanent summit vents and sporadically active, mostly ephemeral flank vent systems.

The second stress condition started to appear on the summit since sometime between 2001 and 2004, and has been characterized by an overall NE–SW trending extension direction (**Figure 6**). This extension, well-captured by the strain analysis in **Figure 5A** (2005) and, later, in **Figure 5C** (2007), was responsible for the development of the NW–SE striking fractures and fissures, as well as of the related feeder dikes, propagating from the SEC and responsible for the build-up of the NSEC (**Figure 2B**). The geodetic data show that the related NE–SW-oriented dilatation on the volcano summit has been transient, and mostly observed during periods of inflation (**Figure 5**).

It is proposed that this transient stress field results from the enhanced instability of the upper eastern flank of the volcano during inflation periods. Following the 2002–2003 eruption, the eastern flank of Etna underwent a major reorganization, with accelerated eastward slip of the area to the SW of the Pernicana Fault System (Piano Provenzana area, **Figure 7**; Neri et al., 2004, 2005, and references therein). In the following years, the eastward slip of the medium to lower slope immediately

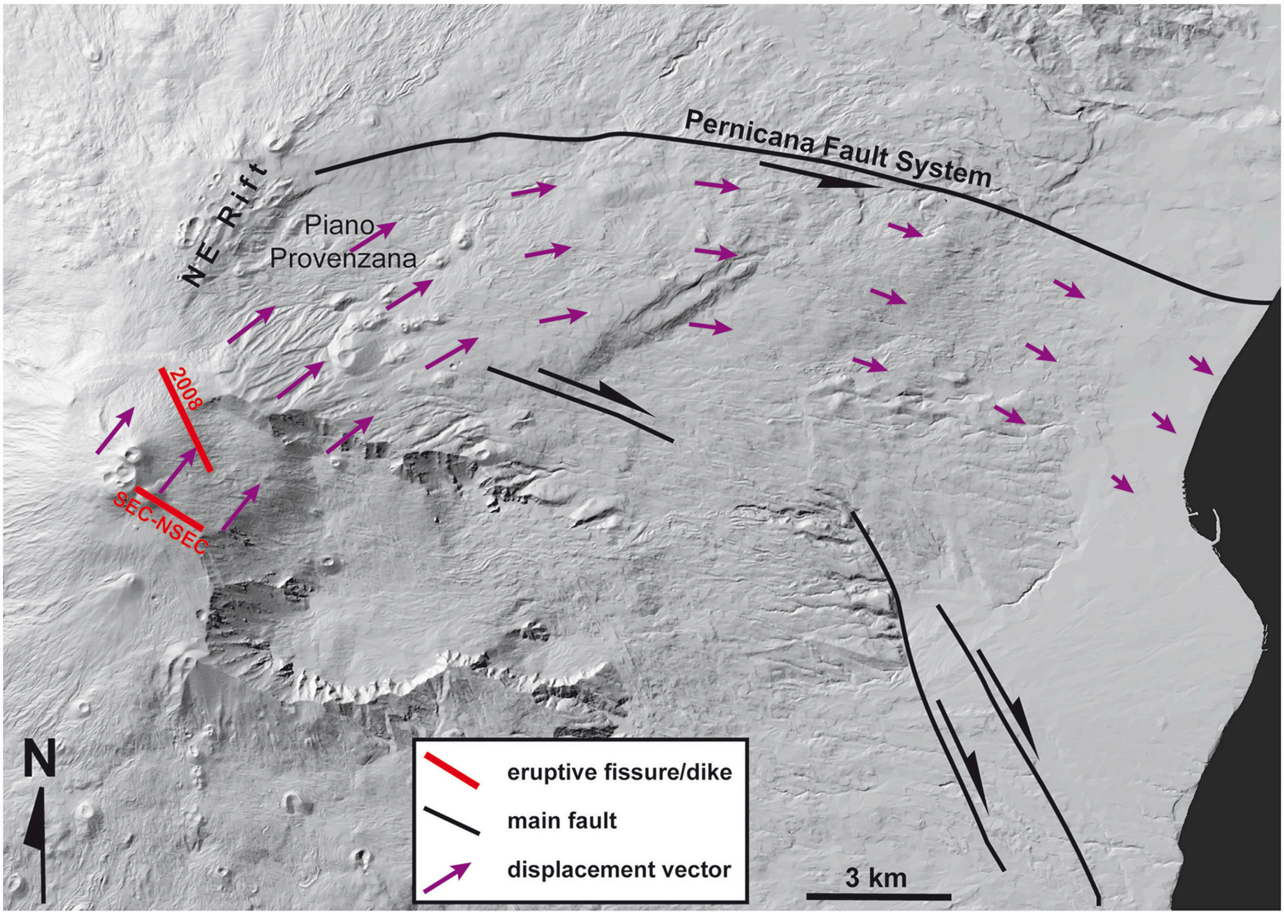

FIGURE 7 | Schematic summary of the relationships between flank instability and the development of the recent (post-2003) eruptive fissures on the summit of Etna, during the repeated periods of inflation of the volcano. Flank instability is summarized by the direction and amount of displacement indicated by the purple arrows observed between 2003 and 2011 (based on the following sources: **Figure 5** of this study; Neri et al., 2004; Solaro et al., 2010; Bonaccorso et al., 2011; Guglielmino et al., 2011; Alparone et al., 2013; Bonforte et al., 2013). The eruptive fissures refer to the dikes emplaced from the SEC, toward SE, from 2004 to 2015 (SEC–NSEC in Figure), as well as to the dike responsible for the 2008 eruption (Bonforte et al., 2013). The arcuate configuration of the displacement vectors is responsible for the eastward slip of the NE flank of the volcano, as well as for providing the dilatation accommodating the emplacement of the dikes feeding the shown eruptive fissures (in the summit area). The topography in (a) is based on a DEM from Bisson et al. (2016).

to the south of the Pernicana continued, promoting during periods of inflation an overall NE movement of the NE part of the summit, (Piano Provenzana area, **Figure 7**). In this way, this highest part of the edifice responded to the decrease in buttressing induced by the eastward slip of the medium slope of the volcano immediately to the south of the Pernicana Fault System. Therefore, the post 2002–2003 evolution of the volcano summit during periods of inflation has been characterized by an overall vortex-like kinematics, with NE trending displacement vectors from the SEC to the Piano Provenzana area, becoming E–W to the south of the central portion of the Pernicana Fault System, and then WNW–ESE in the distal portion of the volcano south of the Pernicana Fault System (**Figure 7**; Bonaccorso et al., 2011; Guglielmino et al., 2011; Alparone et al., 2013; Bonforte et al., 2013). This clockwise rotation of the slip vectors in the eastern flank of the volcano marks the relaxation of the significant acceleration of the instability that took place during the 2002–2003 eruption (Acocella et al., 2003). This clockwise rotation in the displacement vectors on the eastern flank of Etna may result from: (a) the curved geometry of the NE Rift—Pernicana Fault System, developing along a similar clockwise trend; (b) the presence of a topographic gradient dominated by the Etna summit (to the west-southwest) and the sea level (to the east); (c) the rotation of the displacement vectors to the side of active strike-slip faults producing earthquakes; these show motions toward the fault approaching the area epicenter, parallel to the fault nearby the epicenter and far from the fault passing the epicenter; a similar rotational pattern has been geodetically captured during recent earthquakes, as for example at the Hector Mine event in 1999 (Fialko et al., 2001).

The post-2003 volcanic activity at Etna has been significantly affected by this major stress variation. The emplacement of the NW–SE striking dikes feeding the 2004–2005 and the 2006 eruptions, as well as of the long-standing 2008–2009 eruption, is related to the development of the ∼NE–SW trending dilatational stress field at the summit of the volcano (**Figure 7**; Neri and Acocella, 2006; Neri et al., 2006; Bonaccorso et al., 2009; Bonforte et al., 2013). However, it is mostly with the development of the proto-NSEC, from 2007, that the shift in the axis of Etna's summit activity becomes evident. The development of the proto-NSEC in fact has provided a permanent gauge, or stress marker, highlighting this new condition of instability of the upper eastern flank of the volcano. This stress field promoted the formation of a new NW–SE oriented magmatic system through the development of multiple dikes, probably propagating from the conduit of the SEC. It is likely that this new magmatic system is very shallow, not deeper than 1–2 km, as it is resulting from flank instability. The increased eruptive frequency of the volcano since the development of this NW–SE trending system indicates that the accelerated instability of the volcano flank also somehow enhanced the shallow rise and extrusion of magma, leading to a greater efficiency of magma transport through the SEC–NSEC conduit.

The growth of the NSEC thus provides an interesting example of how instability-induced stress variations within a volcano may induce significant shifts in the locus of volcanic activity. Even though information is poor, it is likely that also the birth and development of the other summit craters at Etna (as for example the SEC) may have been promoted by similar variations in the summit stress field due to previous episodes of flank instability. Disruption of the portion of the central conduit system that feeds the Voragine and Bocca Nuova craters during the major intrusive and flank slip events of 2001 and 2002–2003 furthermore led to the deactivation of these craters for a decade; in fact, only in 2011–2015 did this portion of the feeder system (Voragine and Bocca Nuova) become fully re-established.

Increasing Volcanic Hazard?

The possibility to alter in a permanent way the shallow magmatic paths following episodes of flank instability remains an important feature to consider in the summit evolution of an active volcano, as well as to forecast the opening of new vents (Cappello et al., 2012, 2013). Indeed, the shift of the location of volcanism from the SEC to the NSEC is not only significant from a structural point of view, as it also changes, probably increasing, the context of volcanic hazards at the volcano. In particular, the growth of a new cone on the western rim of the Valle del Bove may promote further instability (as recently observed; Bonforte and Guglielmino, 2015), both of the cone itself and of the slope upon which it rests, which by now have merged into a continuum. Repeated intrusion of magma through the flanks of the cone, especially in its eastern sector, has in fact led to small to moderate size collapse events in late-2013 and early 2014; the largest of these events, on 11 February 2014, entrained hot, active lava, resulting in a hot, pyroclastic-flow-like avalanche. In addition, the heightened efficiency and faster speed of magma transport through the widened conduit has led to an increase in the vigor of lava fountaining and tephra generation, and many lava flows generated at the NSEC are significantly longer than the lava flows emitted by earlier paroxysms at the SEC. For example, the 10 May 2008 lava flow from the proto-NSEC reached a length of >6 km and stopped only 2 km from the outskirts of the town of Zafferana Etnea (Vicari et al., 2011; Behncke et al., 2016). Between 2011 and 2013, numerous villages on the south-eastern, eastern and north-eastern flanks of Etna have experienced repeated heavy tephra falls, often causing material damage. Higher upslope tourist facilities and popular hiking areas have repeatedly received rather intense tephra fallout, including clasts up to 0.5 m in diameter at more than 5 km distance from the NSEC (De Beni et al., 2015).

The growing number of these paroxysms (Behncke et al., 2005) inspired the development of a methodology for the near-real-time forecasting of lava flow hazards (Vicari et al., 2009). The methodology, based on near-real-time infrared satellite data to drive numerical simulations of lava flow paths, was tested at Etna to evaluate the hazard of lava flows emitted during the 12–13 January 2011 lava fountain (Vicari et al., 2011). By using SEVIRI satellite thermal data with low-spatial and high temporal resolution, we obtained a system of early warning combined with a preliminary estimate of the lava discharge rates. These satellite-derived discharge rate estimates were used as input to the MAGFLOW model (Del Negro et al., 2015; Cappello et al., 2016), allowing us to effectively simulate the rate of advancing and the maximum length of the lava flow. In this way, an eruptive scenario has been provided promptly enough for a response to be effective. Moreover, by simulating the inundation areas for diverse typologies of possible future eruptions at the NSEC, we produced a hazard map that may consider any abrupt change in the eruptive conditions, furnishing the probable paths of lava flows and the associated inundation probability. The results obtained from the hazard map suggest that summit eruptions like at the NSEC should generally pose no threat to the local population, with the added value that all the developed procedures required only a short time of intervention (from few minutes to hours), representing a critical point during an emergency.

In summary, the eruptive activity at the NSEC, with its frequent intense and widespread tephra falls and outpouring of lava flows capable of flowing over long distances enough to invade vulnerable areas on the flanks of Etna, may represent new challenges to population and authorities, where the notion of Etna being a largely effusive and non-explosive volcano is still widely held. The progressive intensification of summit activity at the volcano and the increased speed at which new summit vents are born and grow in locations that are structurally increasingly unstable, make us suspect that the problems caused by the activity of the NSEC will remain a constant feature of Etna's activity in the near future.

CONCLUSIONS

This study has shown how volcanic activity at Etna changed its location in the last decade. Activity migrated from the SE Crater to the New SE Crater, at the base of the former cone, in less than a decade. This shift involved the development of dike fed-eruptive fissures, pit craters and, finally, the NSEC cone itself. Geodetic and structural data suggest that the NSEC developed under the dilatational stress on the volcano summit promoted by accelerated flank instability, mainly along the Pernicana Fault System, during inflation periods. In particular, the NE–SW oriented dilatation in the NSEC area may result from a vortex-like displacement of the eastern flank of the volcano immediately to the south of the Pernicana Fault System. In fact, the direction of this displacement progressively rotates from NE–SW in the upper slope of the volcano (NSEC and Piano Provenzana areas) to E–W in the middle slope and ESE–WNW in the lower slope. The development of the NSEC is not only important from a structural point of view, as its formation may also have lead to an overall increase in the volcanic hazard; this is suggested by the increased proximity to the upper slope of the Valle del Bove, in a topographically more unstable area, and increased explosivity of the eruptions. The case of the NSEC at Etna shows how flank instability may control the distribution and impact of volcanism, including the prolonged shift of the summit vent activity in a mature volcano.

AUTHOR CONTRIBUTIONS

MN and VA coordinated the research and mainly wrote the manuscript. AB provided geodetic data. BB, GG, and CN provided volcanological field and satellite data. All authors contributed ideas and input to the research and writing of the paper.

ACKNOWLEDGMENTS

Editors A. Costa, G. Wadge, and R. Sulpizio promoted the Research Topic. Reviewers R. Sulpizio and A. Tibaldi provided constructive suggestions. Thanks are due to European Organisation for the Exploitation of Meteorological Satellites (EUMETSAT) for SEVIRI data (http://www.eumetsat.int) as well as to G. Aiesi, F. Calvagna, S. Consoli e B. Saraceno, and all INGV colleagues who collaborate to the GPS surveys on Etna.

REFERENCES

Acocella, V., Behncke, B., Neri, M., and D'Amico, S. (2003). Link between major flank slip and eruptions at Mt. Etna (Italy). *Geophys. Res. Lett.* 30, 2286. doi: 10.1029/2003GL018642

Acocella, V., and Neri, M. (2003). What makes flank eruptions? The 2001 Etna eruption and its possible triggering mechanisms. *Bull. Volcanol.* 65, 517–529. doi: 10.1007/s00445-003-0280-3

Acocella, V., and Neri, M. (2009). Dike propagation in volcanic edifices: overview and possible developments. *Tectonophysics* 471, 67–77. doi: 10.1016/j.tecto.2008.10.002

Allard, P., Behncke, B., D'Amico, S., Neri, M., and Gambino, S. (2006). Mount Etna 1993–2005: anatomy of an evolving eruptive cycle. *Earth Sci. Rev.* 78, 85–114. doi: 10.1016/j.earscirev.2006.04.002

Alparone, S., Andronico, D., Lodato, L., and Sgroi, T. (2003). Relationship between tremor and volcanic activity during the Southeast Crater eruption on Mount Etna in early 2000. *J. Geophys. Res.* 108, 2241. doi: 10.1029/2002JB001866

Alparone, S., Barberi, G., Bonforte, A., Maiolino, V., and Ursino, A. (2011). Evidence of multiple strain fields beneath the eastern flank of Mt. Etna volcano (Sicily, Italy) deduced from seismic and geodetic data during 2003-2004. *Bull. Volcanol.* 73, 869–885. doi: 10.1007/s00445-011-0456-1

Alparone, S., Cocina, O., Gambino, S., Mostaccio, A., Spampinato, S., Tuvè, T., et al. (2013). Seismological features of the Pernicana – Provenzana Fault System (Mt. Etna, Italy) and implications for the dynamics of north-eastern flank of the volcano. *J. Volcanol. Geotherm. Res.* 251, 16–26. doi: 10.1016/j.jvolgeores.2012.03.010

Andronico, D., Branca, S., Calvari, S., Burton, M., Caltabiano, T., Corsaro, R. A., et al. (2005). A multi-disciplinary study of the 2002–03 Etna eruption: insights into a complex plumbing system. *Bull. Volcanol.* 67, 314–330. doi: 10.1007/s00445-004-0372-8

Andronico, D., and Cristaldi, A. (2007). *Il Parossismo Eruttivo Del 4–5 Settembre 2007 al Cratere di SE: Caratteristiche Del Deposito di Caduta Distale*. Internal report. Available online at: http://www.ct.ingv.it/Report/RPTVETCEN20070904.pdf

Andronico, D., Cristaldi, A., and Scollo, S. (2008). The 4–5 September 2007 lava fountain at South-East Crater of Mt Etna, Italy. *J. Volcanol. Geotherm. Res.* 173, 325–328. doi: 10.1016/j.jvolgeores.2008.02.004

Barreca, G., Bonforte, A., and Neri, M. (2013). A pilot GIS database of active faults of Mt. Etna (Sicily): a tool for integrated hazard evaluation. *J. Volcanol. Geother. Res.* 251, 170–186. doi: 10.1016/j.jvolgeores.2012.08.013

Behncke, B., Branca, S., Corsaro, R. A., De Beni, E., Miraglia, L., and Proietti, C. (2014). The 2011–2012 summit activity of Mount Etna: Birth, growth and products of the new SE crater. *J. Volcanol. Geotherm. Res.* 270, 10–21. doi: 10.1016/j.jvolgeores.2013.11.012

Behncke, B., Calvari, S., Giammanco, S., Neri, M., and Pinkerton, H. (2008). Pyroclastic density currents resulting from interaction of basaltic magma with hydrothermally altered rock: an example from the 2006 summit eruptions of Mount Etna, Italy. *Bull. Volcanol.* 70, 1249–1268. doi: 10.1007/s00445-008-0200-7

Behncke, B., De Beni, E., and Proietti, C. (2013). *Misure GPS Del Nuovo Cono Discorie Del Cratere di SE, Etna.* Report INGV of May 3, 2013. Available online at: www.ct.ingv.it (in Italian).

Behncke, B., Fornaciai, A., Neri, M., Favalli, M., Ganci, G., and Mazzarini, F. (2016). LiDAR surveys reveal eruptive volumes and rates at Etna, 2007-2010. *Geophys. Res. Lett.* 42, 4270–4278. doi: 10.1002/2016gl068495

Behncke, B., and Neri, M. (2003). Cycles and trends in the recent eruptive behavior of Mount Etna (Italy). *Can. J. Earth Sci.* 40, 1405–1411. doi: 10.1139/e03-052

Behncke, B., Neri, M., and Nagay, A. (2005). "Lava flow hazard at Mount Etna (Italy): new data from a GIS-based study," in *Kinematics and Dynamics of Lava Flows*, Vol. 396, eds M. Manga and G. Ventura (Boulder, CO: Spec. Pap. Geol. Soc. *Am.*), 189–209.

Behncke, B., Neri, M., Pecora, E., and Zanon, V. (2006). The exceptional activity and growth of the Southeast Crater, Mount Etna (Italy), between 1996 and 2001. *Bull. Volcanol.* 69, 149–173. doi: 10.1007/s00445-006-0061-x

Belousov, A., Voight, B., and Belousova, M. (2007). Directed blasts and blasts-generated pyroclastic density currents: A comparison of the Bezymianni 1956, Mount St Helens 1980, and Soufrière Hills, Monteserrat 1997 eruptions and deposits. *Bull. Volcanol.* 69, 701–740. doi: 10.1007/s00445-006-0109-y

Bertagnini, A., Calvari, S., Coltelli, M., Landi, P., Pompilio, M., and Scribano, V. (1990). "The 1989 eruptive sequence," in *Mt. Etna 1989 Eruption*, eds F. Barberi, A. Bertagnini and P. Landi (Giardini, Pisa: Consiglio Nazionale delle Ricerche-Gruppo Nazionale per la Vulcanologia), 10–22.

Bisson, M., Spinetti, C., Neri, M., and Bonforte, A. (2016). Mt. Etna volcano high-resolution topography: airborne LiDAR modelling validated by GPS data. *Int. J. Digit. Earth* 9, 710–732. doi: 10.1080/17538947.2015.1119208

Bonaccorso, A., Bonforte, A., Calvari, S., Del Negro, C., Di Grazia, G., Ganci, G., et al. (2011). The initial phases of the 2008–2009 Mount Etna eruption: a multidisciplinary approach for hazard assessment. *J. Geophys. Res.* 116, B03203. doi: 10.1029/2010JB007906

Bonaccorso, A., Bonforte, A., and Gambino, S. (2015). Twenty-five years of continuous bore-hole tilt and vertical displacement data at Mount Etna: insight on long-term volcanic dynamics. *Geophys. Res. Lett.* 42, 10,222–10,229. doi: 10.1002/2015GL066517

Bonaccorso, A., Bonforte, A., Gambino, S., Mattia, M., Guglielmino, F., Puglisi, G., et al. (2009). Insight on recent stromboli eruption inferred from terrestrial and satellite ground deformation measurements. *J. Volcanol. Geotherm. Res.* 182, 172–181. doi: 10.1016/j.jvolgeores.2009.01.007

Bonaccorso, A., Bonforte, A., Guglielmino, F., Palano, M., and Puglisi, G. (2006). Composite ground deformation pattern forerunning the 2004–2005 Mount Etna eruption. *J. Geophys. Res.* 111, B12207. doi: 10.1029/2005JB004206

Bonaccorso, A., and Calvari, S. (2013). Major effusive eruptions and recent lava fountains: balance between erupted and expected magma volumes at Etna volcano. *Geophys. Res. Lett.* 40, 6069–6073. doi: 10.1002/2013GL058291

Bonforte, A., Bonaccorso, A., Guglielmino, F., Palano, M., and Puglisi, G. (2008). Feeding system and magma storage beneath Mt. Etna as revealed by recent inflation/deflation cycles. *J. Geophys. Res,* 113, B05406. doi: 10.1029/2007JB005334

Bonforte, A., Branca, S., and Palano, M. (2007). Geometric and kinematic variations along the active pernicana fault: implication for the dynamics of Mount Etna NE flank. *J. Volcanol. Geotherm. Res.* 160, 210–222. doi: 10.1016/j.jvolgeores.2006.08.009

Bonforte, A., Gambino, S., and Neri, M. (2009). Intrusion of eccentric dikes: the case of the 2001 eruption and its role in the dynamics of Mt. Etna volcano. *Tectonophysics* 471, 78–86. doi: 10.1016/j.tecto.2008.09.028

Bonforte, A., and Guglielmino, F. (2015). Very shallow dike intrusion and potential slope failure imaged by ground deformation: the 28 december 2014 eruption on Mount Etna. *Geophys. Res. Lett.* 42, 2727–2733. doi: 10.1002/2015GL063462

Bonforte, A., Guglielmino, F., and Puglisi, G. (2013). Interaction between magma intrusion and flank dynamics at Mt. Etna in 2008, imaged by integrated dense GPS and DInSAR data. *Geochem. Geophys. Geosyst.* 14, 2818–2835. doi: 10.1002/ggge.20190

Cappello, A., Bilotta, G., Neri, M., and Del Negro, C. (2013). Probabilistic modeling of future volcanic eruptions at Mount Etna. *J. Geophys. Res.* 118, 1–11. doi: 10.1002/jgrb.50190

Cappello, A., Ganci, G., Calvari, S., Pérez, N. M., Hernández, P. A., Silva, S. V., et al. (2016). Lava flow hazard modeling during the 2014–2015 fogo eruption, Cape Verde. *J. Geophys. Res.* 121, 2290–2303. doi: 10.1002/2015jb012666

Cappello, A., Neri, M., Acocella, V., Gallo, G., Vicari, A., and Del Negro, C. (2012). Spatial vent opening probability map of Mt. Etna volcano (Sicily, Italy). *Bull. Volcanol.* 74, 2083–2094. doi: 10.1007/s00445-012-0647-4

Carveni, P., Romano, R., Caltabiano, T., Grasso, M. F., and Gresta, S. (1994). The exceptional explosive activity of 5 January 1990 at SE-Crater of Mt Etna volcano (Sicily). *Boll. Soc. Geol. It.* 113, 613–631.

De Beni, E., Behncke, B., Branca, S., Nicolosi, I., Carluccio, R., D'Ajello Caracciolo, F., et al. (2015). The continuing story of Etna's New Southeast Crater (2012-2014): evolution and volume calculations based on field surveys and aerophotogrammetry. *J. Volcanol. Geotherm. Res.* 303, 175–186. doi: 10.1016/j.jvolgeores.2015.07.021

Del Negro, C., Cappello, A., and Ganci, G. (2015). Quantifying lava flow hazards in response to effusive eruption. *Geol. Soc. Am. Bull.* 128, 752–763. doi: 10.1130/B31364.1

Del Negro, C., Cappello, A., Neri, M., Bilotta, G., Hérault, A., and Ganci, G. (2013). *Lava flow hazards at Mount* Etna: constraints imposed by eruptive history and numerical simulations. *Sci. Rep.* 3:3493 doi: 10.1038/srep03493

Falsaperla, S., Behncke, B., Langer, H., Neri, M., Salerno, G. G., Giammanco, S., et al. (2014). "Failed" eruptions revealed by pattern classification analysis of gas emission and volcanic tremor data at Mt. Etna, Italy. *Int. J. Earth Sci. (Geol Rundsch)* 103, 297–313. doi: 10.1007/s00531-013-0964-7

Falsaperla, S., Cara, F., Rovelli, A., Neri, M., Behncke, B., and Acocella, V. (2010). Effects of the 1989 fracture system in the dynamics of the upper SE flank of Etna revealed by volcanic tremor data: the missing link? *J. Geophys. Res.* 115, B11306. doi: 10.1029/2010JB007529

Falsaperla, S., and Neri, M. (2015). Seismic footprints of shallow dyke propagation at Etna, Italy. *Sci. Rep.* 5, 11908. doi: 10.1038/srep11908

Favalli, M., Fornaciai, A., Mazzarini, F., Harris, A. J. L., Neri, M., Behncke, B., et al. (2010). Evolution of an active lava flow field using a multitemporal LIDAR acquisition. *J. Geophys. Res.* 115, B11203. doi: 10.1029/2010JB007463

Fialko, Y., Simons, M., and Agnew, D. (2001). The complete (3-D) surface displacement field in the epicentral area of the 1999 Mw7.1 Hector Mine earthquake, California, from space geodetic observations. *Geophys. Res. Lett.* 28, 3063–3066. doi: 10.1029/2001GL013174

Ganci, G., Bilotta, G., Cappello, A., Hérault, A., and Del Negro, C. (2015). "HOTSAT: a multiplatform system for the satellite thermal monitoring of volcanic activity," in *Detecting, Modelling and Responding to Effusive Eruptions,* eds A. Harris, T. De Groeve, F. Garel, and S. A. Carn (London: Geological Society of London Special Publication), 426.

Ganci, G., Harris, A. J. L., Del Negro, C., Guéhenneux, Y., Cappello, A., Labazuy, P., et al. (2012). A year of fountaining at Etna: Volumes from SEVIRI. *Geophys. Res. Lett.* 39, L06305. doi: 10.1029/2012GL051026

Ganci, G., James, M. R., Calvari, S., and Del Negro, C. (2013). Separating the thermal fingerprints of lava flows and simultaneous lava fountaining using ground-based thermal camera and SEVIRI measurements. *Geophys. Res. Lett.* 40, 5058–5063. doi: 10.1002/grl.50983

Ganci, G., Vicari, A., Bonfiglio, S., Gallo, G., and Del Negro, C. (2011a). A texton-based cloud detection algorithm for MSG-SEVIRI multispectral images. *Geomatics Nat. Hazards Risk* 2, 279–290. doi: 10.1080/19475705.2011.578263

Ganci, G., Vicari, A., Fortuna, L., and Del Negro, C. (2011b).The HOTSAT volcano monitoring system based on combined use of SEVIRI and MODIS multispectral data. *Ann. Geophys.* 54, 544–550.

Garel, F., Kaminski, E., Tait, S., and Limare, A. (2015). "A fluid dynamics perspective on the interpretation of the surface thermal signal of lava flows," in *Detecting, Modelling and Responding to Effusive Eruptions,* eds A. J. L. Harris, T. De Groeve, F. Garel, and S. A. Carn, S.A (Geological Society of London Special Publication), 426.

Guest, J. E. (1973). The summit area of Mount Etna prior to the 1971 eruption. *Philos. Trans. R. Soc. London A* 274, 63–78. doi: 10.1098/rsta.1973.0026

Guglielmino, F., Bignami, C., Bonforte, A., Briole, P., Obrizzo, F., Puglisi, G., et al. (2011). Analysis of satellite and in situ ground deformation data integrated by the SISTEM approach: the April 3, 2010 earthquake along the Pernicana fault (Mt. Etna – Italy) case study. *Earth Planet. Sci. Lett.* 312, 327–336. doi: 10.1016/j.epsl.2011.10.028

Langer, H., Falsaperla, S., Messina, A., Spampinato, S., and Behncke, B. (2011). Detecting imminent eruptive activity at Mt Etna, Italy, in 2007–2008 through pattern classification of volcanic tremor data. *J. Volcanol. Geotherm. Res.* 200, 1–17. doi: 10.1016/j.jvolgeores.2010.11.019

Lanzafame, G., Neri, M., Coltelli, M., Lodato, L., and Rust, D. (1997). North-south compression in the Mt. Etna region (Sicily): spatial and temporal distribution. *Acta Vulcanologica* 9, 121–133.

McGuire, W. J., and Pullen, A. D. (1989). Location and orientation of eruptive fissures and feeder-dykes at Mount Etna: influence of gravitational and regional stress regimes. *J. Volcanol. Geotherm. Res.* 38, 325–344. doi: 10.1016/0377-0273(89)90046-2

Neri, M., and Acocella, V. (2006). The 2004–05 Etna eruption: Implications for flank deformation and structural behaviour of the volcano. *J. Volcanol. Geotherm. Res.* 158, 195–206. doi: 10.1016/j.jvolgeores.2006.04.022

Neri, M., Acocella, V., and Behncke, B. (2004). The role of the Pernicana Fault System in the spreading of Mount Etna (Italy) during the 2002–2003 eruption. *Bull. Volcanol.* 66, 417–430. doi: 10.1007/s00445-003-0322-x

Neri, M., Acocella, V., Behncke, B., Giammanco, S., Mazzarini, F., and Rust, D. (2011). Structural analysis of the eruptive fissures at Mount Etna (Italy). *Ann. Geophys.* 54, 464–479. doi: 10.4401/ag-5332

Neri, M., Acocella, V., Behncke, B., Maiolino, V., Ursino, A., and Velardita, R. (2005). Contrasting triggering mechanisms of the 2001 and 2002–2003 eruptions of Mount Etna (Italy). *J. Volcanol. Geotherm. Res.* 144, 235–255. doi: 10.1016/j.jvolgeores.2004.11.025

Neri, M., Behncke, B., Burton, M., Giammanco, S., Pecora, E., Privitera, E., et al. (2006). Continuous soil radon monitoring during the July 2006 Etna eruption. *Geophys. Res. Lett.* 33, L24316. doi: 10.1029/2006GL028394

Neri, M., Mazzarini, F., Tarquini, S., Bisson, M., Isola, I., Behncke, B., et al. (2008). The changing face of Mount Etna's summit area documented with Lidar technology. *Geophys. Res. Lett.* 35, L09305. doi: 10.1029/2008GL033740

Pesci, A., and Teza, G. (2007). Strain rate analysis over the central Apennines from GPS velocities: the development of a new free software. *Bollettino Geodesia Sci. Affini* 56, 69–88.

Puglisi, G., and Bonforte, A. (2004). Dynamics of Mount Etna Volcano inferred from static and kinematic GPS measurements. *J. Geophys. Res.* 109, B11404. doi: 10.1029/2003JB002878

Puglisi, G., Briole, P., and Bonforte, A. (2004). "Twelve years of ground deformation studies on Mt. Etna volcano based on GPS surveys," in *Mt. Etna:*

Volcano Laboratory. AGU Geophys. Monograph series, eds A. Bonaccorso, S. Calvari, M. Coltelli, C. Del Negro, and S. Falsaperla (Washington, DC: AGU), 143, 321–341.

Solaro, G., Acocella, V., Pepe, S., Ruch, J., Neri, M., and Sansosti, E. (2010). Anatomy of an unstable volcano through InSAR: multiple processes affecting flank instability at Mt. Etna, 1994–2008. *J. Geophys. Res.* 115, B10405. doi:10.1029/2009JB000820

Spampinato, L., Ganci, G., Hernández, P. A., Calvo, D., Tedesco, D., Pérez, N. M., et al. (2013). Thermal insights into the dynamics of Nyiragongo lava lake from ground and satellite measurements. *J. Geophys. Res.* 118, 5771–5784. doi: 10.1002/2013jb010520

Vicari, A., Ciraudo, A., Del Negro, C., Herault, A., and Fortuna, L. (2009). Lava flow simulations using discharge rates from thermal infrared satellite imagery during the 2006 Etna eruption. *Nat. Hazards* 50, 539–550. doi: 10.1007/s11069-008-9306-7

Vicari, A., Ganci, G., Behncke, B., Cappello, A., Neri, M., and Del Negro, C. (2011). Near-real-time forecasting of lava flow hazards during the 12–13 January 2011 Etna eruption. *Geophys. Res. Lett.* 38, L13317. doi: 10.1029/2011GL047545

Conflict of Interest Statement: The authors declare that the research was conducted in the absence of any commercial or financial relationships that could be construed as a potential conflict of interest.

frontiers in Earth Science

ORIGINAL RESEARCH
published: 29 November 2016
doi: 10.3389/feart.2016.00103

Determining the Stress Field in Active Volcanoes Using Focal Mechanisms

Bruno Massa[1,2]*, Luca D'Auria[2,3], Elena Cristiano[2] and Ada De Matteo[1]

[1] Dipartimento di Scienze e Tecnologie, Universitá degli Studi del Sannio, Benevento, Italy, [2] Istituto Nazionale di Geofisica e Vulcanologia, Sezione di Napoli, Osservatorio Vesuviano, Napoli, Italy, [3] Istituto per il Rilevamento Elettromagnetico dell'Ambiente, Consiglio Nazionale delle Ricerche, Napoli, Italy

Stress inversion of seismological datasets became an essential tool to retrieve the stress field of active tectonics and volcanic areas. In particular, in volcanic areas, it is able to put constrains on volcano-tectonics and in general in a better understanding of the volcano dynamics. During the last decades, a wide range of stress inversion techniques has been proposed, some of them specifically conceived to manage seismological datasets. A modern technique of stress inversion, the BRTM, has been applied to seismological datasets available at three different regions of active volcanism: Mt. Somma-Vesuvius (197 Fault Plane Solutions, FPSs), Campi Flegrei (217 FPSs) and Long Valley Caldera (38,000 FPSs). The key role of stress inversion techniques in the analysis of the volcano dynamics has been critically discussed. A particular emphasis was devoted to performances of the BRTM applied to volcanic areas.

Keywords: stress field, focal mechanism, BRTM, volcano-tectonics, monitoring

OPEN ACCESS

Edited by:
Antonio Costa,
National Institute of Geophysics and Volcanology, Bologna, Italy

Reviewed by:
Eisuke Fujita,
National Research Institute for Earth Science and Disaster Prevention, Japan
Mimmo Palano,
National Institute of Geophysics and Volcanology, Roma, Italy

***Correspondence:**
Bruno Massa
massa@unisannio.it

Specialty section:
This article was submitted to Volcanology, a section of the journal Frontiers in Earth Science

Received: 30 April 2016
Accepted: 11 November 2016
Published: 29 November 2016

Citation:
Massa B, D'Auria L, Cristiano E and De Matteo A (2016) Determining the Stress Field in Active Volcanoes Using Focal Mechanisms. Front. Earth Sci. 4:103. doi: 10.3389/feart.2016.00103

INTRODUCTION

Theoretical Background to Stress Field Inversion

In last decades focal mechanisms have shown to be very useful to infer about the stress field within the Earth. Being seismicity a common feature of both quiescent and erupting volcanoes, the study of volcano-tectonic earthquakes is an effective tool to retrieve spatial and temporal patterns in the pre-, syn-, and inter-eruptive stress fields. Stress changes associated with magma migration and more in general with the dynamics of magma chambers and hydrothermal systems are causally linked to these earthquakes. Hence retrieving the stress field pattern in volcanoes has important implications in studying their dynamics and the interaction with the regional tectonic stress field (Umakoshi et al., 2001; Pedersen and Sigmundsson, 2004; Segall, 2013; Cannavò et al., 2014; D'Auria et al., 2014a,b).

Rocks in the Earth lithosphere possess a specific state of stress strictly related to the tectonic setting of the region. The state of stress at any given point can be represented geometrically as a Stress Ellipsoid, a tri-axial solid built with the Principal Stress Components (PSC) $\sigma_1 > \sigma_2 > \sigma_3$ as main axes. The shape of this ellipsoid can be expressed using the Bishop's ratio $\Phi_B = (\sigma_2 - \sigma_3) / (\sigma_1 - \sigma_3)$ (Bishop, 1966). It expresses the relationship between the intermediate and maximum PSC respect to the minimum one and can assume values varying from 0 to 1. In a general tri-axial state of stress $\sigma_1 > \sigma_2 > \sigma_3 \neq 0$, and the $\Phi_B \approx 0.5$. A slip event along a fault surface occurs when the accumulated energy exceeds the internal strength of the rock (Reid, 1910). The rupture starts at the hypocenter and then propagates along the whole fault plane. Analysis of seismograms allows the retrieving of information about the seismogenic structure responsible for an event. Byerly (1928) proposed a method that allows the reconstruction of the Fault Plane Solution

(FPS) of an earthquake, which is a stereographic projection representing the geometry of a seismogenic structure. It can be easily explained picturing a focal sphere ideally located around the earthquake hypocenter. The focal sphere can be separated into four dihedra, two contractional, and two dilatational, delimited by two planes known as Nodal Planes (the main and the auxiliary planes). The main nodal plane represents the actual fault, with the slip occurring during the earthquake being along the direction orthogonal to the auxiliary plane (**Figure 1**). Therefore the geometry of the FPS is tightly linked to the fault kinematics. At the center of the contractional dihedra is located the P-axis (compressive) while the center of extensional dihedra (dilatational) hosts the T-axis. The neutral B-axis corresponds to the intersection of nodal planes (**Figure 1**). P, T, B axes are mutually normal. The relationship between P and T axes of a FPS and the actual σ_1 and σ_3 stress directions is not straightforward. The aim of stress inversion techniques is precisely to determine it. A FPS can be reconstructed a posteriori, starting from the analysis of the first arrival of P-waves at an adequate number of seismographs arranged around the hypocenter. Using the equal-area stereographic projection technique (lower hemisphere), each station can be plotted using the angular coordinates of the direct seismic ray leaving the hypocenter. Stations falling in a contractional quadrant will record a downward first P-wave arrival (void circle of **Figure 1A**). Conversely, stations falling in a dilatational quadrant will register an upward first P-wave arrival (solid circle of **Figure 1A**). Plotting this information on an equal-area stereographic projection net it is possible to find a couple of nodal planes that is able to divide up the plot into four quadrants, corresponding to the four dihedra of the focal sphere (**Figure 1**). Nowadays, these procedures are implemented in a wide range of algorithms performing the determination of the FPS automatically. One of the most commonly used algorithms is FPFIT (Reasenberg and Oppenheimer, 1985). It is a suite of Fortran codes for calculating and displaying earthquake fault-plane solutions. FPFIT finds the double-couple fault plane solution (source model) that best fits a given set of observed first motion polarities for an earthquake.

Starting from observed fault kinematics or focal mechanisms, various stress inversion procedures can be implemented. These procedures allow the reconstruction of the reduced stress field that carries information about the stress orientation and the ratios between principal stresses. Inversion of focal mechanism datasets became a common task in studies aimed at constrain seismotectonic stress field in active tectonic areas (Carey-Gailhardis and Mercier, 1992; Gillard and Wyss, 1995; Hardebeck and Hauksson, 2001; Massa, 2003; Angelier and Baruah, 2009; De Matteis et al., 2012) and more recently also in volcanic environments (Wyss et al., 1992; Cocina et al., 1997; D'Auria et al., 2014a,b; Plateaux et al., 2014). A wide range of graphical and analytical methods were proposed by authors in last decades (e.g., Angelier and Mechler, 1977; Gephart and Forsyth, 1984; Carey-Gailhardis and Mercier, 1987; Lisle, 1987, 1988; Michael, 1987; Angelier, 1990, 2002; Rivera and Cisternas, 1990; D'Auria and Massa, 2015). Stress inversion procedures are based on the Wallace-Bott hypothesis: shear traction acting on a fault plane (irrespective of newly formed structure or a reactivated preexisting one) causes a slip event in the direction and sense of the shear traction itself (Wallace, 1951; Bott, 1959; Angelier and Mechler, 1977; Yamaji, 2007). Analytical techniques of stress inversion are based on the systematic comparison of the actual slip vector with respect to the theoretical (modeled) maximum shear stress acting on the same surface in response to the active stress field (**Figure 2**). Graphical approaches are based on the definition of a probability function (or an equivalent formulation) on the whole focal sphere. They allow the

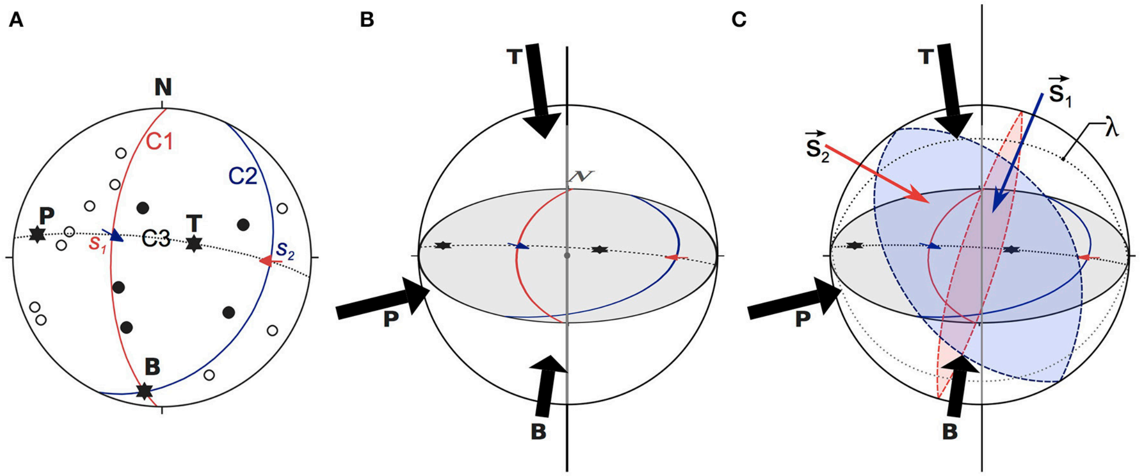

FIGURE 1 | The Byerly's Fault Plane Solution. (A) A FPS is a stereographic projection representing the double-couple model of the seismogenic source; equal-area stereographic projection technique (lower hemisphere), void circles are P-wave *downward* first arrivals, solid circles are P-wave *upward* first arrivals, C_1 and C_2 are nodal planes with associated slip vectors s_1 (pole to C_2) and s_2 (pole to C_1), P- (compressive) T- (tensional) and B-axes (neutral) are also plotted; **(B)** Three-dimensional view of a Focal Sphere, the FPS of **(A)** represents the stereographic projection (on the equatorial plane) of the geometrical elements intersecting the lower hemisphere. **(C)** 3-D perspective of the FPS (see text for details).

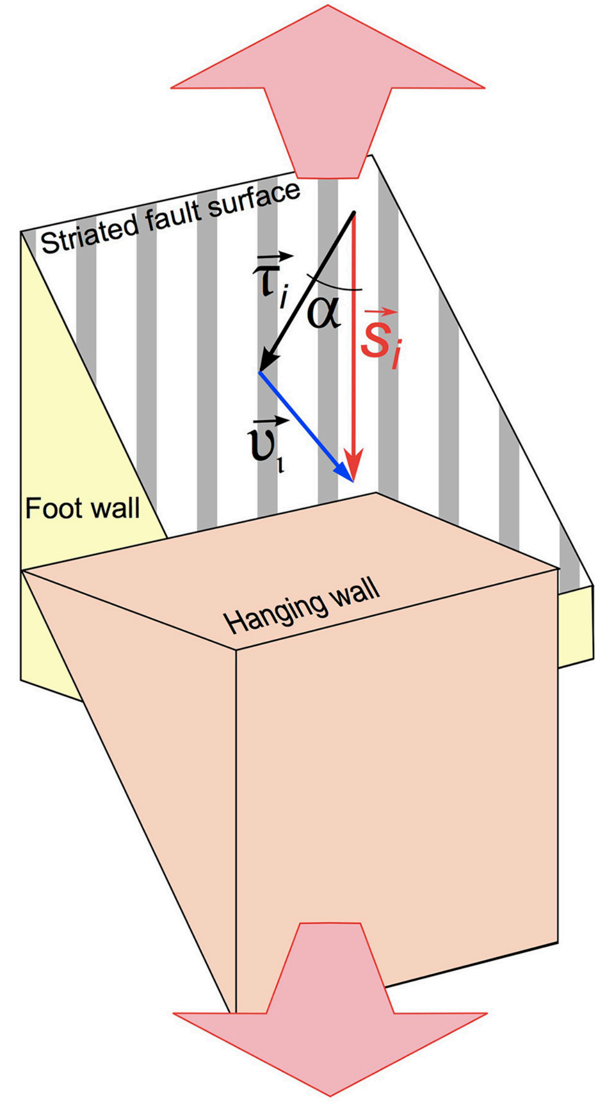

FIGURE 2 | Misfit criteria adopted in stress inversion procedures. α angle formed between the actual slip vector (s_i) and the theoretical shear stress (τ_i) acting on each fault of the analyzed dataset (Carey and Brunier, 1974; Angelier, 1990); υ_i, the vector difference between s_i and τ_i (Angelier, 1990).

determination of a range of possible attitudes for principal stress axes using hand stereo-plot. Right Dihedra Method (RDM) represents the simplest of graphical stress inversions (Angelier and Mechler, 1977). It basically consists of averaging the focal spheres of a focal mechanisms dataset. In the late 80's, RDM was improved adding an additional geometrical constrain and was re-proposed as Right Trihedra Method (Lisle, 1987, 1988). Both RDM and RTM are able to manage both planes of focal mechanism regardless the pre-selection of the actual fault plane. D'Auria and Massa (2015) proposed a novel Bayesian approach for the determination of the stress field from focal mechanism datasets (BRTM). This method can be regarded as a re-visitation of the RTM in a sound probabilistic framework. It provides a probability function over the focal sphere for both σ_1 and σ_3 principal stress directions (**Figure 3**). BRTM algorithm has shown to be robust and efficiently enough to manage all kind of kinematics and nodal plane attitudes. A comparison of the BRTM performances to respect a classical Direct Inversion Method (Angelier, 1990, 2002) and the Multiple Inverse Method (Yamaji, 2000), confirms that BRTM is able to successfully manage both homogeneous and heterogeneous datasets (see Figure 2 in D'Auria and Massa, 2015). Furthermore BRTM allows both a reliable determination of the principal stress axes attitude and a quantitative estimation of the corresponding confidence regions (D'Auria and Massa, 2015). Finally, to give a complete and accurate inversion the corresponding Bishop's ratio Φ_B can be determined, exploiting the BRTM results, following the approach proposed by Angelier (1990; **Figure 3**). In case of heterogeneous datasets result of stress field inversion could be misleading. The problem can be approached using different un-supervisioned techniques (e.g., Angelier and Manoussis, 1980; Yamaji, 2000). Among those, the Multiple Inverse Method (Yamaji, 2000), makes use of a resampling technique of the analyzed dataset, through the construction of many data subsets, inverted separately using an analytical approach (Otsubo et al., 2008). Results can be plotted on a stereographic projection to outline graphically different clusters of stress tensors, corresponding to the different components of the stress field acting in the lithospheric volume associated to the dataset. The major drawback of this technique is the difficulty in attributing to the retrieved stress field components a proper spatio-temporal collocation. Therefore heterogeneous datasets can be approached, more properly, taking into account spatial and possibly temporal variations of the stress pattern (Wyss et al., 1992; Hardebeck and Michael, 2006; D'Auria et al., 2014b). In other words, these methods take into account the spatio-temporal distribution of the data, providing as results not a single stress tensor, but a spatially (and possibly temporally) variable stress field. Applying the BRTM to subsets of FPS corresponding to a given sub-volume of the area under investigation allows retrieving the spatial pattern of the stress field. This is an essential approach in the analysis of seismological dataset of volcanic districts. In the next section we show the application of stress inversion procedures to three different volcanic areas. Analyses were carried out on datasets available from previous studies. For Mt.Somma-Vesuvius and Campi Flegrei we used data from D'Auria et al. (2014a,b). For the Long Valley Caldera, data are freely accessible to users via the Internet (NCEDC, 2014). We preferred to invert published datasets to novel ones as this allows a more efficient comparison of obtained results got with different processing approaches.

This study aims at highlighting the key role played by stress inversion procedures in the analysis of the volcano dynamics. In detail, we show the methodological potential offered by the BRTM here tested on seismological datasets collected at three different volcanoes.

CASE STUDIES

In order to show the capability of the stress inversion procedures on volcanoes, we applied the BRTM to determine the spatial variations of the stress field in three different volcano-tectonic environments: the Mt. Somma-Vesuvius Volcano (Southern

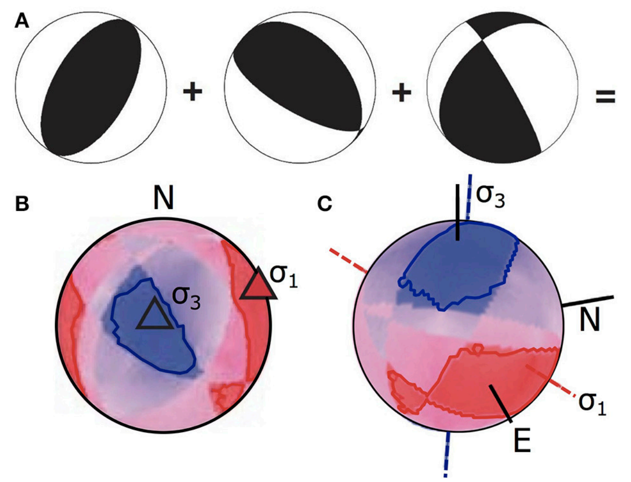

FIGURE 3 | Results of the BRTM applied to a synthetic dataset (A) made up of three FPSs (black = dilatational dihedra); **(B)** 2-D plot on a Lambert equiareal, lower-hemisphere projection; **(C)** tridimensional view of the BRTM results over the focal sphere (After: D'Auria and Massa, 2015, modified).

Italy; **Figure 4**), the Campi Flegrei Caldera (Southern Italy; **Figure 4**) and the Long Valley Caldera (California-Sierra Nevada border, USA; **Figure 9**). In the following we report a synthesis of the key results, focusing on the relationship between the local active stress fields and the background regional ones.

Mt. Somma-Vesuvius

The Somma-Vesuvius (**Figures 4**, **5**) is the youngest volcano of the Neapolitan district, it is characterized both by explosive and effusive activity (Santacroce, 1987). Its oldest products are dated 0.369 ± 0.028 Ma ($^{40}Ar/^{39}Ar$ age from Brocchini et al., 2001). The last eruption of Vesuvius occurred in 1944 and after this event it has become quiescent, showing only fumarolic activity and low seismicity ($M \leq 3.6$). Since 1964 to nowadays the seismicity started to increase in the occurrence and in the magnitude (Giudicepietro et al., 2010), with four episodes (1978–1980, 1989–1990, 1995–1996, 1999–2000) of strong increased strain release rate, occurrence and magnitude rate (D'Auria et al., 2013). The Mesozoic basement of the volcano is displaced by both SW- and NW-dipping normal fault systems and secondarily by NE-SW and E-W faults (Bianco et al., 1998; Ventura and Vilardo, 1999; Zollo et al., 2002; Acocella and Funiciello, 2006; **Figure 4**). Mesoscale faults and eruptive fractures striking NW-SE, NE-SW and ENE-WSW affect volcanic units outside the Somma caldera (Rosi et al., 1987; Andronico et al., 1995; Ventura and Vilardo, 1999; D'Auria et al., 2014a, **Figure 1** for a review). Seismicity at Mt. Somma-Vesuvius shows the presence of two different seismogenic volumes: a top volume (above sea level) and a bottom one (1–5 km depth). These two volumes appear to be separated by a volume with a markedly reduced seismic strain release, possibly corresponding to a ductile sedimentary layer buried at about 1000 m b.s.l. (Bernasconi et al., 1981; Borgia et al., 2005; D'Auria et al., 2014a).

At Mt. Somma-Vesuvius we analyzed a dataset consisting of 197 FPSs of earthquakes recorded from 1999 to 2012 with $0 < M < 3.6$ (D'Auria et al., 2014a). All the events were relocated by D'Auria et al. (2014a) using a nonlinear probabilistic approach in a 3-D velocity model (Lomax et al., 2001; D'Auria et al., 2008). FPSs were computed using P wave polarities (Reasenberg and Oppenheimer, 1985). Only events with at least six first motion observations were used to derive FPSs (**Figure 5**). Kinematics of the analyzed FPSs are quite equally represented in the three extreme categories, dip-slip normal, dip-slip reverse and strike-slip (**Figure 5D**). The stress field has been computed on a regular three-dimensional grid of 1-km spacing. For each grid node all the FPSs within a radius of 1-km have been considered for the inversion. The stress field has been computed only at volumes containing at least five FPSs. A synthesis of BRTM results is reported in **Figure 6**. For the top-volume (slice for depth −1 km, corresponding to the portion of the edifice lying above the sea level) the retrieved σ_1 is sub-horizontal overall trending NW-SE, corresponding to a sub-vertical σ_3 and the related Φ_B is <0.5. Results for the bottom volume are summarized for depths of 1, 3, and 5 km. At 1 km depth slice σ_1 moderately plunges toward ENE and corresponds to a sub-horizontal σ_3 trending NNW-SSE. In this case $0.3 < \Phi_B < 0.5$. At 3 km depth slice the attitude of the σ_1 is highly variable overall plunging toward NNW. It corresponds to a sub-horizontal σ_3 trending E-W in the axial sector, SW-NE and NW-SE at the most external volumes with a Bishop's ratio $0.4 < \Phi_B < 0.5$. At the deepest depth slice (5 km), σ_1 is sub-horizontal trending NNE-SSW to NW-SE, corresponding to moderately to high plunging $\sigma_3$trending ENE-WSW, the Φ_B is high variable experiencing values from 0.2 to 1 (**Figure 6**). The marked differences in the stress field pattern retrieved within the two seismogenic volumes (**Figure 6**, slice -1 vs. slices 1-3-5) can be addressed to the effect of the aforementioned decoupling ductile layer. The faulting style active in the top-volume is compatible with a spreading process involving the exposed Somma-Vesuvius edifice, as proposed by various previous studies (see references in D'Auria et al., 2014a). The strain field resulting from the subsidence of the Vesuvius and the asymmetric spreading of the southern portion of the Somma edifice creates an overall NS compression (see Figure 17 in D'Auria et al., 2014a). This ongoing process is also the source of the persistent seismicity located within the top-volume (Borgia et al., 2005; D'Auria et al., 2013, 2014a; **Figures 5**, **6**). Additionally, the low Φ_B values associated to stress inversion in the top volume confirm that the retrieved fields are strongly driven by the σ_1. According to previous studies, the bottom-volume seems to be deeply related to a regional background stress field slightly perturbed by local heterogeneities in the volcanic structure and by the complex topography of the volcano. The intermittent behavior of the seismic activity in the deepest volume is probably due to a relation with the dynamics of the hydrothermal system: the pore pressure within the hydrothermal system can be perturbed by episodes of fluid injection that essentially influence the stress field pattern in the bottom-volume (**Figures 5**, **6**; Chiodini et al., 2001; D'Auria et al., 2014a). The Φ_B values associated to stress inversion in the bottom volume show that for the 1- and 3-km depth-slices the three principal stresses

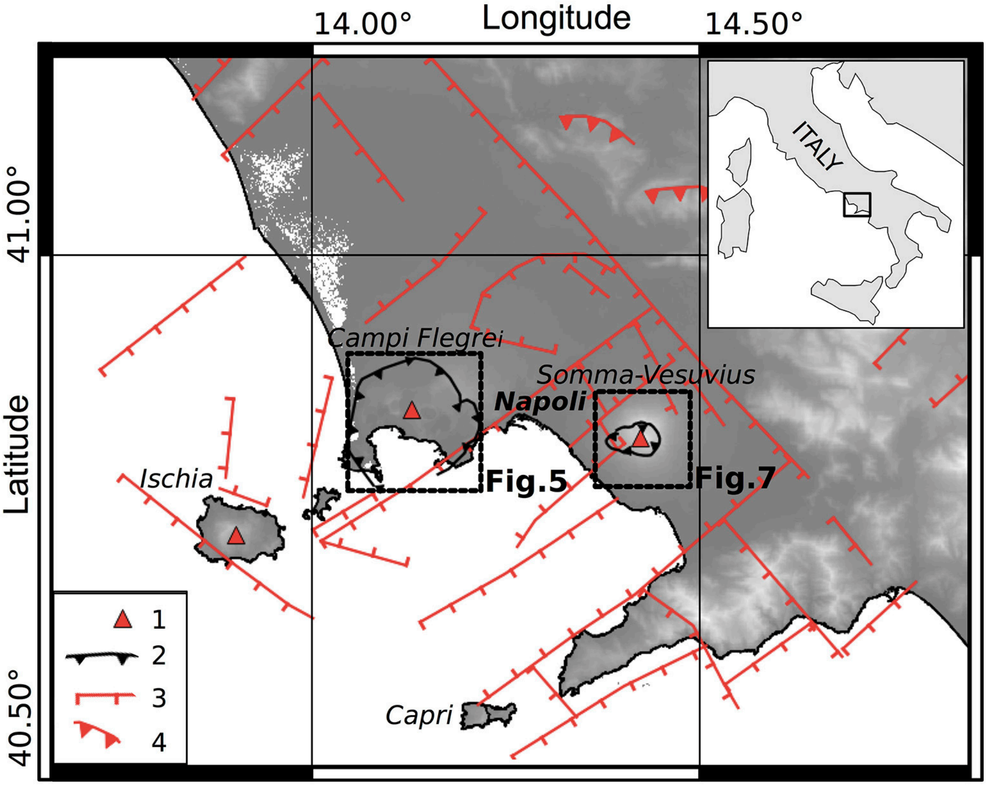

FIGURE 4 | Tectonic setting of the Campi Flegrei-Vesuvius area. (1) Main volcanoes; (2) Campi Flegrei (Campanian Ignimbrite) and Mt. Somma caldera rims; (3) main Plio-Quaternary faults; (4) thrust faults. Dashed squares identify the location of **Figures 5**, **7**. Data from: Ippolito et al., 1973; Di Vito et al., 1999; Lavecchia et al., 2003; Acocella and Funiciello, 2006; Milia et al., 2013; Vitale and Isaia, 2013; D'Auria et al., 2014a,b, and referencer therein.

are well defined (overall, $0.3 < \Phi_B < 0.5$). A quite different result was obtained for the deepest depth-slice, the 5-km one: here Φ_B values show an high variability with values ranging from 0.5 to 1 and a σ_3 overall trending NE-SW. This last result appears in accordance with the local minimum horizontal principal stress component (S_h) measured within the Trecase 1 well (located at the SE slope of the Mt. Somma-Vesuvius) as borehole breakout, showing an elongation in ENE-WSW direction (Montone et al., 2012).

Campi Flegrei

Campi Flegrei caldera (CFc) is located west of the city of Naples (**Figures 4**, **7**). It is a partially submerged collapse caldera shaped by two main eruptive episodes: the Campanian Ignimbrite eruption (40.6 ka, Gebauer et al., 2014) and the Neapolitan Yellow Tuff eruption (14.9 ka, Deino et al., 2004). Between 12 and 3.8 ka there were three eruptive episodes followed by a long period of quiescence until the last eruption of Monte Nuovo in 1538 CE (Di Vito et al., 1999). During the last decades CFc is subjected to seismic activity, gas emissions and intense ground deformations (Chiodini et al., 2001; D'Auria et al., 2011). Recent events of uplift occurred in 1950–1952, 1969–1972, and in 1982–1984 (Del Gaudio et al., 2010). During the 1982–1984 episode there was a strong increase of the seismicity (D'Auria et al., 2011). D'Auria et al. (2014b) performed a detailed analysis of the events occurred during this last crisis in order to determine the spatial-temporal variations of the stress field within the CFc. The joint inversion of seismological and geodetic datasets evidences the presence of a weak NNE-SSW extensional stress field that is progressively overcome by a local volcanic one, active during the 1982–1985 unrest episode (D'Auria et al., 2014b).

The FPS dataset analyzed in this research consists of 217 events with $0 < M < 4$ occurred between 1983 and 1984 supplied by D'Auria et al. (2014b; **Figure 7**). Epicenters are mainly concentrated at the axial sector of the CFc. Hypocentral depths are up to 6 km. The three extreme slip classes are well represented, with a slight prevalence of the dip-slip normal solutions (**Figure 7D**). The stress field has been computed applying the BRTM, using a three-dimensional grid similar to that adopted for Vesuvius: 1-km spaced nodes, for each grid node all the FPSs within a radius of 1-km have been considered for the subset inversions. Only subsets related to volumes containing at least five FPSs have been inverted (**Figure 7**). Results of the BRTM stress inversion procedures are shown in **Figure 8** and summarized for 1, 2, and 3 km depth-slices. Only a few volumes have been inverted for the 1 km depth slice. The resulting σ_1 is high to moderately plunging and corresponds to a sub-horizontal σ_3 trending E-W. The related Φ_B values are in the range 0.5–0.8. At 2 km depth slice the attitude of the inverted σ_1 is variable, with a prevalence of sub-vertical plunges while the σ_3 trends

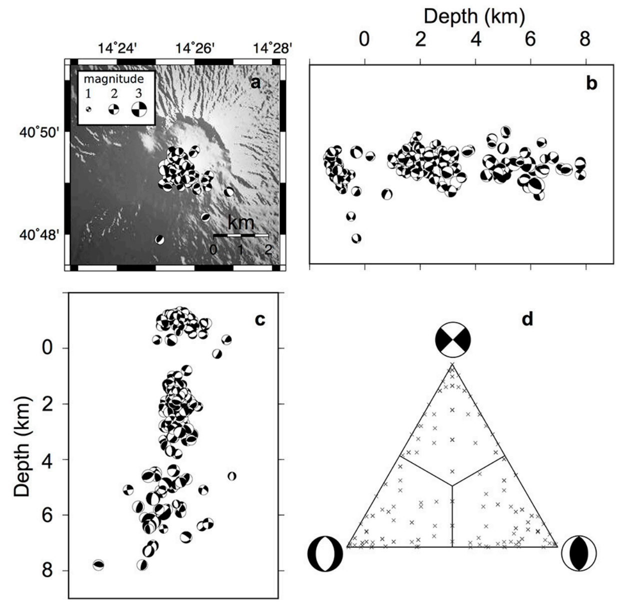

FIGURE 5 | Mt. Somma-Vesuvius. Focal mechanisms dataset plotted on a shaded map **(A)**, on a N-S **(B)**, and an E-W **(C)** cross sections. **(D)** The distribution of focal mechanisms on a triangular Frohlich diagram (Frohlich, 1992). The dataset consists of 197 FPSs of earthquakes recorded from 1999 to 2012 with $0 < M < 3.6$.

mainly NNE-SSW. The corresponding Bishop's ratio is mainly $0.2 < \Phi_B < 0.6$. At 3 km depth slice the attitude of the principal stress axes is variable and the corresponding Bishop's ratio ranges from 0 to 0.8. Nevertheless at this depth too there is a prevalence of sub-vertical plunging σ_1 and a sub-horizontal NNE-SSW trending σ_3. Overall, the key features of the stress field in the area are: a nearly sub-vertical σ_1 at the center of the CFc and a low-plunging σ_1 trending radially in the surrounding areas. The corresponding σ_3 has a roughly horizontal NNE-SSW trend corresponding to the regional extensional stress field. Related Φ_B values vary between 0.3 and 0.8 (**Figure 8**). According to D'Auria et al. (2014b), this result is compatible with the presence of a varying stress field related to a source of deformation, located at about 2.7 km depth, that during inflation and deflation episodes (associated to an increased seismicity) is able to overcome the weak regional extensional stress field having a NNE-SSW trend.

Long Valley

Long Valley caldera (LVc) is located in eastern California at the boundary between the Sierra Nevada block and the westernmost extensional Basin And Range Province (**Figure 9**). LVc develops inside a transfer zone hosted between NNW-SSE trending normal faults (e.g., Dickinson, 1979; Bosworth et al., 2003). This caldera is one of the youngest volcanic systems active in California. LVc has a surface of about 500 km^2 and is surrounded by numerous basins and ranges (like Mammoth Mountain at SW, Glass Mountain at NE, Laurel Mountain at S). It is located near some important ENE dipping normal fault

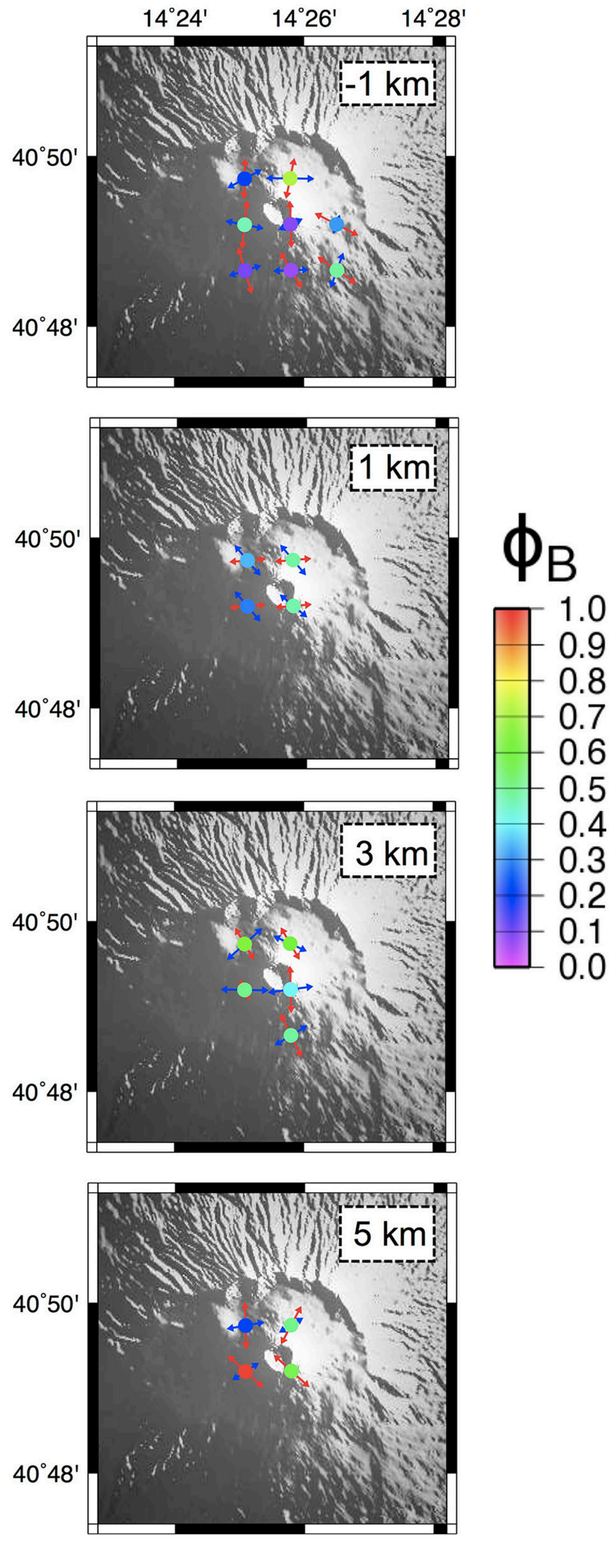

FIGURE 6 | Mt. Somma-Vesuvius. Stress field tensors retrieved from focal mechanisms data using the BRTM. Slices at −1, 1, 3, and 5 km-depth. Stress tensors have been computed over a regular grid of 1-km spacing, considering only nodes containing at least five FPSs. σ_1 and σ_3 axes are plotted as pairs of respectively red-blue arrows. The color of the circles corresponds to the retrieved Φ_B value for each node (see scale on the right).

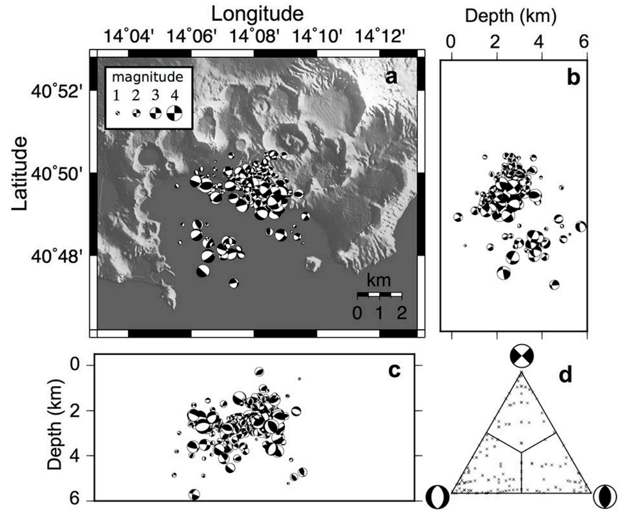

FIGURE 7 | Campi Flegrei. Focal mechanisms dataset plotted on a shaded map **(A)**, on a N-S **(B)**, and an E-W **(C)** cross sections. **(D)** The distribution of focal mechanisms on a triangular Frohlich diagram (Frohlich, 1992). The dataset consists of 217 events with $0 < M < 4$ occurred between 1983 and 1984.

systems: Hartley Springs-Silver Lake Fault system to the North (HS, SL, in **Figure 9**), Hilton Creek and Round Valley Fault systems to the South (e.g., Prejean et al., 2002; Sorey et al., 2003; Bursik, 2009; HC an RV in **Figure 9**). Additionally, the LVc area is bounded to the east by the White Mountain Range and the related SW-dipping border faults (WMt in **Figure 9**). First volcanic activity can be dated approximately 760 ka ago as result of a large explosive eruption, during which more than 600 km^3 of pyroclastics and ash (Bishop Tuff) have been erupted (Bailey et al., 1976). The emplacement of a resurgent dome (RD in **Figure 9**) located almost at the center-western sector of the caldera (started about 600 ka ago) has been causing an intense localized uplift (Hill et al., 1991; Langbein et al., 1993, 1995; Tizzani et al., 2009). Recent activity in the area consists of small eruptions and phreatic explosions at Inyo-Mono Chain (700–550 years ago; IC in **Figure 9**) and at Mono Lake, at NW of the LVc (about 200 years ago; Miller, 1985). Since 1978 seismicity and surface deformations have been continuously recorded in the area of the resurgent dome and in an active seismic zone along the southern margin of the caldera (Langbein, 2003). Location, size and geometry of magma bodies at LVc are still matter of debates (Carle, 1988; Battaglia et al., 1999, 2003a,b; Langbein, 2003; Tizzani et al., 2009; Guoqing, 2015). The regional active stress field in the western Basin and Range Province shows a minimum horizontal principal stress component (S_h) trending ESE-WNW, it rotates roughly to ENE-WSW at the border with the Sierra Nevada Range (Zoback, 1989, 1992; Heidbach et al., 2009). Breakout and seismic data depict a more complex pattern for the S_h across the LVc. NE-SW-trending S_h in the Resurgent Dome and at the South Moat Range, NW-SE-trending S_h in the West Moat and at Mammoth Mts. (**Figure 9**; Moos and Zoback, 1993; Bosworth et al., 2003, and references therein).

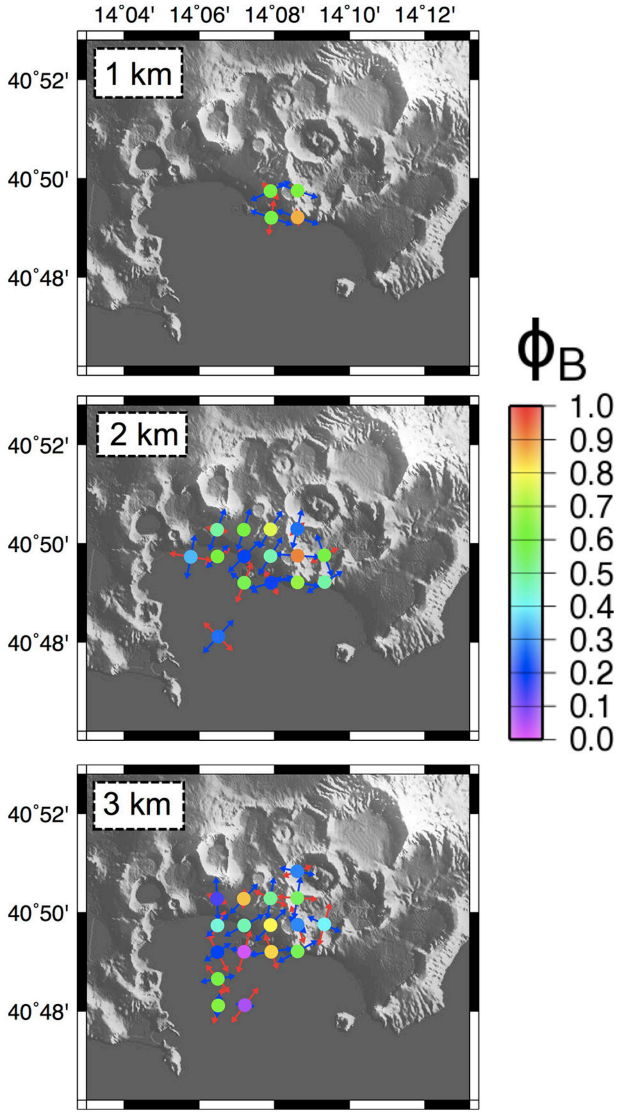

FIGURE 8 | Campi Flegrei. Stress field tensors retrieved from focal mechanisms data using the BRTM. Slices at 1, 2, and 3 km-depth. Stress tensors have been computed over a regular grid of 1-km spacing, considering only nodes containing at least five FPSs. σ_1 and σ_3 axes are plotted as pairs of respectively red-blue arrows. The color of the circles corresponds to the retrieved Φ_B value for each node (see scale on the right).

For the Long Valley Caldera we used a dataset made up of about 38,000 FPSs of earthquakes occurred from 1978 to 2015 ($0 < M < 6.4$; Dataset by: NCEDC, 2014). These data were used to determine, with high resolution, the spatial variations of the stress field using the BRTM approach. In **Figure 9** we plotted only the most energetic 3000 events ($M > 3$) in order to avoid an excessive overlapping of data. Epicenters are densely clustered at the southern sector of the LVc rim at the West Moat-Mammoth Mts.-South Moat Range sector. Additionally, many events are located along key tectonic lineaments of Hilton Creek and Round Valley to the south and along the western border fault of the White Mountains (**Figure 9A**). Hypocenters are

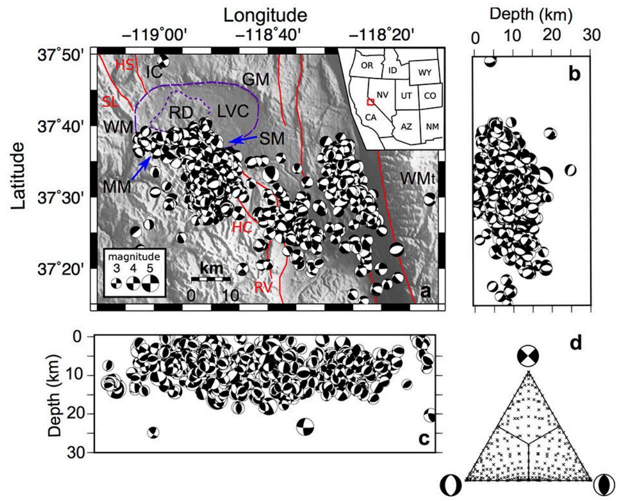

FIGURE 9 | Long Valley. Focal mechanisms dataset plotted on a shaded map **(A)**;, on a N-S **(B)**, and an E-W **(C)** cross sections. **(D)** The distribution of focal mechanisms on a triangular Frohlich diagram (Frohlich, 1992). The dataset consists of 38,000 events with $0 < M < 6.4$ occurred between 1978 and 2015. For sake of clarity only the events with $m >= 3$ are plotted. LVC, Long Valley Caldera (purple dashed line); RD, Resurgent Dome (purple dotted line); IC, Inyo Craters; WM, West Moat; MM, Mammoth Mts.; SM, South Moat; GM, Glass Mts.; WMt, White Mts. Red lines represent the main fault systems of the LVc area: SL, Silver Lake; HS, Hartley Springs Fault; HC, Hilton Creek; RV, Round Valley. See text for data sources.

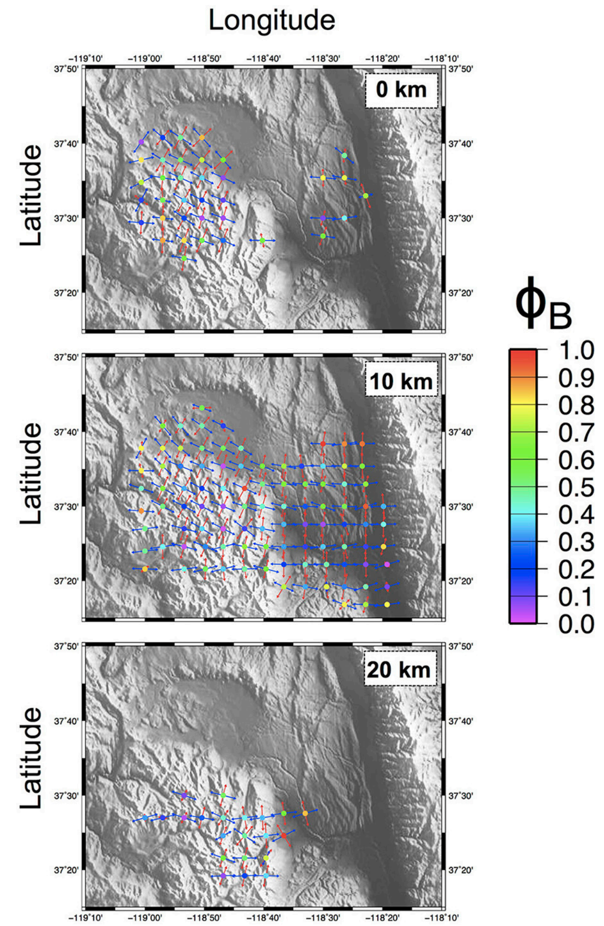

FIGURE 10 | Long Valley. Stress field tensors retrieved from focal mechanisms data using the BRTM. Slices at 0, 10, and 20 km-depth. Stress tensors have been computed over a regular grid of 5-km spacing, considering only nodes containing at least 10 FPSs. σ_1 and σ_3 axes are plotted as pairs of respectively red-blue arrows. The color of the circles corresponds to the retrieved Φ_B value for each node (see scale on the right).

essentially located above 20 km of depth. The shallowest events are concentrated at LVC and RD (**Figures 9B,C**). Kinematics of the analyzed FPSs are quite equally represented in the three main categories, with a slight prevalence of dip-slip ones (**Figure 9D**). The stress field has been computed on a regular three-dimensional grid of 5-km spacing. For each grid node all the FPSs within a radius of 5-km have been considered for the inversion. The stress field has been computed only at volumes containing at least 10 FPSs. Results of the stress inversion procedure are summarized in **Figure 10** for depth-slices located at 0-, 10-, and 20-km. At 0 km depth slice most of the events fall in the LVc area, where the attitude of the inverted σ_1 is quite variable, with a prevalence of sub-vertical plunges (NW sector) and sub-horizontal N-S to NE-SW trends in the remaining sectors. The corresponding σ_3 is mainly sub-horizontal trending mainly E-W to NW-SE. The Bishop's ratio values are highly variable, ranging from 0.1 to 0.9. The 10 km depth slice samples most of the events of the analyzed dataset. Results can be divided up in two groups, the eastern one is dominated by a sub-horizontal σ_1 trending N-S associated to a sub-horizontal E-W trending σ_3. For the western sector, the retrieved stress field appears very similar to the one obtained for the shallowest 0-km slice; a sub-horizontal σ_1 overall trending NE-SW associated to a sub-horizontal NW-SE trending σ_3. Bishop's ratio values are highly variable ranging between 0.1 and 0.9, without a clear pattern (**Figure 10**). At the 20-km depth slice the stress inversion procedure highlights the presence of an overall stress field comparable to the corresponding nodes of the 10-km depth slice: in the easternmost region, a sub-horizontal NNW-SSE trending σ_1, corresponding to a sub-horizontal ENE-WSW trending σ_3. Bishop's ratios show a slight prevalence of lower values $\Phi_B < 0.5$. Summing up, a strong background stress field seems to dominate the investigated volume: it is characterized by a sub-horizontal NNW-SSE-trending σ_1 and a sub-horizontal ENE-WSW-trending σ_3. This field is clearly evidenced by the inversion results at the deepest slices in particular at 20-km depth slice (**Figure 10**). The region at the south of the caldera rim experiences a clock-wise rotation of the $\sigma_1 - \sigma_3$ axes up to 45°, as shown at 0- and 10-km depth slices (**Figure 10**). Our results can be interpreted as the effect of the interaction between a background regional stress field with the local volcano-tectonic structures. The presence of two distinct stress patterns at 10-km depth slice clues the presence of a regional stress field, characterized by a sub-horizontal σ_1 roughlytrending from N-S to NNW-SSE associated with a sub-horizontal σ_3 trending from E-W to NNE-SSW. The retrieved background stress field drives the evolution of the main tectonic trends of the area (**Figure 8A**), overcome in the western sector by a local volcano-tectonic regime, involving mainly the shallowest lithospheric portion. This last allows the above mentioned clock-wise rotation of the $\sigma_1 - \sigma_3$ axes well documented at the −10-km slice (**Figure 10**). Our results are in agreement with S_h found in previous studies, derived by the analyses of earthquake focal mechanisms, borehole breakouts, fault offsets, hydraulic fracturing, and alignment of young volcanic vents. In detail, the $\sigma_1 - \sigma_3$ axes attitude derived for the easternmost subset inverted at −20-km slice is in good agreement with the ENE-WSW-trending S_h retrieved at the border with the Basin and Range and Sierra Nevada Range (Moos and Zoback, 1993; Prejean et al., 2002; Bosworth et al., 2003, and references therein).

DISCUSSION AND CONCLUSIONS

In volcanic environments, a spatio-temporal analysis of the stress fields represents a valuable approach to infer the volcano dynamics (Wyss et al., 1992; Hardebeck and Michael, 2006; Gudmundsson et al., 2009; Plateaux et al., 2014; Costa and Marti, 2016). Stress field variations play a key role in driving magmas and/or fluids migration. On the other hand, injection of fluids can be responsible for local variations of the stress field allowing the reactivation of locked faults. Stress changes may influence fluid circulation within the shallow crust and they can be also responsible for the triggering of tectonic earthquakes associated to strong variations in the dynamics of volcanic eruption and behavior of hydrothermal phenomena (Linde and Sacks, 1998; Hill et al., 2002; Walter et al., 2007).

During the last decades, a wide range of stress inversion techniques has been proposed, some of them specifically conceived to manage seismological datasets. Several key aspects, that could impact on the reliability of retrieved results, require a short discussion. First of all, the discernment of the actual fault plane among the nodal planes of a FPS represents a known critical step in many analytical techniques of stress inversion. (e.g., Gephart and Forsyth, 1984; Michael, 1987; Angelier, 1990). A good solution can be an a-posteriori approach that pick the actual fault following a best-fit procedure or a massive computational approach on small datasets (Michael, 1987). Of course, it implies a complication in the processing procedure that can hide pitfalls. Only a few analytical methods do not require this choice, for instance Angelier (2002) based on the slip shear component criterion. Additionally, all graphical (e.g., RDM) or graphical-derived (e.g., RTM, BRTM) techniques do not require this pre-selection; this is a valuable asset that makes these processing approaches as robust as they are simple. As premised, graphical-derived methods are based on the implementation of an algorithm that is able to figure a probability function over the focal sphere for both σ_1 and σ_3 principal stress attitude. The analytical implementation of the classical graphical methods allows the efficient managing of large datasets following a proper statistical approach (e.g., RDTM; Ramsay and Lisle, 2000). Generally, the output of these procedures needs a strong graphical post-processing in order to obtain an adequate representation of results (e.g., MORE; Massa, 2003). BRTM proposes a solution to this limitation offering a standard procedure of data ingestion, processing and graphical post-processing in both 2- and 3-Dimensional rendering. All these task can be performed through the use of editable scripts run in the same computational environment. A known drawback of stress inversion procedures (for both graphical and analytical) is that they generally lack of a robust statistical estimation of the uncertainty on the retrieved tensors. To overcome this lack, BRTM performs an estimation of solution uncertainty and trough the implementation of the approach of Jackson and Matsu'ura (1985), BRTM is able to delimit the confidence intervals around the σ1 and σ3 retrieved axes (D'Auria and Massa, 2015). Another key aspect to consider is that very frequently datasets to be processed are large and heterogeneous. Without an a-priori selection, many datasets collect faults/FPS related to different stress fields. For instance, seismological datasets collected across wide lithospheric volume, mesoscale faults hosted in a limited rock volume but generated during different tectonic events, etc. The solution to identify the different contributions from multiple sources can be a clustering approach as the MIM (Yamaji, 2000; Otsubo et al., 2008) or the application of other automatic analytical procedures (Angelier and Manoussis, 1980). These approaches allows the identification of the different stress fields but they are not designed to give a quantitative assessment of the solution quality; additionally they are not able to locate the spatial distribution of the retrieved tensors (Yamaji, 2000; D'Auria and Massa, 2015). The relevance of this point becomes larger considering the seismological datasets collected in volcanic areas. Here, the retrieving of stress field spatial variations represents a crucial task: sensible variation in stress axes attitude can characterize stress field active in contiguous volumes (e.g., D'Auria et al., 2014a,b; Plateaux et al., 2014). For this reason, unsupervisioned stress inversions performed on an unselected dataset can be quite useless. A similar discussion can be done for the analysis of stress field temporal variations. The ideal way to obtain a reliable stress field inversion would be the analysis of a dataset covering a time interval as short as possible, in order to consider the responsible stress field quite constant in its parameters (i.e., the attitude of principal stress axes and the related Φ_B). The preliminary temporal selection of data can be unfeasible in case of mesoscale faults also when collected in a limited volume of rock: several tectonic "phases" could have superimposed in the geological record. Conversely, the temporal selection of data can be conveniently done in the analysis of seismological datasets where the focal parameters are well known. In volcanic environments, a spatio-temporal analysis of the stress fields represents the best way to infer about the volcano dynamics (Wyss et al., 1992; Hardebeck and Michael, 2006; D'Auria et al., 2014b; Plateaux et al., 2014). In this perspective, a supervisioned splitting of data in 3D sub-volumes represents the best solution to retrieve the spatial distribution of active coeval stress fields. As a final consideration about the stress inversion procedures, it should be noted that the publication of a rigorous formulation of a technique is not enough to determine its success. A strong limitation to the dissemination of a processing procedure consists of the availability of a free or open-source platform of implementation. Available methods are frequently implemented by authors and freely distributed to the community only as PC programs. For instance, the Direct Inversion algorithm was implemented by the author in the executing software TENSOR (Angelier, 1990), the Multiple Inverse Method can be performed through a set of executable supplied by the author (Yamaji, 2000), RDM and RTM can be applied using RDTM, supplied by authors both as executing program than as code (Ramsay and Lisle, 2000). The availability of an editable code represents a key point to allow a flexible use of a technique, allowing, in addition, a facilitation in its spreading over the community. A BRTM implementation in MATLAB® was proposed by the Authors, allowing a basic stress-inversion procedure and an advanced plot of results (**Figure 3**; D'Auria and Massa, 2015). The implementation of the basic inversion algorithm can be easily exported to open-source and free platform. Results can be plotted using the preferred platform. The graphical post-processing proposed by D'Auria and Massa (2015) was implemented in MATLAB®. It would be useful a revision in order to make it available to free platforms.

According to previous researches, the new stress-inversions discussed in this paper (**Figures 6**, **8**, **10**), have shown that the stress field in the studied volcanoes results from the interaction of a regional background field with local volcanic structures and dynamics. In detail, during the 1983–1984 seismic crisis in the Campi Flegrei area, a sub-vertical σ_1 dominates the axial volume of the caldera. Conversely, a low-plunging σ_1 appears trending radially in the surrounding volumes. The corresponding σ_3 attitudes are roughly sub-horizontal NNE-SSW trending, in accordance with the regional S_h retrieved by breakout data (Montone et al., 2012). The retrieved stress fields are in accordance with Zuppetta and Sava (1991). The background regional stress field has been also modeled by D'Auria et al. (2014b) using a joint inversion of a geodetical-seismological dataset, obtaining a sub-horizontal σ_3 trending N-S. This result is in good accordance with the Mt. Somma-Vesuvius where D'Auria et al. (2014a) found a very similar configuration for the regional stress field. The retrieved variability of the stress field can be related to fluids migration within a planar crack probably located at shallow depth and possibly responsible for unrest episodes (D'Auria et al., 2014b; Macedonio et al., 2014). At Mt. Vesuvius, rheological variations of the involved geological units and the action of key volcano-tectonic structures seem to play a significant role in determining the local stress fields (**Figures 4–6**; D'Auria et al., 2014a). The configuration of the retrieved stress fields shows the superposition of two volumes with a marked difference in their evolution history. A top volume dominated by a gravitational volcanic spreading that allows the setting of extensional stress fields (low Φ_B values and sub-vertical σ_1) active in the analyzed sub-volumes. A bottom volume strictly related to a regional extensional background stress field in accordance with the S_h derived by breakout data (**Figure 6**; Borgia et al., 2005; Montone et al., 2012; D'Auria et al., 2014a). The computation of the stress field using the BRTM on a regular three-dimensional grid allows the 3-D figuration of the stress fields "simultaneously" acting from the surface to about 8-km depth (**Figures 5**, **6**). This approach appears very useful in supporting studies on the volcano-dynamics of complex system as the Mt. Somma-Vesuvius. Finally, analyses performed at Long Valley Caldera show a complex configuration of the stress field pattern associated to a volcanic district developed inside a transfer zone hosted between NNW-SSE trending normal faults (e.g., Dickinson, 1979; Bosworth et al., 2003). A dataset of 38,000 FPSs allows to retrieve with high resolution, the spatial variations of the stress field active in the first 20 km of depth. A regional background stress field dominates the deepest portion of the investigated volume accordingly to the ENE-WSW-trending S_h retrieved at the border with the Basin and Range and Sierra Nevada Range (Moos and Zoback, 1993; Prejean et al., 2002; Bosworth et al., 2003). In the shallowest lithospheric portions this regional stress field has been overcome by the volcano-tectonic regime; this is clear in particular at the 10 km depth-slice (**Figures 9**, **10**). The managing of the very large dataset has been approached using a regular sampling of data inverted using the BRTM. The result is a very detailed figuration of the spatial variation of the active stress fields in the 500 km^2 Long Valley Caldera, one of the youngest volcanic systems active in California.

The above results confirm that the application of stress inversion procedures to volcanic environments provides crucial information about the volcano dynamics with particular care to its interaction with regional tectonics. In detail, BRTM has shown to be very efficient in managing heterogeneous datasets in a user-friendly processing environment, with a clear graphic output and an efficient evaluation of the regions of confidence around the retrieved principal stress axes. The proposed processing approach of FPS datasets in active volcanic areas is suitable to be applied to a wide range of contexts. Finally, the results presented in this work suggest that these methods could be useful also as a near real-time monitoring tool to characterize spatial and temporal variations in the stress field linked to a volcanic unrest (e.g., Toda et al., 2002; Plateaux et al., 2014). A final consideration concerns the relevance of the stress-inversion approach based on the integration and/or the joint inversion of seismological and geodetical datasets. The joint inversion of ground deformation and focal mechanism is more efficient than the mere comparison of the results obtained by the separate inversion (Segall, 2013; D'Auria et al., 2014b; Viccaro et al., 2016). Spatial-temporal analysis of the stress field derived from seismological datasets associated to a continuous recording of ground deformations (remote and/or field classical techniques) could be a reliable tool to monitor volcano dynamics and infer about their evolution.

AUTHOR CONTRIBUTIONS

BM, LD, EC, and AD: rock mechanics, stress inversion, join inversion, and focal mechanisms.

FUNDING

This research is financially supported by: MED-SUV project (European Union's Seventh Programme for research, technological development and demonstration, Grant Agreement Number 308665); Università degli Studi del Sannio FRA 2014–2015 "Modeling of geological processes" (P.I. B. Massa).

ACKNOWLEDGMENTS

Thanks are due to the two Referees, Eisuke Fujita and Mimmo Palano, to the Associate Editor Antonio Costa and to the Chief Editor Valerio Acocella for the constructive and valuable review that greatly improved the manuscript. BRTM can be accessed as Electronic Supplement to D'Auria and Massa (2015) following the link: http://srl.geoscienceworld.org/content/early/2015/03/17/0220140153 (Last accessed on 31st October 2016).

REFERENCES

Acocella, V., and Funiciello, R. (2006). Transverse systems along the extensional Tyrrhenian margin of central Italy and their influence on volcanism. *Tectonics*, 25:TC2003. doi: 10.1029/2005TC001845

Andronico, D., Calderoni, G., Cioni, R., Sbrana, A., Sulpizio, R., and Santacroce, R. (1995). Geological map of Somma-Vesuvius volcano. *Period. Mineral.* 64, 77–78.

Angelier, J. (1990). Inversion of field data in fault tectonics to obtain the regional stress. III—A new rapid direct inversion method by analytical means. *Geophys. J. Int.* 103, 363–376. doi: 10.1111/j.1365-246X.1990.tb01777.x

Angelier, J. (2002). Inversion of earthquake focal mechanisms to obtain the seismotectonic stress IV—A new method free of choice among nodal planes. *Geophys. J. Int.* 150, 588–609. doi: 10.1046/j.1365-246X.2002.01713.x

Angelier, J., and Baruah, S. (2009). Seismotectonics in Northeast India: a stress analysis of focal mechanism solutions of earthquakes and its kinematic implications. *Geophys. J. Int.* 178, 303–326. doi: 10.1111/j.1365-246X.2009.04107.x.

Angelier, J., and Manoussis, S. (1980). Classification automatique et distinction de phases superposées en tectonique cassante. *C. R. Acad. Sci. Paris* 290, 651–654.

Angelier, J., and Mechler, P. (1977). Sur une méthode graphique de recherche des contraintes principales également utilisable en tectonique et en séismologie: La méthode des diédres droits. *Bulletin de la SocieÌĄteÌĄ GeÌĄologique de France* 19, 1309–1318.

Bailey, R. A., Dalrymple, G. B., and Lanphere, M. A. (1976). Volcanism, structure and geochronology of Long Valley caldera, Mono County, California. *J. Geophys. Res.* 81, 725– 744. doi: 10.1029/JB081i005p00725

Battaglia, M., Roberts, C., and Segall, P. (1999). Magma intrusion beneath Long Valley caldera confirmed by temporal changes in gravity. *Science* 285, 2119–2122. doi: 10.1126/science.285.5436.2119

Battaglia, M., Segall, P., Murray, J., Cervell, P., and Langbein, J. (2003a). The mechanics of unrest at Long Valley caldera, California: 1. Modeling the geometry of the source using GPS, leveling and two-color EDM data. *J. Volcanol. Geother. Res.* 127, 195–217. doi: 10.1016/S0377-0273(03)00170-7

Battaglia, M., Segall, P., and Roberts, C. (2003b). The mechanics of unrest at Long Valley caldera, California. 2. Constraining the nature of the source using geodetic and micro-gravity data. *J. Volcanol. Geother. Res.* 127, 219–245. doi: 10.1016/S0377-0273(03)00171-9

Bernasconi, A., Bruni, P., Gorla, L., Principe, C., and Sbrana, A. (1981). Risultati preliminari dell'esplorazione geotermica profonda nell'area vulcanica del Somma-Vesuvio. *Rend. Soc. Geol.* 4, 237–240.

Bianco, F., Castellano, M., Milano, G., Ventura, G., and Vilardo, G. (1998). The Somma-Vesuvius stress field induced by regional tectonics: evidences from seismological and mesostructural data. *J. Volcanol. Geother. Res.* 82, 119–218. doi: 10.1016/S0377-0273(97)00065-6

Bishop, A. (1966). The strength of solids as engineering materials. *Geotechnique* 16, 91–130. doi: 10.1680/geot.1966.16.2.91

Borgia, A., Tizzani, P., Solaro, G., Manzo, M., Casu, F., Luongo, et al. (2005). Volcanic spreading of Vesuvius, a new paradigm for interpreting its volcanic activity. *Geophys. Res. Lett.* 32:L03303, doi: 10.1029/2004GL022155

Bosworth, W., Burke, K., and Strecker, M. (2003). Effect of stress fields on magma chamber stability and the formation of collapse calderas. *Tectonics* 22:1042. doi: 10.1029/2002TC001369

Bott, M. (1959). The mechanisms of oblique slip faulting. *Geol. Mag.* 96, 109–117.

Brocchini, D., Principe, C., Castradori, D., Laurenzi, M. A., and Gorla, L. (2001). Quaternary evolution of the southern sector of the Campania Plain and early Somma-Vesuvius activity: insights from the Trecase 1 well. *Mineral. Petrol.* 73, 67–91. doi: 10.1007/s007100170011

Bursik, M. (2009). A general model for tectonic control of magmatism: Examples from Long Valley Caldera (USA) and El Chichón (México). *Geofísica Int.* 48, 171–183. Available online at: http://www.scielo.org.mx/pdf/geoint/v48n1/v48n1a12.pdf

Byerly, P. (1928). The nature of the first motion in the Chilean earthquake of November 11, 1922. *Am. J. Sci.* 16, 232–236. doi: 10.2475/ajs.s5-16.93.232

Cannavò, F., Scandura, D., Palano, M., and Musumeci, C. (2014). A joint inversion of ground deformation and focal mechanisms data for magmatic source modelling. *Pure Appl. Geophys.* 171, 1695–1704. doi: 10.1007/s00024-013-0771-x

Carey, E., and Brunier, B. (1974). Analyse théorique et numérique d'un modéle mécanique élémentaire appliquéàá l'étude d'une population de failles. *C. R. Acad. Sci.* D179, 891–894.

Carey-Gailhardis, E., and Mercier, J. (1987). A numerical method for determining the state of stress using focal mechanisms of earthquake populations: application to Tibetan teleseisms and microseismicity of southern Peru. *Earth Planet. Sci. Lett.* 82, 165–179. doi: 10.1016/0012-821X(87)90117-8

Carey-Gailhardis, E., and Mercier, J. L. (1992). Regional state of stress, fault kinematics and adjustments of blocks in a fractured body of rock: application to the micro-seismicity of the Rhine graben. *J. Struct. Geol.* 14, 1007–1017. doi: 10.1016/0191-8141(92)90032-R

Carle, S. F. (1988). Three-dimensional gravity modeling of the geologic structure of Long Valley Caldera. *J. Geophys. Res.* 93, 13237–13250. doi: 10.1029/jb093ib11p13237

Chiodini, G. L., and Marini, and, M., Russo (2001). Geochemical evidence for the existence of high-temperature hydrothermal brines at Vesuvio volcano, Italy. *Geochim. Cosmochim. Acta* 65, 2129–2147. doi: 10.1016/S0016-7037(01)00583-X

Cocina, O., Neri, G., Privitera, E., and Spampinato, S. (1997). Stress tensor computations in the Mount Etna area (Southern Italy) and tectonic implications. *J. Geodynamics* 23, 109–127. doi: 10.1016/S0264-3707(96)00027-0

Costa, A., and Marti, J. (2016). Stress field control during large caldera-forming eruptions. *Front. Earth Sci.* 4:92, doi: 10.3389/feart.2016.00092

D'Auria, L., Esposito, A. M., Lo Bascio, D., Ricciolino, P., Giudicepietro, F., Martini, M., et al. (2013). The recent seismicity of Mt. Vesuvius: inference on seismogenic processes. *Ann. Geophys.* 56:S0442, doi: 10.4401/ag-6448

D'Auria, L. F., Giudicepietro, I., Aquino, G., Borriello, C., Del Gaudio, D., Lo Bascio, M., et al. (2011). Repeated fluid-transfer episodes as a mechanism for the recent dynamics of Campi Flegrei caldera (1989–2010). *J. Geophys. Res.* 116:B04313, doi: 10.1029/2010JB007837

D'Auria, L., Martini, M., Esposito, A., Ricciolino, P., and Giudicepietro, F. (2008). "A unified 3D velocity model for the Neapolitan volcanic areas," in *Conception, Verification and Application of Innovative Techniques to Study Active Volcanoes*, eds W. Marzocchi and A. Zollo (Napoli: INGV-DPC), 375–390.

D'Auria, L., and Massa, B. (2015). Stress inversion of focal mechanism data using a bayesian approach: a novel formulation of the right trihedra method. *Seism. Res. Lett.* 86, 968–977. doi: 10.1785/0220140153

D'Auria, L., Massa, B., Cristiano, E., Del Gaudio, C., Giudicepietro, F., Ricciardi, G., et al. (2014b). Retrieving the stress field within the campi flegrei caldera (southern italy) through an integrated geodetical and seismological approach. *Pure Appl. Geophy.* 172, 3247–3263. doi: 10.1007/s00024-014-1004-7

D'Auria, L., Massa, B., and De Matteo, A. (2014a). The stress field beneath a quiescent stratovolcano: the case of mount Vesuvius. *J. Geophys. Res.* 119, 1181–1199. doi: 10.1002/2013JB010792

Deino, A. L., Orsi, G., Piochi, M., and De Vita, S. (2004). The age of the neapolitan Yellow Tuff caldera-forming eruption (Campi Flegrei caldera–Italy) assessed by 40ar/39ar dating method. *J. Volcanol. Geother. Res.* 133, 157–170. doi: 10.1016/S0377-0273(03)00396-2

Del Gaudio, C., Aquino, I., Ricciardi, G. P., Ricco, C., and Scandone, R. (2010). Unrest episodes at Campi Flegrei: a reconstruction of vertical ground movements during 1905–2009. *J. Volcanol. Geother. Res.* 195, 48–56. doi: 10.1016/j.jvolgeores.2010.05.014

De Matteis, R., Matrullo, E., Rivera, L., Stabile, T. A., Pasquale,G., and Zollo, A. (2012). Fault Delineation and Regional Stress Direction from the Analysis of Background Microseismicity in the southern Apennines, Italy. *Bull. Seismol. Soc. Am.* 102, 1899–1907. doi: 10.1785/0120110225

Dickinson, W. R. (1979). "Cenozoic plate tectonic setting of the Cordilleran region in the United States," in *Pacific Coast Paleogeography Symposium 3; Cenozoic Paleogeography of the Western United States*, eds J. M. Armentrout, M. R. Cole, and H. TerBest Jr. (Anaheim, CA: Pac. Sect., Soc. of Econ, Paleontol. and Mineral), 1–13.

Di Vito, M. A., Isaia, R., Orsi, G., Southon, J., De Vita, S., D'antonio, M., et al. (1999). Volcanism and deformation since 12,000 years at the Campi Flegrei caldera (Italy). *J. Volcanol. Geother. Res.* 91, 221–246. doi: 10.1016/S0377-0273(99)00037-2

Frohlich, C. (1992). Triangle diagrams: ternary graphs to display similarity and diversity of earthquake focal mechanisms. *Phys. Earth. Planet. Inter.* 75, 193–198. doi: 10.1016/0031-9201(92)90130-N

Gebauer, S., Schmitt, A. K., Pappalardo, L., Stockli, D. F., and Lovera, O. M. (2014). Crystallization and eruption ages of Breccia Museo (Campi Flegrei caldera, Italy) plutonic clasts and their relation to the Campanian ignimbrite. *Contrib. Mineral. Petrol.* 167:953. doi: 10.1007/s00410-013-0953-7

Gephart, J., and Forsyth, D. (1984). An improved method for determining the regional stress tensor using earthquake focal mechanism data: application to the San Fernando earthquake sequence. *J. Geophys. Res.* 89, 9305–9320. doi: 10.1029/JB089iB11p09305

Gillard, D., and Wyss, M. (1995). Comparison of strain and stress tensor orientation: application to Iran and southern California. *J. Geophys. Res.* 100, 22197–22213. doi: 10.1029/95JB01871

Giudicepietro, F., Orazi, M., Scarpato, G., Peluso, R., D'Auria, L., Ricciolino, P., et al. (2010). Seismological monitoring of Mount Vesuvius (Italy): more than a century of observations. *Seism. Res. Lett.* 81, 625–634, doi: 10.1785/gssrl.81.4.625

Guoqing, L. (2015). Seismic velocity structure and earthquake relocation for the magmatic system beneath Long Valley Caldera, eastern California. *J. Volcanol. Geother. Res.* 296, 19–30. doi: 10.1016/j.jvolgeores.2015.03.007

Gudmundsson, A., Acocella, V., and Vinciguerra, S. (2009). Understanding stress and deformation in active volcanoes. *Tectonophysics* 471, 1–3. doi: 10.1016/j.tecto.2009.04.014

Hardebeck, J. L., and Hauksson, E. (2001). Stress orientations obtained from earthquake focal mechanisms: what are appropriate uncertainty estimates? *Bull. Seismol. Soc. Am.* 91, 250–252. doi: 10.1785/0120000032

Hardebeck, J. L., and Michael, A. J. (2006). Damped regional-scale stress inversions: methodology and examples for southern California and the Coalinga aftershock sequence. *J. Geophys. Res.* 111:B11310, doi: 10.1029/2005JB004144

Heidbach, O., Tingay, M., Barth, A., Reinecker, J., Kurfeß, D. and Müller, B. (2009). *The World Stress Map based on the database release 2008, equatorial scale 1:46,000,000*. Paris: Commission for the Geological Map of the World.

Hill, D. P., Johnston, M. J. S., Langbein, J. O., McNutt, S. R., Miller, C. D., Mortensen, C. E., et al. (1991). *Response Plans for Volcanic Hazards in the Long Valley Caldera and Mono Craters area, California*. Open-File Report, U.S. Geology Survey.

Hill, D. P., Pollitz, F., and Newhall, C. (2002). Earthquake-volcano interactions. *Phys. Today* 55, 41–47. doi: 10.1063/1.1535006

Ippolito, F., Ortolani, F., and Russo, M. (1973). Struttura marginale tirrenica dell'Appennino campano: reinterpretazione di dati di antiche ricerche di idrocarburi. *Mem. Soc. Geol.* 12, 227–250.

Jackson, D. D., and Matsu'ura, M. (1985). A Bayesian approach to nonlinear inversion. *J. Geophys. Res.* 90, 581–591. doi: 10.1029/JB090iB01p00581

Langbein, J. O. (2003). Deformation of the Long Valley caldera, California: inferences from measurements from 1988 to 2001. *J. Volcanol. Geother. Res.* 127, 247–267. doi: 10.1016/S0377-0273(03)00172-0

Langbein, J. O., Dzurisin, D., Marshall, G., Stein, R., and Rundle, J. (1995). Shallow and peripheral volcanic sources of inflativo revealed by modeling two-color geodimeter and leveling data from Long Valley caldera, California, 1988–1992. *J. Geophys. Res.* 100, 12487–12495. doi: 10.1029/95JB01052

Langbein, J. O., Hill, D. P., Parker, T. N., and Wilkinson, S. K. (1993). An episode of re-inflation of the Long Valley caldera, eastern California, 1989–1991. *J. Geophys. Res.* 98, 15851–15870. doi: 10.1029/93JB00558

Lavecchia, G., Boncio, P., Creati, N., and Brozzetti, F. (2003). Some aspects of the Italian geology not fitting with a subduction scenario. *J. Virtual Explor.* 10, 1–42. doi: 10.3809/jvirtex.2003.00064

Linde, A. T., and Sacks, I. S. (1998). Triggering of volcanic eruptions. *Nature* 395, 888–890. doi: 10.1038/27650

Lisle, R. (1988). ROMSA: a basic program for paleostress analysis using fault striation data. *Comput. Geosci.* 14, 255–259. doi: 10.1016/0098-3004(88)90007-6

Lisle, R. J. (1987). Principal stress orientations from faults: an additional constraint. *Annales Tectonicae* 1, 155–158.

Lomax, A., Zollo, A., Capuano, P., and Virieux, J. (2001). Precise, absolute earthquake location under Somma-Vesuvius volcano using a new three-dimensional velocity model. *Geophys. J. Int.* 146, 313–331. doi: 10.1046/j.0956-540x.2001.01444.x

Macedonio, G., Giudicepietro, F., D'auria, L., and Martini, M. (2014). Sill intrusion as a source mechanism of unrest at volcanic calderas. *J. Geophys. Res. Solid Earth* 119, 3986–4000. doi: 10.1002/ 2013JB010868

Massa, B. (2003). *Relazione Tra Faglie Quaternarie e Sismicita NellŠarea Sannita*, Printed, Dottorato di Ricerca in Scienze della Terra e della Vita, XV ciclo., Universita degli Studi del Sannio, Benevento, Italy.

Michael, A. J. (1987). Use of Focal Mechanisms to Determine Stress: a control study. *J. Geophys. Res.* 92, 357–368. doi: 10.1029/JB092iB01p00357

Milia, A., Torrente, M. M., Massa, B., and Iannace, P. (2013). Progressive changes in rifting directions in the Campania margin (Italy): New constrains for the Tyrrhenian Sea opening. *Global Planetary Change* 109, 3–17. doi: 10.1016/j.gloplacha.2013.07.003

Miller, C. D. (1985). Holocene eruptions at the Inyo volcanic chain, California: implications for possible eruptions in Long Valley caldera. *Geology* 13, 14–17. doi: 10.1130/0091-7613(1985)13<14:HEATIV>2.0.CO;2

Montone, P., Mariucci, M. T., and Pierdominici, S. (2012). The Italian present-day stress map. *Geophys. J. Int.* 189, 705–716, doi: 10.1111/j.1365-246X.2012.05391.x

Moos, D., and Zoback, M. D. (1993). State of stress in the Long Valley caldera, California. *Geology* 21, 837–840. doi: 10.1130/0091-7613(1993)021<0837:SOSITL>2.3.CO;2

NCEDC (2014). *Northern California Earthquake Data Center*. Berkeley: UC Berkeley Seismological Laboratory. Dataset.

Otsubo, M., Yamaji, A., and Kubo, A. (2008). Determination of stresses from heterogeneous focal mechanism data: an adaptation of the multiple inverse method. *Tectonophysics* 475, 150–160. doi: 10.1016/j.tecto.2008.06.012

Pedersen, R., and Sigmundsson, F. (2004). InSAR based sill model links spatially offset areas of deformation and seismicity for the 1994 unrest episode at Eyjafjallajökull volcano, Iceland. *Geophys. Res. Lett.* 31:L14610. doi: 10.1029/2004GL020368

Plateaux, R., Béthoux, N., Bergerat, F., and Mercier de Lépinay, B. (2014). Volcano-tectonic interactions revealed by inversion of focal mechanisms: stress field insight around and beneath the Vatnajökull ice cap in Iceland. *Front. Earth Sci.* 2:9, 1–21. doi: 10.3389/feart.2014.00009

Prejean, S., Ellsworth, W., Zoback, M., and Walhouser, F. (2002). Fault structure and kinematics of the Long Valley Caldera region, California, revealed by high-accuracy earthquake hypocenters and focal mechanism stress inversion. *J. Geophys. Res.* 107:2355, doi: 10.1029/2001JB001168

Ramsay, J., and Lisle, R. (2000). *The Techniques of Modern Structural Geology, Volume 3: Applications of Continuum Mechanics in Structural Geology*. London: Academic Press.

Reasenberg, P., and Oppenheimer, D. (1985). *FPFIT, FPPLOT and FPPAGE: Fortran Computer Programs for Calculating and Displaying Earthquake Fault Plane Solutions*. Open File Report U.S. Geological Survey.

Reid, H. F. (1910). "The mechanism of the earthquake," in *The California Earth-quake of April 18, 1906. Report of the State Earthquake Investigation Commission*, Vol. 2 (Washington, DC: Carnegie Institution for Science), 1–192.

Rivera, L., and Cisternas, A. (1990). Stress tensor and fault plane solutions for a population of earthquakes. *Bull. Seismol. Soc. Am.* 80, 600–614.

Rosi, M., Santacroce, R., and Sbrana, A. (1987). *Geological Map of the Somma-Vesuvius Volcanic Complex (Scale 1:25000)*. Roma: CNR,PF Geodinamica, L Salomone.

Santacroce, R. (ed.). (1987). *Somma-Vesuvius, Vol. 114*, Rome: CNR.

Segall, P. (2013). *Volcano Deformation and Eruption Forecasting*. London: Geological Society; Special Publications.

Sorey, M. L., McConnell, V. S., and Roeloffs, E. (2003). Summary of recent research in Long Valley caldera, California. *J. Volcanol. Geother. Res.* 127, 165–173. doi: 10.1016/S0377-0273(03)00168-9

Tizzani, P., Battaglia, M., Zeni, G., Atzori, S., Berardino, P., and Lanari, R. (2009). Uplift and magma intrusion at Long Valley caldera from InSAR and gravity measurements. *Geology* 37, 63–66. doi: 10.1130/G25318A.1

Toda, S., Stein, R. S., and Sagiya, T. (2002). Evidence from the AD 2000 Izu islands earthquake swarm that stressing rate governs seismicity. *Nature* 419, 58–61. doi: 10.1038/nature00997

Umakoshi, K., Shimizu, H., and And Matsuwo, N. (2001). Volcano-tectonic seismicity at Unzen Volcano, Japan, 1985–1999. *J. Volcanol. Geother. Res.* 112, 117–131. doi: 10.1016/S0377-0273(01)00238-4

Ventura, G., and Vilardo, G. (1999). Slip tendency analysis of the Vesuvius faults: implication for the seismotectonic and volcanic hazard assessment. *Geophys. Res. Lett.* 26, 3229–3232. doi: 10.1029/1999GL005393

Viccaro, M., Zuccarello, F., Cannata, A., Palano, M., and Gresta, S. (2016). How a complex basaltic volcanic system works: constraints from integrating seismic, geodetic, and petrological data at Mount Etna volcano during the July-August 2014 eruption. *J. Geophys. Res. Solid Earth* 121, 5659–5678. doi: 10.1002/2016JB013164

Vitale, S., and Isaia, R. (2013). Fractures and faults in volcanic rocks (Campi Flegrei, southern Italy): insight into volcano-tectonic processes. *Int. J. Earth Sci.* 103, 801–819. doi: 10.1007/s00531-013-0979-0

Wallace, R. E. (1951). Geometry of shearing stress and relation to faulting. *J. Geol.* 22, 118–130. doi: 10.1086/625831

Walter, T. R., Wang, R., Zimmer, M., Grosser, H., Luhr, B., and Ratdomopurbo, A. (2007). Volcanic activity influenced by tectonic earthquakes: static and dynamic stress triggering at Mt. Merapi. *Geophys. Res. Lett.* 34:L05304. doi: 10.1029/2006gl028710

Wyss, M., Liang, B., Tanigawa, W. R., and Xiaoping, W. (1992). Comparison of orientations of stress and strain tensor based on fault plane solutions in Kaoiki, Hawaii. *J. Geophys. Res.* 97, 4769–4790. doi: 10.1029/91JB02968

Yamaji, A. (2000). The multiple inverse method: a new technique to separate stresses from heterogeneous fault-slip data. *J. Struct. Geol.* 22, 441–452. doi: 10.1016/S0191-8141(99)00163-7

Yamaji, A. (2007). *An Introduction to Tectonophysics: Theoretical Aspects of Structural Geology*. Tokyo: TERRAPUB.

Zoback, M. L. (1989). State of stress and modern deformation of the northern basin and rangeprovince. *J. Geophys. Res.* 94, 7105–7128. doi: 10.1029/JB094iB06p07105

Zoback, M. L. (1992). First and second-order patterns of stress in the lithosphere: the world stress map project. *J. Geophys. Res.* 97, 11703–11728. doi: 10.1029/92JB00132

Zollo, A., Marzocchi, W., Capuano, P., Lomax, A., and Iannaccone, G. (2002). Space and time behaviour of seismic activity and Mt. Vesuvius volcano, Southern Italy. *Bull. Seismol. Soc. Am.* 92, 625–640. doi: 10.1785/01200 00287

Zuppetta, A., and Sava, A. (1991). Stress pattern at Campi Flegrei from focal mechanisms of the 1982–1984 earthquakes (Southern Italy). *J. Volcanol. Geother. Res.* 48, 127–137. doi: 10.1016/0377-0273(91)90038-2

Conflict of Interest Statement: The authors declare that the research was conducted in the absence of any commercial or financial relationships that could be construed as a potential conflict of interest.

The handling Editor declared a shared affiliation, though no other collaboration, with the authors BM, LD, and EC and states that the process nevertheless met the standards of a fair and objective review.

frontiers in Earth Science

ORIGINAL RESEARCH
published: 28 July 2016
doi: 10.3389/feart.2016.00076

Tectonic Geomorphology and Volcano-Tectonic Interaction in the Eastern Boundary of the Southern Cascades (Hat Creek Graben Region), California, USA

Engielle M. R. Paguican[1, 2]* *and Marcus I. Bursik*[1]

[1] Department of Geology, University at Buffalo, The State University of New York, Buffalo, NY, USA, [2] Department of Geography, Earth System Sciences, Vrije Universiteit Brussel, Brussels, Belgium

The eastern boundary of the Southern Cascades (Hat Creek Graben region), California, USA, is an extensively faulted volcanic corridor between the Cascade Range and Modoc Plateau. The morphology of the region is a result of plate motions associated with different tectonic provinces, faulting, and recurring volcanic activity, making it an ideal place to study the interrelationship between tectonics, volcanoes, and geomorphology. We use the morphometry and spatial distribution of volcanoes and their interaction with regional structures to understand how long term regional deformation can affect volcano evolution. A database of volcanic centers and structures was created from interpretations of digital elevation models. Volcanic centers were classified by morphological type into cones, sub-cones, shields and massifs. A second classification by height separated the larger and smaller edifices, and revealed an evolutionary trend. Poisson Nearest Neighbor analysis showed that bigger volcanoes are spatially dispersed while smaller ones are clustered. Using volcano centroid locations, about 90 lineaments consisting of at least three centers within 6 km of one another were found, revealing that preferential north-northwest directed pathways control the transport of magma from the source to the surface, consistent with the strikes of the major fault systems. Most of the volcano crater and collapse scar openings are perpendicular to the north northwest-directed maximum horizontal stress, expected for extensional environments with dominant normal faulting. Early in the history of a volcano or volcano cluster, melt propagates to the surface using the easiest and most efficient pathway, mostly controlled by the pre-existing normal faults and near-surface stress fields, as indicated by the pervasive vent alignments. Volcano growth continues to be dependent on the regional structures as indicated by the opening directions, suggesting structural control on the growth of the volcanic edifices. The results present a particularly well-defined case in which extension of a volcanic region is accommodated mostly by faulting, and only partly by intrusion to form volcanoes. This is attributed to a low magma supply rate.

Keywords: volcano-tectonic, tectonic-geomorphology, Hat Creek Graben region, California, Southern Cascades, morphometry, spatial distribution, volcano alignments

OPEN ACCESS

Edited by:
Roberto Sulpizio,
University of Bari, Italy

Reviewed by:
Laura Pioli,
University of Geneva, Switzerland
Gianluca Groppelli,
National Research Council, Italy

****Correspondence:***
Engielle M. R. Paguican
engiellepaguican@gmail.com

Specialty section:
This article was submitted to
Volcanology,
a section of the journal
Frontiers in Earth Science

Received: *31 December 2015*
Accepted: *12 July 2016*
Published: *28 July 2016*

Citation:
Paguican EMR and Bursik MI (2016)
Tectonic Geomorphology and
Volcano-Tectonic Interaction in the
Eastern Boundary of the Southern
Cascades (Hat Creek Graben Region),
California, USA. Front. Earth Sci. 4:76.
doi: 10.3389/feart.2016.00076

1. INTRODUCTION

Volcanoes occur in a wide variety of shapes and sizes as a result of the interaction of constructive and destructive geological and environmental processes. The quantitative description of volcano morphology, called volcano morphometry, is a systematic way to characterize the morphology of volcano edifices, allowing for the extraction of information on the processes that interact and factors that control growth history and evolution (Grosse et al., 2012, 2014). At the same time, describing a volcanic field in which volcanoes grow is essential for characterizing key controls on volcano growth in space, which reflects the pathway used by magma to reach the surface, and the existence of any dominantly controlling factor that may have created preferential pathways (Le Corvec et al., 2013). At the surface and through time, the growth or destruction of a volcano is influenced by the volcano-tectonic setting of the region. Studies looking at the influence of regional stress on the direction of sector-collapse and debris-avalanche amphitheater opening have been done for Southeast Asian volcanoes in tectonic settings dominated by strike-slip faults, particularly those in the Philippines, by Lagmay and Valdivia (2006), Japan by Ui et al. (1986), and Indonesia by Bahar and Girod (1983), which showed that the opening direction of such features is at an acute angle relative to the regional maximum horizontal stress. Their results are in disagreement with earlier models by Moriya (1980), Siebert (1984), and Nakamura (1977), which show volcano openings perpendicular to the maximum horizontal stress being more prevalent in extensional regions (Tibaldi, 1995), where tabular conduits and dikes that propagate along normal faults promote collapses perpendicular to the regional maximum horizontal stress. This difference in results may be due to differences in the underlying fault kinematics, the resulting geometry of large-scale sliding and debris avalanching, original crater opening direction due to temporal and topographic stress-field control within a volcanic body (Ui et al., 1986), a dipping substrate, or a spreading basement.

The eastern boundary of the Southern Cascades (herein referred to as the Hat Creek Graben region) in California is an extensively faulted volcanic corridor with spectacular, high, steep scarps in a bedrock of late Tertiary and Quaternary volcanic and sedimentary deposits (Wills, 1991; Muffler et al., 1994; Blakely et al., 1997). It is at the boundary between two distinct geologic and geomorphic provinces (Jenkins, 1938), the Cascade Range on the west and the Modoc Plateau on the east, between Mt. Shasta and Lassen Peak on the north and south, respectively. It is in the transition zone between several significant volcanic and tectonic provinces, including the east-west convergence and subduction of the Gorda Plate underneath the North American Plate, the current north-south shortening within the Klamath Mountain Region on the northwest, and the region of east-west extensional faulting that produced the dominant north- to northwest- striking normal faults, forming the horst and graben topography and voluminous basaltic volcanism (White and Crider, 2006). Volcano morphology is a result of recurring volcanic activity within this diverse tectonic setting, from more than 500 vents over the past 7 Ma (Muffler et al., 1994), making it an important place to study the long-term interrelationship between tectonics, geomorphology, and volcanic activity. Many studies have recently explored the importance of magma in shaping divergent plate boundaries (Wright et al., 2006; Ebinger et al., 2010; Sigmundsson et al., 2015; Acocella and Trippanera, 2016), and here we seek to discern whether some of these ideas also apply to intraplate magmatic provinces experiencing extension, such as the Hat Creek Graben region.

This study aims to provide a tectonic-geomorphic interpretation of the eastern boundary of the southern Cascades—the Hat Creek Graben region. It is hoped that the results will aid in producing a more refined understanding of regional volcano-tectonic interaction and history, which may help guide future hazard assessment. We explore the overall geomorphology and activity of individual volcanoes and the potential effects of regional stress regimes. We characterize local structures within each volcano, and compare the trend of volcano erosional and collapse scars with features in the basement faults, and regional maximum horizontal stress. We furthermore attempt to refine our understanding of the probable kinematics of underlying faults that may cause volcano instability.

2. REGIONAL TECTONIC SETTING AND FAULT SYSTEMS

The tectonics of the Hat Creek Graben region (**Figure 1A**) is dominated by the convergence of the Pacific, Juan de Fuca, Gorda and North American Plates; the rigid block of the Sierran Microplate; and the dominantly extensional western Basin and Range (Hammond and Thatcher, 2005). Subduction of the Juan de Fuca and Gorda Plates underneath the North American Plate forms the Cascadia Subduction Zone and the associated Cascade Arc volcanoes. To the south, the Sierran Microplate behaves as a rigid block that, due to the faster rate of right-lateral shear on its western side, accommodated by the right-lateral San Andreas Transform Fault and associated structures (Dixon et al., 2000; Faulds et al., 2005), is translated northward. This causes compression (north-south shortening) in the Klamath Mountains region on the northwest (McCaffrey, 2005). Furthermore, the motion of the Sierran Microplate contributes to the clockwise rotation of the Oregon forearc, where the Sierran Microplate and Cascadia forearc blocks meet (McCaffrey, 2005). On the eastern boundary of the Sierran Microplate, the Walker Lane accommodates some 15–25% of the total relative plate motion (Faulds et al., 2005), with GPS measured strain rates of about 11 mm yr^{-1} (Dokka and Travis, 1990; Argus and Gordon, 1991; Sauber et al., 1994; Bennett et al., 1999; Dixon et al., 2000; Hammond and Thatcher, 2007). Some of the right-lateral shear related to relative Pacific and North American plate motion is accommodated within the Hat Creek Graben region, and connects with poorly defined zones of deformation between the Gorda, Pacific, and North American plates near the Klamath Mountains (Miller et al., 2001). Crustal stresses related to the complex block motions and volcanic processes drive regional seismicity, and the observed patterns of faulting of the Hat Creek Graben region.

Fault scarps are prominent in the Hat Creek Graben region, especially in places where they displace resistant Pliocene to early Pleistocene basalt, with up to millions of years of accumulated offset (Blakeslee and Kattenhorn, 2013). Major fault systems (**Figure 1B**) identified and described by previous workers include the Hat Creek, Rocky Ledge, McArthur, Soldier Creek, and Pittville Fault Systems.

The Hat Creek Fault System is a late Pleistocene to Holocene (Parrish, 2006; U.S. Geological Survey and California Geological Survey, 2006; Muffler et al., 2010), 47-km long, up to 490-m high, west-facing escarpment along the east side of Hat Creek Valley (Blakeslee and Kattenhorn, 2013). It has a slip rate of about 1-3.6 mm yr^{-1}, and is capable of producing an earthquake of moment magnitude about 6.7, with a recurrence interval of 667 ± 167 yr (Wills, 1991; Blakeslee and Kattenhorn, 2013). The Hat Creek Fault has a component of right-lateral offset along with normal offset (Wills, 1991), with segments connected by relay ramps and monoclines (Muffler et al., 1994). Due to sporadic volcanic activity, surface rupture along the Hat Creek fault has progressively migrated westward since the Late Pleistocene, with older scarps successively abandoned (Blakeslee and Kattenhorn, 2013). North of the Pit River, slip of the Hat Creek Fault probably transfers to the Soldier Creek Fault, which displaces a 1.2 Ma basalt by more than 260 m, giving a long-term vertical separation rate of 0.22 mm yr^{-1}. On the western edge of Hat Creek valley is the 9 km long, north-trending and east-facing Rocky Ledge Fault System. It has a component of right-lateral motion on a dominantly normal structure. The strike-slip component is consistent with the northwest propagation of the Walker Lane Belt, with suggested Holocene activity (Wills, 1991; Austin, 2013). The Rocky Ledge Fault System has an average slip rate of 0.4 ± 0.2 mm yr^{-1}, an order magnitude less than the late Quaternary slip rate on the Hat Creek Fault (Sawyer and Ramelli, 2012). East of and parallel to the Hat Creek fault zone, there are normal faults with a right-lateral component, as well as the west-facing scarps of the McArthur Fault Zone. A steep scarp in alluvium with very weak soil development, a large closed depression that flanks a west-facing scarp in alluvium south of Big Lake, and tonal lineaments in plowed fields indicate Holocene offset along this fault (Wills, 1991). The more northwesterly Pittville Fault extends for about 48 km to the southeast, partly controlling the course of the Pit River and offsetting Brushy Butte, the volcanic center north of Big Lake (Peterson and Martin, 1980). Recent movements are indicated North of the Pit River Valley, where the fault forms a 1–3 m scarp in Late Pleistocene basalt, with open fissures up to 2 m deep on the upthrown side.

3. METHODOLOGY

Shuttle Radar Topography Mission (SRTM), higher-resolution, local LiDAR, and 10-m spacing National Elevation Data (NED) (Gesch et al., 2002) were used in the present study. NED data, covering the area of the Southern Cascades from 40.22 to 41.33 N and 122.08 to 120.22 W in decimal degrees, were acquired from the USGS National Map website (http://ned.usgs.gov), and were the primary dataset used for mapping and interpreting the overall tectonics, geomorphology and volcano distribution. In addition, Landsat satellite images, which have been used to study remote active volcanoes and to map basaltic volcanic fields (Francis and Wells, 1988), were downloaded. The elevation data were loaded in ArcGIS® software and saved as an ENVI compatible file for processing and topographic modeling.

3.1. Topographic Modeling, and Structural and Geomorphological Interpretation

Topographic modeling techniques were applied to the DEM using RSI ENVI® software generated surface parameters, including shaded relief, slope, and aspect maps. Landsat 7 Thematic Mapper Plus (ETM+) and panchromatic band 8 images were processed to combine bands and obtain maximum contrast to check surface features and deposits observed in the DEM. Generated images were compiled using ArcGIS® software.

Geomorphic features, including volcanic, tectonic, and volcano-tectonic features such as volcano edifices, cone and lava fields, and faults, as well as features resulting from gravitational instability and erosion were visually interpreted and described from the images. Interpretations were checked in the field. Structural analysis of the elevation dataset was based on the interpretation of rectilinear features or lineaments of regional scale. Lineaments consist of sharp tonal differences and alignments of geomorphological features like cones, streams and rivers, ridges and crests. Within tectonically active areas such as the Hat Creek Graben region, lineaments usually coincide with the fracture network and the major fracture patterns. Volcanoes are identified from descriptions in previous literature and visually interpreted by their positive relief with a circular or elongated shape, and may have a small crater near the summit. Volcano bases were manually delineated, by following the break in slope around the edifice base. Thus, only the objectively definable, visible edifice was traced and far-reaching fall and flow products were not considered in the delineation. Main lineament directions and volcano base elongations were then defined by the azimuth frequency distribution plotted on rose diagrams. Terrain modeling, geomorphological interpretation, and geomorphometry were then combined to interpret the relationships between the regional stress, basement faults, and volcanoes.

3.2. Volcano Morphometry

Individual volcano base and crater shapefiles were extracted as regions of interest from the DEM and processed using MORVOLC to generate a quantitative characterization of each individual edifice, and to develop a systematic way to compare the edifices. MORVOLC (Grosse et al., 2009) is an IDL-based code that generates a database of quantitative descriptions of the size (height, width, and volume), planview shape (ellipticity and irregularity), and profile shape (height-width ratio, summit width to basal width ratio, and slope) of stratovolcanoes and cones. Morphometric analysis can provide clues to the processes that interact during the growth history, development and evolution of each volcano, and can be used to draw an evolutionary trend

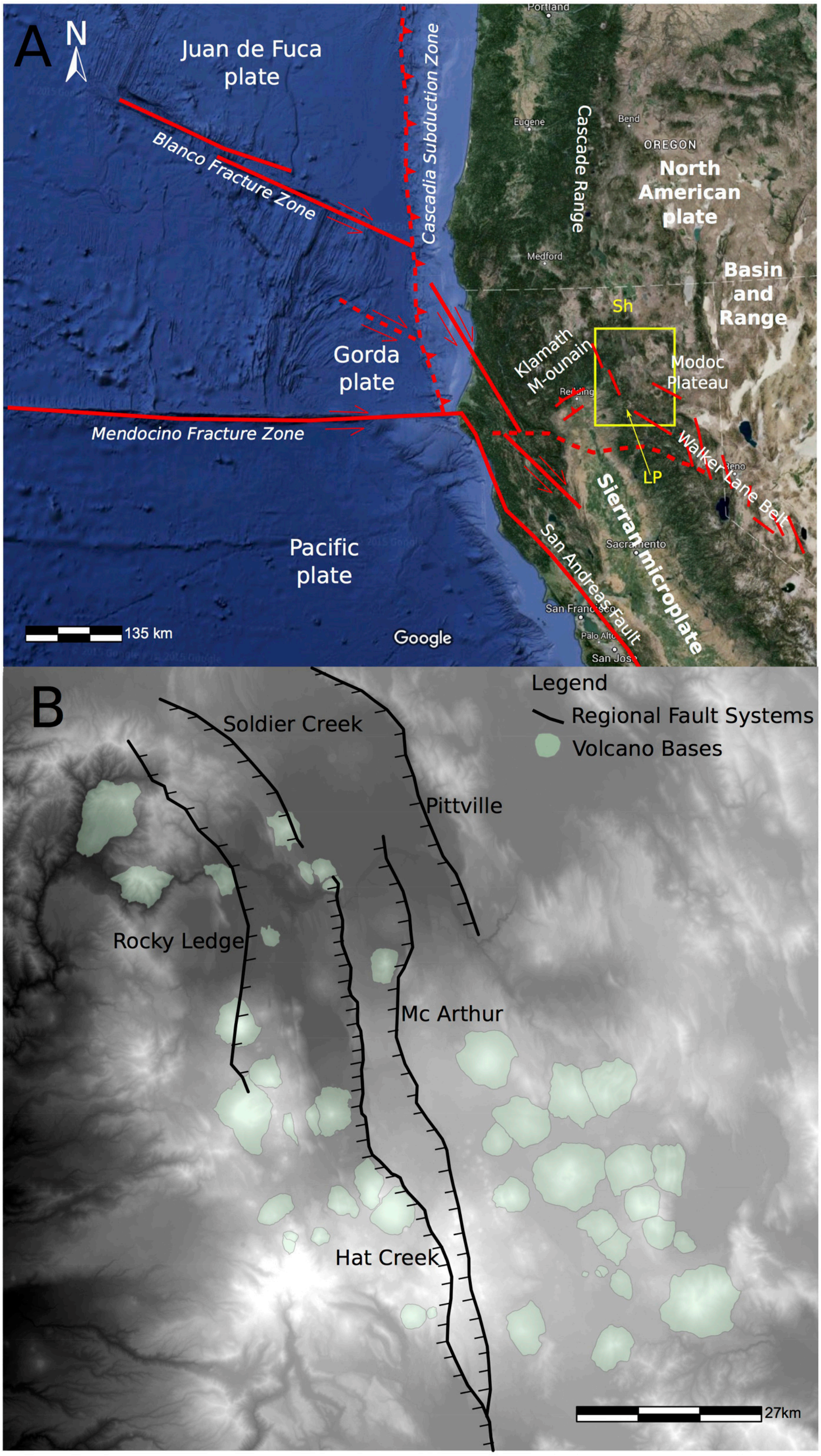

FIGURE 1 | (A) Regional tectonic setting of the eastern boundary of the Southern Cascades (Hat Creek Graben region), California, is dominated by the convergence of the Pacific, Juan de Fuca, Gorda, and North American Plates resulting in the formation of the Cascadia Subduction Zone and its associated Cascade Arc Volcano

(Continued)

FIGURE 1 | Continued
with Lassen Peak (LP) as its southernmost volcano; the rigid block of the Sierran Microplate that acts like a piston compressing the Klamath Mountain on the northern boundary and creating the Ink Creek Fold Belt southwest of Lassen Peak; the Oregon forearc where the Sierran Microplate and Cascadia forearc blocks meet; the dominantly extensional western Basin and Range Region and Walker Lane; and the Hat Creek Graben region (yellow box) that includes the area south of Mt. Shasta (Sh), Pit River Region, Mushroom Rock Anticline, Cinder Butte, Butte Creek, Bald Mountain, Big Lake, Brushy Butte, and Fall River Valley. Modified from Faulds et al. (2005) and Austin (2013). **(B)** General distribution of the regional fault systems and volcanoes.

for volcanoes in a region. MORVOLC calculates a 3D basal surface from the edifice outline using a least-squares criterion, which was used to estimate the volume and height parameters. Elevation contour lines were then generated from the DEM, and a summit region was defined at the elevation where the edifice starts flattening out.

3.3. Volcano Spatial Distribution and Alignments

MORVOLC generated the geographic coordinates of volcano summits that we used as the volcano centroids. These point data sets were used as input information for running the Geological Image Analysis Software (GIAS, www.geoanalysis.org) code in Matlab developed by Beggan and Hamilton (2010). GIAS evaluates the amount of randomness or any patterns of a spatial distribution of points by comparing the mean distance between all the nearest neighbors in the population with those defined by an idealized statistical model (Clark and Evans, 1954), Poisson Nearest Neighbor Analysis is preferred, in the present case. The nearest neighbor distances are determined both for the observed and expected distribution and then their mean distances are calculated to obtain the population-dependent R_0 and R_e (Baloga et al., 2007), respectively. Our observed population consists of the number of volcanoes per subgroup based on their morphometric class. The sample area is a convex hull generated by connecting the outermost points of the population (Hamilton et al., 2010; Le Corvec et al., 2013). To overcome the sample-dependent bias and properly assess the suitability of the PNN analysis, the R and c values were plotted with a confidence interval of 2σ. GIAS outputs a plot of the volcanic centers and the convex hull of the volcanic area, the R and c statistical values, and the skewness vs. kurtosis.

Alignment patterns found by PNN provided important constrains for understanding controls on regional volcanic evolution. Using the area of the convex hull from PNN analysis computed by GIAS, and the observed volcano population based on morphological characterization by MORVOLC, we calculated the normalized distance between the volcanoes used to create alignments, based on the density of the volcanoes. This takes into account the problem of volcanic fields covering a large area even though the mean distance between volcanic centers is generally small, due to magma propagating through new fractures or re-activated pre-existing structures (Valentine and Hirano, 2010). Due to differences in densities and mean distances of volcanic centers for each volcanic field within the Hat Creek region, we applied the relationship between the maximum length for the generation of alignments and the density of volcanic centers originally determined by Le Corvec et al. (2013) for monogenetic volcanic fields. This relationship was used to calculate the maximum length to generate lineaments in the Hat Creek volcanic region. A Three-point Alignments Matlab code used for volcanic alignment analysis (Le Corvec et al., 2013) was used to identify groups of points in a population of volcanic centers that form straight lines (Wadge and Cross, 1988; Connor et al., 1992; Baloga et al., 2007; Bleacher et al., 2009; Le Corvec et al., 2013), and to generate a list of alignment azimuths. Directions of alignments are presented in a rose diagram to find out if there is a a strong controlling factor that results in preferred alignment during volcano growth.

3.4. Volcano Morphology and Regional Stress Relationship

We compared crater morphology and regional stress relationships only for bigger volcanoes, to draw from a homogeneous population. Amphitheaters, breaches, scars or craters were our primary indicator for describing a part of the volcano's history that could be related to regional stress (Lagmay and Valdivia, 2006). We identified volcanoes that show amphitheaters, volcanic scars and breaches. A scar was used to describe craters deformed by major collapse events, including debris avalanches and large landslides. A crater breach is a scar-like deformation brought about by erosion such as by glaciers (cirques) or by meteoric and hydrological events forming gullies and gully heads.

To determine regional stress, we obtained the orientation of the nearest regional maximum horizontal stress node to each bigger volcano from the World Stress Map, a standard global compilation of contemporary tectonic stress (Heidbach et al., 2008). Stress orientation in the map is from various types of stress indicators, such as earthquake focal mechanisms; well bore breakout and drilling induced features; *in-situ* stress measurement such as overcoring, hydraulic fracturing, and borehole slotter; and young geologic data from fault slip analysis and volcanic vent alignments (Heidbach et al., 2008). We then measured the direction at which scars and breaches open using the angle measurement tool in GNU Image Manipulation Program®. The absolute difference between these two angles is the angle difference.

4. RESULTS

4.1. Topographic Modeling, and Structural and Geomorphological Interpretation

4.1.1. Elevation Modeling

The elevation range in the Hat Creek region is from 150 to 3200 m with a mean elevation of 1400 ± 400 m. To simplify initial exploration of terrain development, elevation density slicing was applied to the DEM, generalizing the topography. This process enhanced the regional detail of the DEM. Based on the original and density sliced DEM (**Figures 2A,B**), there are two major elevation profiles: the low elevation areas in cool colors and high areas in warm colors. The low elevation areas are subdivided into four areas based on the continuity of the low elevations compared to adjacent, higher areas: A, B1, B2, and C. The low areas decrease in mean elevation from east to west. The lowest mean elevation (A), darkest blue in **Figure 2A** and magenta in **Figure 2B**, are the Sacramento Valley and Sacramento River and its tributaries from the Klamath Mountains in the north to the western side of Lassen Volcano National Park in the south. This area is separated from the lower area of Lake Britton (B1) on the east by Chalk and Hatchet Mountains, which are both part of the Klamath Mountains. The Pit River, which is the northern main tributary of the Sacramento River, carves the divide between these two mountains. In lightest blue and highest in mean elevation among the three low areas is an area that includes lakes in the southern part of Brushy Butte lava field, and McArthur and Fall River Mills (B2). It is separated from the lower western area (B1), of Lake Britton and Hat Creek Valley, by the Hogback ridge and Saddle and Haney Mountains. The green, flat area consists of Lookout and Bieber areas and Ash Creek State Wildlife Area (C), possibly the easternmost tributary of the Sacramento River.

The high elevation areas are subdivided based on the texture and intensity of warm colors in the DEM and the geographic location (D1, D2, E1, E2). The warm, geographically continuous colors in the southern part of the study area are divided into an area of smooth contours on the western side that coincides with the Cascade Range (D1) and the relatively irregular-edged Modoc Plateau (D2) on the east and northeast sides. Two other high elevation areas are geographically separated and thus are identified as separate profiles: the Klamath Mountains (E1) and Taylor, Jimmerson and Widow Mountains (E2). The elevation density map (**Figure 2B**) highlights the edges of high elevation areas (in green: D1, D2, E1, E2), and the break in slope that marks the base of volcano edifices (in red: insets F, G, H, I, J).

Features observed and mapped include the morphology of the edifices. Mountain ridges that form narrow and linear features (x) are contrasted against volcano edifices, observed as being more equant in planview (insets F, G, J). Stratovolcano bases are identified by the outermost, circular or equant, boundaries (insets F, G:1-2, J). The non-circular and very irregular edges of the base also identify the more complex volcanoes (such as those in insets H and I). "Piedmont" volcanoes (such as in inset G) are formed when the base of one volcano (1) is truncated by or buried under an adjacent edifice (2). Big volcanoes or broad areas of higher elevation relative to adjacent areas (insets H, I) are comprised of concentrations of (sometimes linear) cones (inset H), or are heavily eroded stratovolcanoes (inset I). Smaller stratovolcanoes (insets F, G, J) can also show irregularities of their bases, which can be evidence for collapse, sliding or unequal deposition and erosion. In inset J is an area that has experienced a deep-seated erosional or mass-wasting process.

Other high elevation areas (insets K, L) with differences in the regularity and smoothness of the edges (in green) can indicate areas that may be experiencing varying degrees of erosion. Inset

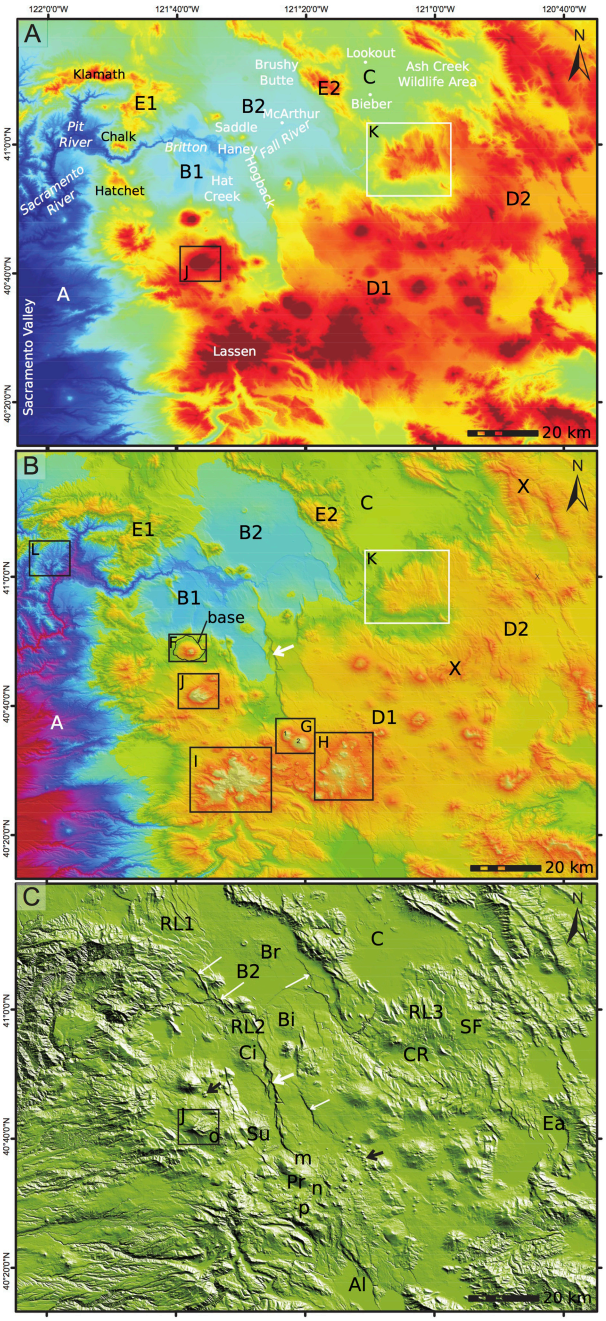

FIGURE 2 | Density-sliced DEM and Shaded Relief Maps of the Hat Creek Graben and its vicinity (Gesch et al., 2002). (A) Highlights the different elevation regions high in warm colors and low in cold colors and **(B)** green as the boundary between the two main regions and red as the break in slope that marks the bases of volcanoes. Based on mean elevation and continuity of elevation vs. adjacent areas, the low elevation areas are subdivided into A: Sacramento Valley and Sacramento River including its main tributary on the north, the Pit River; B1: Hat Creek Valley and Lake Britton, B2: McArthur and Fall River, and C: Lookout, Bieber and Ash Creek Wildlife Area. High elevation areas are subdivided based on texture and intensity of warm colors and geographic location. D1: Cascade Range; D2: Modoc Plateau; E1: Klamath Mountains; and E2: Taylor, Jimmerson and Widow Mountains. Red linear areas marked with x and K (inset) are ridges, features in insets F, G, and J

(Continued)

FIGURE 2 | Continued
denote stratovolcanoes, and insets H and I denote complex volcano edifices. Inset L denotes areas of river erosion. **(C)** Shaded relief image with water bodies: lakes Almanor (Al) and Eagle (EA); reservoirs: Silva Flat (SF) and Catfish (CR); flood plains: B2 and C; volcanoes: Sugarloaf Mountain (Su), Crater Peak (inset J), Prospect Peak (Pr); lava fields: Cinder Butte (Ci), Big Cave (Bi), Brushy Butte (Br), m and n; lava flows (o and p); cones (black arrows); faults (white arrows); and possible lineaments as localized faults (RL1, RL2, RL3). Arrows are drawn perpendicular to the general strike of the lineaments.

K, showing a volcano base with a regular planview edge as indicated by smoother color contour, may indicate a relatively lesser amount and lower rate of erosion, while the volcano in inset L may be experiencing a higher and more stable rate of erosion by a river tributary.

4.1.2. Shaded Relief

The shaded relief map (**Figure 2C**) shows a 3D depiction of the earth's surface. The flat and very smooth surfaces represent: the water bodies such as lakes Almanor (Al) and Eagle (Ea); reservoirs such as Silva Flat (SF) and Catfish (CR); and flood plains such as B2 and C. Rough and sloping areas represent either mountains or mountain ridges if they are elongated, and volcanoes if they are more circular in planview.

Volcanoes having rough surface textures but very few gullies or other linear erosional features, such as Sugarloaf Mountain (Su), have relatively fresh lava (lava is not easily erodible), which may translate into a young relative age of the volcano. Those with rough surface texture or lower slopes, such as Cinder Butte (Ci), Big Cave (Bi), and Brushy Butte (Br), or those being non-circular in planview, such as those in“m” and “n,” are identified as lava fields, as long as there is a recognizable source. Lava flows (“o” and “p”) are also recognizable as having levees on the narrower sides, and subsidiary flows on the edges of the main flow. Cones (black arrows) are easily recognizable as small mounds with relatively smooth and steep slopes. Relative ages of mountains are marked by the existence and density of gullies.

Other surface feature easily recognized on a shaded relief image are faults and linear features. Linear features that show continuity, and coincide with regional fault systems described in the literature, as well as those that show obvious vertical displacement of other features (white arrows), are identified as faults. Identification of linear arrays of cones (black arrows) and faults (white arrows) is a starting point in recognizing more subtle structures. Repeating lineaments (RL1, RL2, RL3) in the same area, and with the same strike, are also likely faults. In recognizing faults, the most obvious ones may not have the biggest offset, but may have the best preserved scarp, which is due to their age, offset, and erosion and deposition rates.

The hillshade image enhances some of what can be picked out in color mapping (**Figure 2C**). The addition of a 3D depiction behind the DEM enhances the surface features observed, while the simplified and generalized version of the shaded relief image confirms the existence of both the surface features and structures that may have been otherwise over-interpreted. Although (**Figure 2C**) is just an enhancement of **Figure 2A**, one of its advantages is that shadows generated by the particular sun angle considered in the generation of the shaded relief image are not emphasized. Shadow emphasis might be helpful for delineating faults (thick white arrow), but this is not always the case for delineating volcano bases like that of Crater Peak (inset J), as the surfaces are of much the same texture, generating the same types of shadows, in all directions.

4.1.3. Slope Modeling

Topographic modeling was also used to generate a slope map (**Figures 3A,B**). The dataset for the study area ranges from 0° to 81.5° with a mean slope of 11°. Steep slopes are emphasized in **Figure 3A**. This color mapping of the slope map is useful for confirming the delineations of faults.

Faults are identified as relatively straight lineaments, often members of a set with consistent strike. Faults in the study area have a considerable amount of vertical movement, as measured by the extent of the area colored yellow. The faults were classified according to the degree of curvature. Faults in RL1, RL2, RL3, for example, are grouped together. Faults that belong to the same set generally have the same orientation, maximum along-strike throw as indicated by maximum cross-strike width, planview curvature, and thus approximately the same age, as should be the case.

The main Hat Creek fault may well have a southern continuation (thick white arrow), which occurs along the northeastern bank of the northwestern lobe of Almanor Lake (Al). To the east of the Hat Creek Fault is the trace of the McArthur fault (thin white arrow), which may continue to the south or southeast as evidenced by the linear cones directly north of AL.

Steep gorges, G1, G2, G3, and G4, are identifiable; they often indicate in this region that the stream segment has been uplifted. Steeply sloping, wide areas, such as S1 and S2 indicate landsliding or a high rate of erosion. A closer look at the steep summits of some volcanoes and domes, such as Chaos Crags (CC) and Crater Peak (CP), shows that these are relatively smooth in texture, compared to stratovolcanoes that have been deformed by violent activity, such as Lassen Peak.

Cones (black arrows) are defined by yellow circular regions that indicate steepness from the base to the summit, with a lower-slope angle, cool colored (blue) region in the middle. Because slope maps emphasize areas of steepness, they are good for delineating lava flow extent, since the edges of lava flows tend to be steep, irregular and narrow relative to adjacent areas. Because slope steepness is a factor in landslide susceptibility mapping, steeper regions on volcanic edifices are at increased risk for landslides and collapses.

Slope maps also indicate relative ages of volcanic edifices. If we compare Burney Mountain, Bald Mountain (Ba) and Hermit Butte (He), for example, Burney Mountain seems to have been covered by younger surface deposits and less affected by erosion than the other two volcanoes.

Another variation in slope map presentation (**Figure 3B**) emphasizes lava fields (labeled 1–11) and their source areas. Areas covered by lava flows, such as those near Sugarloaf Peak (Su), Cinder Butte (Ci), Big Cave (Bi), the area north of Burney

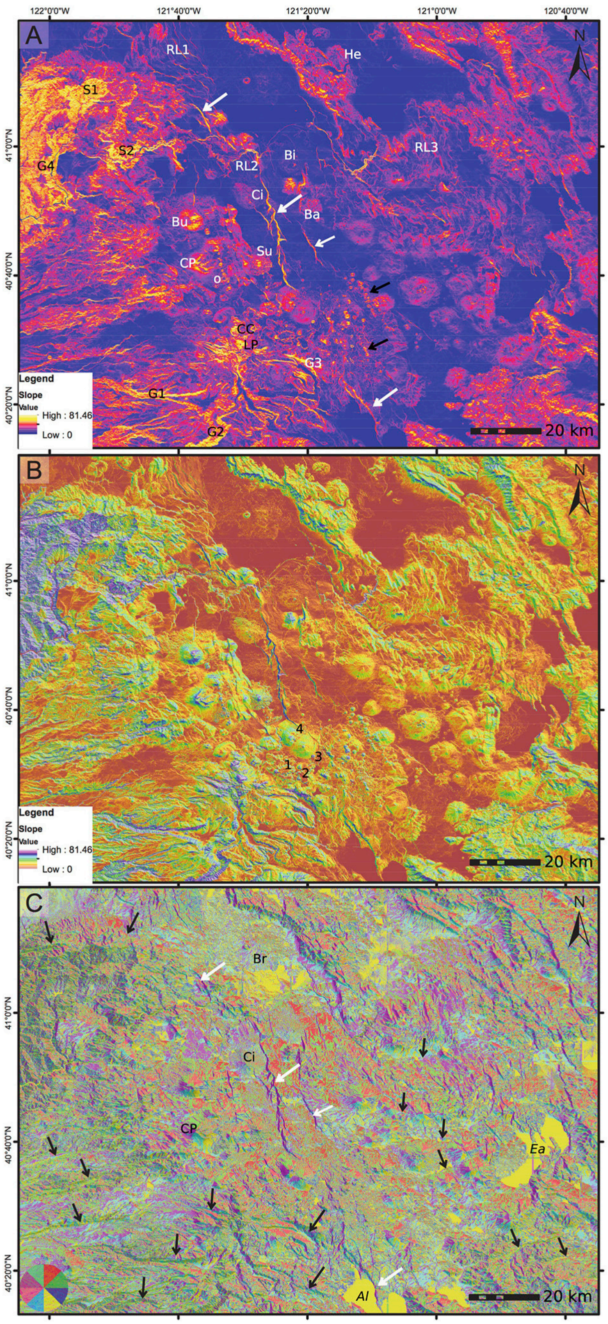

FIGURE 3 | Slope and aspect maps (Gesch et al., 2002). (A) Density sliced slope map where steep areas including volcano and cone summits and fault scarps are yellow, edifices are pink, and relatively flat surfaces and water bodies are blue. The boundaries between the blue and pink areas are the break in slopes that mark a volcano base. Arrows are drawn perpendicular to the general strike of the lineaments. Fault groups based on orientation and strike, degree of curvature and sinuosity are RL1, RL2, RL3. Hat Creek Fault and its projected continuation is shown by thick white arrow. McArthur fault is indicated by a thin white arrow. Steep gorges are marked G1, G2, G3, and G4. Steeply sloping, wide areas are S1 and S2. Stratovolcanoes with known and observed deformed edifices are Crater Peak (CP), Chaos Crags (CC) and Lassen Peak (LP). Other edifices are Sugarloaf Peak (Su), Cinder Butte (Ci), Big Cave (Bi), Bald Mountain (Ba), and Burney Mountain (Bu) and lava fields (o)

(Continued)

FIGURE 3 | Continued

and Hermit Butte (He). **(B)** Emphasizes lava fields and their source areas labeled 1–11. **(C)** Aspect map of the Hat Creek Graben and adjacent areas. Polygon colors and azimuths: red (0–45°), green (45–90°), blue (90–135°), yellow (135–180°), cyan (180–225°), magenta (225–270°), maroon (270–315°), and sea green (315–360°). Water bodies: lakes Almanor (Al) and Eagle (Ea) are in yellow. White and black arrows point at west- and south-facing fault controlled geomorphic features and linear discontinuities.

Mountain (Bu) and the area southeast of Crater Peak (o), have rough texture in the slope map, but a mean slope near zero.

4.1.4. Aspect Modeling

Slope aspect mapping is classified as a continuous terrain segmentation scheme (Miliaresis and Kokkas, 2004). In the current approach, aspect was computed for every DEM grid point (**Figure 3C**). Then the aspect was standardized to eight major geographic directions: N, NE, E, SE, S, SW, W, and NW. Linearity in colored polygon in the figure is another type of evidence for faults (black arrows). Faults with dip-slip component of different orientation can be distinguished with this technique, e.g., those with the western block moving down relative to the eastern block (white arrows). Areas of deposition of rough materials, such as emplaced lava flows or avalanche and slide toes tend to have highly variable, specular color patterns, meaning that the area has slopes facing in many directions on a relatively fine spatial scale, such as at Cinder Butte (Ci), Brushy Butte (Br), and Crater Peak (CP).

4.1.5. Structural and Lineament Mapping

Regional fault systems (**Figure 4A**) were drawn and identified in consultation with previous work as: the Hat Creek, Rocky Ledge, McArthur, Soldier Creek, and Pittville Fault Systems. These fault systems are predominantly normal, with right-lateral components and evidence of activity up to Holocene time (Wills, 1991; Muffler et al., 1994, 2010; Parrish, 2006; U.S. Geological Survey and California Geological Survey, 2006; Sawyer and Ramelli, 2012; Blakeslee and Kattenhorn, 2013). We traced the possible extent of these structures, as well as other shorter, more curvilinear, and relatively minor, faults such as those that affect Burney Mountain (Bu), Crater Peak (CP), West Prospect Peak (WP), Prospect Peak (PP), Bogard Butte (Bo), Whaleback (Wh), and Fox Mountain (Fo) (**Figures 4B–F**). Some of the smaller faults, with strike directions that coincide with faults identified by U.S. Geological Survey and California Geological Survey (2006) to be <130 ka, <1600 ka and >1600 ka, are assumed to be of the same age as the larger faults, and are grouped with them. The smaller faults so mapped are possibly parts of the Walker Spring fault system, and the unnamed faults in the Susanville lake and Big Valley areas, while Other Primary Regional 1 faults are unnamed. Some of our other Primary Regional 2 traces also belong to the <1600 ka faults in the USGS Fault Map.

Most of the faults trend northwest (**Figure 4A**). However, in more detail, the fault strike evolves from north-northwest to more nearly west-northwest, from east to west near the northern edge, while it goes from west-northwest toward north in the

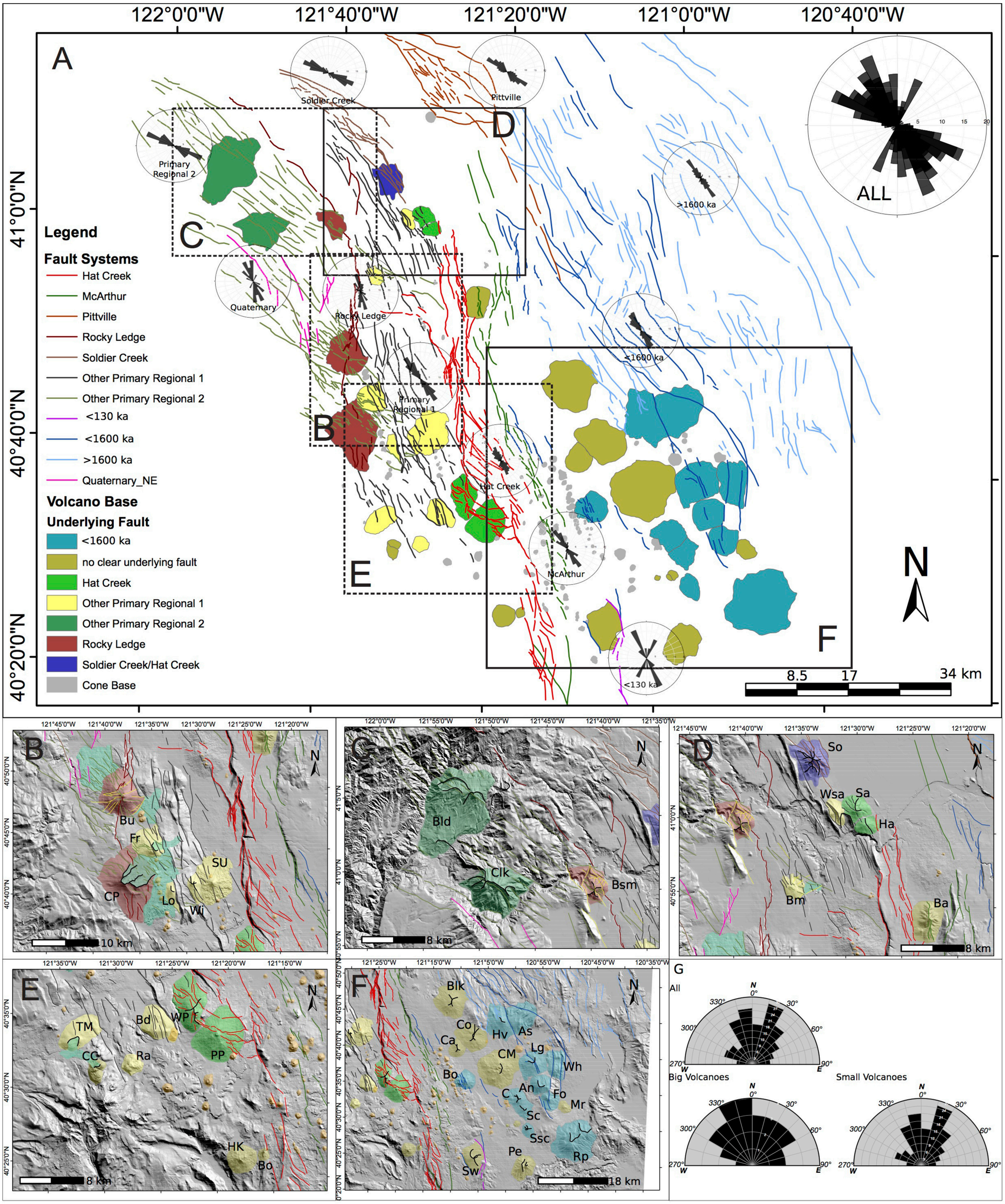

FIGURE 4 | Volcano-tectonic relationships in Hat Creek Graben region. (A) Base map showing fault systems, volcano bases color coded on fault system that mostly affects edifice, and water bodies; rose diagrams of fault strikes by fault system; and locations (squares) of hill-shaded maps **(B–F)** showing fault traces and effects on edifice: edifice instability and collapse, edifice disintegration, and splitting. **(G)** Rose diagrams of volcano base elongations for both big (cones, sub-cones, shields, and massifs) and small (small cones, small sub-cones, and small shields) volcano sub-groups, and all volcanoes. Dataset available in Supplementary Materials.

central to southern part of the study area. The small faults are defined as short lineaments on volcanoes without clear continuity into nearby areas. Such lineaments include the trace just to the northeast of Crater Peak (CP) (**Figure 4B**), which continues northwest up to the northwest side of Burney Mountain (Bu). These traces can contain multiple, short lineaments, but are constrained areally. Another area of localized faulting is the corridor of northwest trending short faults that affect the northern sectors of Prospect (PP) and West Prospect Peaks (WP) (**Figure 4E**). On some volcanic edifices, such as Bogard Butte (Bo), Whaleback (Wh), and Fox Mountain (Fo) (**Figure 4F**), small faults seem to split the edifices. In the case of Crater Peak, the small fault seems to have at least partly resulted from a major collapse. In these cases, the lineaments developed in response to a gravity-driven event that affected the volcano. However, in the case of Bogard Butte, Whaleback and Fox, it appears that the faults have influenced the shape and development of the volcano, suggesting that they are basement features that have propagated into the edifice.

4.2. Volcano Morphometry

Based on the MORVOLC output, we classified the volcanoes of the Hat Creek Graben region using primarily height to basal width ratio (**Figure 5A**). Those with a height to basal width ratio greater than 0.15 were classified as *cones*; those with intermediate values between 0.1 and 0.15 as *sub-cones*, and those with values less than 0.1 as *shields* or *massifs*. These last two were classified further based on height. A second classification based on height was done to differentiate small and large *cones*, *sub-cones* and *shields*. This classification was used to develop an evolutionary trend for volcanoes in the Hat Creek Graben region (**Figure 5B**).

The evolutionary trend begins with cones. Cones can either maintain their height to basal width ratio to increase in volume into larger cones, or enlarge in basal width to become sub-cones. Sub-cones can continuously increase in volume to become a bigger sub-cone, or evolve in basal width into a large but low volcano, a shield, and ultimately into a massif. Lastly, small volcanoes with height and basal width ratios of a shield can grow into massifs. All *morphologically big* volcanoes in the region are those with identified names, as discussed in the geomorphological classification of features in the region (Part 1 of this work). However, some of these previously named, *big* volcanoes needed to be reclassified as small cones, small sub-cones, or small shields, because their heights were less than 350 m (**Figure 5B**). Of the total of 185 drawn volcanic centers in the Hat Creek Graben region, 33 were classified as bigger stratovolcanoes (massifs), and 152 are morphologically smaller, mostly monogenetic cones (**Tables 1**, **2**).

We present x-y scatter plots of volcanoes in the region based on morphological classification parameters (**Figure 5C**). Cones have narrow summit widths, while shields and massifs tend to have broader summits, wider bases and more peaks, and are sometimes more irregular in outline. Basically, shields and massifs are high volcanoes with wide bases. Sub-cones, shields and massifs are voluminous volcanoes compared to cones. Cones are mostly identifiable by their height and high mean slope angle, in which sub-cones follow them closely. Sub-cones, massifs and some shields show the most irregular or elliptical planview shapes (**Figure 6A**).

Volcano bases are elongated (**Figure 4G**), with two modes, north-northwest and northeast; most of this scatter is influenced by the trend of the large population of smaller volcanoes. Big volcanoes also generally trend north-northwest, but this trend is less clear. Volcano bases seem to be elongated consistent with the trend of the directly underlying local structures.

4.3. Volcano Spatial Distribution and Alignments

The Hat Creek Graben region appears to be a volcanic field with distinctive subgroups of volcanoes, having different spatial distributions. Poisson Nearest Neighbor Analysis was applied to the morphologically smaller and bigger volcanoes as subgroups, and separately, to all volcanoes (**Table 2**). The smaller volcano subgroup and the group of all volcanoes have *c* values outside the $\pm 2\sigma$ significance level but *R* less than -2σ, which means they are spatially clustered. The bigger volcano subgroup, however, has *c* values outside the $\pm 2\sigma$ significance level and *R* greater than $+2\sigma$, which means that volcanoes in this group are dispersed relative to the Poisson distribution. Based on the density of volcanoes per subgroup, and using the relationship established using the global database of monogenetic volcanic fields (Le Corvec et al., 2013), we used 5800, 9900, and 6000 m as the maximal distance needed for the recognition of lineaments for smaller and bigger subgroups, and the group of all volcanoes, respectively.

The three-point MATLAB script was used to automatically extract the different alignments of the volcanoes, and plot for each the direction of the alignment on a rose diagram (**Figure 5D**). Bigger volcanoes generated no preferred alignment, while the smaller volcano subgroup and the group of all volcanoes have a north-northwest preferred direction of alignments. Again, this quantitatively determined strike is consistent with the strike of local, tectonic faults.

4.4. Crater Morphology and Stress Field

Only the subgroup of bigger volcanoes was considered for investigating crater opening, either a volcano collapse scar or an erosional breach, because of the prevalence of these features on the bigger volcanoes. The regional maximum horizontal stress and crater opening directions, both in azimuth, were noted for each bigger volcano with crater openings in **Table 1**. For example, as in **Figure 6B** (inset), the maximum horizontal regional stress has an azimuth of 156° near Freaner, Logan and Crater Peak volcanoes, which have summit openings (erosional breaches for Freaner and Logan, and collapse scar for Crater Peak) of 76°, 65°, and 66°, respectively. The angle difference for each of these three volcanoes is the absolute value of the difference between 156°and the summit opening direction, which is 80°, 89°, and 90°, respectively (**Table 1**). A frequency diagram (**Figure 6B**) of the angular difference between the crater opening direction for the bigger volcanoes and the maximum horizontal stress has a mode at about 90°, although crater openings at an acute angle are also found, albeit at lower frequencies. Most of the crater openings are thus perpendicular to the maximum horizontal

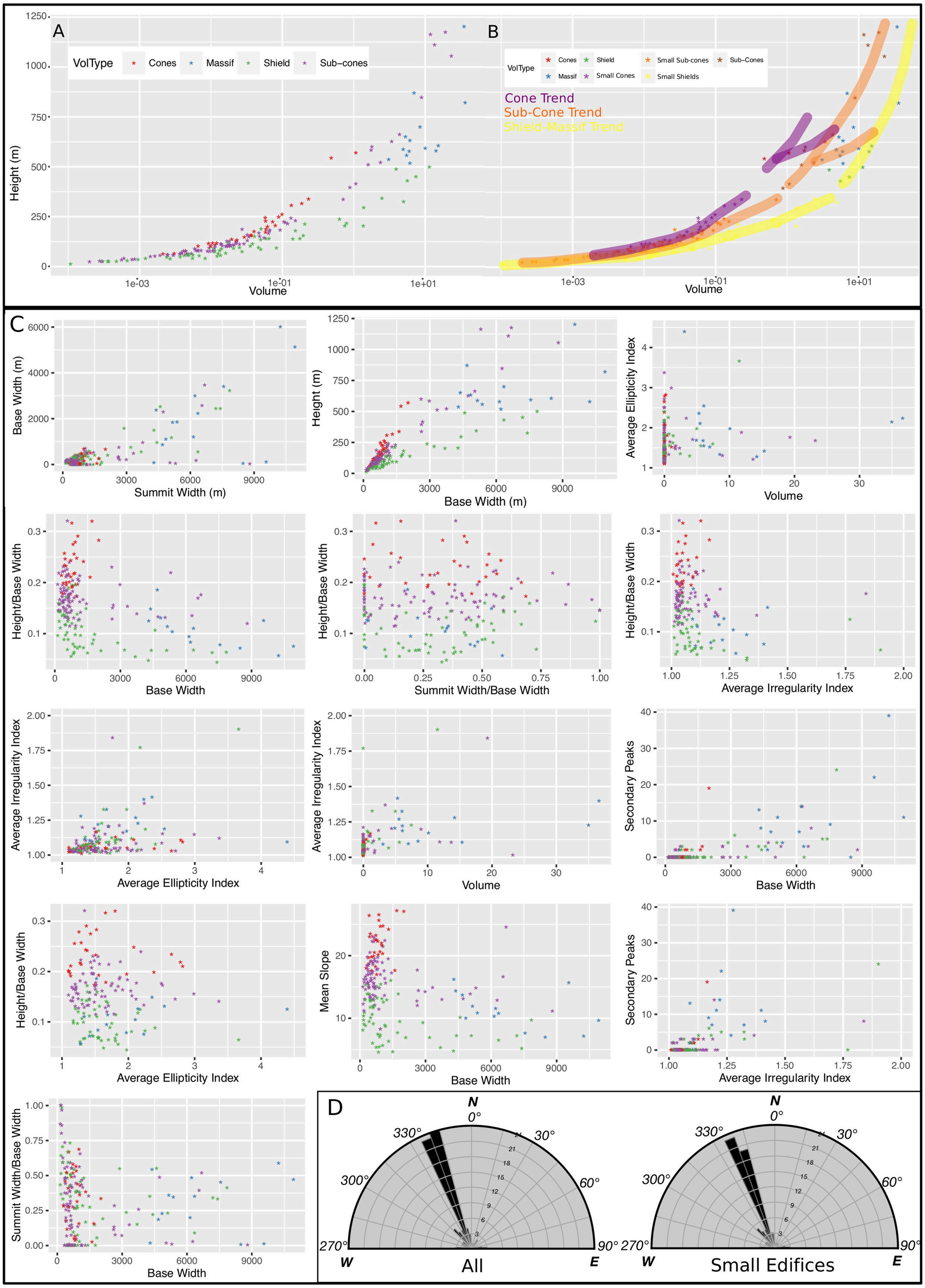

FIGURE 5 | Volcano morphometry. (A) Volume vs. height plots for all volcanoes grouped by morphological classification: cones, sub-cones, shields, and massifs based on their height and basal width ratio; **(B)** A second morphological classification based on height separating bigger and smaller edifices on a volume vs. height plot to draw a volcano evolutionary trend; **(C)** X-Y plots of selected morphometric parameters grouped by morphological type (cones, sub-cones, shields and massifs); and **(D)** A rose diagram showing the preferred direction of alignments that can be formed by at least 3 volcano centroids within 6 km. Dataset available in Supplementary Materials.

TABLE 1 | Morphometry and crater morphology of the Hat Creek Graben region stratovolcanoes.

Name	Type	HeightMax	VolMax	WidthBase	WidthSummit	σH_{max}	Crater direction
0-crater	C	84.61	0.05	1142.83	0.00		
1-crater	A	204.39	0.08	1041.97	374.30		
2-crater	B	183.54	0.09	1135.70	528.73		
3-crater	A	306.50	0.13	1055.52	449.16		
4-crater	C	139.37	0.06	1013.24	26.91		
5-crater	A	126.70	0.02	714.21	0.00		
6-crater	A	315.51	0.19	1308.55	500.73		
7-crater	B	242.07	0.13	1137.36	0.00		
8	A	117.98	0.01	507.83	206.89		
9-crater	A	224.08	0.07	877.83	464.97		
10-crater	B	229.48	0.15	1447.89	509.98		
11-crater	B	219.39	0.11	1060.86	692.81		
12-crater	B	214.63	0.12	1291.19	0.00		
13-crater	A	132.87	0.02	661.04	323.29		
14-crater	B	149.46	0.03	818.74	0.00		
15-crater	A	175.64	0.04	723.62	419.76		
16	A	114.79	0.01	447.11	51.27		
17-crater	B	101.96	0.01	457.38	256.21		
18-crater	A	261.68	0.10	939.22	410.03		
19-crater	B	102.62	0.02	623.90	267.48		
20-crater	A	171.83	0.06	994.90	682.40		
21-crater	B	177.72	0.07	1026.93	574.44		
22	B	52.45	0.00	290.10	83.82		
23-crater	A	154.56	0.04	733.61	378.59		
24-crater	B	76.64	0.01	576.39	79.77		
25-crater	C	47.43	0.00	487.56	0.00		
26-crater	C	55.34	0.00	474.03	227.70		
27-crater	A	135.25	0.02	625.51	0.00		
28	B	187.48	0.03	584.53	226.79		
29	B	108.22	0.02	643.34	47.04		
30-crater	C	139.33	0.07	1227.03	588.47		
31-crater	B	111.39	0.03	765.83	0.00		
32-crater	B	102.78	0.02	673.14	370.83		
33-crater	B	102.82	0.02	674.84	0.00		
34-crater	C	151.75	0.04	783.18	0.00		
35	C	88.47	0.01	629.07	111.51		
36	A	147.91	0.03	775.96	207.36		
37-crater	C	134.52	0.05	1069.24	484.42		
38-crater	B	112.97	0.03	863.77	383.09		
39-crater	B	165.27	0.06	1170.85	484.79		
40-crater	B	143.32	0.06	1125.81	487.76		
41-crater	A	105.69	0.01	528.68	352.49		
42	B	114.39	0.01	534.37	131.56		
43-crater	B	130.47	0.03	799.15	392.52		
44-crater	C	64.24	0.00	477.99	0.00		
45-crater	C	93.98	0.03	786.42	424.89		
46	B	126.67	0.02	591.44	175.94		
47-crater	B	93.58	0.01	508.92	0.00		
48	B	80.06	0.01	450.60	132.66		
49-crater	B	109.34	0.02	628.01	261.94		

(Continued)

TABLE 1 | Continued

Name	Type	HeightMax	VolMax	WidthBase	WidthSummit	σH_{max}	Crater direction
50-crater	C	120.30	0.02	636.28	0.00		
51-crater	B	182.88	0.07	936.56	360.90		
52-crater	B	167.79	0.05	822.82	0.00		
53-crater	B	108.30	0.02	675.58	0.00		
54-crater	B	224.42	0.11	1104.87	0.00		
55-crater	C	187.71	0.05	958.14	0.00		
56	B	158.98	0.03	664.97	97.53		
57	B	104.07	0.01	563.44	215.91		
58-crater	A	187.47	0.06	864.39	486.56		
59	C	51.58	0.01	852.92	322.74		
60	C	94.23	0.05	1310.23	215.51		
61	C	40.92	0.01	743.28	68.89		
62	C	37.97	0.00	430.59	221.30		
63	C	40.09	0.01	583.25	426.13		
64	B	77.89	0.01	682.35	86.88		
65	C	65.40	0.01	825.39	215.03		
66	C	56.35	0.01	885.72	343.24		
67	C	139.26	0.18	2107.28	401.35		
68	C	138.39	0.14	1721.25	251.66		
69	C	91.09	0.02	933.47	247.91		
70	C	113.38	0.04	1179.01	334.75		
71-crater	C	179.44	0.15	1823.35	96.44		
72	B	108.63	0.02	945.42	125.35		
73-crater	C	154.42	0.20	1766.18	0.00		
74	C	74.18	0.03	1040.01	395.14		
75	A	64.44	0.00	362.00	165.14		
76-crater	A	101.59	0.01	434.40	226.27		
77-crater	A	117.40	0.01	477.54	0.00		
78	B	102.70	0.02	605.24	356.17		
79-crater	B	127.52	0.02	564.57	0.00		
80	B	77.40	0.01	524.39	145.68		
81-crater	C	211.84	0.21	1425.68	0.00		
82-crater	A	157.53	0.04	818.09	52.04		
83-crater	B	114.51	0.02	650.72	357.50		
84	B	106.04	0.02	619.50	131.41		
85	C	57.50	0.00	565.37	239.89		
86	A	103.03	0.01	528.98	143.81		
87	B	49.49	0.00	263.73	164.77		
88	B	36.95	0.00	254.93	150.73		
89	A	77.47	0.00	390.64	68.46		
90	B	59.02	0.00	342.86	127.66		
91	B	65.75	0.01	455.40	169.45		
92	B	63.53	0.00	424.76	28.38		
93	B	54.93	0.00	340.69	160.95		
94	B	123.61	0.02	695.64	288.28		
95	B	89.32	0.01	387.70	170.94		
96	B	64.96	0.00	397.58	101.11		
97	B	60.23	0.00	455.70	126.14		
98-crater	B	79.23	0.01	475.31	0.00		
99	B	77.13	0.00	349.00	191.65		

(Continued)

TABLE 1 | Continued

Name	Type	HeightMax	VolMax	WidthBase	WidthSummit	σH_{max}	Crater direction
100	B	150.58	0.05	887.18	39.84		
101	B	63.28	0.00	393.48	77.79		
102	B	92.74	0.01	599.06	70.93		
103	C	87.09	0.01	507.15	300.71		
104	B	112.22	0.01	634.24	113.11		
105	B	99.97	0.02	705.61	193.97		
106	C	74.63	0.01	600.43	303.98		
107	C	25.31	0.00	204.68	201.25		
108	B	26.47	0.00	182.46	182.47		
109	B	57.98	0.00	382.88	184.81		
111	C	26.39	0.00	165.84	84.97		
112	C	25.69	0.00	179.67	115.05		
113	C	57.08	0.01	486.19	324.70		
114	C	13.17	0.00	136.52	58.86		
115	C	28.59	0.00	257.31	85.42		
116	C	25.56	0.00	178.49	65.47		
117	B	75.55	0.00	412.84	70.80		
118	C	79.40	0.01	606.86	212.14		
119	B	78.02	0.01	609.21	192.07		
120	A	248.03	0.09	1001.44	154.58		
121	A	245.45	0.06	776.61	38.08		
122	A	227.57	0.06	828.54	29.72		
123	A	200.54	0.06	919.19	287.44		
124	A	63.50	0.00	296.52	82.74		
125	B	23.34	0.00	160.64	160.65		
126	B	70.80	0.00	363.09	174.56		
127	B	35.82	0.00	215.30	208.05		
128	C	34.88	0.00	245.70	145.70		
129-crater	C	56.29	0.00	410.13	0.00		
130	B	40.44	0.00	185.63	148.57		
131-crater	B	106.93	0.01	506.88	0.00		
132	C	54.39	0.01	618.51	309.63		
133-crater	C	39.82	0.00	251.05	176.48		
134-crater	B	81.29	0.01	430.47	0.00		
135-crater	C	46.17	0.00	341.62	0.00		
136	B	27.79	0.00	141.67	122.89		
137-crater	B	56.99	0.00	331.60	0.00		
138	B	32.73	0.00	208.66	178.63		
139	B	57.79	0.00	352.41	258.45		
140-crater	B	76.94	0.01	547.62	4.20		
Antelope Mountain	Massif	557.75	5.55	5378.46	1851.37	SS = 4°	27
Ashurst Mountain	Shield	499.62	11.53	7851.94	3228.31		
Badger Mountain	Massif	650.39	5.33	4386.47	2371.60		
Bald Mountain	Sub-cones	626.85	3.42	4730.09	2298.75		
Bald Mountain	Massif	1202.07	35.02	9565.24	110.92	NF = 153°	259, 238, 207, 113
Blacks Mountain	Massif	605.71	15.40	8488.95	51.96		
Bogard Buttes	Massif	587.63	4.94	5158.42	1837.69		
BontePeak	A	338.02	0.23	1610.41	38.37		
Brush Mountain	C	236.37	0.63	2887.93	1578.00		
Burney Mountain-crater	Sub-cones	1110.31	13.67	6552.93	2566.33	NF = 156°	307, 111

(Continued)

TABLE 1 | Continued

Name	Type	HeightMax	VolMax	WidthBase	WidthSummit	σH_{max}	Crater direction
Burney Spring Mountain	Massif	536.63	3.10	4297.78	73.10	NF = 156°	293, 111
Cal Mountain	C	295.35	1.38	4423.38	963.10	NF = 156°	247, 66
Campbell Mountain	C	342.72	2.48	5110.78	1168.56	SS = 4°	10, 240
Chalk Mountain	Sub-cones	1174.27	19.33	6685.52	3465.11	NF = 153°	195, 193, 182, 230
Chaos Crags north	Cones	543.46	0.48	1698.41	262.63	NF = 156°	300
Chaos Crags south	Cones	569.94	1.07	2015.65	669.66		
Cone Mountain	C	324.32	4.99	7417.35	2446.71	SS = 4°	278
Crater Mountain-crater	Massif	578.82	14.22	10240.00	6012.92	SS = 4°	68,97
CraterPeak-crater	Sub-cones	1054.51	23.26	8809.16	21.25	NF = 156°	66
Fox Mountain	Massif	632.63	6.11	4850.22	1100.21		
FreanerPeak	Massif	869.30	6.99	4686.70	864.89	NF = 156°	76
Haney Mountain	B	337.23	0.71	2624.56	344.25	NF = 156°	44
Harkness Mountain	Sub-cones	521.40	2.39	3760.78	959.82		
Harvey Mountain	Massif	592.13	10.12	7563.22	3408.96	SS = 4°	25
Logan Mountain	Shield	450.59	7.50	7194.79	2435.96	SS = 4°	321
Logan Mountain	Sub-cones	600.12	1.81	2612.66	291.51	NF = 156°	65
Merrill Mountain	C	215.82	0.79	3194.44	751.84		
Mudleft	C	103.07	0.04	938.09	66.45		
Mudright	C	92.44	0.08	1501.66	410.10		
Pegleg Mountain	Massif	577.98	6.00	6148.08	1209.84	SS = 4°	89
ProspectPeak-crater	Massif	699.11	8.53	6352.69	2226.61		98
RakerPeak	Sub-cones	395.72	0.88	2637.22	746.77		
Roop Mountain	Massif	820.53	36.66	10924.98	5125.81		61
Saddle Mountain	Sub-cones	511.10	1.61	3332.40	492.58		14
SCampbell Mountain	C	203.86	1.36	4282.21	1491.79		345
SLongLake	C	67.64	0.02	912.56	255.52		221
SofSCampbell Mountain	C	202.66	0.75	3691.73	551.48		54
Soldier Mountain	Sub-cones	662.69	4.38	5045.36	84.61		40
SugarloafPeak	Sub-cones	847.47	8.96	6274.42	170.30		
Swain Mountain	Shield	429.74	5.62	6355.22	557.52	SS = 4°	1,290
Table Mountain	Shield	487.35	3.92	4590.87	2526.60	NF = 156°	7, 232, 195, 240, 306
WestProspectPeak	Sub-cones	1163.52	11.90	5306.43	46.43		
Whaleback Mountain	Massif	518.45	6.12	6219.10	2998.09	SS = 4°	62, 99
WilcoxPeak	Sub-cones	583.33	1.76	2985.07	205.76	NF = 156°	27, 108
WSaddle Mountain	Sub-cones	414.88	1.08	2674.36	199.76		

Height and width are in m; Volume is in m^3; σH_{max} *is the maximum horizontal stress orientation (azimuth, in degrees) and tectonic regime (SS = strike-slip or NF = normal faulting) nearest to each volcano edifice with crater opening or collapse scar (stress data from Heidbach et al., 2008); crater directions are in degrees; volcano types A, B, and C refer to small cones, small sub-cones, and small shields that fall within the lower purple, orange, and yellow lines in* ***Figure 5B****. Dataset available in Supplementary Materials.*

stress, which is consistent with the observation of Tibaldi (1995) and models by Moriya (1980) and Siebert (1984).

5. DISCUSSION

Several regional fault systems are oriented northwest-southeast; these are comprised of normal faults with right-lateral components. Individual faults within these systems pass through or underneath most of the volcanoes. The stratovolcanoes contain clear traces of the regional faults, or manifestations of collapse or erosional features on their edifices that can be related to the faults. Cones are more prevalent in the southeastern part of the study area.

5.1. Magma Propagation

The Hat Creek Graben region consists of volcano subgroups that have different spatial distributions; smaller volcanoes tend to cluster, while bigger volcanoes are dispersed. The density-dependent, preferred alignments reveal a single north-northwest direction for the small volcano subgroup, and all volcanoes considered together. These observations are consistent with the control of melt production at depth and magma propagation by pre-existing regional structures, and with the control of magma propagation in the near surface by the local stress regime. Melt production is related to the oblique subduction of the Gorda Plate underneath the Northern American Plate, and is manifested in the volcanism at the surface. Regional

TABLE 2 | Properties and results of the statistical analyses for each morphological subgroup (big and small), and for the all the volcanoes in the Hat Creek Graben.

		Smaller	Bigger	ALL
Measured nearest neighbor properties	Number of volcanic centers (N)	152	33	185
	Area Convex Hull (m^2)	3.26E+09	3.54E+09	4.28E+09
	Density (nb volcanic centers/m^2)	4.66E−10	9.33E−11	4.32E−10
	Min distance NN (m)	4.92E+02	4.29E+03	4.92E+02
	Max distance NN (m)	1.83E+05	1.65E+05	1.23E+05
	Mean distance NN (m)	1.60E+04	7.01E+04	2.01E+04
	Standard deviation (1σ)	2.17E+04	4.60E+04	2.36E+04
	Standard deviation (2σ)	4.33E+04	9.19E+04	4.72E+04
	Skewness	4.28	0.62	2.43
	Kurtosis	25.75	−0.80	6.40
Nearest neighbor results relative to the Poisson model	Poisson Re (m)	2.32E+04	5.18E+04	2.40E+04
	R	0.69	1.35	0.83
	Ideal R given N_i	1.04	1.08	1.03
	R negative thresholds at 1σ	1.08	1.19	1.07
	R positive thresholds at 1σ	1.13	1.29	1.12
	R negative thresholds at 2σ	0.99	0.98	0.99
	R positive thresholds at 2σ	0.94	0.87	0.95
	c	−7.25	3.89	−4.33
	Ideal c given N_i	0.84	0.90	0.84
	c negative thresholds at 1σ	1.93	2.07	1.92
	c positive thresholds at 1σ	3.02	3.24	3.00
	c negative thresholds at 2σ	−0.25	−0.27	−0.24
	c positive thresholds at 2σ	−1.34	−1.44	−1.33
Alignment analysis	Distance maximal for the generation of lineaments (m)	5800	9900	6000
	Number of lineaments (m)	85	0	93

NN, nearest neighbor.

and near-surface stresses are influenced by Walker Lane and Cascades tectonism. Extension is accommodated by the pervasive faulting and magmatism. As the area extends, it produces weak regions that provide energy-efficient paths along which magma propagates to the surface.

Normal faults, dominant in the area, influence dike orientation and the generation of alignments at the surface, because dikes are more likely to intercept and follow dipping faults than vertical fractures (i.e., Le Corvec et al., 2013). Near-surface stress also affects magma propagation (i.e., Caputo, 1995) it is possible that high differential stress did not allow stress swap, therefore the intrusions followed the orientation of the earlier dikes. The generation of multiple orientations of volcanic alignments is perhaps attributable to the interaction of near-surface stress field influences and pre-existing fractures.

Magma pressure, which is also a factor in dike propagation (i.e., Jolly and Sanderson, 1997), may be low, so that magma only follows pre-existing fractures that are favorable for reactivation in the prevailing stress field. Although pathways may vary slightly according to stress field at time of propagation and eventual emplacement (i.e., Valentine and Krogh, 2006), in general, they have been consistent through the lifetime of Hat Creek region volcanism.

The propagation of magma that formed the bigger volcanoes is also structurally controlled, because these volcanoes stand atop major regional structures, and the faults affect the stability of the volcanic edifices. The random, dispersed spatial distribution of the bigger volcanoes may be attributed to their long-lived plumbing systems, which are capable of capturing or re-focusing nearby dikes as they propagate to the surface, most of the time erupting from a single vent. Changes in the local stress field caused by the growing edifice may also have enhanced dike capture.

5.2. Edifice Evolution

Most volcanoes in the study area are small, with maximum heights about 250–300 m, and volumes generally less than 1 km^3. Based on the height and basal width ratio, some volcanoes can be classified as cones, which are relatively regular and more nearly circular in planview, have relatively smaller summit areas and narrower basal widths compared to sub-cones and to the bigger and more voluminous shields and massif volcanoes. Quantitative morphology furthermore suggests that volcanoes evolve along several paths: small cones continue to grow as cones, or they grow into sub-cones; small sub-cones continue to grow into bigger sub-cones, or they develop into shields and massifs; and shields can grow into massifs. Underlying major faults systems have greatly influenced the growth, partial destruction, and general evolution of volcano morphology.

Quantitative evaluation furthermore revealed volcanic basal elongations in two main directions, north-northwest and northeast. The existence and magnitude of the northeast mode in the elongations is consistent with spreading parallel to displacements on regional normal faults with right-lateral components, either by preferred feeder dike orientation or by deformation.

5.2.1. Deformed and Collapsing Volcanoes

Several types of volcanic edifice deformation are observed in the Hat Creek Graben region. Some volcanoes show collapse features, others erosional breaches, and some are being split by faulting.

Chaos Crags is a stratovolcano with a known collapse scar (**Figure 4E**). The collapse of the unstable, very steep, soft-cored, and unconsolidated plug dome of Chaos North resulted in a debris avalanche, called the Chaos Jumbles. The jumbles were emplaced as a high yield strength material capable of deforming and shearing in three separate rockfalls about 300 years ago Eppler et al. (1987), damming Manzanita Creek and forming Manzanita Lake. A projection of a northwest striking fault, here part of a Primary Regional 1 group of faults (**Figures 4A,E**), which splits Table Mountain to the northwest, may be masked underneath the Crags and Jumbles. Post-eruptive mass wasting and sedimentation on the slopes of Chaos Crags have masked any evidence for the mechanism of generation of the debris avalanche (Perez, 1998). Activity on the fault could have triggered instability and collapse.

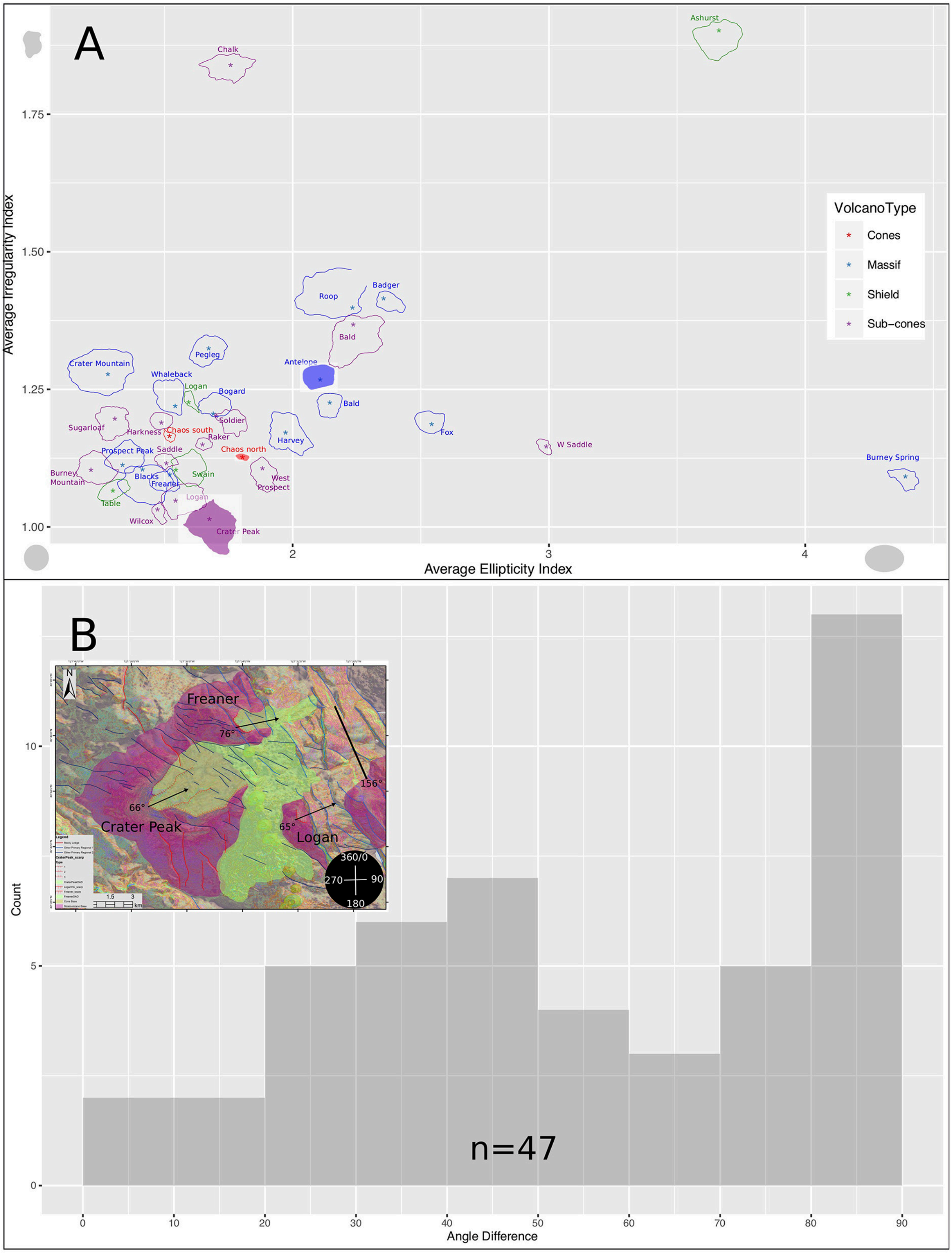

FIGURE 6 | Volcano morphology and breaches. (A) Ellipticity and Irregularity Indices (not to scale) of bigger volcanoes in the Hat Creek Graben region grouped by morphological type as cones, sub-cones, shields and massifs. Filled polygons are those with evidence of collapse scars. **(B)** Frequency diagram showing the relationship between the opening direction of craters and the maximum horizontal stress. Inset is an example of how angle difference is calculated.

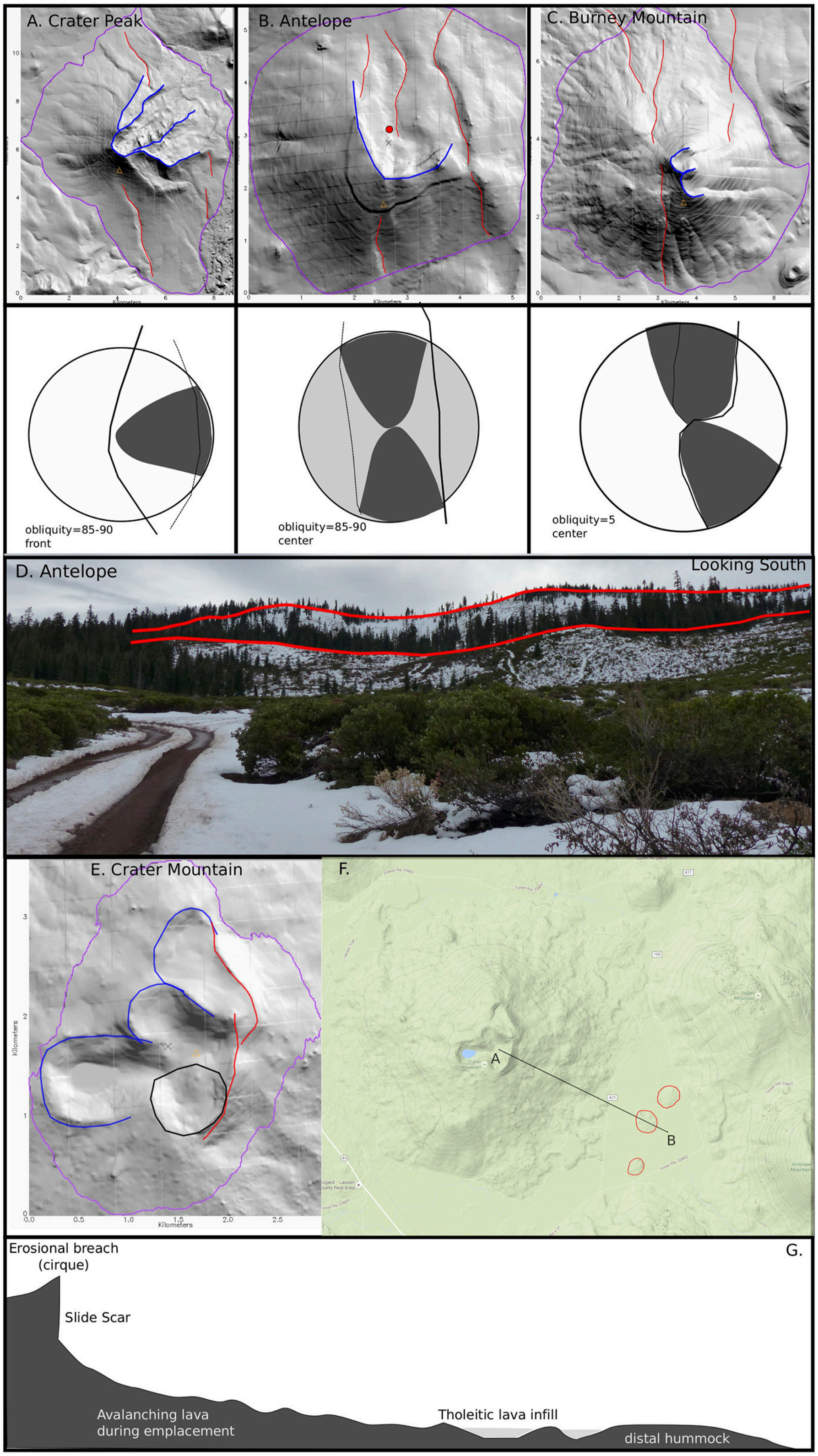

FIGURE 7 | Deformed volcanoes in the Hat Creek Graben region. (A–C) Shaded relief delineated with volcano base (purple), collapse scars or erosional breaches (blue) and structural lineaments (red) for Crater Peak **(B)**, and Antelope **(C)**, and Burney **(D)** Mountains compared with their predictive model cones by Wooller et al. (2009) underneath, where the gray circles represent the edifice; solid lines are main normal faults; dotted polylines are antithetic and minor faults; and gray *(Continued)*

FIGURE 7 | Continued
polygons are unstable sectors; **(D)** View looking at Antelope Mountain Slide scar from the northern sector of the volcano marked as red dot in **(B)**. The red lines are the slide scar (top), and terrace (bottom) that mark the top of the major listric faults that accommodate the sliding of the whole area. **(E)** Shaded relief and **(F)** google earth images, and **(G)** cross section of Crater Mountain Slide. Location of cross section A-B is drawn over google earth image **(F)**. Volcano base (purple); cirques (blue); scar and hummocks (red); possible crater trace (black) are marked.

Crater Peak is another stratovolcano that shows morphological evidence of collapse (**Figure 4B**). Crater Peak has a large and deep-seated scar, and a possible runout deposit elongated toward the northeast marked by a rough surface texture that would be expected in a debris avalanche deposit. The scar was glacially eroded after the collapse, as shown by the smoother, uppermost parts of the amphitheater, which thus resembles, or is in part, a cirque. Comparing the structures and scar elongation direction of Crater Peak to Figure 9E of Wooller et al. (2009), we speculate that the collapse could have been caused by a basement normal fault, with a right-lateral component, possibly the Rocky Ledge Fault (red line in **Figures 4A,B**, thicker black line **Figure 7A**), which passes through the center of the edifice. In this scenario, the Rocky Ledge Fault destabilized and eventually caused a collapse approximately normal to its strike direction.

Relations, confirmed in the field, showed that Antelope Mountain has also collapsed (**Figures 4F**, **7B,D**), with deposits emplaced toward the northeast. From remote sensing, lineaments on the eastern base of the volcano can be traced (**Figures 4A,F**), of the same set that split Whaleback volcano to the northeast. Another set that perhaps influenced the stability of Antelope Mountain more strikes northwest, splits Logan Mountain to the north, and affects the western flank of Fox Mountain. The structures affecting Antelope Mountain are grouped with the <1600 ka faults, are possibly part of the Walker Spring fault system. These may be related to the faults in the Susanville and Big Lake Valley areas, which may have been active during the Holocene.

Based on remote sensing analysis, four more volcanoes notably show evidence of edifice collapse: Crater, Burney and Table Mountains; and Raker Peak. Burney and Table Mountains are deformed, and show morphological traces of edifice collapse structures (**Figures 4B,E**). The structures at Burney Mountain appear to be manifestations of ongoing deformation of the edifice by the Rocky Ledge Fault, the underlying basement fault (**Figure 4B**), which may ultimately result in sector collapse. In the field, Burney Mountain has two small craters that both open to the east. These are likely to have evolved into cirques by small, summit glaciers flowing to the east, leaving behind till, possibly in the form of a moraine, below the northern cirque (**Figure 7C**). The location of lineaments on the northwest and southeast sectors of Burney Mountain is consistent with underlying normal faults with little strike-slip component (**Figure 7C**). The lineaments (in yellow) perpendicular to the Rocky Ledge Fault trace may not be tectonic in origin, but rather lava flow ridges (**Figure 4B**).

Crater Mountain (**Figures 4E–G**) is a relatively "strong" and stable volcano, built mostly of lava flows, with no apparent hydrothermal alteration at the surface, nor any indication that it is built on deformable and weak substrata. At the summit, three craters have been traced, all elongated to the east, which may be modified by glaciers. There may be another, fourth, crater as well. The head-scarp morphology in the summit area, where the north-south scar is drawn (**Figures 7E–G**), suggests some type of gravity failure on the east flank. The scarp could have been made by multiple slides, affecting slightly different sectors. It is possible that a series of slides were emplaced without a thin, weak or wet sliding base, which resulted in slumping or rotation of relatively coherent blocks, forming a toe now exposed as three low mounds or distal hummocks (Paguican et al., 2014). Spaces between hummocks have been infilled by tholeiite lavas.

Raker Peak (**Figure 4E**) is another edifice with an apparent northeastward opening. This sector deformed relative to the others. Although there is no basement fault near the edifice, a river flows across the eastern piedmont, which could have cut the base of the edifice, causing its eventual collapse. It is also possible that a segment of a Primary Regional 2 fault is buried by the volcano.

Last, the southwestern sector of Table Mountain (**Figure 4E**) has a crater-like structure that opens toward the south. The difference in slope steepness between the upper and lower portions of the edifice within the scar is evident.

5.2.2. Volcanoes with Erosional Breaches and their Underlying Faults

Volcanoes with an erosional breach or particular sectors affected by relatively more gullies include Pegleg, Swain, Roop Mountain, Logan, Campbell, South of Campbell, South of South Campbell, and Harvey Mountain (**Figure 4F**); Chalk and Bald Mountains in the north (**Figure 4C**); Raker Peak (**Figure 4E**), Cone and Cal Mountains (**Figure 4F**), Soldier, Haney and, Saddle Mountains (**Figure 4D**), and Burney Spring Mountain (**Figure 4C**) in the east.

Harvey Mountain is bounded to the east by Ashurst volcano. These two stratovolcanoes are separated by a segment of a <1600 ka regional fault that also affects Logan, Antelope and Fox Mountains. On the northeast is a possible erosional feature most likely to develop under the influence of an active normal fault with a strike-slip component. Logan, Campbell and South of Campbell all have erosional features opening toward the northeast or northwest. Of these, only Logan Mountain is clearly traversed by a <1600 ka fault, the same fault that splits Fox Mountain and is related to the slide on Antelope Mountain. The volcano to the south of South Campbell has no apparent nearby fault to which we can relate the north and northwest scars. However, a river flows near the western base, which might have laterally undermined the volcano base, causing instability on the northwestern flank. The western flank of Roop Mountain has gullies. The northeastern sector is the most incised by deep gullies, with major gully heads. Based on its relatively bigger size and volume compared to other volcanoes, and the density and size of gullies, Roop Mountain is probably an old volcanic edifice.

Swain Mountain has traces of two fault on the southwestern and northeastern piedmonts. Two erosional scars are shaped like cirques and have gullies within their walls. Breaks in slope that create benches or terraces within the scar may indicate that this is the most deformed part of the edifice, causing it to be more easily affected by erosional processes. The locations and opening directions of the scars are consistent with deformed sectors of volcanoes affected by normal faults with a strike-slip component occurring at the base and facing toward the edifice (Wooller et al., 2009). Pegleg Mountain also has two scar traces but unlike Swain Mountain, there is no nearby fault that can be explicitly connected to it. Thus, all sectors of the volcano are affected by gullies.

In the northern portion of the Hat Creek Graben region, where both the Rocky Ledge and Hat Creek faults terminate, and more dense Primary Regional 1 and 2 faults, and other Quaternary faults, are delineated, Chalk, Bald, Soldier, Haney, Saddle and Burney Spring Mountains are observed to be heavily traversed by the regional structures. In addition, the volcanoes occur along a major river (the Pit River), so they have many more erosional features and gullies in almost all sectors. They are therefore more affected by both frequent sliding and gully formation than other volcanoes.

On the eastern side of the study area, two volcanic edifices, Cone and Cal Mountains, each, have two erosional scars opening in opposite directions. There is no clear trace of a regional fault or any manifestation of movement of possible faults except for these scars.

5.2.3. Splitting Volcanoes, and the Faults Splitting Them

A few volcanoes are either very young, composed of strong and consolidated materials, or constructed on relatively stable basements. Even though they stand atop regional faults, may remain intact, except for splitting, in which some parts of the edifice move vertically relative to adjacent areas. Splitting volcanoes are affected by through-going faults, deforming yet not causing major instability or collapse. Whaleback, Fox, and Bogard (**Figure 4F**) Mountains are examples of this. Freaner and Wilcox (**Figure 4B**) are splitting elliptical volcanoes, as shown by vertical differences between adjacent parts of the edifices. Some volcanoes, such as West Prospect Peak, Prospect Peak (**Figure 4E**), and Sugarloaf (**Figure 4B**), have retained their ellipticity and regularity, even though faults split them.

5.3. Fault vs. Dike Dominated Regional Extension

In magmatic slow and ultraslow spreading plate boundaries and rift zones, extension is often accommodated by magmatic activity, or diking with associated faulting (Acocella and Trippanera, 2016, and references therein). Normal faults that propagate from the surface downwards and create graben-like structures on the surface are recurrent structural features. Symmetric, minor grabens are observed in Lakagigar and Bardarbunga in Iceland, and Dallol in Afar, induced by single diking episodes. Asymmetric, larger grabens can be seen in Krafla, Iceland, and Fantale, Ethiopia, formed by repeated or distributed diking. At these spreading plate boundaries, extension at depth seems to be accommodated mostly by diking, with normal faulting playing a negligible role. In shallower layers, normal faults and extensional tectonic structures accommodate the deformation, alongside a few feeder dikes (Acocella and Trippanera, 2016, and references therein).

While we cannot rule out the idea that dikes play a major role in extension at depth in the Hat Creek Graben region, and that some of the shorter faults might have been generated by diking episodes, it seems that at shallower levels, regional normal faults accommodate most of the extension. The extent of the Hat Creek Graben region, its regional fault systems with total displacements as high as a few hundred meters, recurrence intervals of a few 100 years, and the influence of the regional fault systems on the development of the volcanoes furthermore suggest that it is unlikely that most accommodation is by diking episodes, even deeper in the crust. The Hat Creek Graben region and the East African Rift are spreading at similar rates of $2.9 \pm 0.8\,\mathrm{mm\ yr^{-1}}$ (Zeng and Shen, 2014) and $3\text{–}4\,\mathrm{mm\ yr^{-1}}$ (Stamps et al., 2008), respectively. However, it appears that the Hat Creek Graben region has a lower magma supply rate because it has smaller volcanoes than does the East African Rift (Grosse et al., 2014). The Hat Creek Graben region presents as an example of a different mechanism of extension in a small rift system associated with a transform plate boundary.

6. CONCLUSIONS

Topographic mapping and modeling, based mostly on NED data, were used to describe the geomorphology and structures of the Hat Creek Graben region. In addition to the obvious, known major geomorphological features, such as Lassen Peak, Pit River and Hat Creek valleys, smaller-scale geomorphological features, including mountain ridges, volcanic edifices, and lava fields, were characterized in detail using different topographic modeling techniques. Initial assessment of the shape and regularity of the volcano bases gave an overview of the processes that have affected or are currently affecting the volcanoes. Erosional features and the density of structures delineated on volcanoes were also noted. The study can serve as a standard for other volcanic areas in the world with strong tectonic interaction.

Using the height and basal width ratios from the morphometric analysis allowed us to classify the individual volcanic edifices of the Hat Creek Graben region as cones, sub-cones, shields and massifs. Separating those less than 350 m high as smaller cones, sub-cones and shields revealed an evolutionary trend of volcanic forms in the region: smaller cones can grow into bigger cones if they increase their height in proportion to their basal width, or evolve into sub-cones if their basal width increases faster than their height. Smaller sub-cones can grow into bigger sub-cones, or grow into the wide variety of shields or massifs; and smaller shields can grow into larger shields or massifs. As volcanoes develop and grow on top of major regional faults, their activity and growth pattern are influenced by regional extension accommodated on north-northwest striking faults that are mostly normal with strike-slip component. The stress regime and fault orientation can cause edifice deformation by collapse, erosion, or splitting. The majority of the deformational features, often manifested as collapse scars or erosional breaches, have opening directions perpendicular to the maximum horizontal stress, similar to those in other extensional settings (Tibaldi, 1995) and may, therefore, be related to the normal component of movement on the underlying faults. A considerable number, however, open at an acute angle and therefore are affected by the right-lateral component of movement on the underlying faults.

Spatial distribution varies for the volcano subgroups in the Hat Creek Graben region. The smaller volcanoes subgroup, and the combined smaller and bigger volcanoes, are clustered with northwest-southeast alignments formed by at least three volcanoes within 6 km of one another, while the bigger volcanoes subgroup is random and dispersed. This implies that the initial and clustered growth of volcanoes in the Hat Creek Graben region is controlled by the pre-existing major structures. Thus, the regional structures and volcanoes within the Hat Creek Graben region are interacting. The spatial dispersion of the bigger volcanoes can be attributed to volcanogenic, near-surface pressure changes—as volcanoes grow and long-lived plumbing systems develop—capable of refocusing local dikes. Thus, in the case of the Hat Creek Graben region, the regional, pre-existing major faults within the crust greatly influenced the initial alignment and distribution of volcanoes, and their continued growth is closely related to local as well as regional strain.

Faults (by slip) and volcanoes (by increasing total crustal volume through dilation during intrusion and propagation of magma to the surface) both accommodate regional extension in the Hat Creek Graben region. However, extension is accommodated more by faulting than by dikes, which along with the small size of the stratovolcanoes, suggests that the magma supply rate is low, with low-pressure, as magma propagates to the surface using the most efficient, easiest, pre-existing fractures. Thus, the propagation of magma to the surface through a complex plumbing system has been insufficient to accommodate much of the extension, which is therefore dominated by normal and other extensional, purely tectonic structures. This is manifested by the dominantly fault-related topography of the Hat Creek Graben region, and the overwhelming control of the tectonic structures on the growth, development, and evolution of volcanoes. The tectonic structures should continue to have a great influence on the stability and deformation of the volcanoes into the future.

We recognize that a more comprehensive factoring in of temporal data, such as description of erosion rates, and dating of collapse events relative to the age of fault activity, will be important for a complete characterization of the morphological and morphometric evolution of the Hat Creek Graben region.

AUTHOR CONTRIBUTIONS

EP and MB both contributed to the conception and design of the work, acquired, analyzed, and interpreted the data for the work. EP executed the detailed analyses, and drafted the manuscript. Revisions were made by both EP and MB. We both approved the version of the manuscript we submitted and we will both be accountable for the accuracy and integrity of this work.

ACKNOWLEDGMENTS

We thank Laura Pioli and Gianluca Groppelli, and the Associate Editor, Dr. Roberto Sulpizio for their comprehensive and constructive reviews. We also thank the Editor in Chief, Dr. Valerio Acocella for his helpful comments. Dr. G. N. Fabbro provided essential help in formatting technicalities and improving the drafts. We are grateful for field assistance by Mr. G. Bursik and Ms. Leandra Marshall. This research was funded in part by NASA grant NNX12AQ10G, and by the State University of New York.

SUPPLEMENTARY MATERIAL

The Supplementary Material for this article can be found online at: http://journal.frontiersin.org/article/10.3389/feart.2016.00076

REFERENCES

Acocella, V., and Trippanera, D. (2016). How diking affects the tectonomagmatic evolution of slow spreading plate boundaries: overview and model. *Geosphere* 12:GES01271.1. doi: 10.1130/GES01271.1

Argus, D. F., and Gordon, R. G. (1991). Current Sierra Nevada-North America motion from very long baseline interferometry: implications for the kinematics of the western United States. *Geology* 19, 1085–1088.

Austin, L. J. (2013). "Fault kinematics from LiDAR analysis of the Rocky Ledge Fault, Shasta County, California," in *Geological Society of America Abstracts with Programs* (Denver, CO: Geological Society of America), 546.

Bahar, I., and Girod, M. (1983). Controle structural du volcanisme indonesien (Sumatra, Java-Bali); application et critique de la methode de Nakamura. *Bull. Soc. Geol. Fr.* XXV, 609–614. doi: 10.2113/gssgfbull.S7-XXV.4.609

Baloga, S. M., Glaze, L. S., and Bruno, B. C. (2007). Nearest-neighbor analysis of small features on Mars: applications to tumuli and rootless cones. *J. Geophys. Res. E Planets* 112, 1–17. doi: 10.1029/2005JE002652

Beggan, C., and Hamilton, C. W. (2010). New image processing software for analyzing object size-frequency distributions, geometry, orientation, and spatial distribution. *Comput. Geosci.* 36, 539–549. doi: 10.1016/j.cageo.2009.09.003

Bennett, R. A., Davis, J. L., and Wernicke, B. P. (1999). Present-day pattern of Cordilleran deformation in the western United States. *Geology* 27, 371–374.

Blakely, R. J., Christiansen, R. L., Guffanti, M., Wells, R. E., Donnelly-Nolan, J. M., Muffler, L., et al. (1997). Gravity anomalies, Quaternary vents, and Quaternary faults in the southern Cascade Range, Oregon and California: implications for arc and backarc evolution. *J. Geophys. Res.* 102:22513. doi: 10.1029/97JB01516

Blakeslee, M. W., and Kattenhorn, S. A. (2013). Revised earthquake hazard of the Hat Creek fault, northern California: a case example of a normal fault dissecting variable-age basaltic lavas. *Geosphere* 9, 1397–1409. doi: 10.1130/GES00910.1

Bleacher, J. E., Glaze, L. S., Greeley, R., Hauber, E., Baloga, S. M., Sakimoto, S. E. H., et al. (2009). Spatial and alignment analyses for a field of small volcanic vents south of Pavonis Mons and implications for the Tharsis province, Mars. *J. Volcanol. Geotherm. Res.* 185, 96–102. doi: 10.1016/j.jvolgeores.2009.04.008

Caputo, R. (1995). Evolution of orthogonal sets of coeval extension joints. *Terra Nov.* 7, 479–490. doi: 10.1111/j.1365-3121.1995.tb00549.x

Clark, P. J., and Evans, F. C. (1954). Distance to nearest neighbor as a measure of spatial relationships in populations. *Ecol. Soc. Am.* 35, 445–453. doi: 10.2307/1931034

Connor, C. B., Condit, C. D., Crumpler, L. S., and Aubele, J. C. (1992). Evidence of regional structural controls on vent distribution: springerville volcanic field, Arizona. *J. Geophys. Res.* 97, 12349–12359. doi: 10.1029/92JB00929

Dixon, T. H., Miller, M., Farina, F., Wang, H., and Johnson, D. (2000). Present-day motion of the Sierra Nevada block and some tectonic implications for the Basin and Range province, North American Cordillera. *Tectonics* 19:1. doi: 10.1029/1998TC001088

Dokka, R., and Travis, J. (1990). Role of the eastern california shear zone in integrated shear along the to historic measurements mm yr present rate mm yr 4 determined. *Geophys. Res. Lett.* 17, 1323–1326. doi: 10.1029/GL017i009p01323

Ebinger, C., Ayele, A., Keir, D., Rowland, J., Yirgu, G., Wright, T., et al. (2010). Length and timescales of rift faulting and magma intrusion: the afar rifting cycle from 2005 to present. *Annu. Rev. Earth Planet. Sci.* 38, 439–466. doi: 10.1146/annurev-earth-040809-152333

Eppler, D. B., Fink, J., and Fletcher, R. (1987). Rheologic properties and kinematics of emplacement of the chaos jumbles rockfall avalanche, Lassen Volcanic National Park, California. *J. Geophys. Res.* 92:3623. doi: 10.1029/JB092iB05p03623

Faulds, J. E., Henry, C. D., and Hinz, N. H. (2005). Kinematics of the northern Walker Lane: An incipient transform fault along the Pacific-North American plate boundary. *Geology* 33, 505–508. doi: 10.1130/G21274.1

Francis, P., and Wells, A. (1988). LANDSAT Thematic Mapper observa- tions of debris avalanche deposits in the Central Andes. *Bull. Volcanol.* 50, 258–278. doi: 10.1007/BF01047488

Gesch, D., Oimoen, M., Greenlee, S., Nelson, C., Steuck, M., and Tyler, D. (2002). The national elevation dataset. *Photogramm. Eng. Remote Sens.* 68, 5–32.

Grosse, P., Euillades, P. A., Euillades, L. D., and van Wyk de Vries, B. (2014). A global database of composite volcano morphometry. *Bull. Volcanol.* 76:784. doi: 10.1007/s00445-013-0784-4

Grosse, P., van Wyk de Vries, B., Euillades, P. A., Kervyn, M., and Petrinovic, I. A. (2012). Systematic morphometric characterization of volcanic edifices using digital elevation models. *Geomorphology* 136, 114–131. doi: 10.1016/j.geomorph.2011.06.001

Grosse, P., van Wyk de Vries, B., Petrinovic, I. A., Euillades, P. A., and Alvarado, G. E. (2009). Morphometry and evolution of arc volcanoes. *Geology* 37, 651–654. doi: 10.1130/G25734A.1

Hamilton, C. W., Fagents, S. A., and Thordarson, T. (2010). Explosive lavawater interactions II: self-organization processes among volcanic rootless eruption sites in the 17831784 Laki lava flow, Iceland. *Bull. Volcanol.* 72, 469–485. doi: 10.1007/s00445-009-0331-5

Hammond, W. C., and Thatcher, W. (2005). Northwest Basin and Range tectonic deformation observed with the Global Positioning System, 1999-2003. *J. Geophys. Res. Solid Earth* 110, 1–12. doi: 10.1029/2005JB003678

Hammond, W. C., and Thatcher, W. (2007). Crustal deformation across the Sierra Nevada, northern Walker Lane, Basin and Range transition, western United States measured with GPS, 2000-2004. *J. Geophys. Res. Solid Earth* 112, 1–26. doi: 10.1029/2006JB004625

Heidbach, O., Tingay, M., Barth, A., Reinecker, J., Kurfeß, D., and Müller, B. (2008). *The World Stress Map Database Release 2008*. doi: 10.1594/GFZ.WSM.Rel2008

Jenkins, O. (1938). *Geomorphic Map of California: California Division of Mines and Geology Map Sheet, Scale Approximately 1:2,000,000.*

Jolly, R., and Sanderson, D. (1997). A Mohr circle construction for the opening of a pre-existing fracture. *J. Struct. Geol.* 19, 887–892. doi: 10.1016/S0191-8141(97)00014-X

Lagmay, A. M. F., and Valdivia, W. (2006). Regional stress influence on the opening direction of crater amphitheaters in Southeast Asian volcanoes. *J. Volcanol. Geotherm. Res.* 158, 139–150. doi: 10.1016/j.jvolgeores.2006.04.020

Le Corvec, N., Spörli, K. B., Rowland, J., and Lindsay, J. (2013). Spatial distribution and alignments of volcanic centers: clues to the formation of monogenetic volcanic fields. *Earth-Sci. Rev.* 124, 96–114. doi: 10.1016/j.earscirev.2013.05.005

McCaffrey, R. (2005). Block kinematics of the Pacific-North America plate boundary in the southwestern United States from inversion of GPS, seismological, and geologic data. *J. Geophys. Res. Solid Earth* 110, 1–27. doi: 10.1029/2004JB003307

Miliaresis, G., and Kokkas, N. (2004). Segmentation and terrain modeling of extraterrestrial chasmata. *J. Spat. Sci.* 49, 89–99. doi: 10.1080/14498596.2004.9635024

Miller, M., Johnson, D. J., Rubin, C. M., Dragert, H., Wang, K., Qamar, A., et al. (2001). GPS-determination of along-strike variation in Cascadia margin kinematics: implications for relative plate motion, subduction zone coupling, and permanent deformation. *Tectonics* 20, 161–176. doi: 10.1029/2000TC001224

Moriya, I. (1980). *Bandaian Eruption and Landforms Associated with It: Collection of Articles in Memory of Retirement of Prof. K. Hishimura*. Technical Report, Tohoku University.

Muffler, L., Blakely, R. J., and Clynne, M. (1994). Late Quaternary normal faulting of the Hat Creek Basalt, Northern California. *Geol. Soc. Am. Bull.* 106, 195–200.

Muffler, L., Robinson, J., Felgar, T., Dutton, D., and Clynne, M. (2010). *Database for the Geologic Map of Lassen Volcanic National Park and Vicinity, California.* Data to accompany Scientific Investigations Map 2899. Available online at: http://pubs.usgs.gov/sim/2899/database.html

Nakamura, K. (1977). Volcanoes as possible indicators of tectonic stress orientation-principle and proposal. *J. Volcanol. Geotherm. Res.* 2, 1–16. doi: 10.1016/0377-0273(77)90012-9

Paguican, E. M. R., van Wyk de Vries, B., and Lagmay, A. M. F. (2014). Hummocks: how they form and how they evolve in rockslide-debris avalanches. *Landslides* 11, 67–80. doi: 10.1007/s10346-012-0368-y

Parrish, J. G. (2006). *Simplified Geologic Map of California.* California Geological Survey, Map Sheet 57. Available online at: http://www.conservation.ca.gov/cgs/information/publications/ms/documents/ms057.pdf

Perez, F. L. (1998). Talus fabric, clast morphology, and botanical indicators of slope processes on the chaos crags (California cascades), U.S.A. *Geogr. Phys. Quat.* 52, 1–22. doi: 10.7202/004861ar

Peterson, J., and Martin, L. (1980). *Geologic Map of the Baker-Cypress BLM Roadless Area and Timbered Crater Rare II Areas, Modoc, Shasta, and Siskiyou Counties, Northeastern California.* U.S. Geological Survey, Miscellaneous Field Studies Map 1214-A. Available online at: https://pubs.er.usgs.gov/publication/mf1214A

Sauber, J., Thatcher, W., Solomon, S., and Lisowski, M. (1994). Geodetic slip rate for the Eastern California shear zone and the recurrence time of Mojave Desert earthquakes. *Nature* 367, 264–266. doi: 10.1038/367264a0

Sawyer, T., and Ramelli, A. (2012). *Structural Analysis, Evaluation, and Quaternary Activity of the Hat Creek and Rocky Ledge Faults, Shasta County, Northeastern California*. Technical Report, Piedmont Geosciences Report, October 2012.

Siebert, L. (1984). Large volcanic debris avalanches: characteristics of source areas, deposits, and associated eruptions. *J. Volcanol. Geotherm. Res.* 22, 163–197. doi: 10.1016/0377-0273(84)90002-7

Sigmundsson, F., Hooper, A., Hreinsdóttir, S., Vogfjörd, K. S., Ófeigsson, B. G., Heimisson, E. R., et al. (2015). Segmented lateral dyke growth in a rifting event at BárÃřarbunga volcanic system, Iceland. *Nature* 517, 191–195. doi: 10.1038/nature14111

Stamps, D. S., Calais, E., Saria, E., Hartnady, C., Nocquet, J. M., Ebinger, C. J., et al. (2008). A kinematic model for the East African Rift. *Geophys. Res. Lett.* 35, 1–6. doi: 10.1029/2007GL032781

Tibaldi, A. (1995). Morphology of pyroclastic cones and tectonics. *J. Geophys. Res.* 100, 24521–24535. doi: 10.1029/95JB02250

Ui, T., Yamamoto, H., and Suzuki-Kamata, K. (1986). Characterization of debris avalanche deposits in Japan. *J. Volcanol. Geotherm. Res.* 29, 231–243. doi: 10.1016/0377-0273(86)90046-6

U.S. Geological Survey and California Geological Survey (2006). *Quaternary Fault and Fold Database for the United States*. Available online at: http://earthquake.usgs.gov/hazards/qfaults/

Valentine, G., and Krogh, K. (2006). Emplacement of shallow dikes and sills beneath a small basaltic volcanic center The role of pre-existing structure (Paiute Ridge, southern Nevada, USA). *Earth Planet. Sci. Lett.* 246, 217–230. doi: 10.1016/j.epsl.2006.04.031

Valentine, G. A., and Hirano, N. (2010). Mechanisms of low-flux intraplate volcanic fields - Basin and Range (North America) and northwest Pacific Ocean. *Geology* 38, 55–58. doi: 10.1130/G30427.1

Wadge, G., and Cross, A. (1988). Quantitative methods for detecting aligned points: an application to the volcanic vents of the Michoacan-Guanajuato volcanic field, Mexico. *Geology* 16, 815–818.

White, I., and Crider, J. (2006). Extensional fault-propagation folds: mechanical models and observations from the Modoc Plateau, Northeastern California. *J. Struct. Geol.* 28, 1352–1370. doi: 10.1016/j.jsg.2006.03.028

Wills, C. J. (1991). Active faults north of Lassen Volcanic National Park, Northern California. *Calif. Geol.* 44, 49–72.

Wooller, L., van Wyk de Vries, B., Cecchi, E., and Rymer, H. (2009). Analogue models of the effect of long-term basement fault movement on volcanic edifices. *Bull. Volcanol.* 71, 1111–1131. doi: 10.1007/s00445-009-0289-3

Wright, T. J., Ebinger, C., Biggs, J., Ayele, A., Yirgu, G., Keir, D., et al. (2006). Magma-maintained rift segmentation at continental rupture in the 2005 Afar dyking episode. *Nature* 442, 291–294. doi: 10.1038/nature04978

Zeng, Y., and Shen, Z. K. (2014). Fault network modeling of crustal deformation in California constrained using GPS and geologic observations. *Tectonophysics* 612–613, 1–17. doi: 10.1016/j.tecto.2013.11.030

Conflict of Interest Statement: The authors declare that the research was conducted in the absence of any commercial or financial relationships that could be construed as a potential conflict of interest.

Advantages of publishing in Frontiers

OPEN ACCESS
Articles are free to read,
for greatest visibility

COLLABORATIVE PEER-REVIEW
Designed to be rigorous
– yet also collaborative,
fair and constructive

85

FAST PUBLICATION
Average 85 days from
submission to publication
(across all journals)

COPYRIGHT TO AUTHORS
No limit to article
distribution and re-use

TRANSPARENT
Editors and reviewers
acknowledged by name
on published articles

SUPPORT
By our Swiss-based
editorial team

IMPACT METRICS
Advanced metrics
track your article's impact

GLOBAL SPREAD
5'100'000+ monthly
article views
and downloads

LOOP RESEARCH NETWORK
Our network
increases readership
for your article

Frontiers
EPFL Innovation Park, Building I • 1015 Lausanne • Switzerland
Tel +41 21 510 17 00 • Fax +41 21 510 17 01 • info@frontiersin.org
www.frontiersin.org

Find us on